

Terahertz Time Domain Spectroscopy of Amino Acids and Sugars

Thesis by

Matthew Kelley

In Partial Fulfillment of the Requirements

for the Degree of

Doctor of Philosophy



California Institute of Technology

Pasadena, California

2013

(Submitted April 23, 2013)

© 2013

Matthew Kelley

All Rights Reserved

I dedicate this thesis to the Blake Lab, that it may help some poor graduate student find aid while working with THz-TDS or the laser system.

Acknowledgements

I would like to thank my labmates, as for many years they were few and far between. In particular, I will never forget working with Rogier Braakman on the hot electron bolometer, traveling to Hawaii and Australia, playing “pool ball” (a game we invented in Hawaii) watching and discussing the NBA far too much, or arguing endlessly because we were both hard-headed enough not to give in at all when we thought we were right.

Daniel Holland has been my labmate for the longest period of time. Dan’s many quirks and atypical opinions and practices always left things interesting. His attention to detail contrasts with my natural state, and really opened up a lot of holes in my thought processes and supposed knowledge. Dan constantly introduced me to new scientific experiments and concepts that he had read about. When I was going through tough personal times in 2010, Dan displayed genuine concern and compassion. I am very thankful to Dan for this display.

While my labmates proved very helpful in thinking about science, mostly we shared a deep sense of camaraderie due to the academic situation that we were in. Namely, we were all in a lab situation where we were both completely untrained due to lack of senior students and had relatively little supervision. We also underwent a change in the direction of the lab in 2008 when ultrafast lasers were acquired.

This is not to demean the intentions of our adviser, Geoff Blake. Geoff always wanted us to learn how to educate ourselves and to be capable of thinking of and executing our own research projects. This often meant giving us the opportunity to fail. He supported whatever interests

we had whether academic or not and often engaged us in discussion about bigger picture issues.

Thanks also to Marco Allodi, the “new” student who was to be my replacement well over three years ago. In working with him and teaching him the ways of the lab, I found many holes in my own understanding of things and he helped to further refine the THz-TDS spectrometer.

Thanks also to my more recent labmates: Brandon Carroll, Ian Finneran, Brett McGuire, and Sergio Ioppolo. I would also like to thank Laurence Yeung and Kana Takematsu, two of the other experimental physical chemistry students that entered graduate school at the same time that I did. We did problem sets together and remain friends and colleagues today.

While academic support has been discussed, this section would be woefully incomplete if I left out the emotional support of my friends and roommates. In my first year, I lived in the Catalina Graduate Apartments with Mike Rubel. Mike was a *n*th year graduate student who helped me to weather the turmoil of settling into a new place and dealing with the realization that most people at Caltech must learn to accept — that I was not as smart as I thought I was and had a *lot* to learn.

Kana, Laurence and I also joined a group of people in weekly potlucks and games. Through the potluck group, I met Eve Stenson, Brian Standley, Jessie Rosenberg, and Neil Halelamien, and we rented a house together for several years, which we dubbed “The Keep.” This became the default location for the weekly potlucks. During this time, I spent some time volunteering with the Caltech Y, specifically helping to run our monthly trips to Union Station, a homeless shelter in Pasadena, where we cooked rather complex meals for the residents. Kai Shen, the leader at the time, invited me to join Prufrock, an eating group at Caltech, in which we took turns cooking for each other once a month. I did join and met a variety of students from many disciplines in all years of study. In 2008 we were forced to move out of The Keep due to the real estate crisis of 2008 and I moved into the Prufrock house as a core member. Unfortunately, my stay there did not last long, as we lost the pest control battle to fleas and Caltech Housing

decided to repurpose the house after presumably getting rid of the problem. I then moved back in with Neil and his brother Marvin in a new house. While I was very angered by the situation at the time, it was a good move for me, as I became very close with Neil and Marvin, and really felt like I had a home for the first time at Caltech.

I should also mention the Caltech Floorball Club, of which I have been a member since late 2005. Physical activities have been very important to me at Caltech, but my involvement in most has been short-lived in comparison to Floorball. With Floorball, a game like indoor-hockey but played with a hollow plastic ball, I felt like a real part of a team and a community, along with having the opportunity to release stress through physical activity. A large part of this is due to Andrew and Meredith Beyer, my friends and the leaders of the club for many years. While we have never won a tournament, we have gotten close many times, and our skills have vastly improved.

Lastly, I would like to thank Chris Nederveld and Alex Cheng, two of my closest friends, who I met playing online video games, for some of the most fun and carefree times I've ever had.

My family, while physically distant during the process of obtaining my Ph D, have had perhaps the most impact on my success to date. Both my mother and father instilled in me the importance of education from a young age. I remember first becoming interested in astronomy — particularly in planets — in the third grade. My dad helped me to find books and pictures from telescopes in books at the library. Later, when I became interested in chemistry, he provided equal assistance in applying for college, scholarships, REU or SURF programs during the summer, and ultimately graduate school. But, perhaps what most enabled my success was the large amount of money put forth. My parents insisted that we go to good schools throughout our education, despite the cost, which was not always easy to bear. One of the biggest decisions in this regard was choice of high school. The school that I wanted to

go to, and that was academically superior, also cost the most money of the prospects by a large margin. Through financial aid, my own work throughout high school, and my parents' willingness to spend a large portion of their money on education, I was able to attend. There, in AP Chemistry, I was inspired by my teacher, Dr. Claire Baker, to pursue physical chemistry in college. I also wish to thank my family for support during the tough times in my life, before and during graduate school, and, yes Mom, I am finally done now.

Abstract

A time-domain spectrometer for use in the terahertz (THz) spectral range was designed and constructed. Due to there being few existing methods of generating and detecting THz radiation, the spectrometer is expected to have vast applications to solid, liquid, and gas phase samples. In particular, knowledge of complex organic chemistry and chemical abundances in the interstellar medium (ISM) can be obtained when compared to astronomical data. The THz spectral region is of particular interest due to reduced line density when compared to the millimeter wave spectrum, the existence of high resolution observatories, and potentially strong transitions resulting from the lowest-lying vibrational modes of large molecules.

The heart of the THz time-domain spectrometer (THz-TDS) is the ultrafast laser. Due to the femtosecond duration of ultrafast laser pulses and an energy-time uncertainty relationship, the pulses typically have a several-THz bandwidth. By various means of optical rectification, the optical pulse carrier envelope shape, i.e. intensity-time profile, can be transferred to the phase of the resulting THz pulse. As a consequence, optical pump-THz probe spectroscopy is readily achieved, as was demonstrated in studies of dye-sensitized TiO_2 , as discussed in chapter 4. Detection of the terahertz radiation is commonly based on electro-optic sampling and provides full phase information. This allows for accurate determination of both the real and imaginary index of refraction, the so-called optical constants, without additional analysis. A suite of amino acids and sugars, all of which have been found in meteorites, were studied in crystalline form embedded in a polyethylene matrix. As the temperature was varied between

10 and 310 K, various strong vibrational modes were found to shift in spectral intensity and frequency. Such modes can be attributed to intramolecular, intermolecular, or phonon modes, or to some combination of the three.

Contents

Acknowledgements	iv
Abstract	viii
1 Introduction	1
1.1 Terahertz Time Domain Spectroscopy	8
1.1.1 Ultrafast Lasers	10
1.1.2 Ultrafast Pulse Principles and Optics	14
1.1.2.1 The Fourier Transform	15
1.1.2.2 Dispersion and Chirp	16
1.1.2.3 Pulse Shaping	19
1.1.2.4 Nonlinear Effects	20
1.1.2.5 Phase Matching	22
1.1.3 Techniques for THz-TDS Emission	24
1.1.3.1 Photoconductive THz Generation	24
1.1.3.2 Optical Rectification	26
1.1.3.3 Tilted Pulse Front	29
1.1.3.4 Two-Color Laser-Induced Plasma	32
1.1.3.5 DFG-Based THz	37
1.1.4 Detectors	38

1.1.4.1	Electro-Optic Detection	39
1.1.4.2	Air-Based Detection	42
1.1.5	Determination of Optical Constants	44
1.1.6	Time-Resolved Spectroscopy	49
2	THz TDS as Implemented in the Blake Group	50
2.1	Introduction and Overview	50
2.2	Laser Systems	52
2.2.1	Oscillators	52
2.2.2	Regenerative Amplifier	54
2.3	Delay Line	55
2.4	THz Emission Techniques	57
2.4.1	Optical Rectification	58
2.4.1.1	ZnTe	58
2.4.1.2	GaP	59
2.4.2	Plasma-based Emission	60
2.4.2.1	Phase Compensation	62
2.4.3	Field Strength Calculation	64
2.5	Electro-Optic Detection	66
2.5.1	Lock-In Amplifier	67
2.5.2	Oscilloscope Based Detection	67
2.5.2.1	Pulse Normalization	68
2.6	Air-biased Coherent Detection	69
2.7	Purging Considerations	72
2.8	Noise and Limits to Signal Processing	73

2.8.1	Laser Noise	74
2.8.2	Shot Noise	74
2.8.3	Electronic Noise	75
2.8.4	Etalon Removal	76
3	THz Torsional Modes of Amino Acid and Sugar Crystals	78
3.1	Introduction	78
3.2	Amino Acids and Sugars	80
3.3	Experimental	85
3.4	Results	87
3.4.1	Amino Acids	87
3.4.1.1	γ -Aminobutyric Acid	88
3.4.1.2	Glutamic Acid	95
3.4.1.3	Glycine	96
3.4.1.4	Glycolaldehyde	97
3.4.1.5	Aspartic Acid	99
3.4.1.6	2-Aminoisobutyric Acid	100
3.4.1.7	Alanine	103
3.4.2	Sugars	106
3.4.2.1	Xylose	106
3.4.2.2	Sucrose	108
3.4.2.3	D-Ribose	112
3.4.2.4	D-Mannose	113
3.4.2.5	D-Arabinose	115
3.4.2.6	D-Glucose	118

3.4.2.7	D-Fructose	120
3.5	Discussion	121
3.5.1	Theory	125
3.6	Conclusions	127
4	Time-Resolved THz Spectroscopy	129
4.1	Introduction	129
4.2	GaAs	129
4.3	Dye-Sensitized Solar Cells	131
5	Future Prospects	135
5.1	Introduction	135
5.2	Improvements to THz spectroscopy	135
5.2.1	Air-Based Coherent Detection	136
5.2.2	Single-Shot Detection	137
5.2.3	OPA-Tuned Two-Color Plasma Emission	139
5.2.4	THz Pulse-to-Pulse Noise Reduction	140
5.2.5	Other Improvements	141
5.3	Future Experiments: THz Nonlinear Spectroscopy and Coherent Control	143
5.3.1	Two-Dimensional Far-Infrared Spectroscopy	144
5.3.2	Coherent Control	147
5.3.2.1	Pulse Shaping	155
5.3.2.2	Ladder Climbing	156
6	Appendices	194
6.1	Matlab Code for THz Scanning Software	194

6.1.1	Continuous Scan	199
6.1.2	Pulse Normalization Scan	200
6.2	Matlab Code for Optical Constant Determination	205
6.3	Laser Alignment and Maintenance	209
6.3.1	Mantis	210
6.4	THz Optical Alignment	213
6.5	Autocorrelator	214

List of Figures

1.1	A graphical comparison of frequency scales	3
1.2	A standard experimental layout for THz-TDS experiments.	9
1.3	An 18 cycle pulse with both the normalized electric field strength (blue) and amplitude (green) plotted.	10
1.4	Timescale of various processes and reactions related to chemistry.	11
1.5	The sum of a) 9, b) 19, c) 99, and d) 999 evenly spaced modes around 374.7 THz (800 nm) following the gain profile of Ti:Sapphire with assumed Gaussian intensity and 40 nm bandwidth output pulse. Of note is the intensity scale, which increases dramatically as the number of modes increases; along with the time with respect to the cavity length, which is set by the speed of light divided by the round trip time.	13
1.6	A prism pair for dispersion compensation by negatively chirping a pulse.	18
1.7	Linearly chirped and unchirped pulses at a center wavelength of 800 nm.	20
1.8	A depiction of the process of optical rectification at 800 nm.	26
1.9	A standard experimental layout for electro-optic (EO) detection	39
1.10	Reference and sample THz waveforms demonstrating the effect of constant $n(\omega)$ and $k(\omega)$	45
1.11	A depiction of the intricacies of optical constant determination in an enclosed cell.	48

1.12	A standard experimental setup for time resolved THz-TDS, wherein an optical probe pulse excites the sample, while the changes to the THz spectrum are monitored as a function of time.	49
2.1	A comparison of the base-10 logarithmic FFT magnitude of the pulses seen in the next figure.	52
2.2	Comparison of THz sources and detectors showing the improvement in frequency coverage resulting from the extra intensity and bandwidth of the plasma source. .	53
2.3	A typical spectrum of the Mantis as sensed by an Ocean Optics USB4000 spectrometer. The “noise” at the peak is due to etalons in the detector.	54
2.4	A direct comparison of 1 mm thick ZnTe and 0.2 mm thick ZnTe emitters as detected by the same 1.0 mm thick ZnTe wafer demonstrating the overall superior performance of the thinner wafer. The water stick spectrum is shown for comparison purposes.	59
2.5	A normalized comparison of GaP and ZnTe emitters as detected by the same 1.0 mm thick ZnTe wafer. The GaP spectrum is weighted more toward higher frequencies.	60
2.6	The in-line phase compensator used for THz generation via two-color laser plasma. The device’s main purpose is to orient the 800 and 400 nm beams with the same polarization.	64
2.7	A) The noise spectrum of the Legend as sensed by the EO balanced detector setup. B) The noise spectrum of the Evolution as sensed by a heavily filtered Si photodiode detector, model PDA36A from Thorlabs.	75
2.8	The full spectrum of a THz scan showing noise at 60 and 120 Hz. The balanced detector output is shown in red.	75

3.1	Three stereotypical potential energy surfaces, each showing differing behavior of the energy level spacing.	79
3.2	The molecular structure of the species studied using THz-TDS. The optimized or crystalline structure is used where appropriate.	81
3.3	From the top and left to the bottom, the forms of GABA present in the gas phase (1-4), with the tG form being the most energetically favored followed closely by the GG and gG forms. The tt phase is presented because it was found to be an appropriate model for the crystalline modes. The carbons are also labeled in the standard format. The zwitterionic gt structure, as determined from X-Ray and neutron scattering, is also presented. The Gg structure is the lowest energy in solution.	83
3.4	The measured transmission through a GABA pellet pressed with micronized high-density polyethylene as a function of temperature.	88
3.5	The measured transmission through a GABA/polyethylene pellet at room temperature compared with predicted results from DFT calculations, scaled by a factor of 0.88, on the tt structure of GABA. B3LYP/aug-cc-pVTz with a modified Lorentzian lineshape.	91
3.6	The measured transmission through a GABA/polyethylene pellet at room temperature compared with predicted results from DFT calculations, scaled by a factor of 0.63, on the gt crystal structure of GABA. CAM-B3LYP/cc-pVTz with a modified Gaussian lineshape.	92
3.7	The measured transmission through a glutamic acid pellet as a function of temperature compared with predicted results from DFT calculations, scaled by a factor of 1.3. The spectrum was generated from harmonic results using CAM-B3LYP/cc-pVTz with a modified Lorentzian lineshape.	95

3.8	The measured transmission through a glycolaldehyde acid pellet as a function of temperature.	98
3.9	The measured transmission through an aspartic acid pellet at 295 K using the two-color plasma THz source.	99
3.10	The log of the FFT spectrum of an α -aminoisobutyric acid pellet as a function of temperature.	102
3.11	The measured transmission through an α -aminoisobutyric acid pellet at 295 K using the two-color plasma THz source.	102
3.12	The measured transmission through an α -Alanine pellet as a function of temperature.	103
3.13	The measured transmission through a D-Xylose pellet as a function of temperature.	106
3.14	The measured transmission through a pellet consisting of 10% xylose and 90% micronized high-density polyethylene. A simulated spectrum represented by Gaussian features with height represented by the calculated intensity, FWHM manually determined (~ 0.03 THz), and frequency scaled by a factor of 0.79	108
3.15	The measured transmission through a pellet consisting of 10% sucrose and 90% micronized high-density polyethylene. A simulated spectrum represented by Gaussian features with height represented by the calculated intensity, FWHM manually determined (~ 0.03 THz), and frequency scaled by a factor of 0.88	109
3.16	The measured transmission through a sucrose pellet pressed with micronized high-density polyethylene.	111
3.17	The measured transmission through a D-Ribose pellet as a function of temperature.	112

3.18	The measured transmission through a D-Mannose pellet pressed with micronized high-density polyethylene as a function of temperature.	115
3.19	The measured transmission through a D-Mannose pellet at room temperature compared with predicted results from DFT calculations at the CAM-B3LYP/cc-pVTz level, scaled by a factor of 0.955 with a modified Gaussian line shape. . . .	117
3.20	The measured transmission through a D-Arabinose pellet as a function of temperature.	118
3.21	The measured transmission through a D-fructose pellet at room temperature compared with predicted results from DFT calculations, at the CAM-B3LYP/cc-pVTz level and scaled by a factor of 0.7 with a modified Gaussian line shape.	121
3.22	The measured transmission through a D-Fructose pellet as a function of temperature.	123
4.1	The measured change in THz signal, at peak intensity, as a function of pump-probe delay for low temperature grown GaAs illuminated under various experimental geometries. This demonstrates the importance of co-linear pumping for a true signal to be measured, even when the sample is at a THz beam waist.	130
4.2	The measured change in THz signal, at peak intensity, as a function of pump-probe delay for dye-sensitized TiO ₂ . The signal has been significantly smoothed using the Savitzky-Golay method, with care taken to maintain the same rise time and shape of the peak signal.	134
5.1	Simulation of the FFT amplitude spectrum of pulses with a carrier frequency of 1.2 THz for varying duration and phase.	152
5.2	Simulation of the time domain waveforms of pulses with a carrier frequency of 1.2 THz and varying duration and phase.	152

6.1	The graphical user interface for the continuous scan option for use with the lockin amplifier.	194
6.2	The graphical user interface for the pulse normalization scan option for use with the oscilloscope.	195
6.3	The absorption coefficient of chloroform, $\alpha(\omega)$, cm^{-1} , measured in 1 cm pathlength between two quartz windows.	209
6.4	The real index of refraction, $n(\omega)$, of chloroform measured in 1 cm pathlength between two quartz windows.	209

List of Tables

1.1	Frequency Conversions	3
1.2	Pulse Envelope Shapes	16
1.3	Parameters for common EO and OR materials [27, 29]	39
3.1	GABA Results	94
3.2	Glutamic Acid Results	97
3.3	Glycolaldehyde Results	99
3.4	L-Aspartic Acid Results	101
3.5	L-2-Aminobutyric Acid Results	104
3.6	Alanine Results	105
3.7	Xylose Results	107
3.8	Sucrose Results	110
3.9	D-Ribose Results	114
3.10	D-Mannose Results	116
3.11	D-Arabionse Results	119
3.12	D-Glucose Results	120
3.13	D-Fructose Results	122
5.1	Predictions for Ring Puckering Modes	150

Chapter 1

Introduction

The origin of life on earth, though much debated, is not known. Thanks in large measure to the broad landscape of possible chemical pathways available, no consensus exists on the method of formation of the relatively unstable organic molecules that make up life from their inorganic parent atoms and molecules. The famous experiment of Miller and Urey demonstrated the production of a host of organic molecules, including many of the amino acids that are required to form proteins, from volatile gases exposed to an electrical discharge [1, 2]. However, there are debates about the validity of both the gases used and the reducing atmosphere assumed in such experiments [3] as well as the fact that the products are racemic, favoring neither L nor D enantiomers – unlike those found in biological molecules on Earth, which have an exclusive chirality.

The assembly of an Earth-sized planet, especially one with a satellite as large as the Moon, involves cataclysmic events. Thus, the late extraterrestrial delivery of water and organics is a common theme in many of the leading theories that seek to explain the formation of the basic constituents of life such as nucleic and amino acid monomers, in the assembly of such constituents to form larger the polymeric components of life (nucleic acids, proteins, carbohydrates), and even in the formation of life itself. Amino acids, nucleobases, and sugars have all been found in the carbon-rich meteorites known as carbonaceous chondrites, among the earliest solid bodies to have formed in the inner solar system and whose refractory components pos-

sess the same elemental composition as the Sun. Numerous organic compounds, including the amino acid glycine, have been found in comets as well. The chaotic dynamical environment of the early solar system leads to frequent collisions of both asteroids and comets with the early Earth. Such impacts involve enormous amounts of kinetic energy, and the resulting pressure and temperature profile for the impacting material is such that nearly all of the chemical bonds are broken in the aftermath of the collision [4]. The Earth is a small target, however, and so small bodies scattered into the inner solar system will typically only strike the planet after many, many orbits, during which the Earth can sweep up any dust particles it encounters. The survival fraction of organic material is increased greatly by this process, and so the reduced carbon delivered by interplanetary dust particles is predicted to be several orders of magnitude greater than the that delivered by larger bodies.

Validation of such theories can be achieved in part by comparing the physical and chemical evolution of current star-forming regions with the composition of primitive (that is, the least altered by the processes of their assembly or subsequent evolution) bodies in solar system via astronomical observation. The first such regions to be studied by radio and millimeter wave telescopes and interferometers are called “hot cores,” fairly extensive regions of heated gas and dust near massive young stars that emit brightly in molecular lines; thus regions in which the chemical composition and spatial distribution of molecules can be investigated in detail. Similar physical conditions and even longer time scales are reached in the protoplanetary disks that encircle young, Sun-like stars, but over a much smaller spatial extent. Thus, the emission from such objects is rather weaker than that from hot cores, and only recently have astronomical facilities advanced to the stage where the direct investigation of planet(esimal)-forming environments is feasible.

The list of chemical species detected in the interstellar medium (ISM) and circumstellar disks now exceeds 150 entries [5]. Of these neutral molecules and ions, less than 10% have ten

Table 1.1: Frequency Conversions

	Frequency (THz)	Wavelength	Wavenumber (cm ⁻¹)	Photon Energy
Radio and Microwave	~DC - 0.3	1 m - 1 mm	0.01 - 10	0.00012 - 1.2 meV
Far Infrared/THz	0.3 - 30	1,000 - 10 μm	10 - 1000	1.2-124 meV
Mid Infrared	30 - 120	10 - 2.5 μm	1000 - 4000	124-496 meV
Near Infrared	120 - 400	2500 - 750 nm	4000 - 13,350	0.496-1.65 eV
Visible	400 - 790	750 - 380 nm	13,350 - 26,350	1.65-3.26 eV

Frequency conversion for various electromagnetic radiation bands.

or more atoms, and those having more than 13 atoms are exceedingly rare [6]. In comparison, biologically relevant amino acid monomers have between 10 and 27 atoms – with an average of 19 atoms – whereas simple sugars and sugar alcohols have between 14 and 28 atoms. Each of these groups, however, are known to individually make up more than $\sim 3\%$ of the available organic carbon found in meteorites [7]. This demonstrates that the knowledge of interstellar and nebular chemistry is severely limited. To understand the reasons behind the size limitations imposed on astronomical observations, one must understand both the spectroscopy of such molecules and the telescopes and instruments used to acquire data on the molecular content of star- and planet-forming regions.

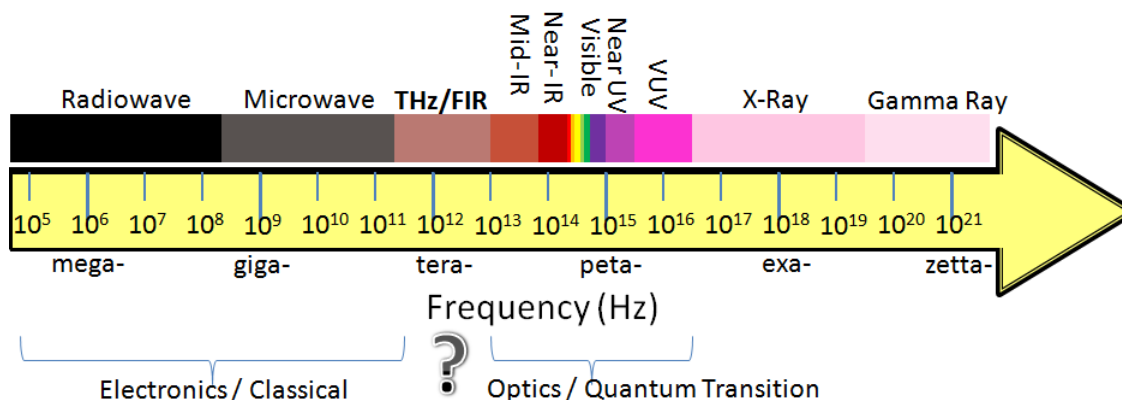


Figure 1.1: A graphical comparison of frequency scales

At distances of >300 light years, all molecules in hot cores have been detected by the remote

sensing made possible by spectroscopy at visible, infrared, radio, or microwave \rightarrow submillimeter-wave frequencies. Table 1.1 and Figure 1.1 describe conversions between the units commonly used for describing the energy of photons. For the purpose of this thesis, only the microwave to far-infrared regions of the spectrum will be considered further. The microwave and submillimeter frequency bands correspond primarily to the energy of quantized molecular *rotation* in the gas phase. In the general, so-called asymmetric top case, molecules have three moments of inertia, the angular motion analog to mass. These are directed along the orthogonal A , B , and C “principal” axes of the molecule, which intersect at the center of mass. The moments of inertia are designated as $I_A \leq I_B \leq I_C$, where $I = \sum m_j r_j^2$ is a sum over each atom along the relevant principle axis. In order to demonstrate the dependence of the rotational spectrum on size, the simple case of a linear molecule ($I_A = 0, I_B = I_C$) will be presented below. The general analysis can be extended to asymmetric top molecules in which $I_A \neq I_B \neq I_C$ [8].

For linear molecules, the rotational Hamiltonian operator is $\hat{H} = \frac{\hat{J}^2}{2I}$, and the Schrödinger equation becomes

$$\frac{\hat{J}^2\psi}{2I} = E\psi = \frac{J(J+1)\hbar\psi}{2I} = BJ(J+1)\psi \quad (1.1)$$

where $B = \frac{\hbar}{2I}$. For polar molecules, the electric dipole selection rules are $\Delta J = \pm 1$ and thus

$$h\nu_{J+1 \leftarrow J} = B(J+1)(J+2) - BJ(J+1) = 2B(J+1) \quad (1.2)$$

Thus, the frequency of each transition is inversely proportional to the moment of inertia and, generally, to the mass and size of the molecule. In asymmetric tops, far more transitions are allowed, since the presence of inequivalent moments of inertia creates both a more complex energy level structure and new selection rules. As molecules become larger and more complex, internal motions, such as inversion or internal rotation of a methyl group, can further split energy levels and make the spectrum even more dense. For example, I assigned more than 4500

transitions of methyl acetate, a molecule that I studied early in my Ph D work, in just the frequency bands between 6-18 GHz, 70-120 GHz, and 220-360 GHz. Beyond the increase in the existing number of states, thermodynamics and statistical mechanics dictate the population of each state. With increased number of states, the number of molecules in each state is diminished, causing a decrease in the light absorption or emission of the molecule/quantum state. One can imagine that if many species are present, each having thousands of transitions with characteristic line widths of ≥ 1 MHz, the ability to identify the larger and less abundant molecules can be compromised. This is exactly what is observed in complex hot cores as millimeter-wave spectra are commonly “confusion” limited due to the spectral line density and line broadening resulting from molecules with differing velocity components within the same field of view [9–11].

For any population distribution that is remotely Boltzmann in nature, there is reason to believe that as higher frequency bands are studied, the line density will eventually drop. Hence, higher frequency observatories have recently begun or will soon begin to function, whose design and location are largely motivated by circumventing the large THz absorbance of water in the Earth’s atmosphere. These observatories include the *Herschel* Space Telescope, the 747SP-based Stratospheric Observatory for Infrared Astronomy, *SOFIA*, and the Atacama Large Millimeter/sub-millimeter Array, ALMA, located in the driest mid-latitude location on earth that extends for hundreds of square kilometers at high altitude. Recent data from *Herschel* on the Orion KL nebula, a source that is spectral-line-confusion-limited at millimeter wavelengths, indicate that the line density does indeed decrease at higher frequencies, with $\sim 23\%$ of frequency space occupied by lines from 858.1 - 958.1 GHz and only $\sim 7\%$ occupied from 1788.4-1898.5 GHz [12]. This reduced line density could allow for the study of molecules that have low lying vibrational states using high resolution THz spectroscopy. Such studies form one of the fundamental driving forces for the research carried out in this thesis.

Indeed, one of the main obstacles to the studies of molecular complexity in star- and planet-forming environments, now that appropriate observatories exist, is that laboratory spectra for most prebiotic molecules do not exist in the THz spectral region, so astronomical data cannot be analyzed completely. The most relevant cause of this is the lack of conventional THz sources and detectors [13, 14]. Conventional sources of THz radiation include blackbody radiation, generation by means of electronic oscillators, and continuous wave (CW) lasers. Each suffers from one of many problems, not limited to the following, as we describe next: low output power, lack of tunability, the requirement of continuous cryogenic cooling, large size, high cost, and/or prohibitive complexity.

Spectroscopy in the far-infrared (FIR) or THz was first performed using thermal radiation, most commonly with a grating based spectrometer feeding a single detector [15]. Fourier-transform (FT) instruments, that record signals in the time- (or path difference-)domain, allowed for faster data acquisition and a concomitant signal-to-noise ratio (SNR) improvement as a consequence of the multiplex, or Fellgett's, advantage – which is pertinent when the SNR is limited by the noise of the detector rather than the source (shot) noise [16]. Challenges to spectroscopic studies with FT-FIR instruments stem from the very low photon flux of thermal sources in the FIR region, the often low resolution of the technique because of the requirement of moving a mechanical delay line over a fixed distance while maintaining high signal-to-noise over the entire range, and the lack of quality beamsplitters [17].

Classical electronic sources of sub-millimeter or THz radiation, typically generated by frequency multiplication of solid state microwave sources such as YIG or Gunn oscillators, have a number of desirable properties. They can have extremely narrow (CW) line width, good frequency tunability (at least at frequencies below 1 THz), and superb phase stability and control. The downside is that the power drops precipitously as frequencies approach 1 THz, and the possibility of extensions to frequencies in the upper ranges of the THz band (say >5-10

THz) is remote. This is also true for related vacuum electronic sources such as backwards-wave oscillators (BWOs), klystrons, traveling wave tubes (TWTs), and gyrotrons [18]. Such vacuum devices operate classically by converting the kinetic energy of an electron current into an emitted electromagnetic field. Due to ballistic, collisionless current flow, such devices can output higher powers than do solid phase sources, but often lack tunability.

Continuous wave lasers that operate directly in the FIR can provide extremely high power, but often lack frequency tunability, are prohibitively expensive, or require very complicated setups. Such lasers include optically pumped THz lasers (OPTLs) [19, 20], quantum cascade lasers (QCLs), and free electron lasers (FELs). In OPTLs, a CO₂ 9-11 μm grating-tuned laser pumps gas phase rovibrational lines that create population inversion on transitions in the THz region, most commonly in methanol, CH₃OH. The CW output power can be greater than 1 W, but is essentially fixed tuned to the rotational transitions pumped in the gas of choice. The output of this laser can be adjusted via tunable sidebands added by ultrafast Schottky diodes, but the power drops substantially when tuned away from resonance.

Quantum cascade lasers (QCLs) utilize custom-tailored fabricated semiconductor structures to form two dimensional quantum wells, with THz lasing typically based on inter-subband transitions [21]. The first QCL to be successfully operated below the semiconductor optical photon energy was demonstrated in 2001 [22]. Since then, operation has achieved by successively more sophisticated designs with continuous wave operation over frequencies from $<0.8 \rightarrow 5$ THz, at temperatures >100 K, and with power levels exceeding 100 mW [21, 23]. Unfortunately, all of these desirable characteristics have not yet been combined into one package, and commercial availability is sparse to non-existent. Limited tunability has been demonstrated by incorporating microelectromechanical systems (MEMS) [24–26], with the maximum tunability being 8.6% [25]. Lastly, FELs permit the generation of intense radiation at virtually any THz to infrared frequency by the acceleration of electrons to near light speed through custom magnetic

structures. The downsides are extreme expense and size, broad line width(s), and relatively poor signal-to-noise due to significant output energy fluctuations. Thus, laser sources for THz generation have limited use, but there is significant room for improvement in the realm of both QCLs and FELs.

1.1 Terahertz Time Domain Spectroscopy

Due to the limitations described above, there is a pressing need for a convenient THz spectroscopy approach with good wavelength coverage, high sensitivity, and moderate resolution. Thanks to the performance and increasing availability of ultrafast (femtosecond) lasers, TeraHertz-Time Domain Spectroscopy, or THz-TDS, is now perhaps the most common method in THz science, worldwide. While THz-TDS is perhaps most similar as a technique to FT-FIR in that it shares many of the same problems involving the extremely large bandwidth of the source, it shares characteristics of both thermal and laser-based approaches. For example, fully coherent generation is achieved in THz-TDS using ultrafast lasers and optics rather than the blackbody radiation commonly used in FT-FIR. Thus, while the emission bandwidth in THz-TDS spans many octaves as is true in FT-FIR experiments, the coherent light source enables phase stable detection schemes, like those used in the electrical (i.e. RF and microwave) domains. This stands in stark contrast to incoherent FT techniques in the optical and IR regions of the spectrum where intensity-based detectors are used. Practically, the signal-to-noise of THz-TDS instruments typically exceed FT-FIR only at longer wavelengths (that is, for frequencies below 2-3 THz). However, THz-TDS approaches provide the unique ability to acquire phase-sensitive and stable spectra at high frequency and to easily probe ultrafast (sub-picosecond) dynamics of various systems due to the generation and detection methods employed. In addition, THz-TDS techniques will likely find increased application throughout the optical, chemical and materials

sciences in the near future due to the availability of tailored single- through multi-cycle pulses containing ever higher frequencies and the interest in phase stable detection for coherent control purposes.

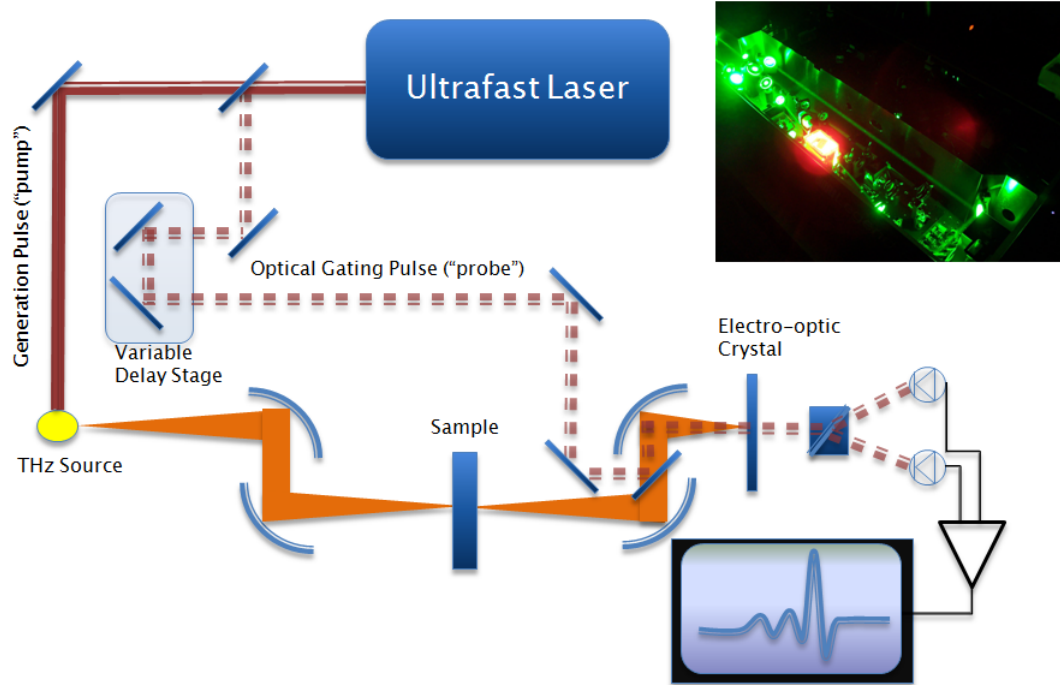


Figure 1.2: A standard experimental layout for THz-TDS experiments.

A typical THz-TDS instrument design is outlined in Figure 1.2. Generally, a femtosecond-class laser pulse train is split into two components, with most of the optical power dedicated to a beam for THz generation, and the remainder forming a weak ‘probe’ beam used for ‘gating’ the optical detection of the THz electric field. Once generated, the THz source beam passes through a sample and is focused onto a THz electric field detector co-linearly with the probe beam. Via some interaction, usually the linear electro-optic effect, a signal proportional to the THz electric field is recorded. One of the two beams is variably delayed with respect to the other, most commonly using a movable mechanical stage, in order to probe the THz field at different times. In this way, the time-dependent THz field is mapped out (typically over the course of many pulses). Afterwards, the optical constants can be accessed in the frequency

domain via the complex Fourier Transform. In Chapter 2 I describe the implementation of a THz-TDS machine in the Blake group. Here, I first describe the essential components of such an instrument in general terms, and lay out the present state of the art in the field.

1.1.1 Ultrafast Lasers

The heart of the THz-TDS technique is the ultrafast laser, which outputs light pulses with femtosecond (fs) duration, as can be seen in Figure 1.3. Manipulation of such lasers and the short pulses that they generate is thus necessary for successful operation of the Blake group THz-TDS instruments, and the basics will be reviewed below. The key feature of ultrafast pulses is the relatively few number of optical cycles contained therein, which results in a temporal duration, down to < 5 fs, that is short compared to the physically relevant processes of interest to chemists, as can be seen in Figure 1.4. The short pulses result in high instantaneous power, up to >1 TW. As discussed in Section 1.1.3, THz generation exploits the transfer of the optical pulse envelope shape to an output electromagnetic wave via various processes in crystalline solids [27–29] and gases [30–33].

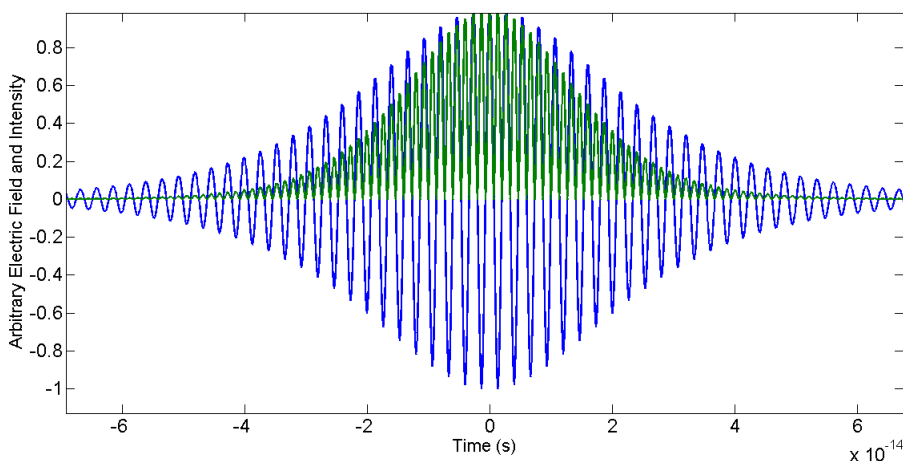


Figure 1.3: An 18 cycle pulse with both the normalized electric field strength (blue) and amplitude (green) plotted.

The most commonly employed femtosecond laser, and the most widely available commer-

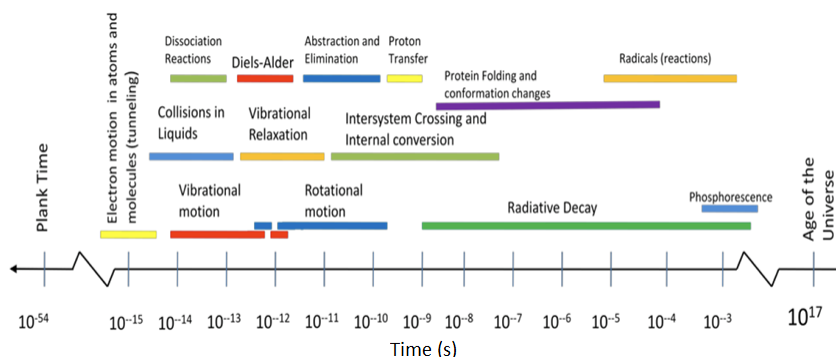


Figure 1.4: Timescale of various processes and reactions related to chemistry.

cially, is based on a Titanium-doped Sapphire (Ti:Sapphire) crystal as the gain medium [34]. Two configurations are commonly available commercially, the ultrafast oscillator [35] and the regenerative amplifier [36]. Both are used in the Blake group, in two separate THz-TDS systems. Here I will describe that based on an oscillator-regenerative amplifier based high pulse energy system, the thesis of Dan Holland describes the development and initial applications of a dual oscillator THz Asynchronous Optical Sampling, or THz-AOS, instrument.

Ultrafast oscillators generate a regular pulse train defined by the round-trip time of the laser cavity – the length of the cavity divided by the speed of light – as defined by a highly reflecting mirror on one end and a partially transparent mirror or output coupler on the other. In the frequency domain, this results in a frequency *comb* [37], with spectral components spaced by repetition rate. For commercial oscillators, the repetition rates commonly span 50 MHz to 3 GHz, and pulse energy is typically at the nJ level (and so average powers of hundreds of milliwatts to Watts). Oscillators rely on what is termed modelocking to establish short pulse durations. The focus here will be on Kerr-Lens mode-locked (KLM) Ti:Sapphire lasers [38, 39], though future Blake group graduate students should be aware of disk lasers [40] based on semiconducting saturable absorber (SESAM)[41, 42] technology, which feature the highest instantaneous and average powers for oscillators. Such oscillators have the significant potential to develop further, enabling plasma generation or optical rectification (OR, see 1.1.3) at very

high repetition rates, for example, and/or at longer wavelengths where phase matching becomes better suited to many nonlinear optical materials.

The principle behind modelocking is the constructive and destructive addition of many laser cavity modes. Longitudinal modes must satisfy the optical cavity conditions, i.e.

$$L = n \frac{\lambda}{2}, \quad (1.3)$$

where, as in the case of a CW laser, λ is not fixed, and $L \gg \lambda$. Since the fluorescence emission profile of Ti:Sapphire is extremely broad, a large number of modes can be supported in principle. If the phase of such modes is constant, as would be the case if they emanate from the same location, constructive interference occurs only for a very short spatial or temporal interval, and a very short pulse is formed. In Figure 1.5, the duration of a pulse with respect to the cavity length is plotted as a function of the number of modes combined, demonstrating the effect of modelocking. In Ti:Sapphire this is enabled by the optical Kerr effect, which causes a nearly instantaneous change to the index of refraction and consequently a preferential focusing of the beam when the intra-cavity power becomes high. This “self-starting” modelocking has the benefit of not requiring an external starter beyond a mechanical shake of a cavity mirror, in most cases.

In contrast, regenerative amplifiers operate by amplifying an already existing “seed” pulse (often one produced by an ultrafast oscillator) in an optically-pumped gain medium, which is also commonly a Ti:Sapphire crystal. In order to accommodate the high power within the gain medium, the input femtosecond seed pulses must first be ‘stretched’ by separating the frequencies of the pulse in time, so as not to destroy sensitive optics with the highly amplified power that results. This process is referred to as chirped pulse amplification (CPA), since optical gratings are typically used to separate individual frequency components in time and to

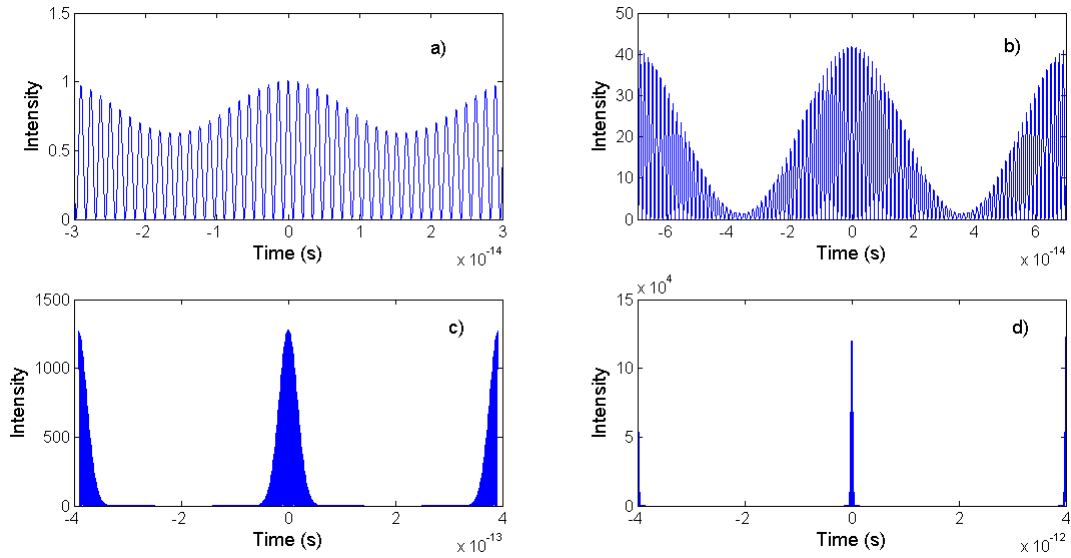


Figure 1.5: The sum of a) 9, b) 19, c) 99, and d) 999 evenly spaced modes around 374.7 THz (800 nm) following the gain profile of Ti:Sapphire with assumed Gaussian intensity and 40 nm bandwidth output pulse. Of note is the intensity scale, which increases dramatically as the number of modes increases; along with the time with respect to the cavity length, which is set by the speed of light divided by the round trip time.

thus broaden the pulse. After stretching from femtoseconds on input to several picoseconds to 1 nanosecond on the output, the pulse can pass through the amplifier cavity safely. After many round trips, at peak gain, the pulse is released from the cavity, typically using timed Pockels cells, which operate by changing the refractive index of a crystal when a large electromagnetic field is applied (see Section 1.1.4.1), and recompressed down to a time-bandwidth limited pulse by prisms or by a grating (see Section 1.1.2.1). The repetition rate of CPAs can range from 100 kHz to <1 Hz, depending on the gain (and thus pulse energy) desired. Average powers now run into the several Watt to tens of Watt range, which correspond to pulse energies from $1 \mu\text{J}$ to > 1 J, or peak powers of several TW. Large facilities that use multiple amplification stages operating on the above principles can reach >1 PW peak power [43, 44]! One downside to CPA is that the output pulse is typically longer than the input pulse, even after compression, due to gain narrowing, because of the effective spectrum bandwidth reduction each trip through the cavity as a result of the maximal gain near the pulse center wavelength. The effective

signal-to-noise can also be limited due to amplified spontaneous emission (ASE) from the pump laser, which limits the gain and is independent of the seed pulse, though regenerative amplifiers typically have lower contribution from ASE relative to other amplifier designs [45].

1.1.2 Ultrafast Pulse Principles and Optics

Proper manipulation and handling of fs pulses is essential for the operation and understanding of THz-TDS instruments and will be summarized below. Many of the same principles also apply to ultrafast THz pulses. When dealing with fs pulses, new optical principles come into play. These arise both from the increased bandwidth intrinsic to short pulses (due to the nature of the Fourier transform) as well as non-linear phenomena due to the high instantaneous field strengths involved. The optical designs therefore differ from conventional optics due the broad frequency content of the pulses in combination with dispersion, or the variance of the refractive index or other optical property with wavelength, in actual materials. If dispersion is not dealt with, it can distort an ultrafast pulse in both shape and phase. Dispersion is typically corrected using prisms, gratings, special dielectric mirrors, or self-phase modulation (SPM) in the case of very high energy pulses. In the most capable and flexible approaches an optical pulse shaper is combined with a pulse shape diagnostic method such as autocorrelation or phase-resolved measurements such as spectral interferometry for direct E-field recovery (SPIDER), frequency-resolved optical gating (FROG), or multi-photon intrapulse interference phase scans (MIIPS) [46]. Pulse compression techniques have allowed the construction of pulses <5 fs in duration, consisting of only a couple of optical cycles at carrier frequencies near 374.7 THz (800 nm). The increased spectral content also means that focusing optics must be carefully considered due to the chromatic aberration.

1.1.2.1 The Fourier Transform

Lasers with very narrow, delta-function-like frequency content must originate from a CW laser with long coherence times. Similarly, pulsed lasers with very broad spectral bandwidth must have very short duration. One might thus hypothesize that the product of bandwidth and pulse duration is limited. Indeed, the so-called time-bandwidth product cannot be reduced below a certain value, which depends on the pulse shape. If minimized, the pulse is said to be transform-limited. That is, the pulse is as short as it can possibly be given its frequency content. This can be thought of as a form of the energy-time uncertainty relation:

$$\Delta E \Delta t \geq \frac{\hbar}{2}, \quad (1.4)$$

where Δt is the pulse duration – not the uncertainty in the time measurement. Hence, this inequality is fundamentally different from the more commonly cited momentum-position relation [47] since t is not an operator and is usually regarded classically in quantum mechanics [48]. In the context outlined here, an ensemble of states that exists for a short duration cannot have a narrow energy distribution.

The time-bandwidth product is given by the following equation:

$$\Delta \omega \Delta t = 2\pi \Delta \nu \tau_p \geq 2\pi c_B. \quad (1.5)$$

The exact shape of ultrafast laser pulses is not easy to determine in everyday laboratory experiments, but c_B is calculated for several common cases in Table 1.2. The energy-time uncertainty relation can be further appreciated through the Fourier transform. Mathematically, the uncertainty relation arises because it is not possible to concentrate a function and its Fourier

Table 1.2: Pulse Envelope Shapes

Envelope Shape	Intensity Profile	τ_p (FWHM)	Spectral Profile	$\Delta\omega_p$ (FWHM)	c_B
Gaussian	$e^{-2(t/\tau_G)^2}$	$1.177\tau_G$	$e^{-(\omega\tau_G)^2/2}$	$2.355/\tau_G$	0.441
sech	$\text{sech}^2(t/\tau_s)$	$1.763\tau_s$	$\text{sech}^2(\pi\omega\tau_s/2)$	$1.122/\tau_s$	0.315
Lorentz	$[1 + (t/\tau_L)^2]^{-2}$	$1.287\tau_L$	$e^{-2 \omega \tau_L}$	$0.693/\tau_L$	0.142
Rectangular	1 for $ t/\tau_r \leq 1$, 0 elsewhere	τ_r	$\text{sinc}^2(\omega\tau_r)$	$2.78/\tau_r$	0.443

Intensity, spectrum and time-bandwidth product for several commonly assumed pulse envelope shapes.

transform,

$$\tilde{E}(\omega) = \mathcal{F}\{E(t)\} = \int_{-\infty}^{\infty} E(t)e^{-i\omega t} dt = |\tilde{E}(\omega)| e^{-i\phi(\omega)} = \sqrt{S(\omega)} e^{-i\phi(\omega)}, \quad (1.6)$$

where $S(\omega)$ is the spectrum, and $\phi(\omega)$ is the spectral phase as a function of frequency. The inverse transform is

$$E(t) = \mathcal{F}^{-1}\{\tilde{E}(\omega)\} = \int_{-\infty}^{\infty} \tilde{E}(\omega)e^{i\omega t} d\omega, \quad (1.7)$$

where $\omega = 2\pi\nu$. The time bandwidth product thus results mathematically from the nature of the Fourier transform.

1.1.2.2 Dispersion and Chirp

The reason for the possible inequality in equation 1.5 is the separation in time of different frequency components, which temporally broadens the pulse envelope compared to the case where they are all in phase. This is often present, at least to some extent, in the laboratory setting because of uncompensated spectral dispersion. Dispersion is the frequency dependent response of a material to electromagnetic waves. Most commonly we are concerned with the refractive index, or the velocity of light, in a material. Both the phase and group velocity must be considered. The phase velocity is the velocity of an individual wave peak component through a material, while the group velocity is the velocity of the pulse envelope as it propagates. Since

the group velocity is the maximum speed that information can be transferred, it is limited by the speed of light, and usually it is less than or equal to the phase velocity. If the two are equal, a pulse propagates without distortion, if not, the pulse will distort as the different frequency components of the light are differently delayed.

The refractive index usually refers to the phase velocity and is defined as:

$$n = \frac{c}{v_{phase}}. \quad (1.8)$$

For most materials, $dn/d\lambda < 0$. This is referred to as normal dispersion. In the case of anomalous dispersion, $dn/d\lambda > 0$. To examine the effects of propagation through a dispersive medium on a bandwidth-limited pulse, the group delay is analyzed. The group delay is a measure of the spectral phase, which can be expanded into a Taylor series if $\Delta\omega \ll \omega$. The group delay can be defined as

$$\tau_g \simeq \frac{d\phi}{d\omega} = \phi'(\omega_0) + \phi''(\omega_0)\Delta\omega + \frac{1}{2}\phi'''(\omega_0)\Delta\omega^2 + \dots, \quad (1.9)$$

where $\phi'(\omega_0)$ is the group delay (fs), which is a linear phase shift, $\phi''(\omega_0)$ is the group delay dispersion (or GDD, fs²), and $\phi'''(\omega_0)$ is the third-order dispersion (TOD, fs³). Typically only the GDD is considered, with higher order terms neglected. The group delay is always specified with respect to a given optic or medium of a pre-defined length. Thus, another often cited parameter is the group velocity dispersion (GVD), which is simply the GDD per unit length. To predict the change to a pulse the index as a function of frequency must be known.

Two common results of dispersion are linear positive and negative “chirp”. Positive chirp occurs when the red wavelengths of a pulse are temporally ahead of the blue wavelengths, and results from normal dispersion (because redder wavelengths typically have higher phase

velocity), whereas in a negatively chirped pulse the blue wavelengths lead the red, and results from anomalous dispersion. An example of a positively chirped pulse is given in Figure 1.7.

Dispersion and chirp serve to broaden pulses and lower the peak field strength. This becomes increasingly important as the pulse becomes shorter. For example, a 5 fs pulse at 800 nm will broaden to 25 fs after 1 mm of BK7 glass or 2 m in air, whereas an 800 nm/100 fs pulse will only broaden by 0.1 fs through the same media. This is quite important for ultrafast THz spectroscopy since the time-dependent generation depends upon the pulse envelope. Further, since the THz electric field detection is “gated” by such pulses, an overly broadened pulse limits the temporal resolution in the sensing the THz field (and thus, via the Fourier transform, the frequency content of the reconstructed THz pulse). Meanwhile, since the peak pulse amplitude is also reduced, the efficiencies of any non-linear optical processes are reduced, as will be discussed in the following Section 1.1.2.4.

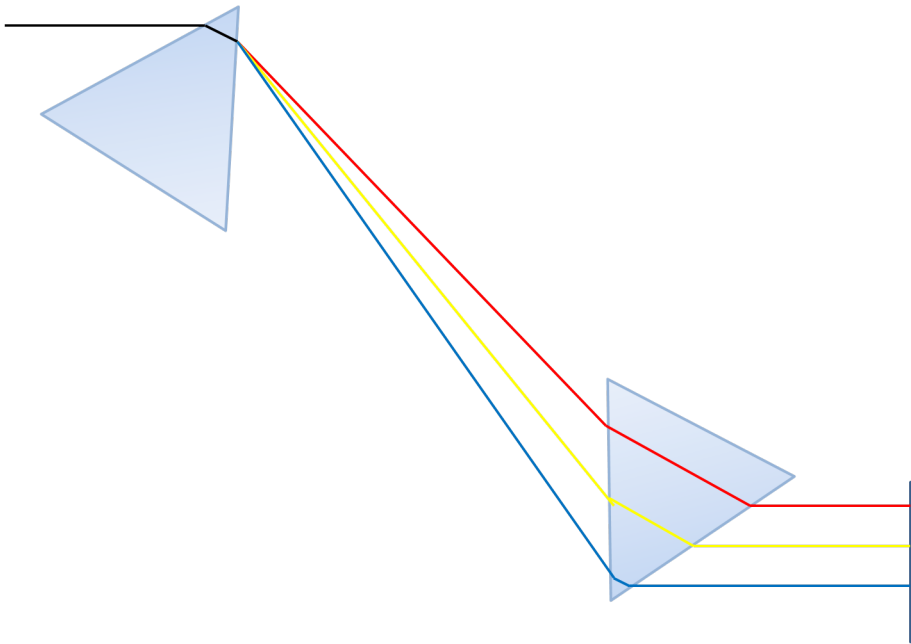


Figure 1.6: A prism pair for dispersion compensation by negatively chirping a pulse.

Three techniques are typically employed to correct for chirp: prism pairs, grating pairs, and negative dispersion mirrors. In a prism pair arrangement, as depicted in Figure 1.6, the

input pulse is spread spatially by the first prism and collimated in the second. Afterwards, a flat reflector sends the pulse back along the same path, and the spatial chirp is eliminated. The geometry is such that the bluer wavelengths travel a shorter distance through the high index material of the prism and thus the pulse is effectively negatively chirped. A four-prism arrangement is also used when separation of output and input pulses is desired. The loss can be quite low at 800 nm if the prisms are placed at Brewster's angle. Gratings can be used in similar ways, but often possess significantly larger angular dispersion than prisms, so larger chirps can be established. In order to accommodate the larger dispersion, lens are often required in combination with the dispersive elements in order to keep the size manageable. Another advantage of gratings is that both second and third order dispersion can be controlled by changing the angle of the grating. Lastly, negative GVD or chirped mirrors feature a many layered dielectric structure designed to allow different penetration depths versus wavelength, and thus are capable of inducing different temporal retardation based on light frequency. This allows for negative chirping or shaping of the pulses. Such mirrors can be designed to buyer specifications, but the price for such custom fabrication is quite high. Typically the negative dispersion is not large for a single bounce, and as such, many bounces must often be used in order to shape the pulse.

1.1.2.3 Pulse Shaping

Special mention should be made of optical pulse shapers, which are able to modify the pulse shape almost arbitrarily [49]. Typical optical pulse shaping techniques involve the spectral dispersion of the pulse of interest, followed by spatial light modulation of the phase or a combination of both phase and amplitude of the frequency components of the pulse, and recombination to form a tailored time-domain waveform [50, 51]. Typically, spectral dispersion is performed by a combination of gratings, or in some cases, a series of prisms [52] or a

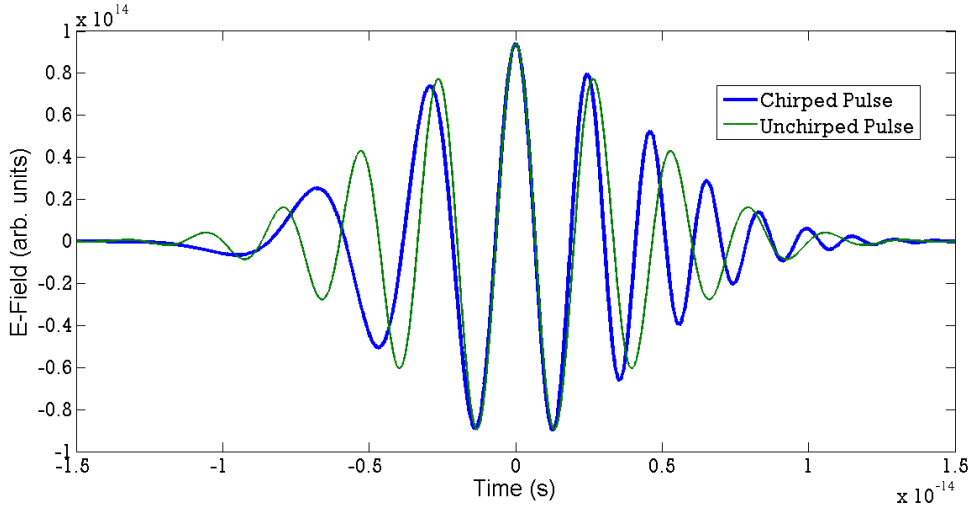


Figure 1.7: Linearly chirped and unchirped pulses at a center wavelength of 800 nm.

virtually-imaged phase array (VIPA) [49, 51]. Phase modulation is most commonly achieved using a spatial light modulator (SLM), consisting of many pixels of individually controllable liquid crystals. Acousto-optic modulators (AOM) and VIPAs are also commonly employed [51]. Finally, amplitude control can be achieved by stacking two of these devices at the focal plane of the pulse shaper.

1.1.2.4 Nonlinear Effects

At sufficiently high intensities, light can modify the optical properties of a material. That is, the optical properties depend non-linearly on the optical field strength. Typically light induces a linear polarization, or dipole moment per unit volume, but at higher intensities the polarization can respond non-linearly. The polarization of a medium is relevant since time varying polarizations give rise to electric fields. A power series expansion of the polarization, $\tilde{P}(t)$, results in the following expression:

$$\tilde{P}(t) = \chi^{(1)}\tilde{E}(t) + \chi^{(2)}\tilde{E}^2(t) + \chi^{(3)}\tilde{E}^3(t) + \dots \equiv \tilde{P}^{(1)}(t) + \tilde{P}^{(2)}(t) + \tilde{P}^{(3)}(t) + \dots \quad (1.10)$$

where $\chi^{(n)}$ is the n -th order non-linear optical susceptibility [53]. The second-order nonlinear polarization is only relevant to non-centrosymmetric materials that do not have inversion symmetry, such as some crystals. Centrosymmetric materials such as gases, liquids, and amorphous solids all demonstrate inversion, and $\chi^{(2)}$ processes, such as second-harmonic generation (SHG) (a special case of sum frequency generation, or SFG), are not observable. $\chi^{(3)}$ processes occur in both centrosymmetric and non-centrosymmetric media.

Many nonlinear effects are important to THz-TDS research. SHG, for example, is a source of higher frequency optical light such as that used in time resolved “pump-probe” THz-TDS applications (Chapter 4), two-color plasma THz generation (See 1.1.3.4 and 2.4.2), and as a pump source for ultrafast oscillators (See 1.1.1). Optical rectification (OR) is effectively inter-pulse difference frequency generation, and is used extensively in THz generation in crystals (See 1.1.3.2). The linear electro-optic (EO) effect, or Pockels effect, is effectively the inverse of OR, and is used in THz detection via EO active crystals (Section 1.1.4.1). Four-wave mixing, a $\chi^{(3)}$ process, is commonly employed in the plasma-based generation and detection of THz radiation (See Section 1.1.3.4 and Section 2.4.2).

The refractive index can change at high light intensities and is described as

$$n = n_0 + 2\bar{n}_2 |E(\omega)|^2, \quad (1.11)$$

where \bar{n}_2 is the second-order index of refraction. The change of refractive index with intensity (typically an increase) is called the optical Kerr effect, in relation to the Kerr electro-optic effect, where the index of a material changes based on the square of the strength of an applied DC electric field. To relate this to material polarization, it is found that

$$\bar{n}_2 = \frac{3\pi\chi^{(3)}}{n_0} \quad (1.12)$$

when a single strong laser beam induces the nonlinearity and the effect is measured on that beam. When the effect is measured with a separate, much weaker, probe beam the second-order index of refraction is given by

$$\bar{n}_2 = \frac{6\pi\chi^{(3)}}{n_0} . \quad (1.13)$$

It is also common to relate \bar{n}_2 to intensity, I , rather than $|E(\omega)|^2$. In this case,

$$n_2 = \frac{4\pi}{n_0 c} \bar{n}_2. \quad (1.14)$$

Typical values for n_2 are 10^{-16} cm²/W [53]. In addition to the importance of Kerr-Lens mode-locking (see Section 1.1.1), this is important to phase matching and to self-phase modulation (SPM). Phase matching is important in all non-linear processes, as is discussed at further length in the next section. SPM, the change in phase of light due to n_2 , and filamentation due to self-focusing occurs in media when n_2 becomes large with respect to the linear index. The change in the phase is given by:

$$\Delta\phi = \phi_{\text{NL}}(t) = -n_2 I(t) \omega_0 L / c. \quad (1.15)$$

Since $\partial\omega = (\Delta\phi)/\partial t$, the optical spectrum is broadened, or, conversely, the pulse is self-steepened in the time-domain, because the leading edge of the pulse shifts to lower frequencies and the trailing edge shifts to higher frequencies. SPM and filamentation are central to plasma-based THz generation as well as forming a general method for pulse shortening and broadening [54].

1.1.2.5 Phase Matching

Phase matching, broadly, involves ensuring the greatest possible constructive overlap of interacting electromagnetic waves in a sample. It is extremely important to optimizing nonlinear

effects, and involves matching the wave vectors, \mathbf{k} , of all fields to maximize the coherent addition of waves in the forward direction, where

$$\mathbf{k} = \frac{n\omega}{c}, \quad (1.16)$$

where $n = [\epsilon^{(1)}(\omega)]^{1/2}$, and $\epsilon(\omega)$ is the dielectric constant. With no non-linear contribution, $n = [\epsilon^{(1)}]^{1/2}$ is the linear index of refraction. For an isotropic medium, the wave vector is guaranteed to point in the direction of propagation, that is, in the direction of both the group velocity and phase velocity vectors. For an anisotropic medium, the wave vector points in the direction of propagation of the phase velocity. Finally, in dispersive media, each frequency component must be treated separately.

The wave-vector mismatch is, in the case of SFG,

$$\Delta k = k_1 + k_2 - k_3, \quad (1.17)$$

where 1 and 2 are input photons and 3 is the output photon. Ideal phase-matching entails $\Delta k = 0$, which maximizes the SFG efficiency. The efficiency of SFG is given by

$$I_3 = I_{3_{max}} \frac{\sin(\Delta k L/2)}{(\Delta k L/2)^2}, \quad (1.18)$$

and drops off quickly as Δk moves away from 0. Due to dispersion and the different frequency of the input and output waves, perfect phase matching is generally impossible. However, in some cases, the match can be improved. For example, an anisotropic crystal has differing indices of refraction along its unique crystallographic axes. Such a crystal is referred to as birefringent. The orientation of a birefringent crystal can be changed with respect to the input polarization of the light beams to increase phase matching and the length of interaction, L . In a homogeneous

medium, to avoid deconstructive interference of waves, the length of interaction must be fixed, or the polarization of a field flipped every coherence length [55], l_c , where

$$l_c = 2/\Delta k. \quad (1.19)$$

The coherence length can also be modified by changing the pressure, temperature, or other physical property that affects the index of refraction of the medium.

1.1.3 Techniques for THz-TDS Emission

The techniques discussed in this section span THz pulse generation from ultrafast oscillator and amplifier sources. With higher optical pulse energies many more techniques are viable, so amplifier-based sources are preferentially considered here. Typical THz pulse energies with table top systems are ~ 1 nJ, which limits experiments to the linear regime [56]. The Blake group, amongst others, is considering nonlinear THz experiments, including ladder climbing and the coherent control of large amplitude molecular dynamics (see Chapter 5). Several promising new methods offer the possibility of generating the peak THz powers required for the proposed nonlinear experiments.

1.1.3.1 Photoconductive THz Generation

The modern implementation of what are termed photoconductive antennas was originally developed as a means of checking the performance of high speed electronics that avoids the inherent distortion of transmission lines, which work well at lower bandwidths and frequencies but not near THz frequencies [57]. Later it was realized that this technique was the most efficient approach to generating THz radiation when limited optical pulse energy is available, as in the case of an ultrafast oscillator source, due to a weak dependence on pump fluence. The heart

of the technique is ultrafast carrier generation in a semiconductor paired with an antenna for far-field emission [13, 57]. The laser beam is focused onto a semiconductor crystal between electrodes that have been deposited onto it, impulsively exciting the sample and changing the conductivity by generating electron-hole carrier pairs. Typically a large DC bias is applied to the electrodes to facilitate acceleration of charges in the material. The source of THz emission in this case is very similar to the classical Hertzian dipole [58, 59].

A quantitative explanation of the emission is derived from Maxwell's equations:

$$\nabla \times \vec{E}(t) = \frac{\partial \mu(t) \vec{H}(t)}{\partial t} \quad (1.20)$$

$$\nabla \times \vec{H}(t) = \sigma(t) \vec{E}(t) + \frac{\partial \epsilon(t) \vec{E}(t)}{\partial t}, \quad (1.21)$$

where $\mu(t)H(t) = B(t)$ is the magnetic flux, $H(t) = \sigma(t)E(t)$ is the current density, and $\epsilon(t)E(t) = D(t)$ is the electric displacement. Any time dependent change to μ , σ , or ϵ will cause the emission of radiation. Picosecond time scale acceleration of charge or changes in conductivity, σ , results in THz emission. The most common semiconductor used for photoconductive generation of THz radiation is GaAs, and the technique is commonly limited by the breakdown voltage, or the maximum bias voltage of the antenna. A hard limit is 30 kV/cm for continuous DC bias, which is the breakdown voltage or dielectric strength of air at standard temperature and pressure [60] – though the breakdown of air is time-dependent and if the DC bias is pulsed, higher fields can be applied [61].

At low optical pump power, the peak emitted THz electric field strength scales linearly with optical fluence (J/cm^2), but at higher pump fluence the radiated field intensity slowly approaches the bias field [62], and even reaches a maximum when high bias fields are used due to carrier-carrier screening [63, 64]. If a large spacing between electrodes is used, the field can be focused and has reached values of >150 kV/cm with a pulsed 10.7 kV/cm bias field [63]. The

disadvantage of this method is that, while the required pump fluence is low, the power supplies required to reach high bias field strengths over large distances typically must be pulsed to avoid electrical breakdown in the material or air. This can introduce significant noise and typically offers degraded signal-to-noise performance as compared to DC biased emitters. For oscillator based systems, a common design to circumvent the high bias field is a metal-semiconductor-metal interdigitated electrode structure, which creates effective fields of 100 kV/cm from an applied bias of only 50 V, allowing for much more efficient THz generation, with detected fields approaching 100 V/cm [65–67] for oscillator driven emitters. Another caveat of the photoconductive antenna approach is that the usable frequency range typically only extends from 0.3–3.5 THz. This is unavoidable unless a different semiconductor with faster response is used, or the backward emitted THz radiation is collected [68, 69].

1.1.3.2 Optical Rectification

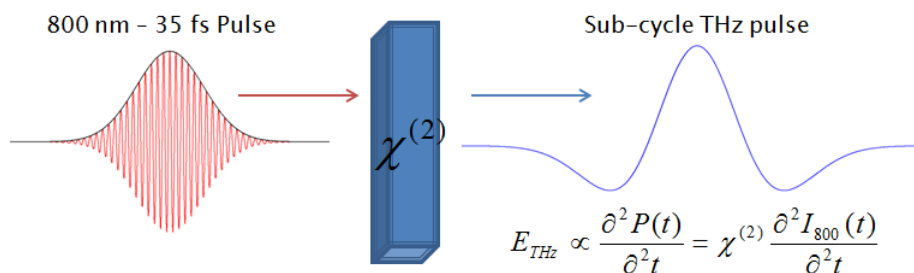


Figure 1.8: A depiction of the process of optical rectification at 800 nm.

When the optical pump energy becomes sufficiently large, as in the case of regenerative amplifier sources, other THz emission techniques dominate typical experimental designs due to their simplicity and higher emitted field strength. In particular, THz-TDS has typically relied on optical rectification (OR) in ZnTe pumped by 800 nm femtosecond pulses from a Ti:Sapphire amplifier as a source of THz radiation (See Figure 1.8). THz generated by OR is better considered as the result of difference frequency generation (DFG) performed on distinct,

but close, frequency components of the same pulse; the red and blue parts of the spectrum mix to generate a sub-single cycle THz pulse. Pure optical rectification involves the creation of a static DC field in the crystal [70]. If there are two frequency components, extending the nonlinear polarization equations from section 1.1.2.4 yields:

$$\tilde{E}(t) = E_1 e^{-i\omega_1 t} + E_2 e^{-i\omega_2 t} + c.c. \quad (1.22)$$

The second-order polarization, from equation 1.10, is then

$$\begin{aligned} \tilde{P}(t) = \chi^{(2)} \tilde{E}(t)^2 = \chi^{(2)} [E_1^2 e^{-2i\omega_1 t} + E_2^2 e^{-2i\omega_2 t} + 2E_1 E_2 e^{-(\omega_1 + \omega_2)t} + 2E_1 E_2^* e^{-i(\omega_1 - \omega_2)t} \\ + c.c.] + 2\chi^{(2)} [E_1 E_1^* + E_2 E_2^*] \end{aligned} \quad (1.23)$$

where the first two terms describe SHG, the third term describes SFG, the fourth term DFG, and the last term is OR.

Phase matching and the coherence length are also of critical importance to efficient OR.

The perfect phase matching condition is given by [71]

$$\Delta k = k(\omega_{\text{opt}} + \omega_{\text{THz}}) - k(\omega_{\text{opt}}) - k(\omega_{\text{THz}}) = 0. \quad (1.24)$$

From Equation 1.19, the coherence length in this case can be defined as

$$l_c(\omega_{\text{THz}}) = \frac{\pi c}{\omega_{\text{THz}} |n_{\text{opt}}(\omega_0) - n_{\text{THz}}(\omega_{\text{THz}})|}, \quad (1.25)$$

where n_{opt} and n_{THz} are the optical and THz indices for the central optical and THz frequencies, respectively. Even in the closest matching crystal, $\langle 110 \rangle$ ZnTe, the indices are quite different at, for example the common THz frequency of 1 THz, $n_{\text{THz}} = 3.12$ THz, and the optical wavelength of 800 nm, $n_{\text{opt}} = 2.85$. This mismatch results in a coherence length of only 0.55 mm, which

does not allow for significant THz signal to be produced from an optical pulse. Beyond the small coherence length, the above treatment ignores the bandwidth of the pulses.

This is particularly troubling for THz radiation, where pulses have several octaves of frequency content and markedly different indices in optical materials. Typical index or phase matching schemes such as the use of birefringence result in a narrow bandwidth. Fortunately, better phase matching can be achieved in this case, if the dispersion of the optical pulse is considered. Since $\omega_{\text{opt}} \gg \omega_{\text{THz}}$, Equation 1.24 can be approximated as

$$\frac{k(\omega_{\text{THz}})}{\omega_{\text{THz}}} \approx \left(\frac{\partial k}{\partial \omega} \right)_{\text{opt}}. \quad (1.26)$$

Thus, in this case it is the optical group velocity, as specified by the group index, that is used to establish the phase matching condition and not the phase velocity, since it is the pulse envelope of the optical pulse and not the phase of the frequency components that is relevant to THz generation. Since the group index, n_{gr} is defined as

$$n_{gr} = n - \lambda \left. \frac{dn}{d\lambda} \right|_{\lambda_{\text{opt}}}, \quad (1.27)$$

Equation 1.25 can be rewritten as

$$l_c = \frac{\pi c}{\omega_{\text{THz}} \left| n_{\text{opt}} - \lambda_{\text{opt}} \left. \frac{dn_{\text{opt}}}{d\lambda} \right|_{\lambda_{\text{opt}}} - n_{\text{THz}} \right|}. \quad (1.28)$$

With these considerations, the coherence length improves by almost an order of magnitude over the range from 0 \rightarrow 3 THz.

While ZnTe is perhaps the most frequently chosen material for THz optical rectification at 800 nm, it has several severe limitations. Most worrisome is that ZnTe has a relatively low bandgap, and two-photon absorption of the pump beam occurs at low powers relative to

the damage threshold of the material [72]. The two-photon absorption generates free charge carriers, which strongly absorb THz radiation. This limits the excitation pulse energy to below what is commonly available in amplified Ti:Sapphire systems. Secondly, ZnTe has its lowest optical phonon mode at 5.3 THz, significantly limiting the frequency coverage of a THz-TDS instrument. This complication can be partially avoided by switching crystals for higher frequency emission, to GaP for example, which has its lowest phonon mode at 11 THz [28, 73], but at the cost of low frequency performance and field strength. Lastly, the relevant nonlinear coefficient of ZnTe, d_{41} , which has a value of 68.5 pm/V, is lower than that of other nonlinear crystals such as lithium niobate, LiNbO₃, for which d_{eft} is 168 pm/V. The efficiency of OR will be further discussed in Section 1.1.4.1. The typical maximum electric field strengths generated by OR in ZnTe using 800 nm excitation are ~ 1 -5 kV/cm, though fields up to >10 kV/cm have been achieved using large area emitters [72] and > 50 kV/cm in extraordinary cases [74].

1.1.3.3 Tilted Pulse Front

All of the problems with ZnTe have caused researchers to investigate alternative ways of establishing phase matching in other crystals. One of the most successful is to create an angle between the directions of propagation of the optical pump and THz pulse. As we saw in the last section, the optical group velocity is that which should be considered for proper velocity matching – the absolute frequency of the optical pulse is of little consequence. Thus, the angle may be established by tilting the front of the optical pump pulse, as occurs in the pulse compression schemes described in Section 1.1.2.2, using a frequency separating element such as a grating or prism and a focusing element such as a lens. The phase matching condition is now

$$v_{\text{opt}}^{gr} \cos \gamma = v_{\text{THz}}^{ph}, \quad (1.29)$$

where γ is the tilt angle, which makes the projection of the the visible group velocity, $v_{\text{opt}}^{\text{gr}}$, equal to the THz phase velocity, $v_{\text{THz}}^{\text{ph}}$ [75]. This matching works when $v_{\text{opt}}^{\text{gr}} \geq v_{\text{THz}}^{\text{ph}}$, which is common for most crystals. Titled pulse front excitation enables phase matching over significant lengths in materials which ordinarily have vastly different indices of refraction for light at THz and optical frequencies, but at the cost of experimental complexity. For example, the index of LiNbO₃ is over two times greater at 1 THz than that at 800 nm [29], which does not allow for collinear phase-matched propagation.

Hebling *et al.* [29, 76] have recently remedied these difficulties via tilted pulse front excitation of a LiNbO₃ prism, yielding THz pulses having 1000 times larger energy when compared to those generated in ZnTe at the same pump energy. The LiNbO₃ prism requires a tilt angle of $\sim 63^\circ$, which in turn requires a pump pulse tilt angle of 78° , as can be seen from the following equation:

$$\tan \gamma = \frac{1}{n_{\text{opt}}^{\text{gr}}} \tan \gamma^\circ, \quad (1.30)$$

where γ° is the external tilt angle. A line focus was used on the crystal by employing cylindrical lenses as pump focusing elements. With 20 mJ 800 nm pulses at 10 Hz, THz pulses with 10 μJ energy were generated. For reference and for comparison purposes, the reported THz peak power was 5 MW, the average power was greater than 1 mW, the peak power at a 1 mm focus was 500 MW/cm², and the peak field was 600 kV/cm [29]. The internal efficiency was reported to be 800% by measuring the redshift of the pump spectrum, indicating a cascaded process [77]. Hirori *et al.* have demonstrated field strengths of greater than 1.2 MV/cm in LiNbO₃ [78] by improving focusing and pulse propagation through the OR material. The THz energy is also predicted to improve by a factor of three to five by cryogenically cooling the lithium niobate crystal, allowing for lower THz absorption in the crystal and has very recently been demonstrated [79]. Improvements can also be made by going to longer pump

wavelengths (1.55 μm , typically), due to an improvement in most of the crystals considered for OR, and by further improvements to the focusing [80]. For example, 0.5 nJ THz pulses at a repetition rate of 1 MHz were demonstrated using a Yb-fiber laser pumped tilted pulse front scheme [29], with scaling to 2 nJ anticipated. The main limitation of this technique is the small bandwidth of the pulses and lack of tunability. The bandwidth of the pulses generated is peaked near 1 THz and becomes signal-to-noise limited by 3 THz, for room temperature operation. However, no other alternative offers such high fields below 3 THz, so the technique is worth considering further. Multi-cycle THz pulses with tunable bandwidth and center THz frequencies have also been demonstrated recently using a shaped optical pulse train [81]. This could make certain nonlinear THz experiments more feasible and allow for specific absorption of THz radiation. Lastly, bandwidth control of the excitation pulse must be limited to achieve high conversion efficiency due to loss Raman scattering processes at high bandwidth and sub-100 fs pulse duration [82]. The theory of the technique is laid out by Bakunov et al. [83]

The phase matched tilted pulse front OR efficiency, η_{THz} , is given by Hebling *et al.* as, [29]

$$\eta_{\text{THz}} = \frac{2\omega_{\text{THz}}^2 d_{\text{eff}}^2 L^2 I_{\text{opt}}}{\epsilon_0 n_{\text{opt}}^2 n_{\text{THz}} c^3} \cdot e^{-\alpha_{\text{THz}} L/2} \cdot \frac{\sinh^2[\alpha_{\text{THz}}(L/4)]^2}{(\alpha_{\text{THz}} L/4)}, \quad (1.31)$$

where ϵ_0 is the vacuum permittivity, L is the length of the nonlinear crystal, α_{THz} is the THz absorption coefficient, and d_{eff} is the effective nonlinear optical coefficient for optical rectification, which can be generally related to the nonlinear susceptibility through the relationship $d_{ijk} = 1/2\chi_{ijk}^{(2)}$. As an aside, d_{ijk} represents a lattice displacement which causes changes to the potential of the crystal and a perturbation of the optical polarizability produced by changing the electronic energy levels of the crystal (non-lattice or electronic interaction) [84]. The efficiency equation ignores linear and 2-photon absorbance at optical pump wavelengths, which makes CdTe and GaAs unusable for OR at 800 nm and lowers the efficiency of ZnTe, as well

as dispersion for both the THz and optical pulses. A complete efficiency equation should also consider other nonlinear effects in the crystal such as two-photon absorption. However, the results are useful for comparison purposes, and are presented in Table 1.3 for common crystals using Equation 1.31.

1.1.3.4 Two-Color Laser-Induced Plasma

As seen in the previous section, the main difficulties with using crystals for THz pulse generation is the inevitable dispersion (index matching) and absorption of THz photons by the crystal. A novel solution to these problems relies on what can be modeled as a four-wave mixing-like process ($\chi^{(3)}$) in gaseous plasmas [32, 85–88]. To generate the plasma, a portion of the output of a Ti:Sapphire amplifier at 800 nm is doubled and the combined two-color beam is focused in a gas to generate a plasma due to multi-photon absorption or ionization initiated by tunneling, wherein the Coulomb barrier is suppressed by the laser field. Here the pulse duration, and consequently bandwidth, is the limiting factor, *not* index matching or absorption. However, pulse duration and bandwidth are inversely correlated, so when shorter pulses are used, the spectrum shifts to the mid-infrared [30, 89]. Also, filamentation can cause self-steepening or self-compression, further increasing the bandwidth of the pump and THz pulses [54]. Thus, usable, and coherently emitted, bandwidths of up to 75 THz [30] or more have been observed, particularly when the third harmonic is included [31] or the 2ω field is detuned from the second harmonic of the ω_0 field [90].

The THz pulses also have very high reported peak powers; though, due to a variety of non-optimum experimental conditions and different detection methods, the maximum generated pulse energy under ideal conditions is unknown. However, it is not unreasonable to expect that pulses with energies of up to hundreds of μJ can be generated. The highest reported THz pulse energies are 15 μJ , using an amplifier providing 50 fs, 30 mJ pulses at 10 Hz [30]. However,

this study did not employ phase compensation [91] to temporally overlap the second harmonic and fundamental pulses and used air as the generation medium, which has very large THz absorption (due to the water therein). Liu *et al.* have measured fields of 35 kV/cm when using 700 μJ pulses, but claim improvements extending to over 1 MV/cm using higher optical pulse energy and careful control of the THz collection and focusing system [86]. These claims seem reasonable based on the observed square law dependence on the pump energy [32]. Ultimately, the square law dependence falls off at higher pump powers due to absorption and scattering of THz radiation by the higher plasma densities as well as a dephasing of the THz, ω_0 , and $2\omega_0$ pulses due to velocity mismatch [30, 92]. Generally, however, the THz radiation yield increases linearly with filament length, i.e. with decreasing focusing of the optical beams. Interestingly, the THz emission profile in the far field is donut shaped [30]. The polarization is often elliptical [93].

There are several prominent theories for the origin of THz emission from two-color plasmas. The first, and most basic, employs a standard nonlinear optical model in which the $\chi^{(3)}$ of some medium, either neutral gas or a combination of ions and electrons in the plasma, allows for four-wave rectification (FWR) where the carrier frequencies of three input fields sum to zero [32]. Much as optical rectification is the inverse of the linear electro-optic effect, it was hypothesized that filamentation is the inverse of the THz field-induced second harmonic (TFISH) process, in which the THz field and an optical field at ω_0 combine to form an optical field at $2\omega_0$. This was first demonstrated by the founders of the two-color plasma emission technique [94], but is very similar to the DC version, electric field-induced second harmonic generation, or EFISH [95]. The process can be described by the third-order polarization

$$P_i^{(3)}(t) = \chi_{ijkl}^{(3)} E_j^{2\omega_0}(t) E_k^{\omega_0}(t) E_l^{\omega_0}(t), \quad (1.32)$$

and is found to be most efficient when all beams are polarized in the same direction, i.e.

$\chi_{xxxx}^{(3)} = \chi_{yyyy}^{(3)} > \chi_{xxyy}^{(3)} = \chi_{yyxx}^{(3)}$, where the non-vanishing tensors for an isotropic medium are

listed. Phenomenologically, the process follows the predictions of this model. Since the $2\omega_0$

term is produced from the fundamental, the overall scaling is

$$P_i^{(3)} \propto \mathcal{E}_{\omega_0}^4(t) \cos \phi, \quad (1.33)$$

where $\mathcal{E}_{\omega_0}^4(t)$ is the electric field strength profile of the fundamental optical pulse and ϕ is the phase difference between the second harmonic and fundamental. The behavior as the phase between the two fields is varied serves as a test of the principle, but is not conclusive. This is accomplished most easily by tilting a microscope coverslip in the beam, or by varying the distance from the frequency doubling crystal to the plasma (which leads to relative phase changes due to the differing indices for ω_0 and $2\omega_0$).

Two significant discrepancies are seen in experiments as compared to the FWR predictions. First, threshold behavior is observed near the field density required to form a plasma in air [96]. Second, the process is remarkably efficient, producing pulses with field strengths far greater than that commonly achieved from OR with the same pulse energy. Yet, due to overall process dependence on a third-order nonlinearity, the THz field should be orders of magnitude less. Thus, Kim, *et al.* have developed a theory in which the plasma forms a non-vanishing transverse photocurrent, which, via Maxwell's equations, emits THz radiation [30, 92, 97]. In this model, the THz emission from ionization in a symmetry-broken laser field arises as a result of the asymmetric current generated. The two-color field is given by

$$E_{2C} = E_{\omega}(t) \cos(\omega t) + E_{2\omega}(t) \cos(2\omega t + \phi) \quad , \quad (1.34)$$

which results in a sharply peaked repetitive wave when $\phi = 0$. Ionization takes place when the peak field is high, and the ions and electrons are accelerated by E_{2C} . The velocity can be written as

$$v(t) = -(e/m_e) \int_{t'}^t E_{2C}(t) dt, \quad (1.35)$$

where e and m_e are the electron charge and mass and t' is the ionization time. Generally the electrons and ions oscillate at the laser frequencies but also are found to acquire a drive velocity of

$$v_d(t') = \frac{eE_\omega \sin(\omega t')}{m_e \omega} + \frac{eE_{2\omega} \sin(2\omega t' + \phi)}{2m_e \omega}. \quad (1.36)$$

The classical motion of the electrons emits radiation, much as is the case in photoconductive antennas. This treatment neglects the effects of electron motion arising from interaction with the nucleus and the free-free transitions that can be seen in electron energy spectra [98].

Based on these caveats, Karpowicz *et al.* [98] performed quantum mechanical simulations by solving the time-dependent Schrödinger equation, where the Hamiltonian in atomic units is

$$\frac{1}{2}(p + A)^2 + V(r), \quad (1.37)$$

where A is the laser vector potential, p is the kinetic momentum operator, and V is the atomic potential. The interaction of single atoms and electrons is not found to produce THz radiation, and so bremsstrahlung, or radiation from the deceleration of a charged particle, was considered. While usually incoherent, bremsstrahlung is shown to be coherent within a half-cycle of the THz wave. The resulting process is described by two steps: asymmetric ionization followed by disruption of the original trajectories by the surrounding gas or plasma emitting coherent THz radiation in an “echo” process.

Besides increasing the THz pulse energy via a pump energy increase, there are several other

routes to improvement. Experiments were first performed in air or nitrogen [32] at ambient pressure, which is far from ideal. The generated THz field intensity increases as the ionization potential (IP) decreases [86]. For example, a peak field amplitude increase of more than an order of magnitude is observed when using n-butane, with an IP of 10.63 eV, as compared to nitrogen, which has an IP of 15.8 eV [86, 99, 100]. Using linear scaling, trimethylamine, which has an IP of 7.82, should yield another factor of five increase. A significant fraction of the improvement is expected to be a result of the higher plasma density and longer filament length that can be achieved in lower IP gases.

Additional gains can also be realized by more complex frequency mixing schemes. When the third Ti:Sapphire harmonic was combined with the second harmonic and fundamental, the power was observed to increase by a factor of 10 with respect to the more common two-color technique [31]. The spectrum shifted farther into the mid-infrared and reached 100 THz (3300 cm^{-1}) using the three color technique, and the power-law scaling in this case is extremely high order – with estimates ranging from $(E_{\text{pump}})^5$ to $(E_{\text{pump}})^8$ depending on the frequency range considered. Unfortunately, the pump energy was limited to 400 μJ in this study and the generated pulses were estimated to have energies on the order of nJ, and the spectrum below 400 cm^{-1} (12 THz) was neglected due to the detection method. Recently, much higher fields were demonstrated when the wavelength of the fundamental, and consequently the second harmonic, were increased, because of an anticipated scaling with of the THz yield of $\lambda^{4.6}$. The maximum was found at 1.8 μm , with the THz field estimated at 4.4 MV/cm with only 420 μJ total pump energy [101]. This dramatic increase is believed to be the result of — in the plasma current model — the increase in THz energy proportional to the square of the photocurrent density, which scales according to λ .

1.1.3.5 DFG-Based THz

One of the most promising techniques for THz and mid-infrared pulse generation above 3 THz is difference frequency mixing with optical parametric amplifiers (OPA). Such an approach provides passive carrier envelope phase stabilization and is similar to techniques in the near infrared and visible regions of the spectrum [102–104]. Extremely high intensity pulses can be produced, fully tunable from 10 to 72 THz. A significant problem with such a setup is the lack of commercial availability of the components. In fact, due to the experimental complexity, there has only been one experimental demonstration of the technique [102], in which a fs-Er:fiber oscillator output is split and amplified to give pulses at 1.55 μm and 1.2 μm . One is doubled and serves as the seed to a conventional Ti:Sapphire based amplifier and the other is compressed to 8 fs and used to gate electro-optic detection. This output, 5 mJ, pumps two OPAs and provides the seed for both OPAs by white light generation in sapphire. One OPA has a signal wavelength that can be varied between 1.1 and 1.5 μm and the other is fixed to 1.1 μm . The signals are then mixed using type-II DFG in a GaSe crystal, or AgGaS₂ for higher frequencies. The results are astounding. The maximum peak field measured was 108 MV/cm, which in this case corresponds to a pulse energy of 19 μJ , the peak power reached 10^8 W, and the intensity was of order 15 TW/cm²! The photon conversion efficiency was 14%, which is three orders of magnitude higher than OR, by virtue of mixing the full spectrum of the pulses, as opposed to solely the wings, in OR. If there was any doubt that such fields can generate non-linearities, the authors observed THz-induced continuum generation, interband luminescence, and damage to their detector when the pulses were not attenuated.

Besides the complicated experimental setup, a secondary concern is that the pulses generated are multi-cycle. In a follow-up study, pulses that were closer to single-cycle were generated using thinner GaSe crystal and a longer pump wavelength, which increases the bandwidth of the OPA

due to lower GVD and better group velocity matching, but at the cost of reduced peak fields of 10 MV/cm [103]. Lastly, emission is restricted on the low frequency end to 10 THz in GaSe due to strong dispersion near a reststrahlen band at 6 THz [105].

1.1.4 Detectors

In conventional THz-TDS, electro-optic (EO) detection is commonly employed. In EO detection, the electric field of the radiation is directly sensed via the Pockels (linear electro-optic) effect. A small portion of the laser beam that generates the THz radiation is split off and variably time delayed to gate the detection. Here, any polarization rotation induced by the electric field of the THz pulse in the crystal is sensed by the combination of a polarizer and a pair of detectors. This allows for the THz electric field to be directly sensed as a function of time. The main drawbacks to the EO detection technique are THz absorption by the crystals and group velocity mismatch between the THz and probe waves, causing the technique to not be broadly applicable. The extreme bandwidths of some of the THz sources discussed above have caused some to employ different techniques, including the use of common mid-infrared pyroelectric [30], MCT [31], and thermopile [102] detectors. The main drawback of these detectors is the lack of phase and frequency information unless interferometry is used. Alternative broadband, coherent, phase sensitive methods have also been demonstrated. These include detection via THz field-induced second harmonic generation (TFISH) [32, 106] and detection by THz radiation enhanced fluorescence emission [33]. Multiple crystals can be employed to avoid phonon-resonance absorption of radiation, and EO characterization of pulses up to 72 THz has been demonstrated in 90 μm thick GaSe [102], with flat spectral phase up to 105 THz [105].

Table 1.3: Parameters for common EO and OR materials [27, 29]

Material	d_{eff} (pm/V)	n_{opt}^*	$n_{800\text{nm}}^{\text{gr}}$	n_{THz}	$n_{1.55\mu\text{m}}^{\text{gr}}$	α_{THz}	FOM (10^{-5} $\text{pm}^2\text{cm}^2/\text{V}^2$)
CdTe	81.8	2.74	3.26* [107]	3.24	2.81	4.8	21.7*
GaAs	65.6	3.40	4.18*	3.59	3.56	0.5	10.1*
GaP	24.8	3.18	3.67	3.34	3.16	0.2	1.80
ZnTe	68.5	2.85	3.13	3.17	2.81	1.3	17.1
GaSe	28.0	2.86	3.13	3.27	2.82	0.5	2.86
sLiNbO ₃	168	2.09	2.25	4.96	2.18	17	59.1
sLN 100K	168	2.09	2.25	4.96	2.18	4.8	100
DAST	615	2.38	3.39	2.58	2.25	50	350

* = The index at 1.55 μm is used for evaluation for CdTe and GaAs, due to strong absorbance at 800 nm. For DAST, the THz index at 0.8 THz is used, but for all others, 1 THz is chosen. The FOM for OR is derived using Equation 1.31 and neglecting all non-variable terms using $L = 1$ mm.

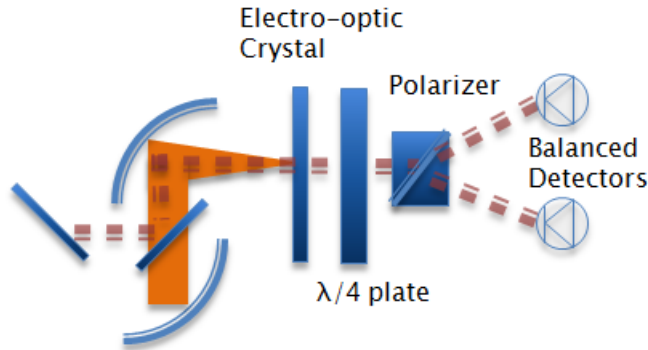


Figure 1.9: A standard experimental layout for electro-optic (EO) detection

1.1.4.1 Electro-Optic Detection

The use of crystals for ultrafast electro-optic detection was pioneered by Valdmanis et al. in 1986 [108]. The linear electro-optic (EO) effect has the same basis as optical rectification. The portion of the non-linear response can be generalized as

$$p_i^{\omega_1-\omega_2} = \chi_{ijk}^{\omega_1-\omega_2} E_j^{\omega_1} E_k^{\omega_2}. \quad (1.38)$$

In this picture optical rectification results if $\omega_2 \rightarrow \omega_1$,

$$p_i^0 = \chi_{ijk}^0 E_j^{\omega_1} E_k^{\omega_1}, \quad (1.39)$$

and the EO effect results if $\omega_2 \rightarrow 0$ and

$$p_i^{\omega_1} = \chi_{ijk}^{\omega_1} E_j^{\omega_1} E_k^0. \quad (1.40)$$

Thus, when the THz pulse, which is a pseudo-DC electric field, and an optical pulse, ω_1 , are incident on a medium with second order nonlinearity, a polarization at optical frequencies is generated. This variably retards one component of the optical probe pulse, changing the polarization at the output of the crystal depending on the electric field strength of the THz pulse. The clamped electro-optic coefficient, r_{ijk} is relatively easy to measure with an applied DC electric field and a laser beam, as seen from Equation 1.44, whereas the nonlinear optical coefficient for optical rectification, d_{ijk} , is more difficult to characterize. However, the two are closely related since both relate back to the nonlinear susceptibility. Indeed, it is found that

$$\chi_{ijk}(\omega; \omega, 0) = -n_i^2(\omega)n_j^2(\omega)r_{ijk}(\omega), \quad (1.41)$$

where i and j typically have the same value [109]. It is then possible to relate the OR optical coefficient to the effective nonlinearity as follows: [29, 84]

$$d_{\text{eff}} = n_{\text{opt}}^4 r / 4. \quad (1.42)$$

A list of relevant parameters for common EO and OR materials is given in Table 1.3 [27, 29].

Similar to the case of emission by OR, detection by EO is often performed with ZnTe or

GaP crystals because of the similarity of the THz phase velocity and group velocity of the 800 nm probe light [73]. The match of the appropriate phase and group velocities occurs at ~ 1 THz for ZnTe and 6 THz for GaP [28]. At higher frequencies the velocity mismatch grows larger and thinner crystals must be used to preserve the match. This reduces the observed response significantly as can be seen from the following equation for the transmission signal seen by a detector in an EO setup, T , where

$$T = \frac{1 + \sin \Gamma}{2} \quad (1.43)$$

and

$$\Gamma = \frac{\pi E_{\text{THz}} L}{V_{\lambda/2}} = \frac{2\pi n_0^3 r_{41} E_{\text{THz}} L}{\lambda}. \quad (1.44)$$

Here, L is the crystal length and $V_{\lambda/2}$ is the half wave voltage. Planken *et al.* derive a similar expression, which is more commonly cited, for the intensity difference of the polarization components, ΔI , in a balanced detection setup using ZnTe,

$$\Delta I(\alpha, \phi) = I_p \frac{\omega n^3 E_{\text{THz}} r_{41} L}{2c} (\cos \alpha \sin 2\phi + 2 \sin \alpha \cos 2\phi), \quad (1.45)$$

where I_p is the probe intensity, α is the angle between the (001) axis and the THz beam polarization, and ϕ is the angle between the probe polarization and the (001) axis. In practice, these angles are usually experimentally maximized, but for reference, the maximum occurs when $\phi = \alpha + 90$ or $\phi = \alpha$ at $\alpha = 90$ or 270 degrees, with the amplitude of the signal switching signs between these cases. The power of the THz radiation, W , can be estimated if the area of the THz beam waist, A , in the crystal is known [32] via

$$W = \epsilon_0 c n A \int_{-\infty}^{\infty} E^2(t) dt. \quad (1.46)$$

For reference, $\sim 72.5\%$ of the total power occurs in the “peak” area, defined where the electric field is positive around time $t=0$, in a non-phase shifted THz pulse generated by two-color plasma and detected by GaP. Because of its natural birefringence, GaSe can be used as a tunable EO detector above 10 THz, with the same low-frequency limitations that hold for emission. Tunability is achieved by changing the angle of incidence to allow for phase matching of the interacting waves in a type-II phase matching configuration. Additionally, the relevant electro-optic coefficient, r_{22} , is higher. For ZnTe at 800 nm, $V_{\lambda/2} \sim 3$ kV, or alternatively, $r_{41} \sim 4$ pm/V [105].

Electro-optic detection, as discussed above, is in the form most commonly used in THz-TDS experiments, employing a split and simultaneous detection of both polarization components of the probe beam. However, for imaging and single-shot detection purposes, a “zero bias” or “zero optical transmission” point scheme is sometimes employed. In such a scheme, the EO detection crystal is placed between crossed polarizers and the transmission minimized using a phase compensator. The transmission through the crystal can then be spatially resolved using a CCD array, for example. Though not as optimal as the balanced detection setup, the modulation depth can easily exceed 9 % using modern technology [110].

1.1.4.2 Air-Based Detection

While EO approaches have been quite successful for THz field detection, the bandwidth coverage is limited unless the crystal length is reduced to a thickness that drops the response significantly. Also unavoidable are absorptions from the transverse optical (TO) phonon modes in the crystal. Thus, for the coherent detection of a very broadband source, such as THz emission from two-color plasmas, the third-order nonlinearity in an isotropic medium, typically gases, can be used to increase phase matching bandwidth and virtually eliminate absorptions. The process by which the THz field is sensed is THz field-induced second harmonic (TFISH) generation, which

was first studied in the liquid phase in an attempt to learn about liquid dynamics [94]. In this case, the THz pulse, like the static DC field in electric-field-induced SHG [95], induces orientation of the the sample, creating a transient anisotropy in the normally isotropic sample and allowing for SHG of a probe pulse at ω_0 to occur. The polarization at $2\omega_0$, $P_i^{2\omega_0}$ is given by

$$P_i^{2\omega_0} = \frac{3}{2} \rho n_L \chi_{ijkl}(-2\omega_0, 0, \omega_0, \omega_0) E_j^0 E_k^{\omega_0} E_l^{\omega_0}, \quad (1.47)$$

where $E_j^0 = E_j^{THz}$ in the case of a THz field, ρ is the relative density, and n_L is Loschmidt's number, or the number of particles of an ideal gas at a given volume at 0° C and 1 atm. Hence, $n_L = \frac{p_0}{k_b T_0}$, where k_b is Boltzmann's constant. Velocity matching is given by

$$\Delta k = 2k^\omega - k^{2\omega}. \quad (1.48)$$

Beyond changing the medium identity or pressure, not much can be done to improve the match. Geometry is of primary concern along with the focusing of the optical and THz beams. Any application of an external field, if relevant, should be constrained to the coherence length, and the interaction length can be increased by periodically poling the applied electric field [55].

Since the response, $I_{2\omega}$, is detected via the THz pulse-induced SHG of the probe pulse, the measurement is only dependent on I_{THz} and is not intrinsically phase sensitive. This can be circumvented in two ways. First [106], if the probe intensity is high enough to form a plasma, some signal at 2ω will be present due to white light generation from SPM and self-steepening in the filament, and can serve as a “local oscillator” (LO) which mixes with the signal at 2ω due to the TFISH. Then,

$$I_{2\omega} \propto E_{2\omega}^2 = (E_{2\omega}^{\text{signal}})^2 + (E_{2\omega}^{\text{LO}})^2 + 2E_{2\omega}^{\text{signal}} E_{2\omega}^{\text{LO}} \cos(\phi), \quad (1.49)$$

where ϕ is the phase difference between $E_{2\omega}^{\text{LO}}$ and $E_{2\omega}^{\text{signal}}$. Thus, the normalized second harmonic intensity will show modulations related to the *sign* of THz electric field. Written more explicitly in terms of the observed intensity,

$$I_{2\omega} \propto (\chi^{(3)} I_{\omega})^2 I_{\text{THz}} + (E_{2\omega}^{\text{LO}})^2 + 2\chi^{(3)} I_{\omega} E_{2\omega}^{\text{LO}} E_{\text{THz}} \cos(\phi), \quad (1.50)$$

where the substitution $I = E^2$ is used in combination with Equation 1.47, and where the first term dominates when the intensity is low. The second term is the DC contribution from the LO that can be removed by lock-in detection, and the third term dominates when the LO is strong and is the source of coherent detection. Unfortunately, when the LO intensity becomes too large, the offset to the data is large and the shape of the waveform can be modified [111]. This results in a lower dynamic range due to the large background signal.

Alternatively, air-biased coherent detection (ABCD) of THz waves can be employed [112], in which a DC bias is applied to the region where TFISH occurs, and the second harmonic from TFISH and EFISH can mix in the same way as above. The advantage of the DC-biased version is that the phase sensitive LO contribution can remain large (the third term above) while avoiding the THz and optical emission background characteristic of dense plasma filaments created by strong optical fields. The background is reduced to 0 because lock-in detection is used and the DC component is not present within the lock-in bandwidth. This was employed in the Blake group and will be discussed further in Section 2.6, including a discussion of the geometry necessary for appropriate phase matching of the DC, THz, and optical fields.

1.1.5 Determination of Optical Constants

Perhaps the most important use of THz-TDS is the relatively simple determination of the so called optical constants, the real index of refraction, $n(\omega)$, and the imaginary index, $\kappa(\omega)$.

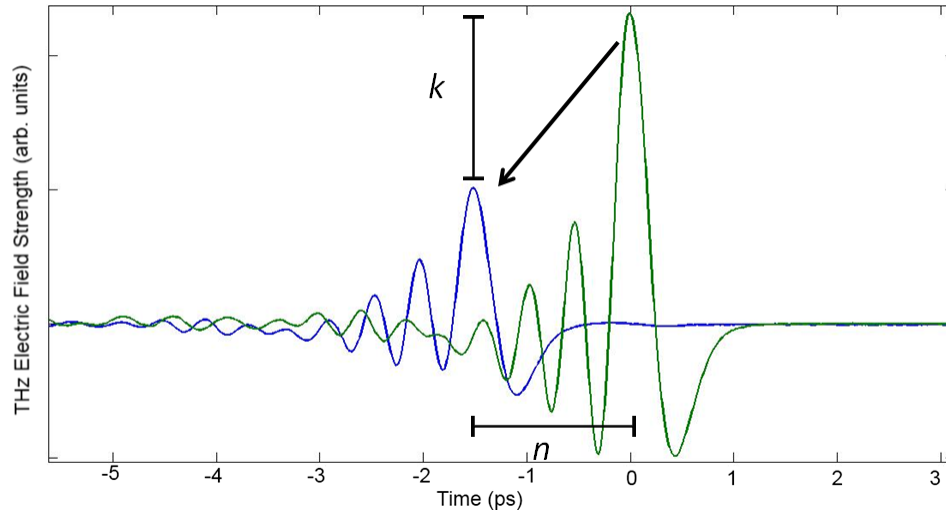


Figure 1.10: Reference and sample THz waveforms demonstrating the effect of constant $n(\omega)$ and $k(\omega)$.

Simplistically, the complex index, \tilde{n} is determined approximately by the propagation coefficient

$$P(\omega, d) = \exp \left[i \frac{\tilde{n}\omega d}{c} \right] \quad (1.51)$$

through a medium, though it is more exactly determined below. The complex index of refraction is a linear combination of the optical constants,

$$\tilde{n} = n(\omega) + i\kappa(\omega), \quad (1.52)$$

where $\kappa(\omega)$ is related to the absorption coefficient, $\alpha(\omega)$, by

$$\alpha(\omega) = \frac{2\omega\kappa(\omega)}{c}. \quad (1.53)$$

There are a couple things to note, since different conventions are frequently used. First, the complex index of refraction, \tilde{n} , is sometimes instead written as

$$n(\omega) - i\kappa(\omega). \quad (1.54)$$

In this case, the propagation coefficient through a material is written as

$$P(\omega, d) = \exp \left[-i \frac{\tilde{n}_a \omega d}{c} \right]. \quad (1.55)$$

Second, the absorption coefficient is commonly defined in base 10 for liquids and solids, as opposed to base e and units nepers/cm for gases. Thus, they are related by a factor of $\ln(10)$, i.e. $\alpha_{\text{nepers}} = \alpha * \ln(10)$. Most forms of spectroscopy determine only the absorption coefficient unless Kramers-Kronig analysis can be employed reliably. FT-IR spectrometers can be modified into an asymmetric version in which the sample is placed in only one arm of the interferometer, an arrangement that can give both optical constants. It is rarely done, however, due to the additional complexity it adds to the experiment and analysis.

In Figure 1.10 the effect of n and k on a typical THz-TDS scan can be seen. The full frequency resolved values of n and k require fitting, as can be seen from Figure 1.11. The observed signal at the detector has contributions from reflection at the sample interface, transmission between interfaces, and propagation through the various media. Typically both reference and sample scans are recorded with the sample placed in air or between windows, for which the optical constants as a function of frequency are already known. Three media are thus considered, with medium 2 being the sample of interest. From the Fourier transform of the time domain signal, the complex frequency spectrum as a function of angular frequency is [113]

$$S_{\text{SAMPLE}}(\omega) = \eta\omega \cdot T_{12}(\omega) \cdot P_2(\omega, L) \cdot T_{23}(\omega) \cdot \sum_{j=0}^{+\infty} \{R_{23}(\omega) \cdot P_2^2(\omega, L) \cdot R_{21}(\omega)\}^j \cdot E(\omega), \quad (1.56)$$

where the terms from the summation in “curly braces” are reflections from the Fabry Perot effect, which are important for thin samples, and $\eta(\omega)$ is the combination of reflection, transmission and propagation coefficients in media 1 and 3. The reflection coefficient at the interface

between a and b is

$$R_{ab}(\omega) = \frac{\tilde{n}_a - \tilde{n}_b}{\tilde{n}_a + \tilde{n}_b}, \quad (1.57)$$

while the transmission coefficient from medium a to b is

$$T_{ab}(\omega) = \frac{2\tilde{n}_a}{\tilde{n}_a + \tilde{n}_b}, \quad (1.58)$$

and the propagation coefficient in medium a through a distance d is

$$P_a(\omega, d) = \exp\left[-i\frac{\tilde{n}_a\omega d}{c}\right]. \quad (1.59)$$

The complex transfer function, $H(\omega)$, is obtained from the ratio of sample and reference signals:

$$H(\omega) = \frac{S_{\text{SAMPLE}}}{S_{\text{REF}}} = \frac{2\tilde{n}_2(\tilde{n}_1 + \tilde{n}_3)}{(\tilde{n}_2 + \tilde{n}_1)(\tilde{n}_2 + \tilde{n}_3)} \cdot \exp\left[-i(\tilde{n}_2 - \tilde{n}_{\text{air}})\frac{\omega L}{c}\right] \cdot \text{FP}(\omega), \quad (1.60)$$

where $\text{FP}(\omega)$ is the Fabry-Perot contribution, which will be neglected here (so $\text{FP}(\omega) = 1$), and

$$S_{\text{REF}} = \eta(\omega) \cdot T_{13}(\omega) \cdot P_{\text{air}}(\omega, L) \cdot E(\omega). \quad (1.61)$$

There is no analytical solution for n_2 and κ_2 , so Equation 1.60 must be solved by computational means. This is discussed further in Section 6.2. After the optical constants have been determined, they can be used to calculate other derived properties such as the relative permittivity or dielectric constant, $\tilde{\epsilon}(\omega)$, and conductivity, $\tilde{\sigma}(\omega)$. For the dielectric constant,

$$\tilde{\epsilon}(\omega) = \epsilon'(\omega) + i\epsilon''(\omega) = \tilde{n}(\omega)^2, \quad (1.62)$$

where [114]

$$\epsilon'(\omega) = n^2(\omega) + \kappa^2(\omega) \quad (1.63)$$

and

$$\epsilon''(\omega) = 2n(\omega)\kappa(\omega). \quad (1.64)$$

The complex conductivity is obtained from

$$\tilde{\epsilon} = \epsilon_{\text{material}}(\omega) + \frac{i\tilde{\sigma}(\omega)}{\omega\epsilon_0}, \quad (1.65)$$

where $\epsilon_{\text{material}}(\omega)$ is the complex permittivity of the base material in the case of a doped sample or of the non-photoexcited sample in the case of time-resolved spectroscopy (ϵ_0 is the permittivity of free space) [115, 116].

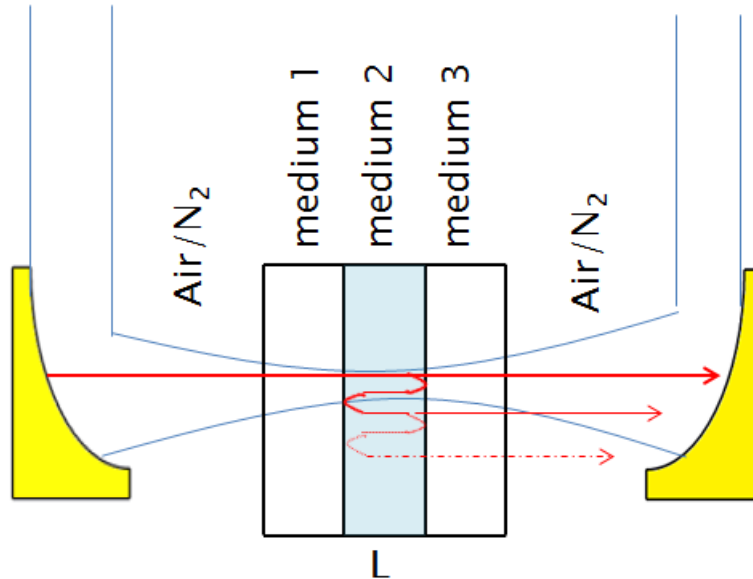


Figure 1.11: A depiction of the intricacies of optical constant determination in an enclosed cell.

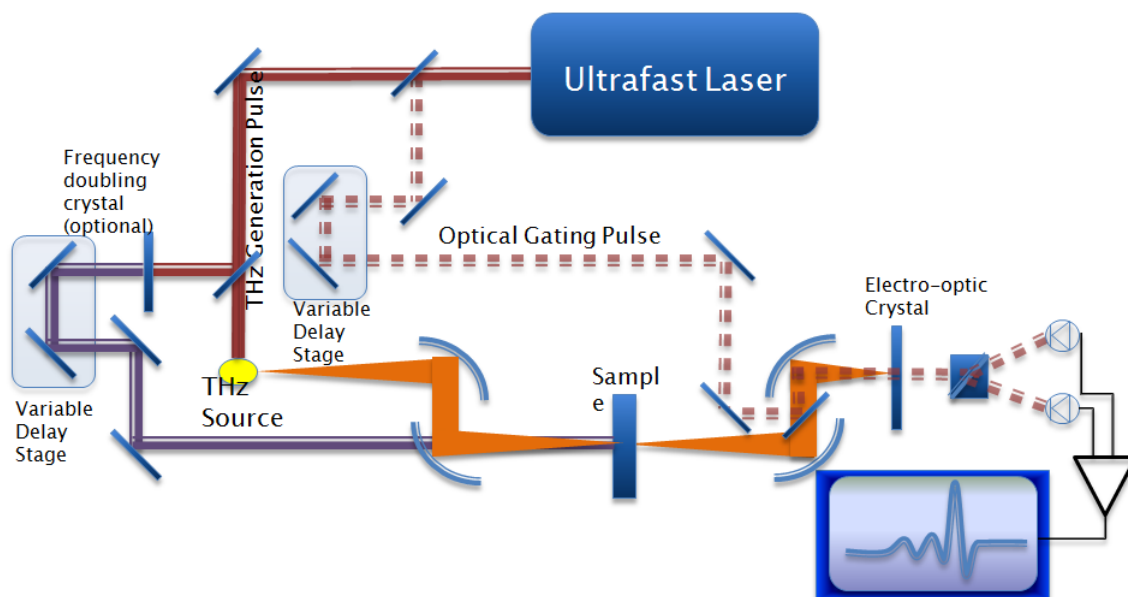


Figure 1.12: A standard experimental setup for time resolved THz-TDS, wherein an optical probe pulse excites the sample, while the changes to the THz spectrum are monitored as a function of time.

1.1.6 Time-Resolved Spectroscopy

The other advantage THz-TDS has over FT-IR or other THz range spectroscopies is the ability to analyze the ultrafast change to the THz optical constants, or parameters derived from these quantities, as a function of time after a change to the sample, typically as induced by an electronically resonant optical excitation pulse. A typical experimental setup is shown in Figure 1.12. Two time delays are swept, giving rise to a 2D scan. Most commonly probed are semi-conductors, since the change in conductivity is often relatively large and thus involves a large change to the THz reflectivity, and chromophores in liquid environments where the solvent response typically dominates at THz frequencies.

Chapter 2

THz TDS as Implemented in the Blake Group

2.1 Introduction and Overview

THz-TDS was first performed in the Blake group in the summer of 2007 using a Spectra Physics Tsunami Ti:Sapphire oscillator on loan from the Heath group and biased photoconductive antennas on GaAs as provided by Ekspla Optics [117]. The emitter-detector pair, though commercially available, only provided qualitative results due to extreme hysteresis in alignment/adjustment and a profound sensitivity to vibration of the bias and signal cables. The latter sensitivity arises because the devices were operated in current mode and very low currents were sensed. The vibrationally-driven noise pickup was so severe that it was common to press a button to start the scan and to tip-toe out of the lab, making sure to gently close the door on the way out.

Thanks to support from the National Science Foundation Chemistry Research Instrumentation & Facilities: Instrument Development (CRIF:ID) program and the National Aeronautics and Space Administration Laboratory Astrophysics program, new ultrafast lasers, including both oscillators and a regenerative amplifier, upgraded THz emitters and detectors, and A/D detection electronics were installed beginning in 2008. Our initial THz-TDS were performed using optical rectification and electro-optic detection in 1 mm thick $\langle 110 \rangle$ ZnTe. The delay

between the optical pump for the THz emitter and optical probe for EO detection pulses was swept by moving a delay stage at constant velocity. The rotation of the probe polarization was sensed by a combination of a quarter wave plate and linear polarizing beam cube in combination with two variable gain photodiodes. The signal of the photodiodes was processed in a difference amplifier and sensed with either a lock-in amplifier or a directly by an oscilloscope that served as a data acquisition card. The data were then stored in memory and averaged and processed after scanning was complete. Later, in the interest of wider bandwidth and higher signal-to-noise/dynamic range, the emitter was replaced by thinner samples of ZnTe, by GaP, or by a two-color plasma source. When broad bandwidth was desired, EO detection was performed with GaP, at the cost of signal strength. Detection by FWM in air was also attempted, as this technique shows promise for detection of signals with very large bandwidth, but has not yet been successfully demonstrated.

Comparisons of the progress so far are presented in the following figures: Figure 2.1 shows the difference in the detected spectrum for two distinct sources and emitters, a 0.2 mm thick ZnTe wafer for emission and a 1.0 mm thick ZnTe wafer for detection versus a plasma emission source and 0.4 mm thick GaP EO detection wafer. The time-domain waveforms are shown in Figure 2.2, where the excellent signal-to-noise is due to long averaging times. In practice, the usable frequency content of the plasma THz pulse with EO detection typically extends to ‘only’ ~ 8 THz (literature reports include results with several tens of THz bandwidth), but the two-color plasma source still extends the useful frequency range by over a factor of two as compared to a ZnTe emitter. In the following sections I detail the major components of the new THz-TDS instrument developed for this thesis.

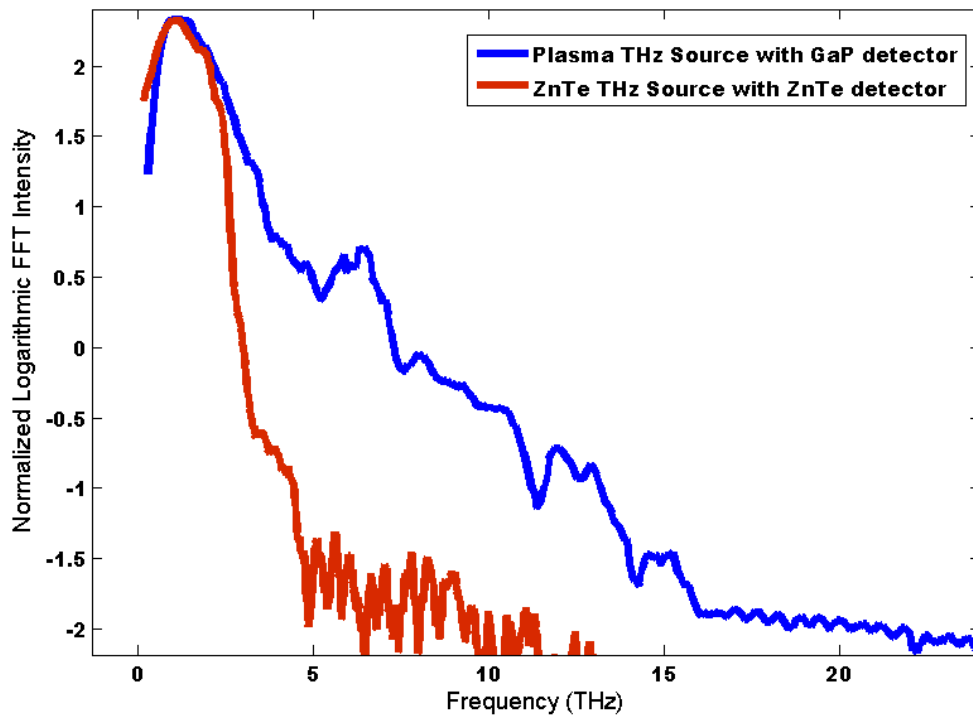


Figure 2.1: A comparison of the base-10 logarithmic FFT magnitude of the pulses seen in the next figure.

2.2 Laser Systems

2.2.1 Oscillators

The original oscillators for the CRIF:ID facility included two Coherent Micra Ti:Sapphire lasers, Kerr-lens mode-locked oscillators capable of supplying nJ femtosecond pulses with controllable bandwidth and frequency. The average power is typically between 400 and 500 mW at a repetition rate of 80 MHz. One of the Micras is intended to be “slaved” to the other and has three ways to control the repetition rate, including a stepper motor on the output coupler and PZT controls on two of the cavity mirrors. The output spectrum of the Micras can have > 120 nm of bandwidth (FWHM). As such, they are quite useful for seeding amplifiers due to their broad bandwidth. The output is chirped, and if compressed, pulses with a time duration of <15 fs can be produced. The pulse duration, chirp, and spectral bandwidth are controlled

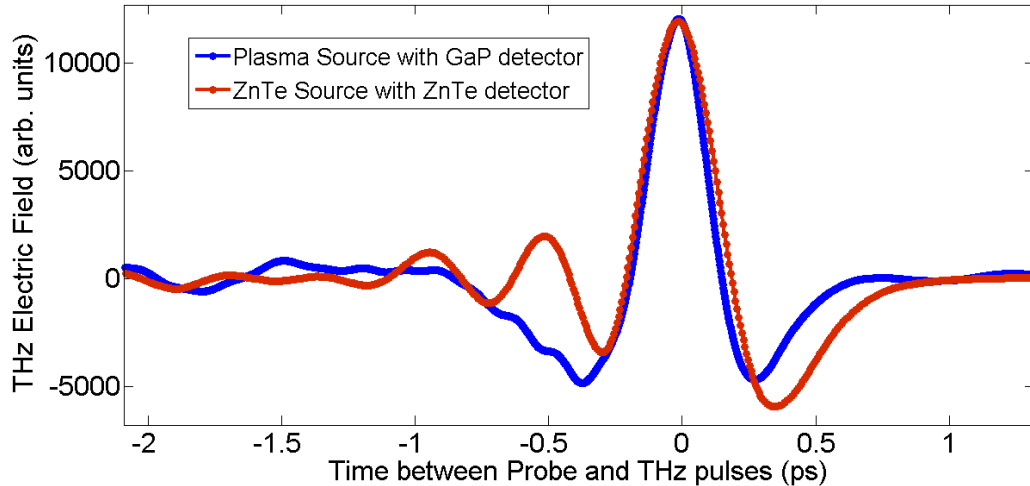


Figure 2.2: Comparison of THz sources and detectors showing the improvement in frequency coverage resulting from the extra intensity and bandwidth of the plasma source.

by the combination of two prisms on translation stages and a hard aperture with controllable width near the high reflector (see Figure 1.6). Later a Mantis oscillator was purchased as a dedicated seed laser for the Blake group regenerative amplifier, described below.

The Mantis is similar to the Micra with a few exceptions. The pump source is an integrated optically pumped semiconductor laser (OPSL) as opposed to a diode pumped solid state (DPSS) laser in the Micra. The OPSL is expected to have a much longer lifetime and is much cheaper than the DPSS, but the beam quality is worse, $M^2 \sim 1$ for the DPSS and $\sim 4-10$ for the OPSL. The power fluctuations are also larger because the laser is not single mode (the Micra lasers are capable of Carrier Envelope Phase, or CEP, stabilization, which requires very low noise pump laser operation). The other main difference is that negative dispersion mirrors are used to control the intracavity dispersion instead of prisms. The spectrum can be changed only slightly by adjusting a set of thin wedges, and the end result is that the bandwidth is reduced compared to the Micra, typically to values of ~ 70 nm. This is sufficient for seeding the amplifier due to a hole in the spectrum at the center wavelength, ~ 800 nm. The Mantis pulse spectral content, as sensed by an Ocean Optics USB4000 VIS-NIR spectrometer, is displayed in Figure 2.3.

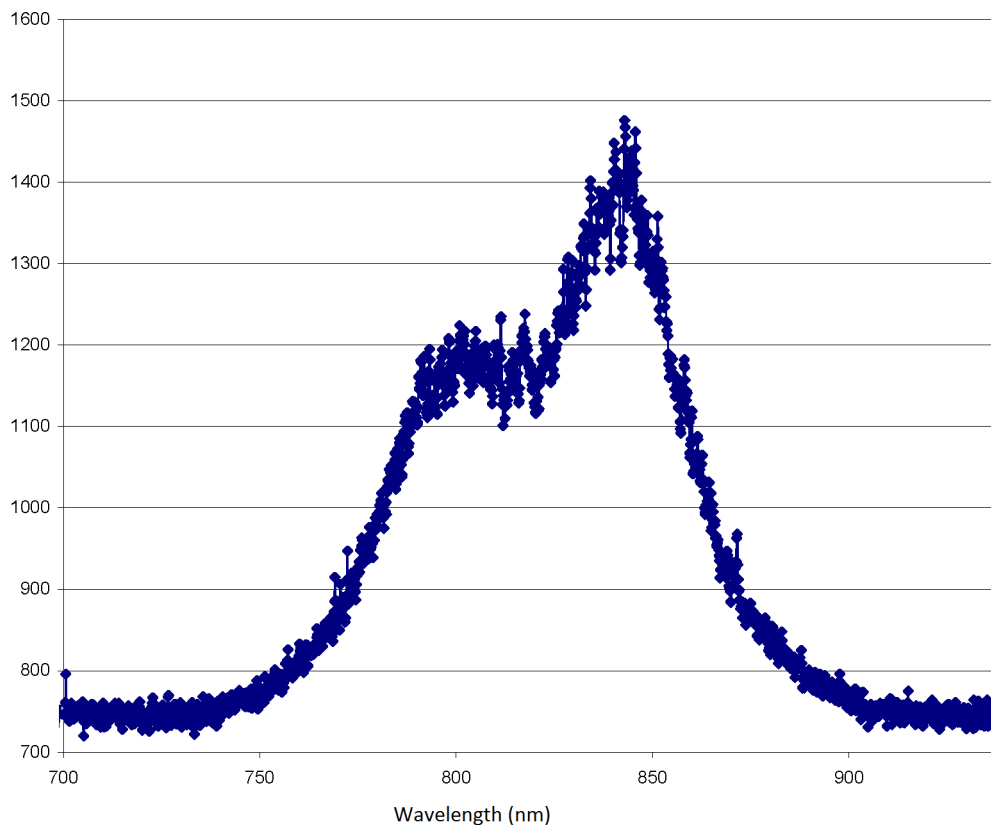


Figure 2.3: A typical spectrum of the Mantis as sensed by an Ocean Optics USB4000 spectrometer. The “noise” at the peak is due to etalons in the detector.

2.2.2 Regenerative Amplifier

One Micra was originally used to seed the Coherent Ti:Sapphire regenerative amplifier, model “Legend Elite USP,” or Legend herein. The Legend features three sections and an integrated pump laser. First the input pulse from the oscillator is stretched temporarily and spatially in the stretcher. Sufficient stretching requires significant physical space, and this section of the Legend is the largest. The pulse is first aligned through an optical isolator in order to prevent feedback into the oscillator. It is then directed onto a grating, which disperses the pulse. After propagating across the cavity, the pulse strikes a curved dielectric mirror which collimates the pulse and redirects it back at the grating. The grating then serves to reduce the size of the pulse spatially. The pulse makes another set of trips through the grating and curved mirror set and

is then sent to the amplifier. The amplifier itself is a large Ti:Sapphire rod which is pumped by the ~ 20 W second harmonic (527 nm) output of a Q-switched Coherent Evolution Nd:YLF laser operating at 1 kHz. The pulse takes on the order of 10-15 round trips in the cavity before being released by the combination of double passed Pockels cell — triggered by a high voltage pulse — and a thin polarizer. The Pockels cell is biased to impart a quarter wave rotation at each pass. The intracavity power is roughly 4.2 W at this point before being passed into the compressor. The compressor serves to shorten the pulse by again using several passes off of a grating. The size of the compressor and the distance the light travels is smaller due to reduced bandwidth in the amplifier due to gain narrowing. As originally delivered, the optimal output was 3.3 W at 1 kHz, which results in 3.3 mJ pulses of ~ 30 fs duration (FWHM). Very recently, the amplifier cavity has been altered to support pumping from one side of the amplifier, which makes the laser easier to align. The Pockels cells were also replaced with less lossy versions, and “afterburner” optics were added to refocus the extra pump light onto the Ti:Sapphire crystal. This results in up to ~ 4.2 W after compression at the output of the Legend, with slightly longer pulses of ~ 35 fs.

2.3 Delay Line

The Ekspla delay line features a protected gold-coated retroreflector, or corner cube, which can be difficult to align and is lossy relative to dielectric mirrors. Beyond that, the delay line was designed for step-scanning, and the constant start and stop motions created significant shaking, which is not ideal for an optical delay line for obvious reasons. The time needed to permit mechanical settling causes a THz scan to be extremely slow. Two motion stages were therefore ordered from Newport (ILS100 and ILS150). The motion is much smoother than the Ekspla delay line, and there are many more motion control options. Two 45° angle of incidence

high reflector (HR) mirrors were mounted on the stage and used to direct the beam back along the direction of incidence. The delay stage was aligned by ensuring that the incident beam was completely level to the optical table and traveled completely parallel to the direction of travel of the stage, which was taken to be parallel to the holes on the optical table. To accomplish this alignment, a set of razor blades — one vertically and the other horizontally oriented — were mounted on translation stages. They were placed at a fixed distances along the direction of propagation and translated into the beam path such that the transmitted power was reduced to 50% of the incident intensity. The steering mirror was then adjusted. This procedure was repeated until no translation was required.

Both delay lines have well-measured pitch and yaw over the entire travel range, but they are not constant and thus are difficult to adjust for. The displacement for the ILS150 was measured as $\sim 24 \mu\text{rad}/100 \text{ mm}$ of travel, which is close to the $30 \mu\text{rad}$ reported by Newport and significantly less than the spec of $100 \mu\text{rad}/100\text{mm}$. Thus, the beam does have some uncorrectable displacement in both the horizontal and vertical axes when propagated a long distance from the delay line. Since the delay line is most frequently used for the THz probe beam, the beam is focused onto both the EO detection crystal and onto the photodiode detectors and the displacement is demagnified significantly. The other use of a delay stage is for the optical pump beam in time-resolved THz-TDS scans. In this case, the stage can be placed close to the sample and the resulting beam displacement is small. In future designs, it is recommended that the delay lines be placed close to the experiment instead of close to the output of the laser to minimize these effects.

Initially, in an attempt to mimic the functioning of the Ekspla delay line, the delay stages were stepped, but this leads to very slow scanning times, as at each point the stage must find its center position, which takes on the order of a second or more. Instead, a routine was designed where the stage was moved with constant velocity, and data were acquired as a function of

the time after a period of constant acceleration. This resulted in much faster data acquisition, and allows for more averaging. Small start time offsets in the signal from scan to scan were observed, probably due to variance in start time. In order to increase the reproducibility of the data when averaging, the data are co-added after centering on the point of greatest amplitude. Details can be found in Sections 2.5.2 and 6.1. Future iterations should include extra points for peak amplitude finding routines by interpolation. Absolute fiducial marks created by the white light fringe of a broadband laser or light emitting diode would serve to improve the scan-to-scan repeatability as would real-time acquisition of the delay line position.

2.4 THz Emission Techniques

A power splitter/variable attenuator was used to control the power directed to the THz emitter (model 990-0070-800-H from Eksma Optics) in EO generation schemes. It consists of a quartz waveplate ($\lambda/2$) followed by two thin film polarizers mounted at the correct angles. The device is not optimal for many reasons. The waveplate causes SHG and slightly modulates the spectral content of the pulses. Most of the SHG is transmitted through the first polarizer, and can be spectrally filtered if necessary. The bigger problem is the spectral range over which the polarizers work, which does not cover the full bandwidth of the Legend pulses. This is well described graphically in the data sheets, but is also discussed here in detail. Given a 3.2 W input beam, a maximum of 2.63 W (82%) is transmitted through the first polarizer, when the beam is *p*-polarized. The residual reflected light consists of the blue part of the spectrum. This is a significant disruption of the pulse spectrum and necessitates a significant change to the time-domain properties of the pulse. When the beam is *s*-polarized, 2.92 W of 3.2 W (91.3%) is reflected by the combination of both polarizers. The red part of the spectrum is transmitted through the first polarizer, but to a lesser extent. Thus, the reflected, *s*-polarized beam was

used in all experiments. This power splitter should not be used if one is concerned with the high or low frequency pulse spectrum or in achieving the shortest possible pulse.

2.4.1 Optical Rectification

After the challenges of THz-TDS experiments with photoconductive antennas, OR in ZnTe as pumped by the Legend was employed as a source of THz radiation. For these experiments, EO detection, also in ZnTe was employed. The combination of the two results in very large signals given appropriate probe intensities. Electro-optic crystals were purchased from Ingcrys in various thicknesses. Initially 1.0 mm thick crystals of ZnTe were used for both emission and detection. Later it was found that thinner emitter crystals gave greater power and broader bandwidth THz pulses. This is attributed to saturation of the emitter and THz absorption of the generated free carriers caused by optical two photon absorption and higher order processes. For EO detection, signal strength was found to correspond to the crystal thickness.

The use of GaP allows for higher bandwidth detection of THz radiation, in principle. However, the signal-to-noise decreases and thus the higher frequency components of the pulse may not be able to be sensed without averaging. Figure 2.5 shows the higher bandwidth of the shorter pulses produced by GaP and detected by 1.0 mm thick ZnTe. The power is normalized and does not show the smaller intensity of the signal compared to ZnTe.

2.4.1.1 ZnTe

Figure 2.4 shows the difference between 0.2 and 1.0 mm thick ZnTe crystals as used as an OR source of THz pulses; in both cases EO detection by a similar 1.0 mm thick ZnTe wafer is used. When used as an emitter at modest input power, ZnTe glows reddish orange. At sufficiently high intensity, the color will change to green. Typically this corresponds to the highest field strength THz pulses, but also entails damage to the crystal over time. A damaged ZnTe crystal

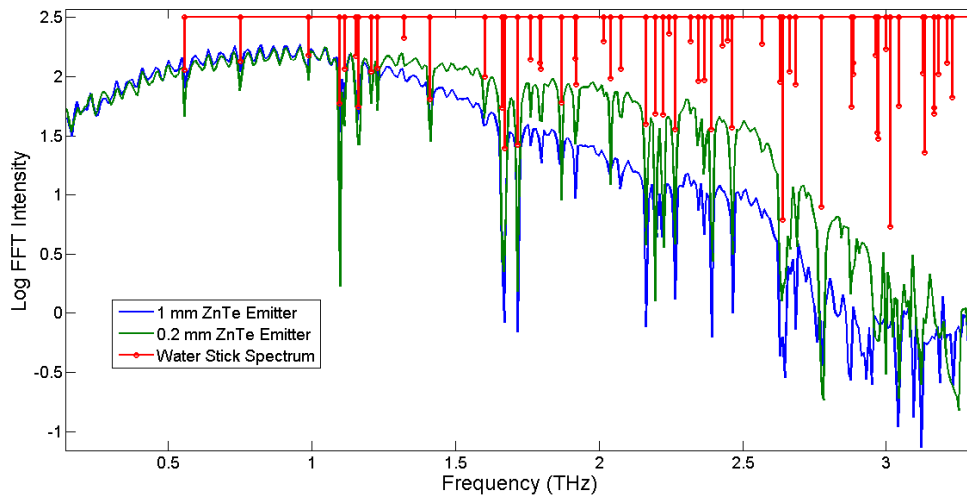


Figure 2.4: A direct comparison of 1 mm thick ZnTe and 0.2 mm thick ZnTe emitters as detected by the same 1.0 mm thick ZnTe wafer demonstrating the overall superior performance of the thinner wafer. The water stick spectrum is shown for comparison purposes.

appears dark relative to an unused crystal. The dark spot usually appears in the center of the crystal where the laser power is highest. Upon darkening, the efficiency of THz generation remains somewhat constant, and thus the damaged crystals can continue to be used. Very clear demonstrations of this can be seen at the focus in detector crystals where opaque marks are easily made when using the unattenuated remains of the pump beam for alignment. It is thus important to remember to always attenuate the pump beam prior to using it for alignment purposes. Typically 0.8 W of the Legend beam are used for pumping ZnTe emitters. A future experiment of interest for the Blake group is the use of a large-aperture ZnTe crystal acquired from Ingrys. It may serve to significantly increase the signal in experiments below 3 THz.

2.4.1.2 GaP

The electro-optic coefficient difference between ZnTe and GaP makes a significant difference in use as an EO sensor. However, when used as a THz emitter, the signal from GaP can compare to or even beat ZnTe for several reasons. First, at the same pump energy the THz signal can compare to that from ZnTe since GaP does not suffer from two-photon optical absorption (and

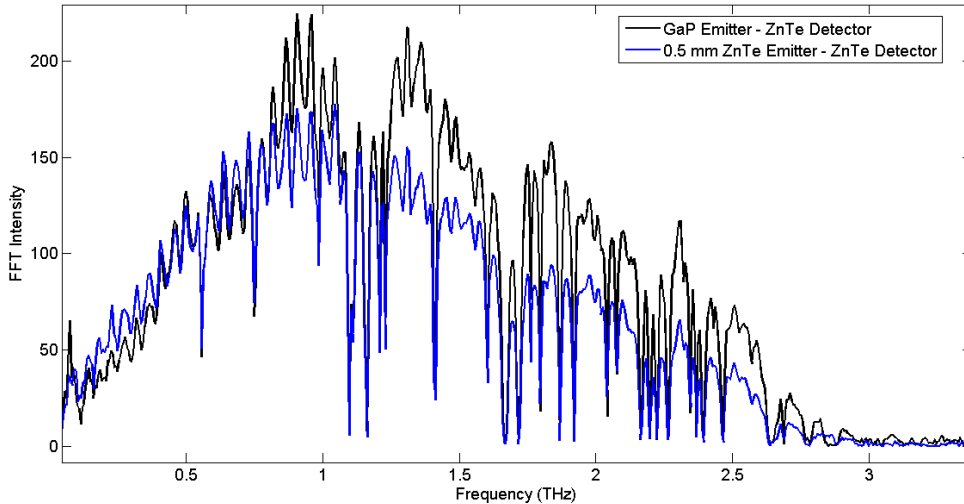


Figure 2.5: A normalized comparison of GaP and ZnTe emitters as detected by the same 1.0 mm thick ZnTe wafer. The GaP spectrum is weighted more toward higher frequencies.

the subsequent absorption of the generated THz radiation by free carriers). Secondly, GaP can be pumped with more energy because of the higher damage threshold due to the absence of two-photon absorption. Lastly, the lowest TO phonon mode GaP lies above 11 THz. Thus, GaP emitters can be effectively used up to 8 THz, thus increasing the bandwidth of the signal and ultimately, the peak field strength. Future experiments should be attempted at higher pump powers with a GaP emitter, as typically GaP was used at similar pump power to ZnTe in the Blake labs solely due to convenience. While the GaP emitter is not expected to have the same high frequency content as the two-color plasma source, it may be less noisy due to its reduced susceptibility to air currents or optical fluctuations.

2.4.2 Plasma-based Emission

In the interest of shorter THz pulses with higher field strengths and greater bandwidths, two-color laser induced plasma THz generation was employed. The first attempts at laser-induced plasma were in the standard experimental setup where the ~ 0.8 W Legend pulse train used for OR in ZnTe was focused through a β -BBO SHG crystal. THz pulses with very small field

strength were sensed. Retrospectively, this was attributed to the pulse compression of the Legend output. It was found that maximum signal from OR corresponds to a chirped output pulse from the Legend, in contrast to the plasma, where shorter pulse durations, and especially transform limited pulses, strongly correlate with higher THz field strengths. Unfortunately at the time, we did not know that this was the case. It was assumed that the difficulty arose from the fact that the phase matching and polarization of the red and blue pulses was not optimum, as had been reported by several papers [91, 118]. This caused us to attempt the GVD and polarization compensation scheme described in the following section. In our second suite of experiments, the plasma was generated by focusing the combined 800 and 400 nm light with either a lens or an off-axis parabolic mirror. If focused before the BBO crystal, a lens can be used, but if the output of the BBO is focused, severe chromatic dispersion in the lens causes a double focus along the direction of propagation and very little THz radiation is observed. Both gold- and aluminum- coated OAPMs were considered and tested. For a pulse centered at 800 nm, the gold OAPM reflects $\sim 96.7\%$ of the incoming power and $\sim 31.7\%$ at 400 nm, or $\sim 81.7\%$ of the total combined power. The aluminum OAPM reflects $\sim 70\%$ of the power at both 400 and 800 nm. The aluminum was chosen, since the THz field should scale proportionally to $E_{800}^2 E_{400}$, and the optical field strength was assumed to be related to the square root of the power, making aluminum $\sim 10\%$ more efficient than gold.

Three different gases or gas mixtures have been used to test the plasma, including air, nitrogen, and argon. The field strength of the emitted THz radiation becomes higher upon purging the enclosed area with nitrogen gas and increases slightly more when switching to an argon purge gas. The increase in observed THz field strength when switching from air to nitrogen is $\geq 12\%$ and $\sim 18\%$ when argon is used instead. The observed results match well with previously observed trends [100, 119]. Larger improvements should result when a gas with a lower IP is used [86], and the expected scaling with IP is of exponential high order

below saturation. The scaling at or near saturation is slower, due to an almost linear increase with optical power in the plasma length even beyond the dephasing limit [119]. We believe this to be consistent with the results of Rodriguez *et al.* [120], where a higher power laser system was used. In the future, if lower pressures are to be used, such as in a gas jet, for example; trimethylamine, with an IP of only 7.82 eV, might be considered [99]. This is more relevant for gas-based detection, however, where the scaling with pulse energy is anticipated to be significantly steeper.

2.4.2.1 Phase Compensation

The phase compensation scheme used [91, 118, 121, 122] was of the “in-line” variety, and is shown in Figure 2.6. It consists of a β -BBO crystal optimized for type I SHG, where the polarization of the SHG pulse is orthogonal to the input pulse, followed by a birefringent calcite plate set to variably delay the 800 nm pulse with respect to the 400 nm pulse. Lastly, a quartz dual-band waveplate is used to impart a $\lambda/2$ retardation at 800 nm and a λ retardation at 400 nm. Both pulses are focused by an off-axis parabolic reflector to form a plasma that emits THz radiation. Initially, a pair of fused silica wedges were used to finely tune the delay between the 800 and 400 nm pulses. This was found to be unnecessary, and tilt tuning of the birefringent plate was used instead. The GVD between the 800 and 400 nm pulse is tuned linearly by varying the angle of incidence from -10 to 10 degrees. Two GVD calcite plates were ordered from Eksma Optics. The first calcite plate can adjust for offsets between -240 and -520 fs. It is 1.7 mm thick and has an optical axis orientation of 55 degrees relative to the surface. The second calcite plate adjusts offsets between -390 and -800 fs. Its measurements are unknown, but could in principle be calculated. For pulses shorter than 50 fs, α -BBO should be used instead of calcite as a birefringent material due to reduced dispersion relative to calcite.

The GVD compensation plate must compensate for the group velocity difference in the

elements of the plasma generation optics as well as any windows, lens, or air through which both beams travel before the plasma is created. The β -BBO crystal is 0.2 mm thick and generates minimal GVD between the 400 and 800 nm pulses due to index-matching based on the cut angle and central frequency of the THz pulses. The GVD of different frequency components of the broadband pulse is of concern, however, and thin material is used to minimize this effect. The effective index, n_{eff} , can be written as a function of the cut angle, Θ_c via the following equation:

$$\frac{1}{n_{\text{eff}}^2} = \frac{\sin^2 \Theta_c}{n_e^2} + \frac{\cos^2 \Theta_c}{n_o^2} \quad (2.1)$$

where e and o refer to the extraordinary and ordinary indices of refraction, which give an effective index of refraction of 1.660523 for β -BBO at $\Omega_c=29.2^\circ$ for both relevant wavelengths. The air also provides a GVD between the 400 and 800 nm component of the pulses of 26.7 fs/m. No more than a meter separated the β -BBO crystal from the focus of the OAPM. The zero-order dual-band waveplate is made from air-spaced single-crystal quartz of unknown thickness (Eksma Optics part number 465-4211). Because of the birefringent nature of the plates, unknown orientation of the optical axes, and unknown thickness, the GVD cannot be estimated *a priori*, but it is significant. Initially, the very low estimate of ~ 5 fs GVD was made based on the 43 μm thickness of quartz used in previous experiments [122, 123], but such a waveplate is a true zero-order waveplate and is not used herein due to better performance of air-spaced waveplates for broadband applications. Factoring out the rest of the optics, the best guess for GVD induced by this optic is actually 350 ± 40 fs. A representative from the company cited the actual value as ~ 346 fs to us in an email.

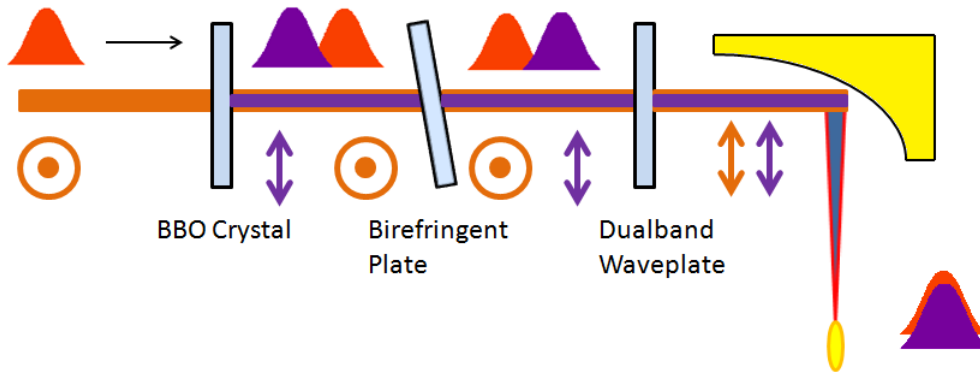


Figure 2.6: The in-line phase compensator used for THz generation via two-color laser plasma. The device's main purpose is to orient the 800 and 400 nm beams with the same polarization.

2.4.3 Field Strength Calculation

The THz field strength can, in principle, be calculated from the response obtained from the measured voltages of the balanced photodiode setup using Equation 1.44. The setup was tested using a ZnTe electro-optic crystal with a thickness of 1 mm. Measurements and calculations for the ZnTe half wave voltage, $V_{\lambda/2}$ range from 3 kV [124] to 5 kV [125], where

$$V_{\lambda/2} = \frac{\lambda}{2n^3r_41}. \quad (2.2)$$

In this case, the numbers reported in Table 1.3 were used, and $V_{\lambda/2} = 4161$ kV. The difference comes from inaccuracies in the measurement of r_41 . EO detection with ZnTe also suffers from other problems, including phase walk-off at low frequencies and absorption. When the bulk of the input THz signal to be rectified is <3 THz, this is not of as much concern. Since a significant part, perhaps even the majority [30], of emission from the two-color source is above or around 3 THz, however, the field strength will be underrepresented. GaP should have been used for this determination since the THz absorption spectrum is low until the onset of the first TO mode at >11 THz, with adequate performance up to 8 THz [73]. Additionally, $V_{\lambda/2}$ is much higher, at 12.8 kV, using the numbers found in Table 1.3.

The procedure for the field strength measurement will be discussed in this paragraph. The signal from the summing amplifier was swapped to give positive polarity for both channels, rather than opposite, as is commonly set for balanced or difference measurements. The signal magnitude was averaged and processed in the same way as the THz-TDS data by the scanning software. Without changing the scale on the oscilloscope, the maximum, minimum, and zero value for a THz scan were recorded in standard balanced detection mode. The zero corrected maximum was compared to the average total signal from both detectors. This ratio was divided by two and added to 0.5, which is the criteria to be balanced, and the $\Gamma=0$ condition of Equation 1.44 was imposed, to give the transmission through one arm of the linear polarization analyzer (polarizing beam cube or Wollaston prism). From this, Γ , in radians, and E_{THz} were determined. The result was corrected for transmission and approximate propagation through 5 mm of high-density polyethylene and for transmission into ZnTe, via Equation 1.58. The end result is ~ 13.2 kV/cm when focused in air, not accounting for high frequency losses in high-density polyethylene, non-ideal focusing, or absorption losses in ZnTe, which might be significant.

To check the peak field-strength, the average power was measured with a Scientech 361 pyroelectric detector. The minimum scale was used and the estimated power was $30 \pm 5 \mu\text{W}$, or ~ 30 nJ/pulse. This must be scaled by a factor of two according to the calibration of Foote *et al.* [126]. Since we want to obtain an estimate of the peak field, we are only interested in the THz power near the peak. Approximately 72.5% of the total power is present in the region defined around time $t=0$ with positive electric field. This estimate was arrived at by integrating the square of the electric field of a typical pulse as generated by two-color plasma and detected by GaP. The peak power was determined to be ~ 30 kW, by fitting a Gaussian-shaped pulse to the region around time $t=0$ with a half-width of 135.5 fs. When focused to a spot size of 1 mm diameter, the peak intensity is ~ 385 GW/m², which gives a peak electric field of ~ 170 kV/cm when focused in air, as specified by the relation of electric field to intensity in SI units,

$E=27.4\sqrt{I}$, which is derived from the following equation [8]

$$I = 1/2\epsilon_0 E^2 c. \quad (2.3)$$

Clearly, there is a large discrepancy in the measured values. Some possibilities will be discussed. First, there may be a severe under-sampling of the frequency content of the pulse in the case of electro-optic detection. This is quite likely due to the limited frequency coverage of ZnTe due to absorptions and phase walk-off in a 1 mm thick crystal. Also possible is poor focusing in the ZnTe crystal or poor alignment. I consider this unlikely due to the strong measured signal, and inability to improve the signal despite many tweaks to the optical alignment. The net effect of all these issues is an underestimate of the true field strength. On the average power measurement side, a possibility is that the plasma emits some radiation that leaks through the filters that is not part of the coherent THz signal, but that is detected by the thermopile detector, thus overestimating the true field strength.

2.5 Electro-Optic Detection

The details of optical components that comprise the electro-optic detection setup are presented here. A Thorlabs polarizing beamsplitter cube, model PBS102, or Wollaston polarizer, model WP10B, was used in combination with an ultrafast-type $\lambda/4$ plate to balance two variable gain photodiode detectors (Thorlabs model PDA36A). The output of the detectors was sent to a summing amplifier (Stanford Research Systems SIM980) with one detector input inverted in the case of oscilloscope based detection, or directly to input channels A and B of the lock-in amplifier. Using the reflection from three beam samplers (Newport model 10B20-01NC.2) in combination with two half wave plates (Ekspla Optics) allows for the power to be varied continuously over a range sufficient to optimize the signal on the photodiodes. The ultrafast

beam samplers are both wedged and have an anti-reflection coating on the reverse side of the optic. Despite both of these considerations, the beam samplers still modulate the frequency spectrum of the transmitted pulse. Presumably this is due to etalon effects, however after the beam and its reflections have translated far enough, the effect should diminish due to the wedge and angled reflections. It is estimated that $\sim 2 \mu\text{W}$ is seen by each detector. Glass coated with a thick layer of indium-tin oxide (ITO) is used as a THz mirror, but remains transparent to the probe beam [100, 127, 128]. The THz electric-field leakage through the mirror is estimated to be $< 0.1\%$ based on measurements performed in our lab. This is used to recombine the THz and probe beams. Both are then focused by a protected gold-coated OAPM onto the detection crystal.

2.5.1 Lock-In Amplifier

An SRS830 lock-in amplifier has also been used in combination with a Thorlabs MC2000 chopper that was synced to the firing of the Legend at a fraction of the repetition rate, typically 1/10 (100 Hz), to detect THz pulses. For high frequency scans with a plasma source, >30 pts/ps are desired for a Nyquist bandwidth of 15 THz. However, when sampling faster than the time constant, the nearby points in the scan can become highly correlated, so the scan rate should be limited. Assuming a time constant of 1 second, this means that a 100 ps scan takes on the order of 50 minutes, not including data transfer and processing time. Acquiring multiple averages, which is necessary to eliminate any laser or electronic drift, thus takes quite a long time. See Section 6.1.1 for more details.

2.5.2 Oscilloscope Based Detection

As we saw in the previous section, the lock-in amplifier setup features a very slow scan rate over the THz signal of interest. In order to decrease the diagnostic and setup time, a faster

alternative was designed. A 1 GHz bandwidth digital scope from LeCroy (Waverunner 104 MXi) was purchased in order to appropriately diagnose the >80 MHz signal from the fast photodiodes in the oscillators. It also has a fairly deep memory and is capable of serving as a data acquisition device for the Legend. Trigger rates of 1 kHz, the repetition rate of the Legend, are feasible. In practice, typically >80 pts/ps are desired, to keep the usable THz signal free of laser or electronic line noise interference. A 100 ps scan then takes only 8 seconds, without considering setup, data transfer, and processing time. Averaging is thus much more feasible and diagnostic scans for alignment can thus be acquired in a matter of seconds. Theoretically, the scans feature a lower signal-to-noise than with the lock-in amplifier, but steps have been taken to reduce noise. In particular, a pulse normalization routine was used in an attempt to reduce pulse-to-pulse fluctuations of laser power and polarization, and the line noise is removed from the signal in the frequency domain by careful sampling considerations, as described next.

2.5.2.1 Pulse Normalization

The pulse normalization routine used was based on the assumption that the observed laser noise arose primarily from changes to the polarization state of the beams, or inadequate balanced detection, allowing power fluctuations to affect the signal [129]. This assumption is believed to be valid because the ZnTe emitter was run close to saturation, limiting power fluctuation of the THz source. The detection was balanced – albeit not perfectly – and canceled power variations of the laser in the detection arm as well. However, the balanced detection approach is very sensitive to polarization variations of the 800 nm pulses. These fluctuations were initially assumed to arise from the high voltage applied to the Pockels cells since any change to the applied voltage will cause a change in the both the polarization and power of the laser due to the nature of the linear electro-optic effect and the polarizer used to remove the pulse from the amplifier cavity. The variation was monitored and processed with a Fourier transform.

Sample data are plotted in Figure 2.7. The noise is primarily at 120 Hz and multiples of 60 up from there. Another set of balanced detectors in combination with a $\lambda/2$ plate was used to reduce these noise spikes. The results are plotted in Figure 2.8. The reduction is not sufficient to warrant continued use of the additional optics and significant extra characterization effort needed when THz-TDS is performed, and this setup is not frequently used. It is more useful for time-resolved THz spectroscopy or pump-probe measurements, however, but in principle these sources of noise can still be filtered well. The pulse normalization scheme might be improved by more careful polarization monitoring of the beams going into the balanced detector setups as well as a total power normalization as detected by a high bit number scope or data acquisition card. The total power correction approach is especially challenging since both the detection and THz emission depend on the optical power, and so the origins of laser noise contributions are not clear. This is discussed more in Section 2.8.

2.6 Air-biased Coherent Detection

Air-biased coherent detection (ABCD) was also attempted. A small portion of the Legend output beam, $\sim 30 \mu\text{J}$, was focused in air between two copper wire electrodes that were biased to near breakdown conditions with a high voltage power supply. A voltage pulser that can be externally triggered was also employed so as to allow for modulation at half of the repetition rate of the laser (or 500 Hz). The voltages delivered by the pulser have a maximum of 5 kV before damaging the device, which is described in further detail in the Ph D thesis of Vadym Kapinus. A photomultiplier tube (PMT) (Hamamatsu h957-08 module with r928 tube) was used to sense the signal in combination with an fast preamplifier (Ortec Model 9301 or VT120). Ultimately, successful detection was not demonstrated due to the contamination of the ESHG signal with SHG from the plasma THz emission source and from other sources such as quartz waveplates.

The most important factor in maximizing the ABCD signal is establishing the strongest possible ESHG signal, where the background second harmonic signal is small relative to the DC field-induced second harmonic, as was observed by the group of X. C. Zhang previously [111, 130]. When the THz field is combined with the optical and DC fields, it modulates the observed SHG signal since it will modify the field that biases the region in which the optical probe beam is focused. As discussed in Section 1.1.4.2, the observed signal is proportional to the LO intensity, which can be increased by increasing the applied electric field as well as the intensity of the probe beam. The problem in this case is not electronic or even laser noise, as in the case of THz signal as detected by EO sampling, but instead shot noise in the SHG signal due to the low number of photons generated by each pulse.

Unfortunately, the optical power in the detection beam cannot be increased indefinitely since at some point around 1×10^{14} W/cm², a plasma will be formed and the SHG will become rapidly dominated by the white light signal from the plasma, which again shows up as a DC offset since it is not removed by chopping. The bias field is also limited to the breakdown voltage of air, which is approximately 30 kV/cm, but varies greatly based on electrode shape and size, atmospheric pressure and composition, and pulse duration. Equation 1.50 does not specify the expected signal levels. Fortunately, the power generated by ESHG has been previously considered for cylindrical electrodes, similar to what were used here [95]. Copper wire electrodes of diameter 1 mm were separated by 3.5 mm. The polarization for the process follows the following equation:

$$P_i^{2\omega} = \frac{3}{2} \rho L \chi_{ijkl}(-2\omega; 0, \omega, \omega) E_j^0 E_k^\omega E_l^\omega, \quad (2.4)$$

where ρ is the relative number density in amagats and L is Loschmidt's number, used to define the amagat, in that 1 amagat is Loschmidt's number, or the number of particles of an ideal gas

at 0 °C and 1 atm. The expected power is

$$\mathcal{P}_{2\omega} = \mathcal{P}_{\omega}^2 [E_y^0(z_0)]^2 \frac{36\pi^4 L^2 \omega^3}{e^2 c^4} \left| \frac{\chi}{\delta k_0} \right|^2 \frac{1}{d} \Gamma(\rho) B(b) Z(z_0) \quad (2.5)$$

where

$$E_y^0(z_0) = \frac{2V}{d \cosh^{-1}(l/2a)} \frac{1}{1 + [2(z - z_0)/d]^2}, \quad (2.6)$$

$$\delta k = 2k_{\omega} - k_{2\omega}, \quad (2.7)$$

$$\Gamma(\rho) = \left[\frac{\rho}{\rho_0} \exp \frac{\rho_0 - \rho}{\rho_0} \right]^2, \quad (2.8)$$

$$\rho_0 = \frac{2}{d |\Delta k_0|}, \quad (2.9)$$

$$B(b) = 4 \left[(b/d)^{1/2} + (d/b)^{1/2} \right]^{-2}, \quad (2.10)$$

$$Z(z_0) = \left\{ 1 + \left[\frac{2z_0}{(b+d)} \right]^2 \right\}^{-1}. \quad (2.11)$$

Here, d is the spacing between equivalent thin electrodes, defined as

$$d^2 = l^2 - 4a^2; \quad (2.12)$$

l is the distance between the electrode centers; a is the electrode radius; z is the coordinate along which the beams propagate between the electrodes; $\Gamma(\rho)$ is a dimensionless factor used to relate the optimum relative number density, ρ_0 , to the actual number density; and $B(b)$ is another dimensionless factor used to relate the beam confocal parameter, $b = 2z_r$, to the extent of the field in the propagating direction, as specified by d , and $Z(z_0)$, which is negligible when the electrode axis plane is located at the beam waist. $\Gamma \Delta k$ is $-119 / \text{m}$ for $\omega = 800 \text{ nm}$, and d is $\sim 3.35 \text{ mm}$. Thus, ρ_0 is ~ 5 and $\Gamma(\rho)$ is 0.19 , indicating a relatively poor correspondence between

the extent of the field in the z direction due to the electrode separation and the coherence length, $\pi d/2$, at atmospheric pressure. Theoretical improvements include changes to the pressure or composition of the gas, or increases in d . Unfortunately, none of these are viable options in air because d cannot be increased while maintaining the maximum applied field, and the scaling is much stronger with the applied field. If a gas cell is constructed, the gas composition and pressure can be optimized. Also, in the future, a “Christmas tree” shaped electrode similar to that found in reference [130] might be employed for on-the-fly optimization. By using a 350 mm focal length lens, b was set to ~ 4 mm, while $B(b)$ was 0.99, thus eliminating any mismatch due to focusing. The formula for $B(b)$ is a bit suspect, however, since when a 250 mm focal length lens was used instead, the efficiency dropped by at least an order of magnitude instead of the predicted 7%. After all numbers are considered, using the appropriate electrostatic units in the cgs system, the predicted number of second harmonic photons generated per pulse ranges between 400 and 1000. After considering the rejection of the three filters, which each transmit about 1/2 of the second harmonic photons and the efficiency of the PMT (20%), the number of photons detected is only expected to be about 7 to 15 per pulse. This number was increased by limiting the number of filters, however the signal was still extremely low, and the shot noise made signal detection unfeasible, even without considering the background SHG from various optics and from the 2-color plasma used for the generation of THz radiation.

2.7 Purging Considerations

While purging is typically performed, it is not necessary if one does not mind missing frequency content at distinct frequencies corresponding to optically deep water lines, which is often not a problem if sufficiently long temporal scans are taken in order to increase the resolution in the frequency domain. If signal-to-noise and dynamic range are high, then a simple scan with

sample and reference can be performed and ratioed to remove the contribution of the water transitions along the THz signal path. However, it is common for there to be significant variations in absorption due to complete, or nearly complete absorption of all radiation at a frequency, causing the signal to be near the noise floor and subject to rather large differences in the ratioed spectrum. This can be removed by any of a number of numerical techniques to effectively remove these points from the spectrum.

2.8 Noise and Limits to Signal Processing

Zhang and Xu introduced the idea of two quantities relevant to THz-TDS noise, the time-domain signal-to-noise ratio and the frequency domain dynamic range [131]. The dynamic range is defined as $D(\omega) = E(\omega)/N(\omega)$ where $N(\omega)$ is the noise equivalent field of the detector, whereas the signal-to-noise ratio (SNR) is usually defined as the ratio of the the peak field to the electronic noise, where there is no signal. The two quantities are not necessarily, and very infrequently, equal. To examine this more closely, consider that the majority of the noise comes from either the THz pulses, $N_{THz} = R(t)E(t)$, or from the probe beam, N_p , where the standard deviation of the fluctuations in each are given as σ_R and σ_p , respectively. The probe beam fluctuations are typically minimized by balanced detection and lock-in detection, and are often small compared with $R(t)$. Since the SNR or time-domain dynamic range is dominated by σ_p , and the frequency-domain dynamic range is dominated by σ_R , the two can have significantly different values. Typically, neither source is dependent on the THz spectrum and are ideally white or 1/f noise dominated. In practice, however, the optical constants as determined by THz-TDS often have strong frequency dependence, largely due to variations in the dynamic range [132]. The overall impact of noise and uncertainty on the measured THz optical constants was analyzed in depth by Withayachumnankul et al. [133].

2.8.1 Laser Noise

Amplifier noise is observed in the EO detection setup. The noise is not white and has line noise related spectral features at 60 Hz, 120 Hz, and multiples thereof. The noise was verified to be optical in nature, and not an electronic artifact, as the phase of the noise on the pulse normalization balanced photodiodes could be switched using a wave plate. Additionally, there are other features that are not reproducible from day to day and that cannot be tracked down. A noise spectrum of the Legend (a) and Evolution (b), is compared in Figure 2.7. The Legend noise is thus not due exclusively to Pockels cell voltage fluctuations as previously thought, but is due to power fluctuations in the Evolution. An attempt to provide ‘clean’ power to the Evolution by using an isolated power supply was made. This did not fix the problem and thus it was concluded that the power rectification inside the Evolution was to blame. Elimination of the line noise from THz data was performed in the case of digital oscilloscope detection by a Fourier filter centered at the frequency of interest. This is described more fully in Appendix Section 6.1. Figure 2.8 shows the intentional offsetting of the THz spectrum from the line noise so that the above procedure could be effective. In the case of lock-in detection, the noise was moved out of the effective 1 Hz bandwidth of the SRS830. The restriction here is just that the chopper be set to a frequency away from the interfering frequencies. Since 100 Hz was typically used, line noise was not found to be problematic.

2.8.2 Shot Noise

The laser shot noise is anticipated to be a very small contribution to the total noise. Even in the probe beam, where the average power is only a few μW , the number of photons per pulse is of the order of 10^8 , and the shot noise is $\sim 0.001\%$. Optical rectification in ZnTe has an approximately 10^{-6} energy conversion factor, but each photon has ~ 374 times less energy, and hence more photons. Thus, the THz shot noise is expected to be less than $10^{-6}\%$. Shot noise

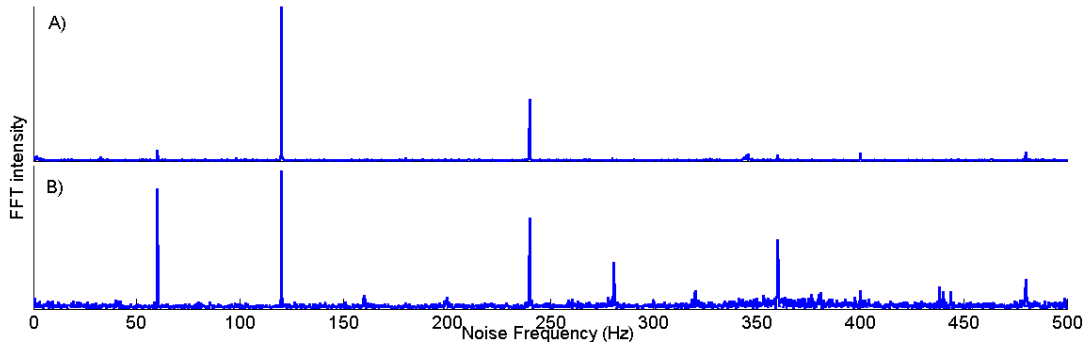


Figure 2.7: A) The noise spectrum of the Legend as sensed by the EO balanced detector setup. B) The noise spectrum of the Evolution as sensed by a heavily filtered Si photodiode detector, model PDA36A from Thorlabs.

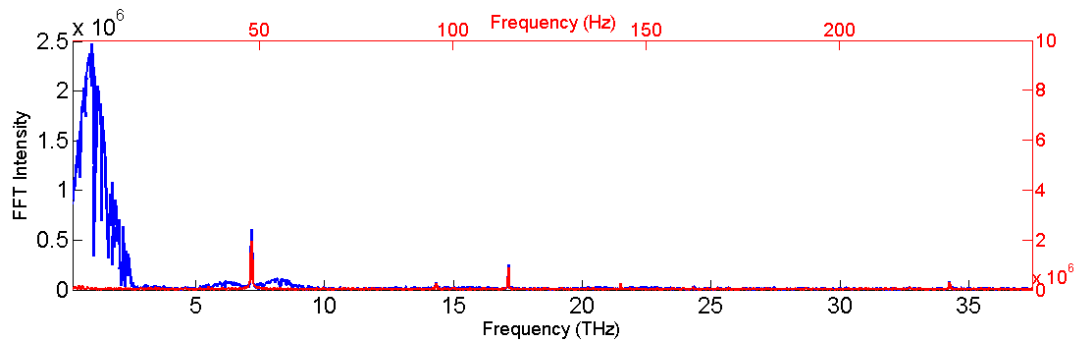


Figure 2.8: The full spectrum of a THz scan showing noise at 60 and 120 Hz. The balanced detector output is shown in red.

is a significant concern however, when considering ABCD, where less than 1000 photons are expected (see Section 2.6) per pulse when fully optimized. This noise is extremely noticeable when optimizing the detection efficiency, since the PMT gain must be turned up and only a few photons are produced per pulse on average.

2.8.3 Electronic Noise

The PDA36A detectors are anticipated to have $240 \mu\text{V}$ RMS noise and a NEP of $7.52 \times 10^{-12} \text{ W}/\sqrt{\text{Hz}}$ on the 10 dB gain setting, where commonly operated [134]. The detectors were set to the 10 dB gain setting for the sake of bandwidth and noise and the fact that the signal appeared most normally shaped at this setting. At the 0 dB setting, strong ringing in the output was observed, with approximately most of the signal being negative going, causing it to

be unacceptable for input for lock-in detection. Even on higher gain settings, the output was observed to both grow in intensity and in FWHM as the input power was increased. Thus, the waveform output of the summing amplifier was integrated in time rather than simply observing the maximum value. The summing amplifier's noise specifications are less clear. It has an output voltage noise of $30 \text{ nV}/\sqrt{\text{Hz}}$ and a crosstalk between channels of -80 dB at 1 kHz , but the performance with faster signals is not specified. The lock-in amplifier has a noise of $6 \text{ nV}/\sqrt{\text{Hz}}$ at 1 kHz , but also with unknown performance at higher frequencies. The CMRR is also expected to be poor, as it decreases by 6 dB/octave above 10 kHz . This is of concern since faster signals are typically used. The bandwidth concern is two-fold. One concern is that the signal is diminished on the inputs to the amplifiers since a good portion of it is thought to be above their bandwidth. At 10 dB gain, the PDA36A has a listed bandwidth of 5.5 MHz , with a large fall-off at higher gain settings. The signal, when not saturated, has a measured rise time of $\sim 70 \text{ ns}$ and has the appearance of a half-cycle pulse with a slight tail at longer times. The SIM980 has an upper bandwidth of 1 MHz but an input slew rate of only $40 \text{ V}/\mu\text{s}$, and the waveforms of the detectors are clearly significantly altered when passing through the amplifier. The lock-in amplifier A-B input signal is unknown, but due to the relative non-availability high performance differential or instrument amplifiers with bandwidth above the 1 MHz level, it is of concern. Beyond the concern of signal loss is the added noise when operating far from specifications, as is described above. In the future, true balanced detectors should be used to minimize the effect of detector mismatch and bandwidth effects in the processing of the signal.

2.8.4 Etalon Removal

While not a true source of noise – only unwanted signal – one of the most troublesome aspects of THz-TDS is the appearance of etalon-related reflections in optical beam blocks, the emitter and detector crystals, and of course, the sample of interest. The most general procedure found in

the literature [135, 136] is to deconvolve the spectrum by fitting delta functions of appropriate amplitude at the time of the reflection and dividing out in the frequency domain. This works well when the amplitude of the reflections is large, and when there is no dispersion, absorption, or phase-shift present. Realistically, this works very poorly for a broadband source since almost all materials have significant dispersion in the THz spectral region, except high resistivity silicon. Phase shifts can occur due to the Gouy phase shift [130, 137–139] or due to the effects of Fresnel reflection [140] and wedged substrates and can cause changes to the spectrum [137, 141].

A time-domain routine was written to remove etalon based reflections without convolution. This allows treatment of dispersion and absorption in materials of known optical constants. The basic procedure is to isolate a section of the spectrum that is free of reflections, demagnify it after fitting, and subtract it from the time-domain trace at the correct position. Phase shifts can also be handled if the spectrum is assumed to remain constant. One would think that a uniform phase shift of the data would remedy the issue of the Gouy phase shift, however, when applying a phase shift, the spectrum remains constant, and the time-domain waveform is thus spectrum dependent.

Overall, removal of etalons is not necessary if a good reference and sample scan are acquired, as their influence is negligible once the spectra are ratioed. This is not the case if there are significant laser fluctuations, as the relative height of the main THz signal to the reflections can vary greatly and the modulations to the frequency spectrum can be large, especially at frequencies where the signal is low. Sample related Fabry-Perot etalons are still troubling, and can be treated in the extraction of the optical constants of the sample.

Chapter 3

THz Torsional Modes of Amino Acid and Sugar Crystals

3.1 Introduction

The THz region encompasses many of the lowest frequency vibrations of moderate-sized molecules and clusters. As one measure of their importance, such modes are quite sensitive to the non-covalent intra- and inter- molecular forces that play key roles in the physical and chemical mechanisms that underlie biological activity. As opposed to vibrational features in the near- and mid-infrared, these low-frequency modes typically entail collective motions of almost every atom in the molecule or cluster and can thus provide “fingerprint”-like identification. Even species with remarkably similar structure(s) such as sugars in pyranose form [142–145], isomers [146], peptides with differences in secondary and tertiary structure and co-crystallized water [147], and polymorphs of pharmaceutical drugs [148] show vast differences in the crystal spectra acquired at THz frequencies, whereas the mid- to near-infrared spectra are often very similar. Such differences have caused many to posit that in solids and well-ordered molecular clusters, the THz spectrum should be dominated by and very sensitive to intermolecular interactions such as the hydrogen bonding between neighboring molecules, or by strong modes that arise due to crystal lattice vibrations or phonons [149]. However, there are non-interacting systems, where hydrogen bonding is not prominent, that show similar spectra in the gas, liquid and solid

phases [150, 151]. We have found similar results, in some cases even when significant hydrogen bonding is anticipated. More accurately, we have found that some far-infrared features are well represented as intramolecular modes while others are cannot be explained as such, usually those lowest in frequency, typically at or below 3 THz.

The intermolecular interactions that give rise to intense transitions in the far-infrared are poorly characterized at present, not only experimentally but by theory as well. The THz molecular spectroscopist’s job, therefore, is to acquire spectra and classify the transitions of a variety of molecules. The parameters that are readily determinable are the transition intensity along with the center frequency and linewidth. If the temperature of the sample is changed, the anharmonicity can also be determined. Some of the simplistic potential energy landscapes are shown in Figure 3.1

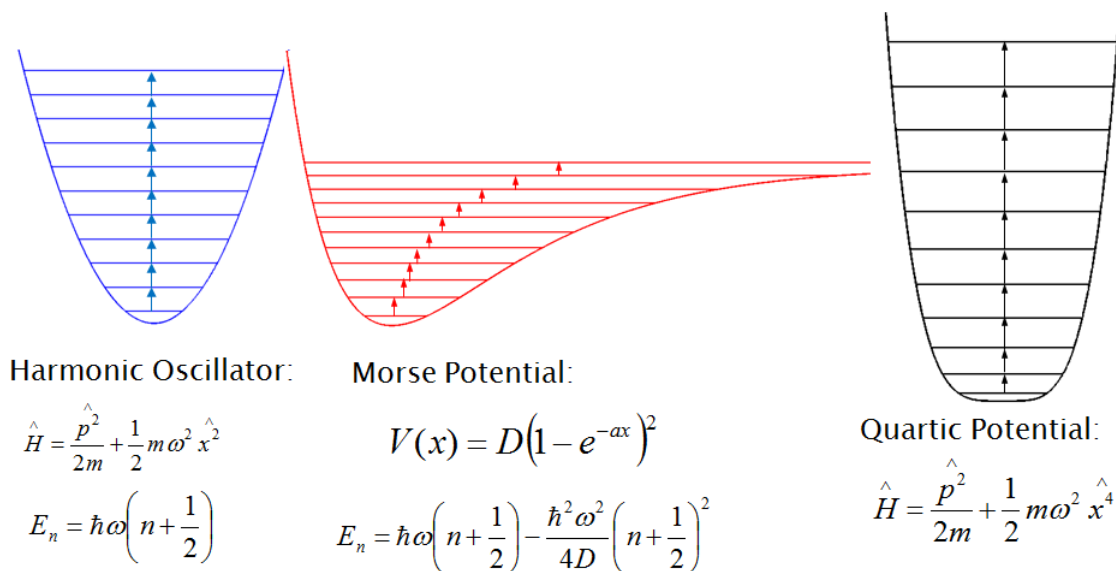


Figure 3.1: Three stereotypical potential energy surfaces, each showing differing behavior of the energy level spacing.

Unfortunately, there is no simple way to correlate the measured spectra to specific molecular motions, and thus *ab initio* and molecular dynamics (MD) simulations must be employed. While at present there is no definitive and practical means of simulating the low frequency modes of

molecular crystals, many methods have been attempted. Perhaps the most successful are the simulations of Jepsen *et al.* [149] and Korter *et al.* [152, 153] that utilize expensive and computationally quite intensive software packages. However, as described below, we find that for the identification and tentative assignment of modes to either the intra- or intermolecular degrees of freedom, *ab initio* calculations on the monomer may often suffice.

Changes to the spectra of molecular crystals with temperature show, in most cases, a blue-shift as the temperature is reduced to 10 K. In most cases this is indicative of an anharmonic, Morse-like potential, where the lowest energy levels are separated by the greatest energy difference. However, since all of the molecules studied herein have many atoms, and the motions studied often have vibrational coordinates that involve many bonds, the potential energy surface can vary with a higher order of the displacement, and quartic-like potentials are sometimes observed. In other cases, both red and blue shifting is observed as a function of temperature due to the interplay of multiple forces. Before turning to a description of our results, we first present a short general discussion of the classes of molecular crystals studied.

3.2 Amino Acids and Sugars

Here, we have chosen to investigate a variety of amino acids and sugars that have been found in the aqueous extracts of ancient meteorites. Such compounds are critical steps on the road toward life, and as such it is an intrinsically interesting question as to their origins in space or on/near early planetary surfaces. The class of carbon-rich meteorites of interest are called carbonaceous chondrites, as they containing up to 5 % carbon [154] by mass. These objects date back to the formation of the Sun and planets, and possibly comprise material that is close in composition to the solar nebula (at least for elements sufficiently refractory to be included into oxides or metal alloys). Some chondrite classes contain an abundance of hydrated silicates and

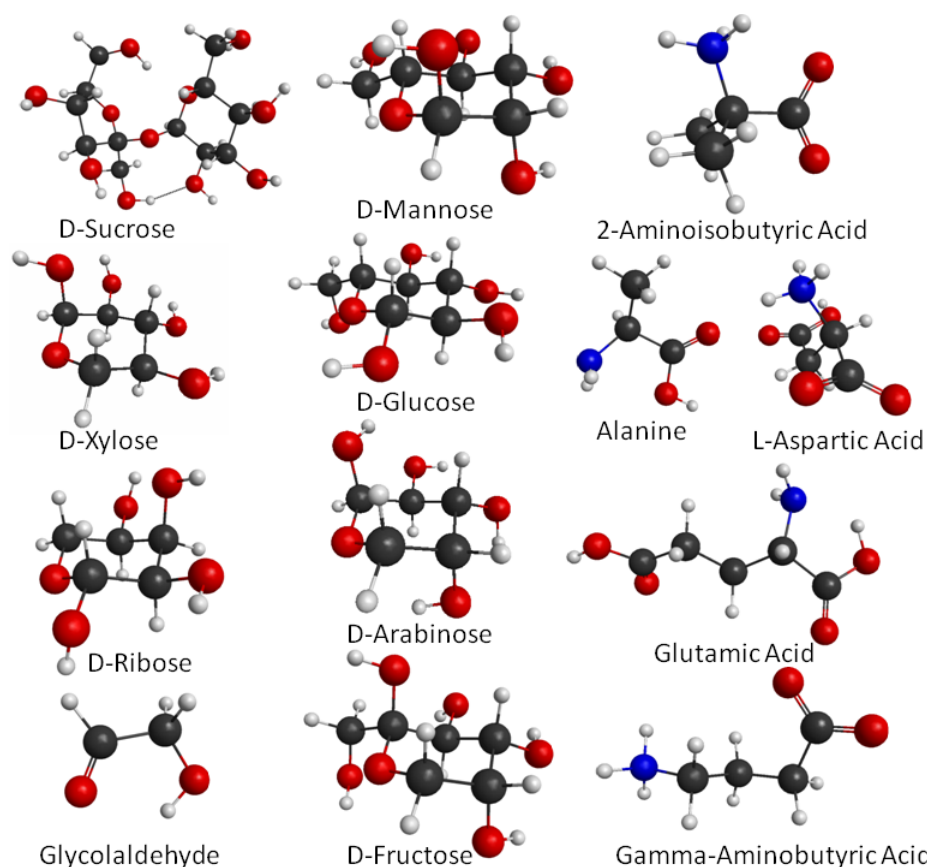


Figure 3.2: The molecular structure of the species studied using THz-TDS. The optimized or crystalline structure is used where appropriate.

volatile organic compounds that would not exist had the meteorite ever undergone significant heating, and as such, might give great insight into the earliest steps toward planets such as the earth. One of such meteorite, called Murchison, fell to Earth in Australia in 1969. It is one of the most well studied chondrites, due to its large size (and therefore mass available for study), abundance of organic compounds, and the fact that it was seen impacting the Earth – thus presumably circumventing the possibility of significant terrestrial contamination [155]. Notably, Murchison has been found to contain ~ 60 ppm amino acids and ~ 60 ppm sugars and sugar-related compounds such as sugar alcohols and acids [156], as well as an abundance of other organic compounds [157]. Just the amino acids alone amount to approximately 3% of the total organic carbon content of carbonaceous chondrites [7]. The general trend of the laboratories findings to date is that there is complete structural diversity, with all isomers of

a given chain length found. Abundances decrease, often exponentially, with increasing carbon number, and an equal concentration of branched and straight-chain isomers are present [157]. While many studies find the composition of the observed amino acids to be racemic, some do find an excess of one enantiomer over the other [158]. However there has been speculation of terrestrial contamination and effects due to aging or extraction procedures [155, 157], and further enantiomeric excess studies are underway in several groups around the world.

Here, L-enantiomers were studied due to their biological relevance, and amino acids with high abundances in meteorites were given preference. For sugars, the simplest biologically relevant sugars were chosen, and while many have not been directly been observed in meteorites, they are known to be necessary for life to form. Most of the chosen samples have a relatively intense and active low-frequency spectrum. We initially began our study in the crystalline phase for convenience, and ultimately to gauge whether the frequencies obtained might be of relevance when studying interstellar ices (that is, to study how significantly the crystalline environment affects the THz properties of molecules and molecular ices/solids). In some small amino acids, even mixing with the opposite enantiomer completely changes the low frequency spectrum, as some modes are due almost exclusively to intermolecular interactions [159]. Our calculations have shown, however, that sometimes the THz transition frequencies predicted for the isolated molecule (and therefore modes that must be intramolecular in nature) are quite applicable to the crystalline form, even where intermolecular interactions are known to be strong. The measurement and (inter)molecular characterization of each mode is thus quite important for the robust identification of any bands to be measured in interstellar ices.

Serving as the prototype for interesting low frequency modes in biologically-active molecules in our studies, we have found that γ -aminobutyric acid, or GABA, has remarkably strong and interesting THz features at low frequency. While nominally an amino acid, it is never incorporated into proteins, but serves mainly as an important – perhaps the most important –

inhibitory neurotransmitter in the central nervous system of mammals [160] and as a regulator of muscle tone [161]. Understanding the lowest frequency modes may help to understand its function in the body. Since it is also one of the most abundant amino acids found in meteorites, it is of significant astrochemical interest as well.

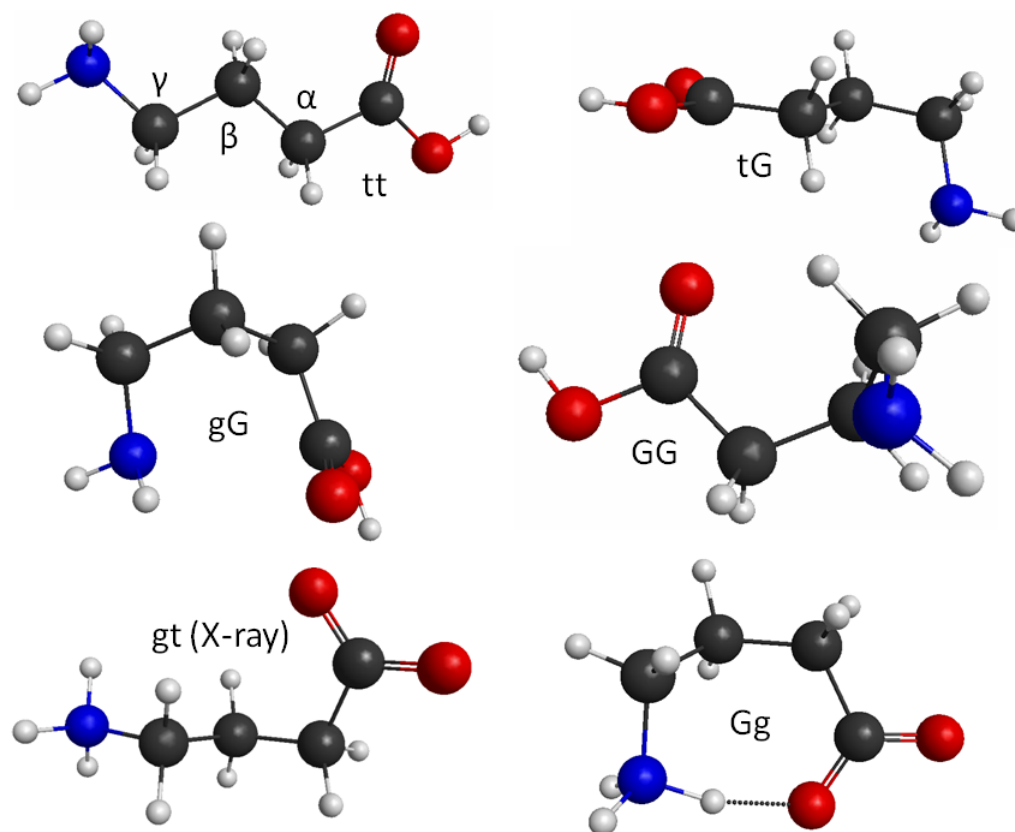


Figure 3.3: From the top and left to the bottom, the forms of GABA present in the gas phase (1-4), with the tG form being the most energetically favored followed closely by the GG and gG forms. The tt phase is presented because it was found to be an appropriate model for the crystalline modes. The carbons are also labeled in the standard format. The zwitterionic gt structure, as determined from X-Ray and neutron scattering, is also presented. The Gg structure is the lowest energy in solution.

The far-infrared spectrum of GABA – and even the mid infrared spectrum – has never before been reported in scientific literature, to our knowledge. However, it has been studied no less than six times using x-ray and neutron scattering [162–169], by microwave spectroscopy [170], by Raman and NMR techniques [171], and by a plethora of theoretical approaches [170,

172]. Though only modest in size, GABA has a number of low-lying isomers that must be considered. The main differences in the structures observed under different conditions are the zwitterionic form, in which GABA exists in the solid and liquid phases (but not in the gas phase), and the configuration around the $C^\gamma-C^\beta-C^\alpha-C_1$ (χ_1) and $N-C^\gamma-C^\beta-C^\alpha$ (χ_2) dihedral angles, where states are labeled as trans (t), gauche+ (G) or gauche- (g). A summary of the relevant structures to be discussed below can be found in Figure 3.3.

Conformational flexibility is seen in all phases. Heavily folded gG or GG conformations are energetically favored in the gas phase due to the $n \rightarrow \pi^*$ interactions between the lone electron pair on the amine nitrogen and the C=O bond of the carboxylic acid group and the dipole-dipole interactions of the NH and C=O bonds. Thermodynamics also indicates that the tG orientation is strongly populated. The microwave results support these chemical inferences, finding nine gas phase conformers populated near room temperature, with the dominant five being ordered in abundance as GG>tG>gG>tt>gt. The predicted ΔG values confirm this ordering at the MP2/6-311++G(d,p) level of theory [170], with slight deviations at the M06-2X/cc-pVTZ level of theory [172]. Surprising, the experimental population statistics strongly disagree with the MP2 predicted relative energies in that the extended, non-folded conformations have greater populations than anticipated due to a higher entropy caused by an increased density of accessible vibrational states [170].

When solvated in water, the conformational preferences are more limited, at least theoretically, with the top two conformers making up a predicted 94% of the total population. The GABA zwitterion dominates and causes strong head-to-head intramolecular hydrogen bonding between the N-H and the negatively charged C-O⁻. Conformationally the gauche-gauche configurations dominate. As seen in our calculations, these conformations are strongly favored for the zwitterion, even without the presence of water solvent molecules, as in [172]. These results are at odds with ¹H NMR spectra at 45°C in D₂O, however, where the populations are mea-

sured as 0.16 for tt, 0.24 for gt, 0.24 for tg, 0.18 for gG and 0.18 for GG [171]. These authors suggest that it is the lack of ions considered in the theoretical calculations which give rise to the preference for the strongly folded conformations. Ions would provide a source for strong intermolecular interactions in solution that serve to stabilize the extended conformations of GABA. Our calculations indicate significant changes to the low frequency spectrum depending on whether the molecule is in the extended conformation or participating in an intramolecular hydrogen bond. Notably, a low frequency mode at ~ 1 THz is present in the case of the extended conformation, where the carboxylate group is free to contort about the C-C $^{\alpha}$ bond. This hypothesis is also backed up by the conformational preferences in the solid state, where the gt form is favored [162, 164, 165, 167] – though a tetragonal tG phase has also been seen recently [163], where the partially extended forms are favored due to packing or intermolecular hydrogen bonding interactions. In the presence of ions, for example in GABA-HCl, the amino acid is in the fully extended, or tt form [166, 168], displaying a neutral carboxylic acid group and a protonated NH $_3^+$ group that, in combination with the Cl $^-$, forms a network of hydrogen bonds. This is a strong indication that ions stabilize the extended conformations relative to the energetically favored folded conformations of the zwitterion.

3.3 Experimental

Details of the THz emission and detection systems can be found in Chapter 2. In cases where the sample was studied as a function of temperature, down to 10 K, we used a Janis CCS-350R OPTICAL cryostat with a closed cycle helium refrigerator from CTI Cryogenics and either crystalline z-cut quartz (ISP Optics) or high-density polyethylene windows. Samples were equilibrated for a minimum of 20 minutes at each temperature step. All molecular solids were used as purchased from Sigma without purification. Samples were ground with mortar

and pestle to reduce the particle size to avoid Mie scattering and to improve mixing with micronized high-density polyethylene (MPP-620XXF, Micro Powders, Inc.), thus reducing sample inhomogeneities. In retrospect, samples should have been recrystallized using standard procedures found in the literature to ensure that samples were in one fully crystalline phase with no contaminants or contributions from amorphous forms. Additionally, since most samples show increased absorption at high frequencies, grinding should have been increased to further limit Mie scattering. It is also possible that this high frequency absorption might arise instead from broad, unstructured absorptions of the molecules subject to investigation. Regardless, the samples are thought by some researchers to be inherently disordered, with the spectral line shapes limited by inhomogeneous broadening even at zero Kelvin [173]. Future studies should perhaps employ waveguide techniques, where sample inhomogeneities can be reduced and narrower line widths have been demonstrated [173]. The downside is that the transmission of such structures is only 20%.

The molecules for which experimental spectra were obtained have also been studied with density functional theory (DFT) using the hybrid Becke three-parameter Lee-Yang-Parr B3LYP functional [174, 175] and the coulomb-attenuating model CAM-B3LYP [176]. The latter helps with long range interactions, and has been shown to produce more accurate frequencies in some cases for the molecules tested herein and for the ring puckering modes simulated previously for a proposition (Table 5.1). Namely, specific comparison of the generated frequencies was run on the molecules xylose and 1,4 dioxin, whose spectra had been measured previously. The starting geometry was taken from the determined crystal structure when possible, though an optimization generally had to be performed before calculating frequencies. The Gaussian 09 keywords “Opt=Verytight” and “Int=Ultrafine” were used, as recommended [177], to improve calculation of the low frequency modes [178]. In most cases, the resulting vibrational frequencies had to be scaled somewhat due to overestimation of the vibrational energy level differences.

Anharmonic calculations were attempted using Gaussian 09 [178], but extreme anharmonicities often resulted when only the lowest energy modes were simulated, causing energy levels and transition frequencies to be below zero in some cases. These results are therefore not reported. Calculations of all modes for a molecule such as GAB can take months or more of computation time, even on multi-core workstations with >100 GB of memory. As a note to anyone attempting such calculations, the input file should specify the use of a read-write file so that the computation can be restarted in the event of a crash with the beginning of the file appearing as follows:

```
%RWF=myrwf  
%NoSave  
%Chk=mychk  
#B3LYP ....
```

3.4 Results

As shown next, the THz spectra show many low frequency bands indicative of collective motions, either inter- or intramolecular. Generally, success was had in predicting spectra from the monomer of the molecular crystal, in some cases even when starting from the crystal structure geometry without optimization. In all but one case, the frequencies were overestimated and were scaled down by a factor ranging between 0.6 and 1.0. The results are summarized in the individual tables found below. The predicted transitions were, in almost all cases, observed experimentally and the predicted intensities were at least qualitatively correct, particularly in their relative frequencies and intensities.

3.4.1 Amino Acids

Amino acids in crystalline form often have a strong low frequency THz spectrum, with the carboxylate torsion usually having significant oscillator strength due to a large transition dipole moment caused by the negatively charged group. It is typically found well below 2 THz in

frequency. The predicted spectra of amino acids were generally found to be a worse fit to experimentally measured spectra than sugars. This is attributed to the fact that the amino acids are generally smaller molecules and are more likely to have strong intermolecular forces due to hydrogen bonding and their zwitterionic nature in the solid state.

3.4.1.1 γ -Aminobutyric Acid

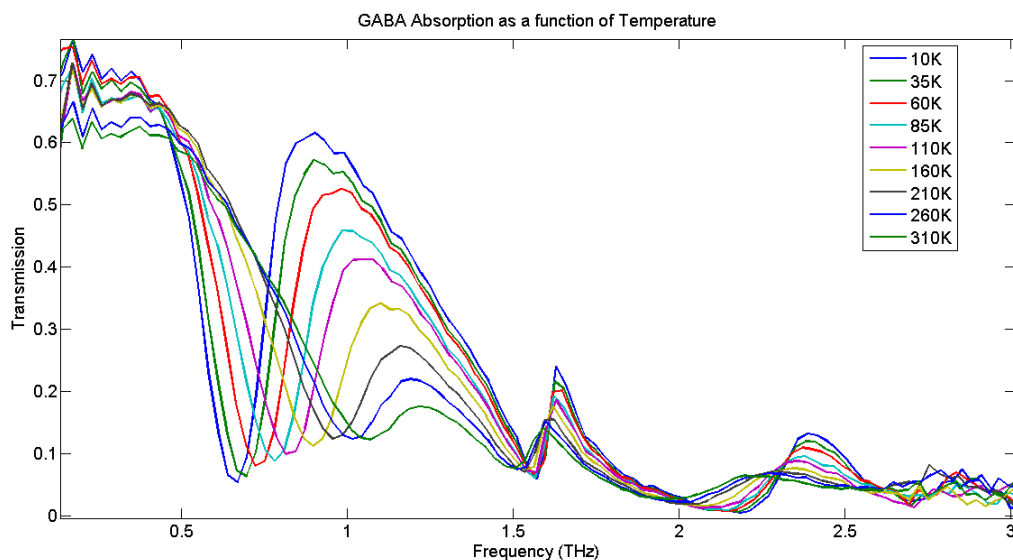


Figure 3.4: The measured transmission through a GABA pellet pressed with micronized high-density polyethylene as a function of temperature.

Gamma-aminobutyric acid (GABA) displays perhaps the most THz interesting spectrum of any molecule that we have studied. No previous investigations are known. There are four well-defined and strong modes observed in the spectrum, with three falling below 3 THz that have been analyzed as a function of temperature. The results can be found in Table 3.1. The rest of the spectrum features weaker modes, or modes that are obscured by the low transmission through the sample at the GABA concentration used. Mode 2 is not predicted by any of our calculations, and is assumed to arise from intermolecular interactions in the crystal. Also notable is that this mode is narrower than the others, all of which are suggested/confirmed to arise from intramolecular modes by the *ab initio* calculations. Experimentally, all of the modes

show marked anharmonicity, with the two higher frequency modes showing the expected shift with temperature characteristic of a Morse-like potential.

Most interesting, though, is the lowest frequency mode, which shows an enormous frequency shift, characteristic of a vibrational potential with significant anharmonicity, as can be seen in Figure 3.4. Not only does the mode significantly shift in frequency, it also shows a *redshift* with decreasing temperature, which is not consistent with a Morse-like potential. This behavior is expected in a quartic or a mixed harmonic-quartic potential well, however, and has been predicted (by Bell, in 1945) [179] in the case of constrained ring systems, such as the ring-puckering, out-of-plane bending motions observed in four- and five- [180] [181], or pseudo four- and five- member, rings. The potential has the form

$$V(x) = \frac{1}{2}kx^2 + ax^4, \quad (3.1)$$

where x is the normal mode coordinate. Chan, *et al.* report that “a small quartic anharmonicity is expected in many low-frequency vibrations merely by virtue of the low force constants and the large vibrational amplitudes associated with these vibrations [182].” In agreement with this, the lowest frequency mode of strait-chain GABA had the lowest calculated force constants of any of the modes of more than 15 molecules that were studied. The four- and five- member rings simulated also show very low force constants.

Constrained ring systems are a unique case in that the potential is fairly well understood, and will be examined for comparison’s sake. If the puckering motion is taken as the normal coordinate, the energy is expected to vary according the fourth power of the amplitude if the only source of potential energy is the bending of the ring bond angles. Since the bond angles in four- and five- member rings are strained due to geometry, there is also a linear dependence on the angle of deformation, and thus a quadratic dependence on the amplitude of the puckering

coordinate. The quartic anharmonicities are expected in situations where the potential energy is dominated by the cancellation of opposing forces, such as the four-membered ring case, where the ring strain is canceled by torsion about the single bonds in the ring. This causes the quartic term to dominate, and thus the potential to be anharmonic. The energy levels of such a system can be described using a quartic oscillator [183], a perturbed harmonic oscillator [184], or, most appropriately, a perturbed quartic oscillator [182]. The general finding, for any potential that has dependence above the normal coordinate squared, is that the energy levels become farther apart as the vibrational quantum number increases, causing a redshift as population is transferred to the lowest energy states. This is what is observed with GABA. The specific molecular motion(s) responsible for the quartic or higher order potential in GABA is unknown, however. At first glance, there is no clear geometrical cause for the potential to depend on higher orders of the displacement as there is in ringed systems. Thus, calculations were performed on GABA in several forms.

We note that calculations and simulations of the crystalline GABA THz spectrum are difficult because the geometry adopted in the solid state form does not resemble any of the conformations lowest in energy when calculated in the liquid phase, where a strong intramolecular hydrogen bond is established between the negatively charged carboxylate group and the positively charged amine group [172]; or those structures isolated in the gas phase [170], where intermolecular hydrogen bonding as stabilized by the $n \rightarrow \pi^*$ interactions between the lone electron pair on the amine nitrogen and the C=O bond of the carboxylic acid group dominate. Many different conformations of both neutral and zwitterionic GABA were therefore calculated including the gt and tG conformations of crystalline GABA as well as various gauche-gauche forms that are strongly energetically favored. Two different crystal structures are known [164, 166]. Unfortunately, when performing an optimization using crystal structure determined coordinates as the starting geometry, the molecule folds onto itself and settles in a gauche-gauche minimum

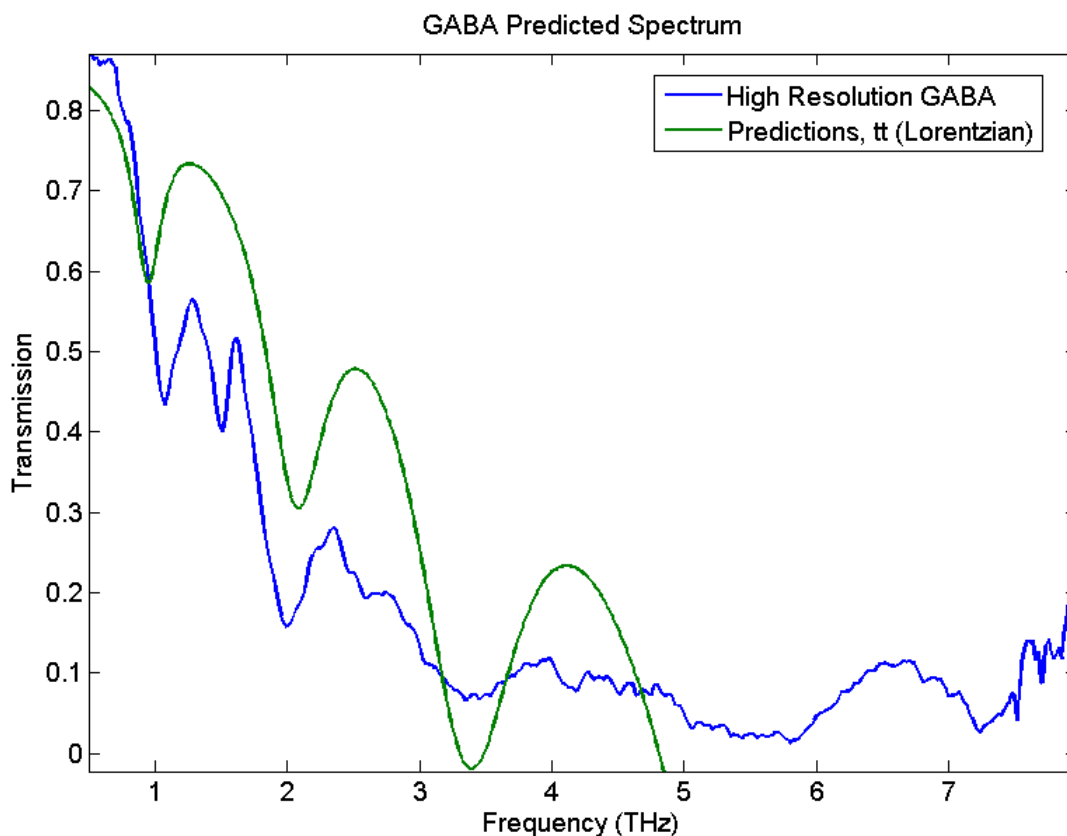


Figure 3.5: The measured transmission through a GABA/polyethylene pellet at room temperature compared with predicted results from DFT calculations, scaled by a factor of 0.88, on the tt structure of GABA. B3LYP/aug-cc-pVTz with a modified Lorentzian lineshape.

structure. This can be avoided by starting with the C_S symmetry-constrained trans-trans zwitterionic configuration, but the lowest frequency is negative, demonstrating non-convergence. When calculating the frequencies using the geometry of the most common crystal structure without optimization, no negative frequencies are observed when using the CAM-B3LYP DFT method, providing indication of a reasonably converged structure. When any of the other methods are used, negative vibrational frequencies are found. The results match the observed results after much scaling, by a factor of 0.63, as can be seen in Figure 3.6.

Strangely enough, even though the acidic proton associated with the zwitterion has shifted location between the two structures, the predicted spectrum has all of the same modes that are predicted for the linear structure. Only the lowest lying modes are shifted significantly,

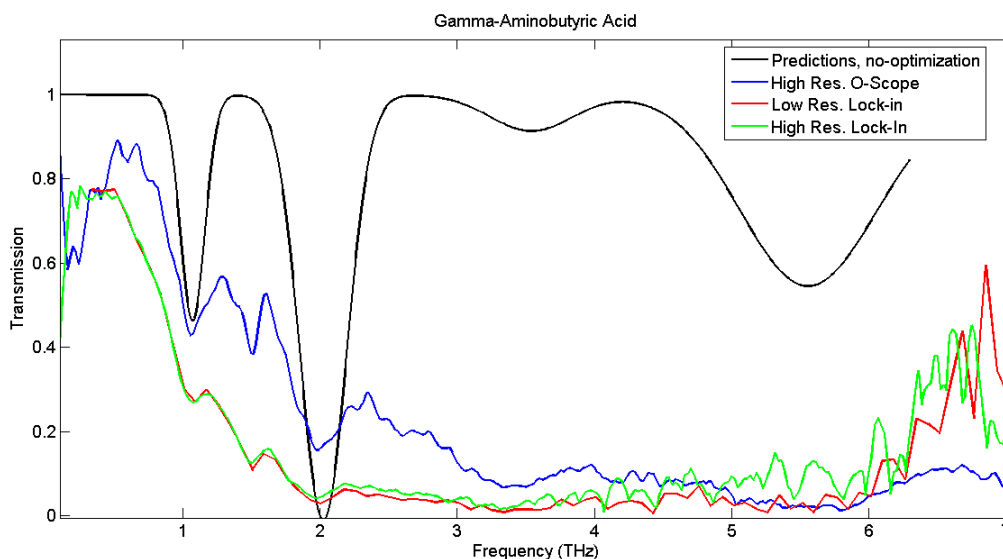


Figure 3.6: The measured transmission through a GABA/polyethylene pellet at room temperature compared with predicted results from DFT calculations, scaled by a factor of 0.63, on the gt crystal structure of GABA. CAM-B3LYP/cc-pVTz with a modified Gaussian lineshape.

though the intensity pattern is completely different, presumably because the structure is not well-converged in the crystalline case, which can give anomalous intensity to the low frequency modes. The observed spectrum matches that predicted for the linear fully trans geometry more closely than that of the lowest energy GG conformer, where the molecule is gauche, presumably so that the amine and carboxylate groups can interact and share a hydrogen. In the GABA-HCl spectrum, the molecule is in the fully trans orientation [166]. The normal mode vibrations for each of these cases were animated and compared. Regardless of the structure, the lowest frequency mode is dominated by the carboxylate group twist or torsion about the C-C α bond or the rotation of the rest of the molecule with respect to the carboxylate. The other observed modes have similar motions associated with them in some cases, but in others the geometries are too different to tell. The low frequency carboxylate twist was referred to previously as a carboxylate group libration [165, 169]. From the neutron scattering data, it was concluded that the libration was harmonic with an amplitude of ~ 25 deg 2 [165]. However, this conclusion was later reconsidered by the same authors in an analysis of the charge-density by X-ray diffraction

that revealed a methylene hydrogen located on the α carbon that carries a positive charge of 0.11 e, which forms a bridge between the negatively charged nitrogen and oxygen atoms. The carboxylate plane is tilted towards that hydrogen, reducing the anticipated distance between the two atoms and granting a preference to rotating toward that atom as opposed to the other nearby H, found on the first carbon atom. This attraction is anticipated to lead to the observed anharmonicity in the torsional motion.

The FT-IR spectrum of the same GABA pellet was obtained with a Nicolet 6700 spectrometer. At the pellet thickness used, the observed spectrum was saturated near the NH, CH stretch, CH₂ bend NH bend, and C=O stretching regions. Polyethylene absorptions, as measured by FT-IR spectra on pure polyethylene pellets, were subtracted from the GABA spectrum. The predicted spectrum from the measured structure in crystal form matches very well with the FT-IR data, and with the observed Raman spectrum [171]. The Raman spectrum taken in neutral solution shows dramatic changes with respect to the crystal spectrum, including the washing out of the low frequency modes, which is indicative of either modes caused by low frequency interactions or, more likely, by an abundance of differing conformations with blended absorption features. In support of the latter, the lines broaden significantly in solution. In the non-zwitterionic forms, where the molecule exists as a carboxylic acid, the very intense C=O stretch is predicted at 55.46 THz (1850 cm^{-1}) in both the tt and gg conformations, but in the crystalline geometry, this extremely strong mode shows up at 49.46 THz (1650 cm^{-1}) instead. In the tetrahedral crystal, the mode is predicted to show up at 1750 cm^{-1} . Clearly the position of the C=O stretch is strongly indicative of the orientation and bonding of GABA. This is also observed in the FT-IR spectrum as the 1850 cm^{-1} mode is absent. There is strong absorption at 1600 cm^{-1} , however, which is almost certainly due to the C=O stretch, as the predicted results must be scaled down in frequency.

Table 3.1: GABA Results

Mode	Temperature (K)	Experimental Freq (THz)	Int.	Calculated Freq. (THz)	Scale Factor	Calculated Int (km/mol)	Fractional GS Population
1	310	1.061	s	0.942	0.88	1.75	0.098
	295	1.05	s	"	"	"	0.103
	260	1.014	s	"	"	"	0.116
	210	0.96	s	"	"	"	0.142
	160	0.897	s	"	"	"	0.182
	110	0.828	s	"	"	"	0.253
	85	0.783	s	"	"	"	0.314
	60	0.731	s	"	"	"	0.414
	35	0.694	s	"	"	"	0.6
	10	0.668	s	"	"	"	0.959
2	310	1.503	m				0.216
	295	1.506	m				0.225
	260	1.513	m				0.252
	210	1.53	m				0.301
	160	1.539	m				0.376
	110	1.556	m				0.496
	85	1.557	m				0.588
	60	1.563	m				0.715
	35	1.566	m				0.884
	10	1.57	m				0.999
3	310	1.968	s	2.063	0.88	3.17	0.287
	295	1.976	s	"	"	"	0.299
	260	2.025	s	"	"	"	0.332
	210	2.032	s	"	"	"	0.393
	160	2.066	s	"	"	"	0.481
	110	2.085	s	"	"	"	0.614
	85	2.124	s	"	"	"	0.709
	60	2.141	s	"	"	"	0.826
	35	2.178	s	"	"	"	0.95
	10	2.184	s	"	"	"	1
4	310	na					
	295	2.605	w				0.356
	260	na					
	210	na					
	160	na					
	110	2.675	vw				0.693
	85	2.688	w				0.783
	60	2.691	w				0.885
	35	2.7	w				0.976
	10	2.708	w				1
5	295	3.34	vs	3.338	0.88	4.233	0.419
6	295	4.17	w				0.493
7	295	5.58	vs broad				0.597
8	295	7.23	s	6.94	0.88	41.2	0.692

The predicted frequencies are calculated using B3LYP/aug-cc-pVTz in Gaussian 09 [178] and multiplied by the Scale Factor. ** Results at 295 K are taken from a separate measurement and while they do not agree in frequency, they are anticipated to be more correct due to their higher spectral resolution and more appropriate calculation of the frequency axis.

3.4.1.2 Glutamic Acid

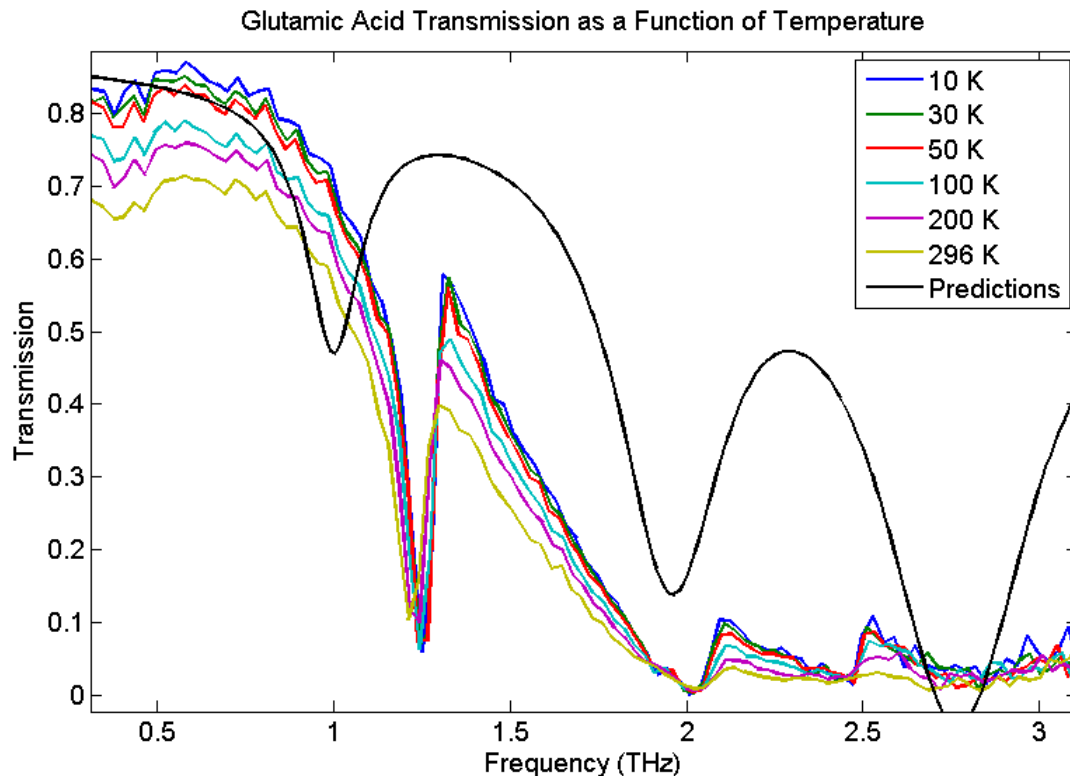


Figure 3.7: The measured transmission through a glutamic acid pellet as a function of temperature compared with predicted results from DFT calculations, scaled by a factor of 1.3. The spectrum was generated from harmonic results using CAM-B3LYP/cc-pVTz with a modified Lorentzian lineshape.

Glutamic acid, or more specifically, L-glutamate, is also a very important neurotransmitter, similar to GABA, and is its chemical precursor *in vivo*; but, instead serves an excitatory function [185]. The IR through THz spectra have been measured many times before [186–190], though the results can be quite different. Taday *et al.*, for example, observed and reported [189] spectra below 2.5 THz that differ considerably from the other studies and our own. It is possible that a different crystalline structure was studied, or more likely, the frequency axis was mis-calibrated, since the spectra look very much like the results presented here otherwise. Matei *et al.* [187] studied polycrystalline samples with FT-IR and found featureless spectra below 3 THz, demonstrating that the low frequency modes are highly sensitive to the orientation of the

molecule. Yan *et al.* [186] performed studies below 2.3 THz, and obtained similar results to Ueno *et al.* [188], who discerned a complex series of peaks above and near 2.46 THz. Our results are similar, as can be seen in Figure 3.7 and Table 3.2, except that we do not see the series of peaks above 2.5 THz. This could be caused by any of several effects such as poor optical alignment, a sample concentration that was too high, or simply due to poor sample preparation, all of which can result in reduced signal-to-noise at high frequencies. The temperature resolved data that we acquired are not extremely accurate as the spectra were acquired in a different temperature sequence than were the blank(s). This was corrected by interpolation as best possible. Additionally, the spectra were averaged, after acquisition on both cooling and warming cycles. Some small differences are seen, perhaps due to insufficient equilibration time. This pellet served as a test case and for some reason was not retested subsequently using the higher frequency bandwidth plasma source. It should be a target in the future. The first peak has a well defined blue-shift with decreasing temperature. Our calculations on the monomer show reasonable agreement with observations after scaling. This is not surprising, given that the geometry found in X-ray studies of the crystalline form is relatively unperturbed relative to the minimized structure [191]. Our calculations, while at a higher level than those of Yan *et al.*, have worse agreement with the observed results. These authors over-predict the frequencies, whereas we under-predict them. The shift to lower frequency, going from 6-311++G(d,p), as they employed, to our cc-pVTz basis set, often has this effect, however. Another major discrepancy is that Hirokawa *et al.* [191] predict the lowest frequency mode to be a torsion of the α carboxylate group, where we predict it to be a torsion of the γ carboxylate group.

3.4.1.3 Glycine

Glycine was found to have no strong absorptions in the region of 0.5-3 THz, or, more likely, it was in its amorphous state, since absorptions have been seen by others using different sample

Table 3.2: Glutamic Acid Results

Mode	Temperature (K)	Experimental Freq (THz)	Int.	Literature Freq (THz)	Calculated Freq. (THz)	Scale Factor	Calculated Int (km/mol)	Fractional GS Population
1	295	1.219	s	1.21, 1.22, 1.67	0.99	1.3	0.863	0.184
	200	1.234	s		"	"	"	0.259
	100	1.243	s		"	"	"	0.451
	50	1.25	s		"	"	"	0.699
	30	1.25	s		"	"	"	0.865
	10	1.25	s		1.74	"	"	0.9975
2	295	2.02	s	1.97, 2.03, 2.22	1.95	1.3	1.496	0.279
	200	2.025	s		"	"	"	0.383
	100	2.023	s		"	"	"	0.620
	50	2.02	s		"	"	"	0.855
	30	2.017	s		"	"	"	0.960
	10	2.014	s		2.24	"	"	0.9999
3	295	—	vw	2.46, 2.46	2.76	1.3	1.926	0.331
	200	2.404	w		"	"	"	0.447
	100	2.458	m		"	"	"	0.694
	50	2.474	s		"	"	"	0.907
	30	2.424	s		"	"	"	0.981
	10	2.471	s		2.53	"	"	1.000

The predicted frequencies were calculated using CAM-B3LYP using cc-pVTz in Gaussian 09 [178] and multiplied by the Scale Factor.

preparation strategies [192]. It should be recrystallized and retested. However, the IR spectrum that we observed agrees with that found in references [187] and [190].

3.4.1.4 Glycolaldehyde

Glycolaldehyde has been detected toward hot core sources by radio and mm-wave observations [193], and while similar compounds have been found in meteorites [156], glycolaldehyde has never been specifically targeted due to its high volatility [194]. The far-infrared spectrum of the crystal has not been reported to our knowledge. The glycolaldehyde spectrum, see Figure 3.8, features several weak absorptions throughout the entire THz region that are not reported in Table 3.3 due to the poor resolution and signal-to-noise presently achieved, as well as sometimes large and untraceable shifts in frequency. There is a band of moderate strength near 2 THz at 10 and 35 K. However, at 60 K and above, the band disappears and the low frequency spectrum

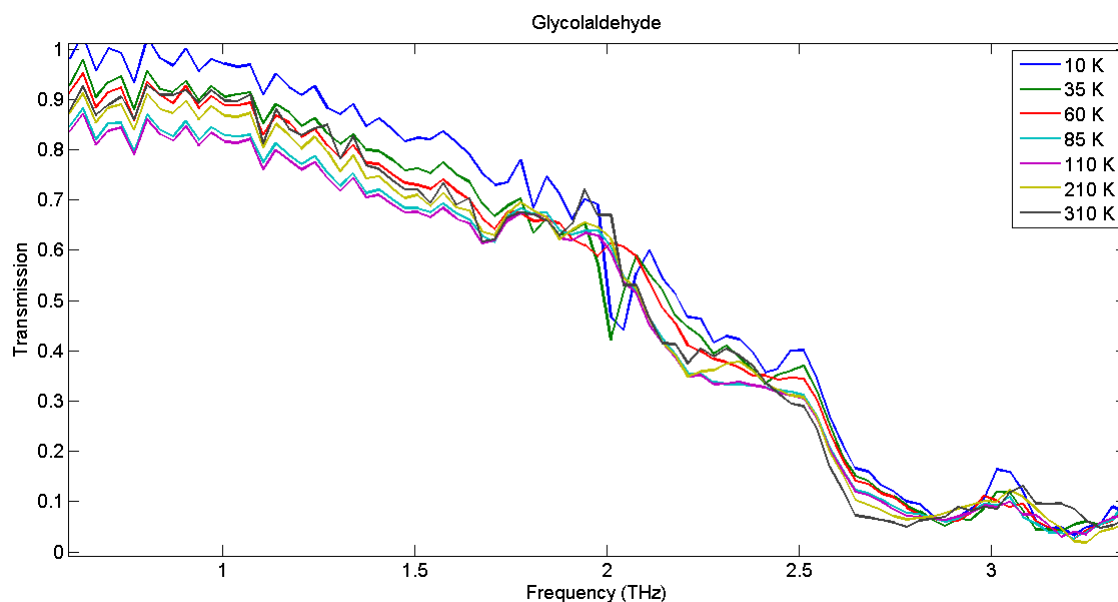


Figure 3.8: The measured transmission through a glycolaldehyde acid pellet as a function of temperature.

shows other changes here and especially at higher temperatures, including the appearance of a broad band at ~ 2.2 THz, which is most likely composed of several weak features weakly visible in the low-temperature spectra. It is possible that this is due to a phase change in the solid or to other significant changes to the hydrogen bonding or other intermolecular interactions with temperature. Future studies should focus on the change to the spectrum as a function of temperature, but with finer temperature steps and improved spectral resolution and SNR.

The crystal structure is thought to be a dimer [195] with a dioxane-like structure, but so far no one has reported a crystal structure as determined by either X-ray diffraction or neutron scattering. The lowest frequency structural mode is predicted to lie near 109 cm^{-1} [196] at the MP2/6-311++G(d,p) level. Here we predict a frequency of 221.3723 cm^{-1} at the B3LYP/ AUG-cc-pVTz level for the lowest energy, cis-cis, conformer. It is tentatively assigned to a feature observed just between 2.8 and 2.9 THz with slight blue shift with decreasing temperature. While the peak frequency does not change much at low temperatures, the absorption to the red side of the peak clearly increases at higher temperatures, possibly demonstrating anharmonicity.

In our calculations, the trans-trans conformer shows extremely strong transitions (20 and 115 km/mol) at low frequencies (80.4 and 215.4 cm^{-1}), but is anticipated to convert to the cis-cis form [197, 198] at even 15 K. Dimer calculations were not performed.

Table 3.3: Glycolaldehyde Results

Mode	Temperature (K)	Experimental Freq (THz)	Int.	Fractional GS Population
1	310	na		0.27
	210	na		0.372
	110	na		0.588
	85	na		0.683
	60	na		0.803
	35	2.009		0.938
	10	2.033	m	1
2	310	2.75	s	0.36
	210	2.78	s	0.482
	110	2.88	s	0.715
	85	2.88	s	0.803
	60	2.88	s	0.9
	35	2.88	s	0.981
	10	2.88	s	1

A summary of the results for glycolaldehyde dimer.

3.4.1.5 Aspartic Acid

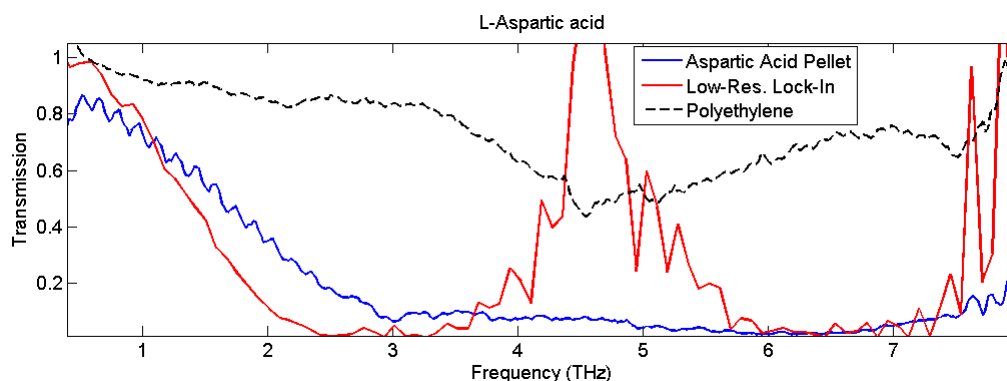


Figure 3.9: The measured transmission through an aspartic acid pellet at 295 K using the two-color plasma THz source.

L-Aspartic acid has no strong absorptions below 3 THz, but does seem to have several strong absorptions in the range of 3-7 THz. These features were not resolved due to saturation starting at about 2.5 THz, as can be seen in Figure 3.9. At low temperatures, aspartic acid

does show a weak absorption at 1.28 THz that fades to almost nothing by temperatures of 110 K. Though the spectrum is not well documented, aspartic acid was used as a substitute for L-asparagine to induce defects into the crystal structure of asparagine monohydrate [199]. No modes were attributed to aspartic acid in the range of 0.5-6 THz, though the maximum concentration was only 12.3%. It has also been studied once before below 2.7 THz [190]. Surprisingly, our calculations on the monomer show many strong transitions at low frequency, including three strong transitions below 3 THz. One caveat is that the bond distances of the converged structure do not show any indications of a possible zwitterionic contribution, and calculations performed from the crystal structure [200] give too many negative frequencies to be useful. The finding of Derissen *et al.*, while determining the crystal structure, is that there is no intramolecular hydrogen bonding, but that intermolecular hydrogen bonding is quite important in the solid state[200]. This agrees with our findings, as the anticipated lowest frequency modes are suppressed or lose significant intensity, presumably due to strong intermolecular forces that serve to severely perturb the molecular potential energy surface with respect to that in the gas phase. Therefore, we suggest that the zwitterion is not stabilized due to intramolecular hydrogen bonding and thus reverts back to the neutral form in our calculations. In this case, either *ab initio* theory is insufficient to describe the normal modes of the system or the sample was amorphous rather than crystalline (or, conceivably, contaminated with water or ions). The lowest frequency mode, again the torsion of the carboxylate group farthest from the amino group, is not observed at a frequency near the predicted value in this case.

3.4.1.6 2-Aminoisobutyric Acid

2-aminoisobutyric acid, α -AIB is one of several non-proteinogenic amino acids that are found to have significant abundance in certain carbonaceous chondrites [201], but not in terrestrial sources. AIB is observed to be one of the most abundant amino acids found in the Murchison

Table 3.4: L-Aspartic Acid Results

Mode	Temperature (K)	Experimental Freq (THz)	Int.	Literature Freq (THz)	Calculated Freq. (THz)	Scale Factor	Calculated Int (km/mol)	Fractional GS Population
1	110	1.28	w	1.35	0.663	0.955	1.45	0.429
	60	1.28	w	"	"	"	"	0.642
	10	1.283	vw	"	"	"	"	0.998
2	295	na	w	2	2.009	0.955	5.2	
3	295	na	vw	2.2	2.26	0.955	1.54	
4	na	na			4.2	0.955	5.82	
5	na	na			6.93	0.955	6.63	

The predicted frequencies are calculated using CAM-B3LYP/cc-pVTz in Gaussian 09 [178] and multiplied by the Scale Factor.

meteorite along with other CM meteorites, and, while still present in other meteorites, it can be reduced in relative abundance by up to 3 orders of magnitude [202]. Interestingly enough, AIB, along with isovaline, another amino acid found in significant abundance in meteorites but not known to be used or produced biochemically, were both found in significant quantity around (but not at) the K/T boundary, which is thought to be the result of an impact of a large meteor or comet with earth, causing an increase in elements (iridium) and molecules thought to be delivered exogenously [203]. In this sense, AIB can be regarded as a tracer for exogenously delivered amino acids. To further potential astronomical investigations of this important species, the far-infrared spectrum was acquired.

The THz spectrum of AIB (Figures 3.10 and 3.11) has not been presented in the literature, shows relatively little absorption at low frequency, with the first strong modes occurring near and above 2.5 THz. Unfortunately, the background used as a ratio for the temperature resolved data was insufficient for AIB because of the lack of absorption at high frequencies. This is thought to be due to a realignment of the spectrometer between scans, and as a consequence, the spectrum ratio shows transmission above 100% at high frequencies. The raw temperature resolved data are shown instead in Figure 3.10. The lowest frequency mode, predicted to be the carboxylate torsion, is very weak, as anticipated by theory, and is calculated at the cor-

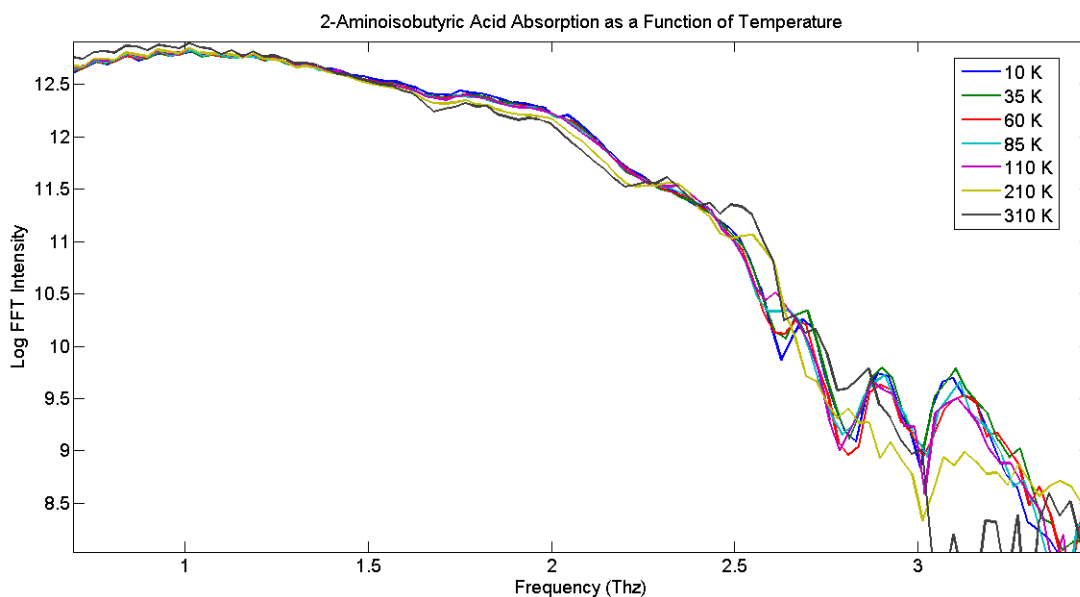


Figure 3.10: The log of the FFT spectrum of an α -aminoisobutyric acid pellet as a function of temperature.

rect frequency with little/no scaling. This band shows a slight red shift as the temperature is reduced, similar to that seen in GABA, but in much less dramatic fashion. The remainder of the modes, up to 6 THz, are though to be lattice or intermolecular modes, since no intramolecular modes are predicted in this region in our DFT calculations. Except for the first mode, all modes show ‘normal’ behavior as a function of temperature, with relatively strong anharmonicity for the second mode. The high frequency scans indicate the presence of weak

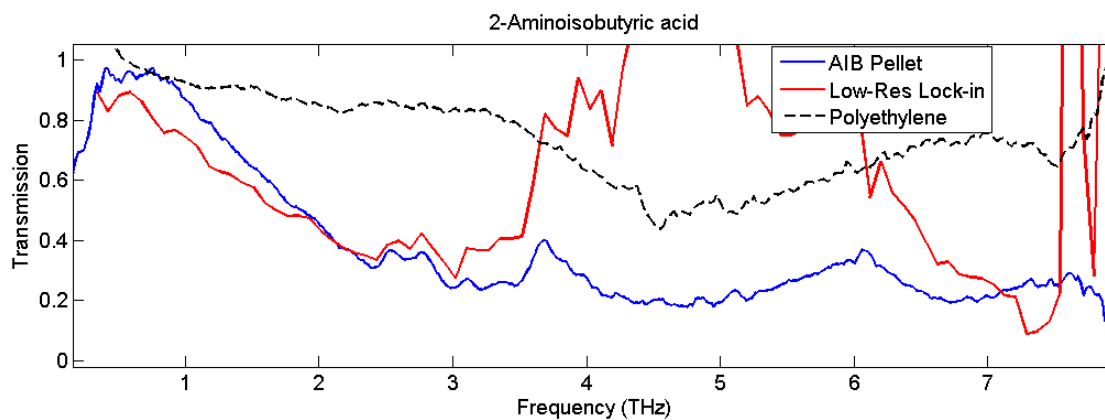


Figure 3.11: The measured transmission through an α -aminoisobutyric acid pellet at 295 K using the two-color plasma THz source.

features on top of very broad absorptions. The very broad feature centered at 4.7 THz is not predicted, and, if real, would be indicative of some lattice or intermolecular modes at higher frequencies than are commonly seen in molecules of such size. It is a bit surprising that the predictions are as accurate as they are, considering the experimental and theoretical evidence for intermolecular bonding, and the fact that the converged structure is not zwitterionic, as is anticipated for the crystalline phase [191]. In the measured crystal structure, the hydrogen positions were not resolved [191], and the geometry minimization from our DFT calculations leads to a non-zwitterionic molecule. Additionally, when the crystalline geometry is used without minimization, or only the hydrogen atoms are minimized, many negative frequencies are found, indicating a non-converged structure.

3.4.1.7 Alanine

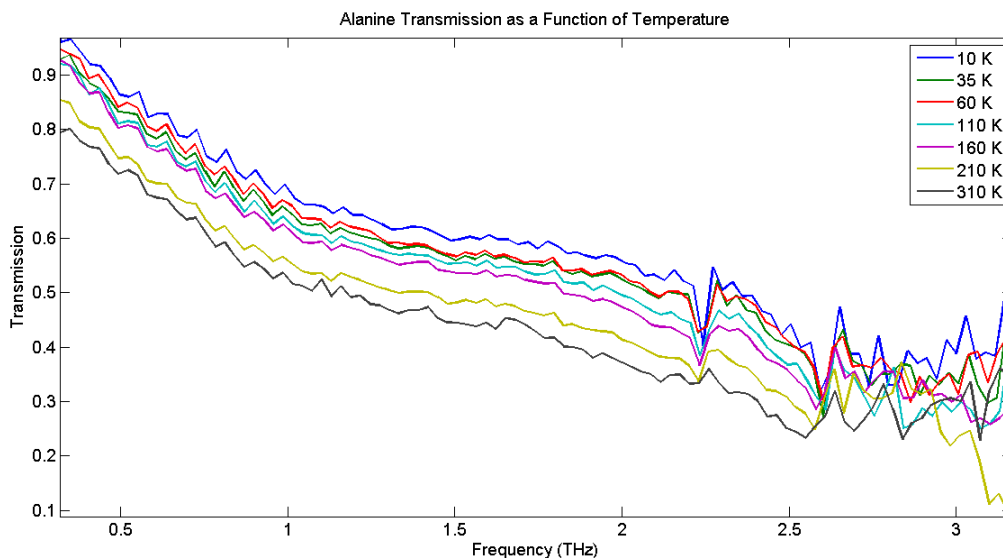


Figure 3.12: The measured transmission through an α -Alanine pellet as a function of temperature.

Alanine is one of the most studied amino acids [159, 173, 190, 204–214] due to its great abundance in both proteins, where it is second only to leucine [215] in occurrence, and in meteorites, where it is the second most abundant amino acid [216]. It is second in simplicity only

Table 3.5: L-2-Aminobutyric Acid Results

Mode	Temperature (K)	Experimental Freq (THz)	Int.	Calculated Freq. (THz)	Scale Factor	Calculated Int (km/mol)	Fractional GS Population
1	310	1.68	w	1.694	1	0.624	0.227
	295	1.676**	w	"	"	"	0.237
	210	1.674	w	"	"	"	0.316
	110	1.67	w	"	"	"	0.516
	85	1.673	w	"	"	"	0.609
	60	1.671	w	"	"	"	0.736
	35	1.669	vw	"	"	"	0.898
	10	1.664	vw	"	"	"	0.9996
2	310	2.46	m				0.334
	295	2.422**	s				0.348
	210	2.481	w				0.451
	110	2.578	m				0.682
	85	2.586	m				0.773
	60	2.624	m				0.878
	35	2.625	m				0.973
	10	2.627	m				1.000
2	310	2.782	w				0.354
	295	2.658**	m				0.368
	210	2.784	w				0.476
	110	2.786	m				0.708
	85	2.793	m				0.797
	60	2.806	m				0.896
	35	2.813	m				0.979
	10	2.825	m				1.000
3	310	no	vw				na
	295	3.003**	m				0.387
	210	3.011	w				0.497
	110	3.018	m				0.7305
	85	3.025	m				0.817
	60	3.012	m				0.910
	35	3.009	m				0.984
	10	3.006	m				1.000
4	295	3.216	m				0.407
5	295	3.47	m				0.431
6	295	4.7	s				0.534
7	295	6.72	s	6.719	1	1.133	0.665
8	na	no	na	7.69	1	1.677	na
9	295	7.87	m	7.829	1	8.697	0.722

The predicted frequencies are calculated using CAM-B3LYP/cc-pVTz in Gaussian 09 [178] and multiplied by the Scale Factor. ** Results at 295 K are taken from separate measurements and thus may not agree exactly in frequency. They are anticipated to be more correct than the other measurements due to their higher spectral resolution and a more appropriate calculation of the frequency axis.

to glycine, and is the simplest chiral amino acid. We therefore have relatively little to contribute, as the spectrum has been taken as a function of temperature using FT-FarIR spectroscopy, dating back to the 80s [204], and with great frequency coverage spanning 20 to 600 cm^{-1} (0.6 - 18 THz). Our observed peaks agree in measured frequency, but with a small shift in frequency of the two lowest frequency bands (these are difficult to constrain at our modest resolution of $\sim 1 \text{ cm}^{-1}$). While we measure a small, but appreciable, blueshift with decreasing temperature, Bandekar *et al.* claim these modes show no shift with temperature, a result they attribute to these modes being associated with hydrogen bond bending, torsion, and skeletal deformations. Since we did not perform high frequency studies of alanine nor calculations, we cannot confirm or deny these assertions – though very accurate calculations performed in the CASTEP [217] code confirm that the vibrations are strongly intermolecular [210]. This is not surprising given the results found from studying other amino acids with THz-TDS.

Table 3.6: Alanine Results

Mode	Temperature (K)	Experimental Freq (THz)	Int.	Literature Freq (THz)	Fractional GS Population
1	310	2.215	vw	2.218,2.23	0.293
	210	2.23	w		0.401
	160	2.233	w		0.49
	110	2.233	w		0.624
	60	2.239	m		0.834
	35	2.239	m		0.954
	10	2.243	m		1.000
2	310	2.55	w	2.54,2.56 0.332	
	210	2.577	w		0.448
	160	2.581	w		0.542
	110	2.609	w		0.679
	60	2.603	m		0.875
	35	2.603	m		0.972
	10	2.603	m		1.000

Literature results are taken at room temperature unless otherwise noted.

3.4.2 Sugars

3.4.2.1 Xylose

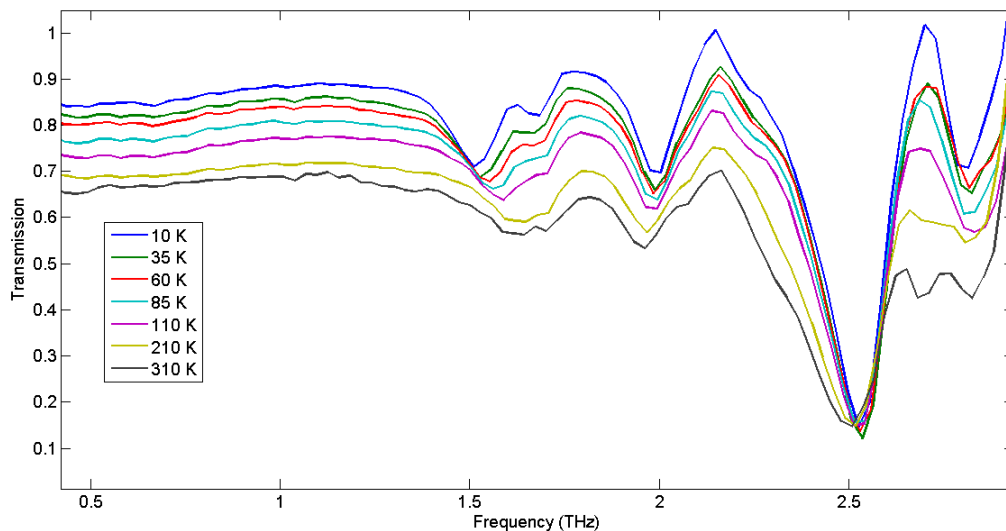


Figure 3.13: The measured transmission through a D-Xylose pellet as a function of temperature.

Xylose has been studied twice before [218, 219], but neither study has gone above 2.5 THz in frequency nor studied changes to the spectrum with temperature. The effect of temperature change on the spectrum caused the misassignment of the two modes at ~ 1.65 THz, that happen to be blended at room temperature, to the same mode. Since one of these modes features anomalous shift with decreasing temperature and other displays relatively harmonic behavior, the two peaks are resolved at lower temperatures. Neither transition is predicted by *ab initio* calculations on the isolated monomer and both are thought to arise from intermolecular forces in the crystal lattice.

The rest of the spectrum of xylose features many weak absorptions that are associated with intermolecular interactions, mostly at low frequency and between 3 and 5 THz, as well as stronger intramolecular vibrational modes that are well predicted by simulation, as can be seen in Figure 3.14.

Table 3.7: Xylose Results

Mode	Temperature (K)	Experimental Freq (THz)	Int.	Literature Freq (THz)	Calculated Freq. (THz)	Scale Factor	Calculated Int (km/mol)	Fractional GS Population
1	310	1.614	w	1.6, 1.67				0.210
	295	1.643**	w					0.219
	210	1.613	w					0.294
	110	1.608	w					0.485
	85	1.556	w					0.577
	60	1.551	w					0.704
	35	1.533	w					0.876
10	1.522	w	0.999					
2	310	1.671	w	1.6, 1.67				0.227
	295	1.643**	w					0.237
	210	1.678	w					0.317
	110	1.69	w					0.517
	85	1.69	w					0.670
	60	1.676	w					0.736
	35	1.68	w					0.898
10	1.666	w	0.9997					
3	310	1.959	w	1.8,1.96				0.265
	295	1.975**	w					0.277
	210	1.958	w					0.366
	110	1.981	w					0.581
	85	1.986	w					0.675
	60	1.99	w					0.797
	35	1.986	w					0.935
10	1.992	w	0.9999					
4	310	2.506	s	2.46	2.657	0.816	1.764	0.325
	295	2.565**	s		"	"	"	0.338
	210	2.518	s		"	"	"	0.440
	110	2.535	s		"	"	"	0.669
	85	2.534	s		"	"	"	0.761
	60	2.54	s		"	"	"	0.868
	35	2.533	s		"	"	"	0.969
10	2.535	s	"	"	"	1		
5	310	2.737 2.824	vw		2.8533	0.816	0.4185	0.352
	295	2.855 2.894**	vw		"	"	"	0.3665
		2.869			"	"	"	
	210	2.75 2.823	vw		"	"	"	0.473
	110	2.756 2.814	vw		"	"	"	0.706
	85	2.793 2.879	vw		"	"	"	0.795
	60	2.803 2.873	vw		"	"	"	0.894
35	2.802 2.930	vw	"	"	"	0.979		
10	2.806 2.929	vw	"	"	"	1		
6	295	3.58	w			0.816		0.441
7	295	4.2	w			0.816		0.495
8	295	5.4	m		5.4153	0.816	10.0266	0.585
9	295	5.74	w		5.808	0.816	1.7171	0.607
10	295	6.34	s		6.277	0.816	12.3554	0.6435
11	295	6.77	s		6.577	0.816	10.5682	0.668
12	295	7.8	vs		8.34	0.816	82.8496	0.719

A summary of the results for xylose. The predicted frequencies are calculated using CAM-B3LYP using cc-pVTz in Gaussian 09 [178] and multiplied by the Scale Factor. ** Results at 295 K are taken from a separate measurement and thus do not agree in frequency. The results at 295 K have higher spectral resolution and a more appropriate calculation of the frequency axis, and are anticipated to be more accurate.

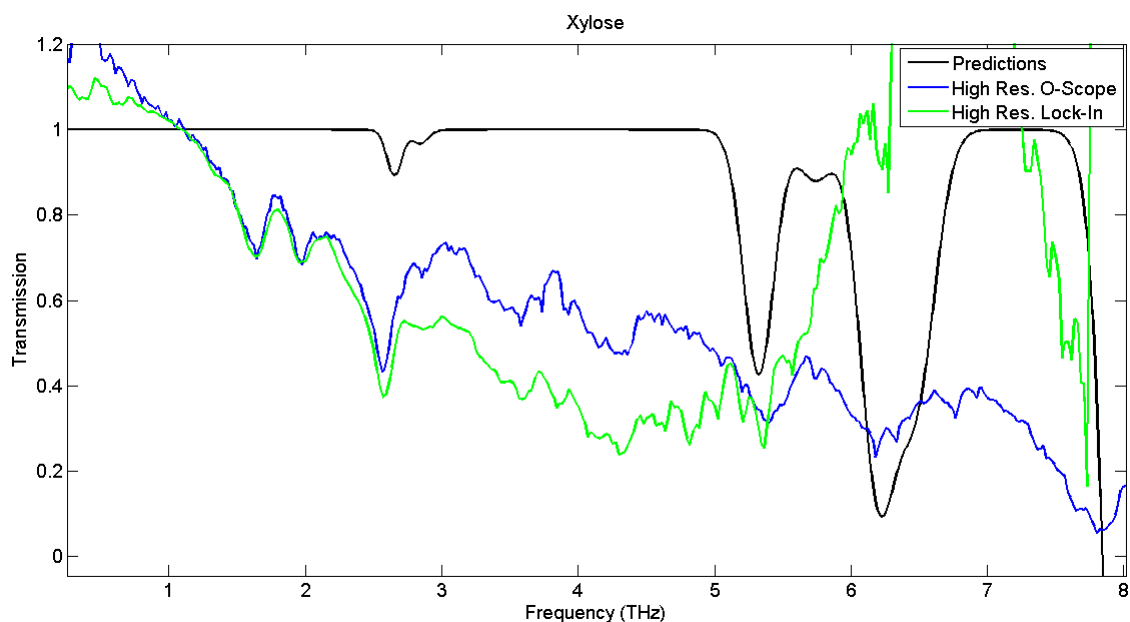


Figure 3.14: The measured transmission through a pellet consisting of 10% xylose and 90% micronized high-density polyethylene. A simulated spectrum represented by Gaussian features with height represented by the calculated intensity, FWHM manually determined (~ 0.03 THz), and frequency scaled by a factor of 0.79

3.4.2.2 Sucrose

Sucrose has been the focus of many studies due to its relevance as a biological molecule and food source, ready availability in crystalline form, and extremely complex low-frequency spectrum that features relatively narrow transition widths.

First, the spectrum was taken up to nominally 4 THz [142], though the signal-to-noise is poor above 3 THz and a mode that we, and others [144] observed near 4 THz is not present. The spectrum was also recorded as a function of temperature, from 10 to 300 K in approximately 40 degree increments. The spectrum at room temperature shows a lack of absorption at 3.5 THz, which was also seen before (and verified on different occasions in our lab). The peak is seen, however, at 10 K. This is likely because the signal goes to zero at lower frequencies as temperature increases due to increased absorption. Both of the high frequency modes were predicted in our DFT calculations. Another possibility is that the peaks at 3.5 and 4 THz in

our samples arise from hydrated sucrose. Anisotropy measurements have also been performed on single crystals of sucrose by two groups, at both room temperature [220] and at 5 K [221], with differing results. The main finding of the anisotropic measurements is that modes can be separated as the crystal is rotated, thus simplifying the complex spectrum that features many overlapping features. In principle, anisotropic measurements might aid in mode assignment, however neither group ventured, even tentatively, to assign any features to a specific vibration.

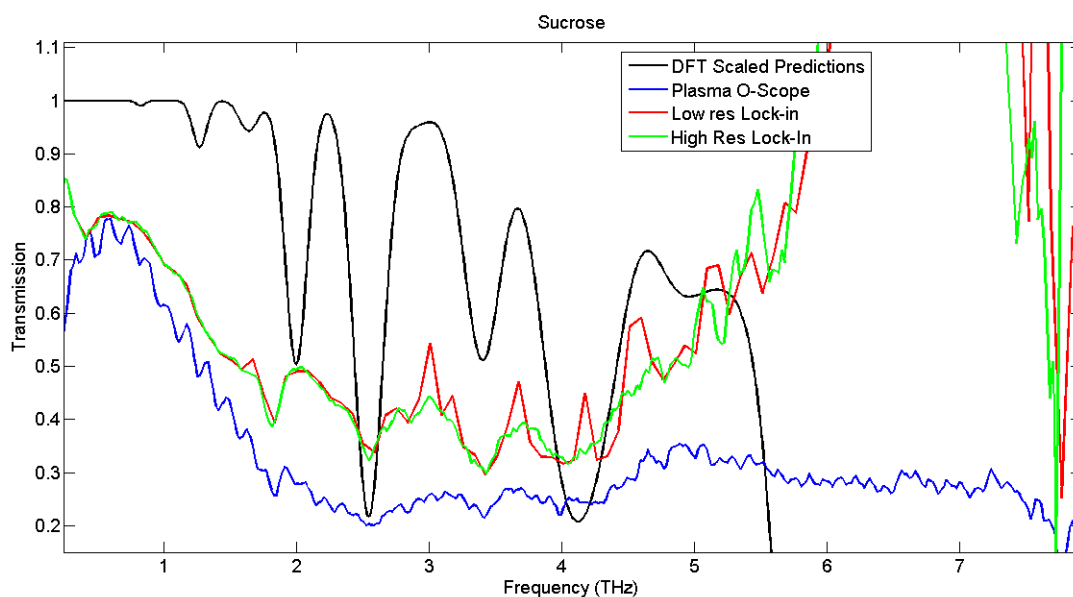


Figure 3.15: The measured transmission through a pellet consisting of 10% sucrose and 90% micronized high-density polyethylene. A simulated spectrum represented by Gaussian features with height represented by the calculated intensity, FWHM manually determined (~ 0.03 THz), and frequency scaled by a factor of 0.88

The changes to the sucrose spectrum with temperature are remarkable. The three lowest frequency modes all show a similar, and previously unseen, shift in transition frequency with temperature. As the sample is cooled from room temperature, the modes first redshift, and then begin to blueshift. These trends were first seen by Walther *et al.* [142]. We observe the same trend, but the temperature dependence and magnitude are slightly different in our study, with a somewhat reduced maximal shift and lower transition temperature, as can be

Table 3.8: Sucrose Results

Mode	Temperature (K)	Experimental Freq (THz)	Int.	Literature Freq (THz)	Calculated Freq. (THz)	Scale Factor	Calculated Int (km/mol)	Fractional GS Population		
1	295	1	vw		0.8249	0.88	0.088	0.150		
2	310	1.415	vw	1.46	1.270	0.88	0.798	0.193		
	295	1.42**	vw		"	"	"	0.202		
	210	1.424	vw		"	"	"	0.272		
	110	1.438	w		"	"	"	0.454		
	85	1.415	w		"	"	"	0.543		
	60	1.41	w		"	"	"	0.670		
	35	1.409	w		"	"	"	0.851		
	10	1.387	w		1.37, 1.38	"	"	"	0.9990	
3	310	1.667	vw	1.66	1.640	0.88	0.5205	0.229		
	295	1.58**	s		"	"	"	0.2395		
	210	1.663	vw		"	"	"	0.319		
	110	1.684	w		"	"	"	0.520		
	85	1.696	w		"	"	"	0.613		
	60	1.697	w		"	"	"	0.740		
	35	1.697	w		"	"	"	0.9005		
	10	1.683	w		1.7, 1.69	"	"	"	0.9996	
4	310	1.809	s	1.8	1.998	0.88	4.52	0.258		
	295	1.83	s		"	"	"	0.269		
	210	1.864	s		"	"	"	0.356		
	110	1.899	s		"	"	"	0.568		
	85	1.916	s		"	"	"	0.663		
	60	1.927	s		"	"	"	0.7855		
	35	1.927	s		"	"	"	0.929		
	10	1.925	s		"	"	"	0.9999		
5	310	2.644	vw	2.57, 2.58	2.5295	0.88	5.45	0.337		
	295	2.56**	s		"	"	"	0.351		
	210	2.638	w		"	"	"	0.455		
	110	2.647	m		"	"	"	0.686		
	85	2.6445	m		"	"	"	0.777		
	60	2.646	m		"	"	"	0.8805		
	35	2.645	m		"	"	"	0.974		
	10	2.657	m		"	"	"	1.000		
6	310	NA	w		2.596	0.88	1.921	0.357		
	295	2.682**			"	"	"		"	
	210	NA			"	"	"		"	
	110	NA not resolved			"	"	"		"	
	85	2.702			m	"	"		"	0.784
	60	2.703			m	"	"		"	0.886
	35	2.703			m	"	"		"	0.976
	10	2.716			m	"	"		"	1.000
7	310	not resolved	w	2.73	"	"	"	0.369		
	295	2.682**			"	"	"		"	
	210	not resolved			"	"	"		"	
	110	2.778			w	"	"		"	0.7095
	85	2.791			w	"	"		"	0.798
	60	2.808			m	"	"		"	0.896
	35	2.818			m	"	"		"	0.979
	10	2.834			m	"	"		"	1.000
8	310	3.018	vw	2.91	2.8995	0.88	0.386	0.3745		
	295	2.85**	vw		"	"	"	0.389		
	210	2.982	vw		"	"	"	0.500		
	110	2.963	w		"	"	"	0.7335		
	85	2.989	m		"	"	"	0.819		
	60	3.003	m		"	"	"	0.911		
	35	3.019	m		"	"	"	0.984		
	10	3.031	s		"	"	"	1		
9	295	3.42	s	3.5	3.403	0.88	4.425	0.427		
10	295	4.05	s	4.3	3.92 and 4.08	0.88	2.47 and 3.88	0.4825		

The predicted frequencies as calculated using CAM-B3LYP using cc-pVTz in Gaussian 09 [178] are multiplied by the Scale Factor. * Results at 295 K are taken from a separate measurement and thus do not agree in frequency. The results at 295 K are anticipated to be incorrect due to possible hydration of the sample, resulting in low specific absorbance.

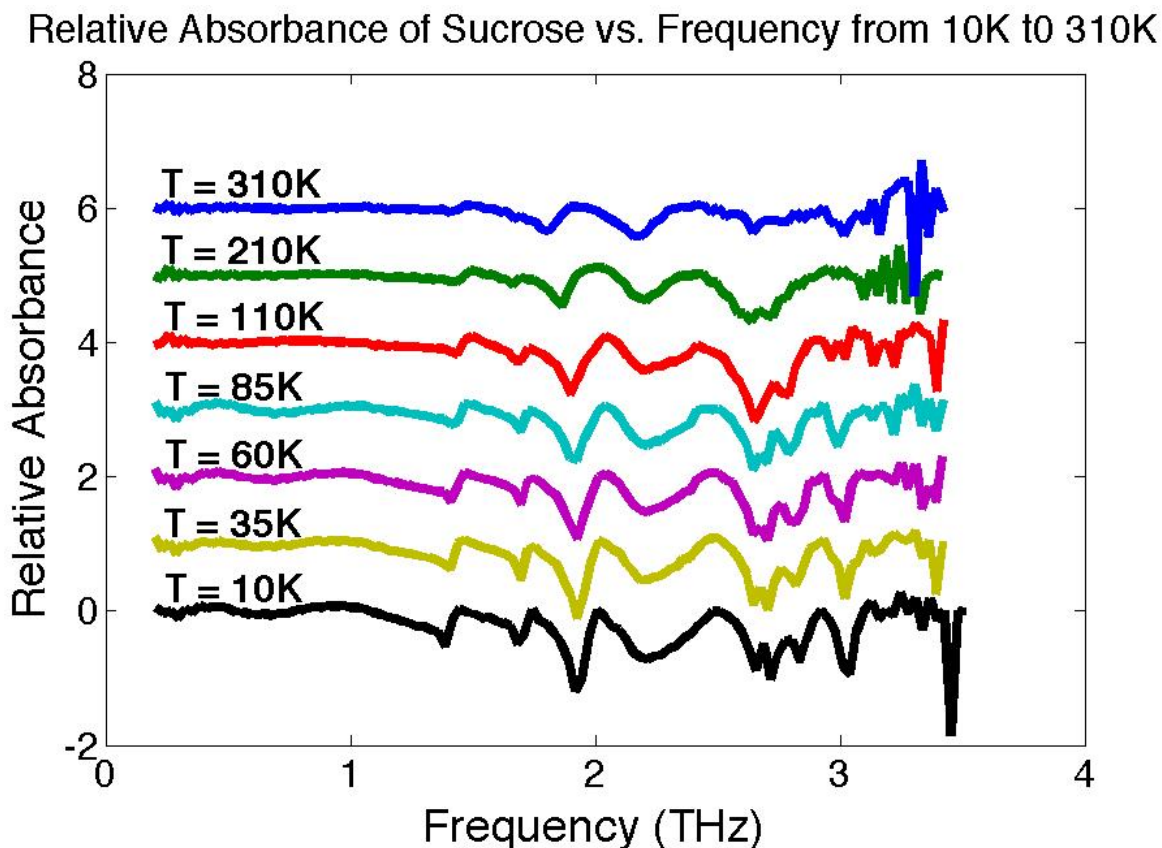


Figure 3.16: The measured transmission through a sucrose pellet pressed with micronized high-density polyethylene.

seen in Figure 3.16. Some of this could be the result of an insufficient number of temperature points in our measurements and the low spectral resolution (~ 50 GHz) of our temperature-resolved measurements. Also, peak centers were not fit here with the same treatment as was performed previously, by fitting Lorentzian curves with adjustable amplitudes and width as parameters. We thus have greater uncertainty in our measurements. Walther *et al.* also studied a fully deuterated version of sucrose and found large shifts to the frequency of the modes when compared to what one might expect in the harmonic approximation, and claim this is due to a softening of the vibrational potentials. We discuss this further below (Section 3.5). For frequencies above 2.5 THz, the unstructured and relatively featureless spectrum at room temperature transitions into a complex and intense pattern of at least 4 transitions at 10 K. Blending of the components as well as broadened transitions is limiting at high temperatures

and persists even at low temperature. While there is nothing fundamentally new to report from our study of sucrose, the good agreement with previous work is confirmation of the fundamental operation of the new THz-TDS instrument.

The same sucrose sample was measured during three occasions in our lab over a period of 3.5 years. As mentioned previously, we see a degradation in the spectra, likely caused by hydration, forming either changes to the crystal structure as it incorporates water, or via the formation of amorphous sucrose. Each successive spectra shows less definition to the spectral structure and a decrease in overall transmission. This can be seen in Figure 3.15 for the last two of the high frequency measurements. Thus, the results as shown in Table 3.8 are taken from the earliest measurements when possible.

3.4.2.3 D-Ribose

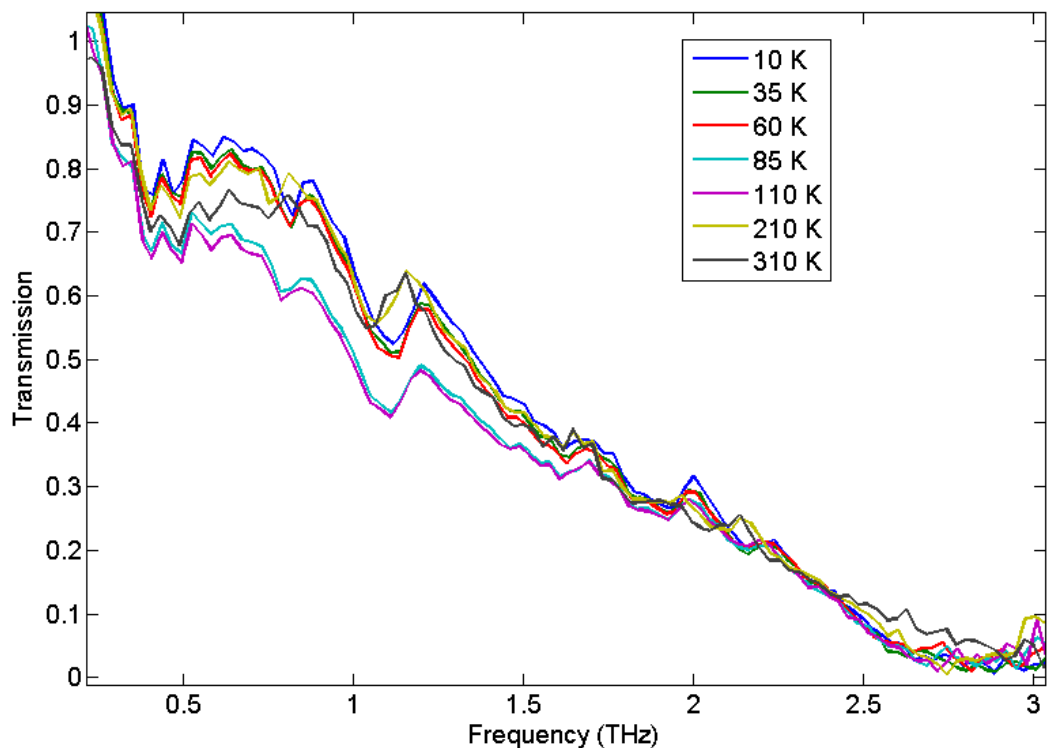


Figure 3.17: The measured transmission through a D-Ribose pellet as a function of temperature.

Ribose was studied as a function of temperature, but not using the high frequency bandwidth plasma source. Its spectrum shows at least four modes that were previously observed [218], as can be seen in Figure 3.17 and Table 3.9. We also observed clear trends when studying the spectrum as a function of temperature, with both of the lowest frequency modes showing the normal blueshift with decreasing temperature. Peaks 3 and 4 do not show many changes with temperature, either in intensity or shift, are split, and are not as clear as in Reference [218]. This likely occurs because either our sample was too concentrated or the sample was partly amorphous, as is common with ribose – which is notoriously hard to crystallize and for which the full crystalline atomic coordinates are still not known [222]. It is clear, however, that the unit cell contains both α and β D-ribose molecules. As such, both were simulated, but neither shows strong modes below 3 THz and so no predictions are reported here. Similar results are found for D-arabinose (Section 3.4.2.5), in that the low frequency modes are not predicted to be intramolecular in character, but some of the modes around 3 THz may well have significant intramolecular character. In this regard, higher frequency spectra would be useful for comparison purposes.

3.4.2.4 D-Mannose

The D-mannose spectrum has never been reported in the literature, to our knowledge. It features several weak absorptions below 2 THz, along with several strong bands from 2 to 3.5 THz. As it is cooled to 10 K, there are major and distinctive changes to the spectrum (See Figure 3.18), including the normal blue shift of all transitions observed as well as apparent splitting of the transition found at 2.4-2.8 THz, which is likely caused by transition narrowing, and the extreme change in frequency, breadth, and intensity of the feature found at 2.9-3.4 THz. Mannose thus demonstrates the necessity for studying molecules at reduced temperatures if a true understanding of the spectrum is desired. Beyond the results listed in Table 3.10, there

Table 3.9: D-Ribose Results

Mode	Temperature (K)	Experimental Freq. (THz)	Literature Freq. (THz)	Int.	Fractional GS Population
1	310	0.75	0.74	vw	0.120
	210	0.758		vw	0.1715
	110	0.7885		w	0.302
	85	0.797		w	0.372
	60	0.8135		w	0.4825
	35	0.8175		w	0.677
	10	0.8236		w	0.981
2	310	1.0435	1.1	m	0.159
	210	1.0686		m	0.225
	110	1.097		m	0.386
	85	1.1093		m	0.468
	60	1.122		m	0.591
	35	1.12		m	0.784
	10	1.1172		m	0.995
3	310	1.55, 1.6	1.57	w	
	210	"		w	
	110	"		w	
	85	"		w	
	60	"		w	
	35	"		w	
	10	"		w	
4	310	1.81, 1.93	1.85	m	
	210	"		m	
	110	"		m	
	85	"		m	
	60	"		m	
	35	"		m	
	10	"		m	

Literature results are taken at room temperature unless otherwise noted. The predicted frequencies are calculated using CAM-B3LYP/cc-pVTz in Gaussian 09 [178] and multiplied by the Scale Factor.

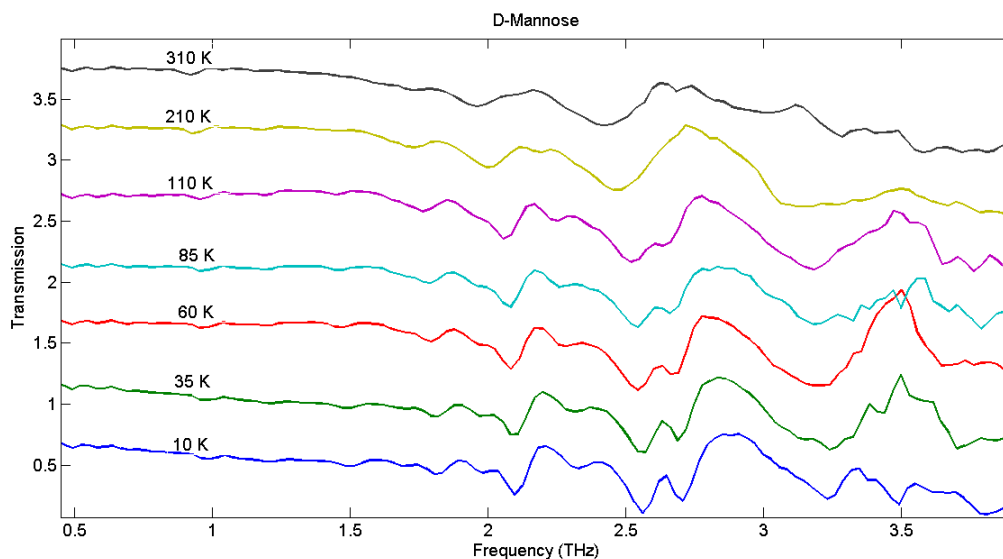


Figure 3.18: The measured transmission through a D-Mannose pellet pressed with micronized high-density polyethylene as a function of temperature.

appears to be a peak at 3.5 THz found in the two lowest temperature scans: however, since this is usually outside the range of our instrument, its presence is debatable. The high frequency spectra taken with lock-in detection are at very low resolution, and suffer from notable issues above 3 THz due to low signal-to-noise and non-removed etalon features (see Figure 3.19). Unfortunately, the high-resolution spectra taken with the oscilloscope show a marked change to the sample, probably caused by hydration. While some of the features are consistent, most show significant changes to the intensity or are shifted in frequency. Nonetheless, the predicted spectrum matches well with the observed data with very little scaling. These results clearly mark some modes as being primarily intramolecular in character, but demonstrate the need for careful sample preparation.

3.4.2.5 D-Arabinose

While D-arabinose has been studied at least twice before [218, 223], we measure distinctive changes to the spectrum as a function of temperature that reveal several modes that have not yet been reported. We note at least two spectral regions that completely change as a function

Table 3.10: D-Mannose Results

Mode	Temperature (K)	Experimental Freq (THz)	Int.	Calculated Freq. (THz)	Calculated Int (km/mol)	Scale Factor	Fractional GS Population
1	310	0.92	vw				0.1405
	295	0.936**	vw				0.147
	210	0.95	vw				0.200
	110	0.969	vw				0.347
	85	0.976	vw				0.424
	60	0.978	vw				0.543
	35	0.983	vw				0.738
	10	0.978	vw				0.991
2	310	n.o.	vw				
	295	n.o.	vw				
	210	n.o.	vw				
	110	1.447	vw				
	85	1.458	vw				
	60	1.465	vw				
	35	1.488	vw				
	10	1.5	vw				
3	310	1.725	vw	1.806	1.5356	0.955	0.245
	295	1.73**	vw	"	"	"	0.256
	210	1.726	vw	"	"	"	0.340
	110	1.773	vw	"	"	"	0.547
	85	1.792	w	"	"	"	0.641
	60	1.793	w	"	"	"	0.766
	35	1.812	w	"	"	"	0.917
	10	1.816	w	"	"	"	0.9998
4	310	n.o.	vw				
	295	n.o.	vw				
	210	n.o.	vw				
	110	1.939	vw				0.578
	85	1.951	vw				0.673
	60	1.954	vw				0.795
	35	1.965	w				0.934
	10	1.979	w				0.9999
5	310	1.953	w				0.278
	295	2.02**	w				0.290
	210	2.0044	m				0.382
	110	2.0655	ms				0.601
	85	2.0775	ms				0.696
	60	2.086	ms				0.815
	35	2.1015	ms				0.944
	10	2.107	ms				1.000
6	310	2.156	vw				0.302
	295	2.174**	w				0.315
	210	2.24	vw				0.412
	110	2.244	vw				0.637
	85	2.266	vw				0.731
	60	2.2823	w				0.844
	35	2.313	w				0.959
	10	2.324	w				1.000
7	310	2.429	wm				0.328
	295	2.46**	s				0.342
	210	2.48	m				0.444
	110	2.5315	vs				0.674
	85	2.5543	vs				0.766
	60	2.5525	vs				0.872
	35	2.571	vs				0.971
	10	2.572	vs				1.000
8	310	2.644	vw				0.342
	295	NR	vw				0.356
	210	2.646	vw				0.461
	110	2.6466	vs				0.6925
	85	2.6597	vs				0.783
	60	2.6705	vs				0.885
	35	2.696	vs				0.975
	10	2.703	vs				1.000
9	310	3.01	w	3.001	2.1292	0.955	0.393
	295	3.082**	w	"	"	"	0.409
	210	3.12	s	"	"	"	0.522
	110	3.171	s	"	"	"	0.756
	85	3.18	s	"	"	"	0.8385
	60	3.192	s	"	"	"	0.924
	35	3.198	s	"	"	"	0.988
	10	3.23	s	"	"	"	1.000
10	295	3.892	m	3.587	2.9733	0.955	0.469
11	295	4.9	m	5.002	13.0845	0.955	0.534
12	295	5.9	s	6.042	7.736	0.955	0.617
13	295	7.55	s	7.29, 7.54	65.73, 20.3	0.955	0.707
14	295	7.73	s				0.716

The predicted frequencies are calculated using CAM-B3LYP/cc-pVTz in Gaussian 09 [178] and multiplied by the Scale Factor.

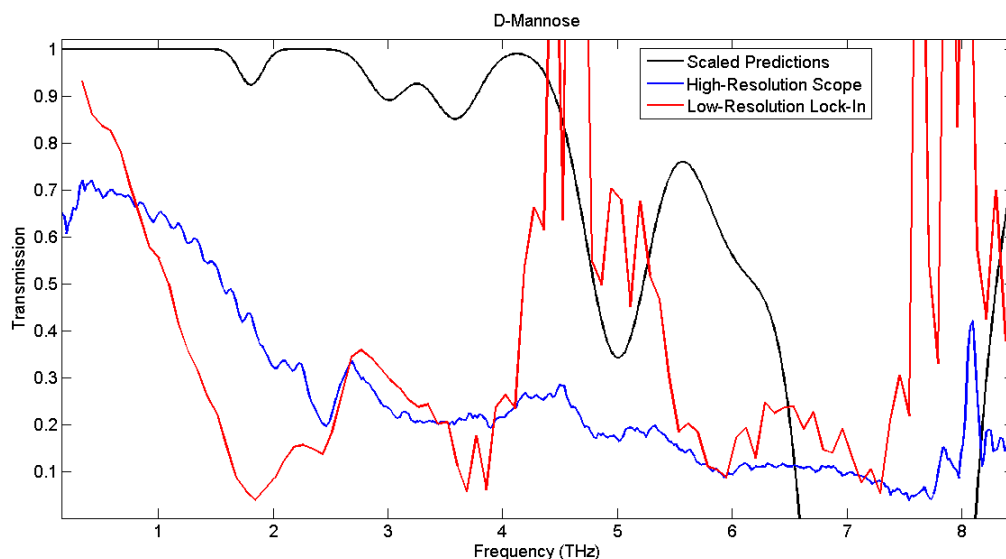


Figure 3.19: The measured transmission through a D-Mannose pellet at room temperature compared with predicted results from DFT calculations at the CAM-B3LYP/cc-pVTz level, scaled by a factor of 0.955 with a modified Gaussian line shape.

of temperature, with peaks becoming severely blended, shifted, or simply disappearing. These two regions can be found at 2.1-2.5 THz, where only one mode appears to exist near room temperature, but for which no fewer than three are seen at 10 K, and at 2.8-3.2 THz, where the sole observed transition at room temperature shifts and splits into two modes near 10 K. Both phenomena can be seen in Figure 3.20. These changes could be indicative of a phase change, though mode 1, at least, is relatively unaffected, which either indicates significant intramolecular character to that mode, or suggests that a phase change is in fact not the cause of the large changes to the THz spectrum. Since the mode is not predicted by our calculations, it suggests that it is likely strongly intermolecular and thus unaffected by the proposed phase change. The previously reported peak at 3.4 THz [223] was seen in our scans, however it is well beyond the usual bandwidth of our spectrometer, but does clearly appear in a few scans, so is listed in Table 3.11. Similar to the case of AIB (Section 3.4.1.6), the spectrum of the pellet shows extended frequencies with respect to the reference and so the transmission at high frequencies is sometimes above 100%, however the shape of the spectrum is expected to be

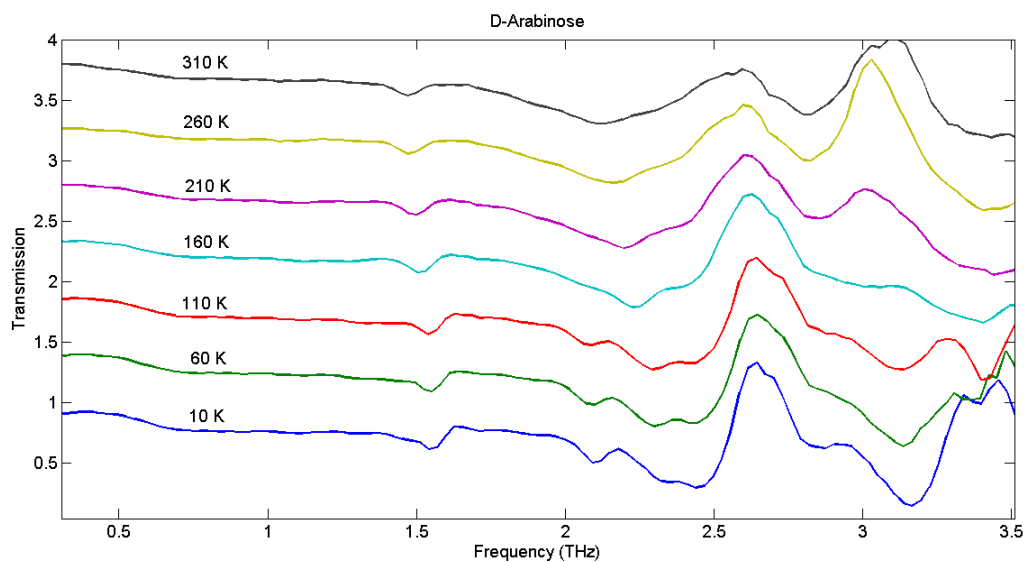


Figure 3.20: The measured transmission through a D-Arabinose pellet as a function of temperature.

generally valid (but broad modes above 3 THz may be more significantly affected). Simulations at the CAM-B3LYP/cc-pVTz level do not predict any of the low frequency modes, but do match up with both of the highest frequency modes detected. It is thus thought that the lowest energy modes are purely intermolecular or phonon-like in nature.

3.4.2.6 D-Glucose

Unsurprisingly, glucose has been studied numerous times [142–145, 223–229], with spectra at liquid helium temperatures [228, 229] and room temperature [227] known since the 1970s. Our results agree with what has been observed qualitatively, though we note very significant changes to the previously reported shapes – not position – of the measured transitions, particularly those near mode 3 at 2.6 THz. All modes show the anticipated shift with decreasing temperature. One of the more interesting studies involved the change to hydration of a D-glucose monohydrate crystal as a function of heating [226], which might serve as a good introductory physical chemistry laboratory, or as a way of understanding and modeling intermolecular hydrogen bonding interactions in such solids. Beyond that, glucose should not be subject of further studies

Table 3.11: D-Arabionse Results

Mode	Temperature (K)	Experimental Freq (THz)	Int.	Literature Freq (THz)	Calculated Freq. (THz)	Scale Factor	Calculated Int (km/mol)	Fractional GS Population
1	310	1.471	m	1.48, 1.5				0.213
	260	1.478	m					0.249
	210	1.491	m					0.298
	160	1.515	m					0.372
	110	1.541	m					0.491
	60	1.544	m					0.710
	10	1.549	m					0.9994
2	310	blend	n.o.					0.277
	260	blend	n.o.					0.321
	210	blend	n.o.					0.381
	160	blend	vw					0.467
	110	2.084	ms					0.600
	60	2.089	ms					0.813
	10	2.099	ms					0.9999
3	310	2.125	s	2.15				0.302
	260	2.155	s					0.349
	210	2.2	s					0.412
	160	2.235	s					0.502
	110	2.296	s					0.637
	60	2.302	s					0.844
	10	2.324	s					1.000
4	310	2.31	n.o.					0.315
	260	2.396	n.o.					0.363
	210	2.405	n.o.					0.428
	160	2.414	n.o.					0.520
	110	2.424	m					0.656
	60	2.436	s					0.8585
	10	2.4455	s					1.000
5	310	2.814	s 2.8					0.3585
	260	2.815	s					0.411
	210	2.851	s					0.482
	160	blend	n.o.					0.577
	110	blend	n.o.					0.714
	60	2.849	vw					0.899
	10	2.868	w					1.000
6	310	n.o.	n.o.		3.002	0.87	1.647	0.387
	260	n.o.	n.o.		"	"	"	0.442
	210	n.o.	n.o.		"	"	"	0.515
	160	3.005	w		"	"	"	0.613
	110	3.129	s		"	"	"	0.749
	60	3.137	vs		"	"	"	0.920
	10	3.165	vs		"	"	"	1.000
7	310	n.r.	vs	3.4	3.424	0.87	1.784	
	260	n.r.	vs		"	"	"	
	210	n.r.	vs		"	"	"	
	160	3.41	vs		"	"	"	
	110	3.41	vs		"	"	"	
	60	3.4	w		"	"	"	
	10	3.4	w		"	"	"	

Literature results are taken at room temperature unless otherwise noted. The predicted frequencies are calculated using CAM-B3LYP/cc-pVTz in Gaussian 09 [178] and multiplied by the Scale Factor.

in the Blake lab.

Table 3.12: D-Glucose Results

Mode	Temperature (K)	Experimental Freq (THz)	Int.	Literature Freq (THz)	Fractional GS Population
1	310	1.434	m	1.43, 1.44	0.2015
	210	1.439	m		0.283
	110	1.449	m		0.470
	85	1.445	m		0.560
	60	1.443	m		0.687
	35	1.452	m		0.864
	10	1.4535	m	1.45	0.9990
2	310	2.045	vw	2.08, 2.10, 2.05	0.2775
	210	2.082	vw		0.381
	110	2.098	vw		0.600
	85	2.108	w		0.694
	60	2.107	w		0.8135
	35	2.105	w		0.944
	10	2.1	w	2.11	0.99995
3	310	2.657	vw	2.61, 2.63, 2.64	0.348
	210	2.7	vw		0.468
	110	2.726	w		0.700
	85	2.751	m		0.790
	60	2.76	m		0.890
	35	2.781	m		0.977
	10	2.761	vs	2.75	1.000

A summary of the results for D-Glucose.

3.4.2.7 D-Fructose

Fructose has been studied several times before [142–144] and we have qualitatively nothing new to present. While we observed the normal shift of the observed transitions as a function of temperature (Figure 3.22), and are the only group to report this incrementally, the 10 K and room temperature spectra have already been measured [142]. We observe a normal and fairly linear shift with temperature, indicating a well behaved potential energy surface. Unfortunately, the sample was too concentrated when doing the temperature dependent measurements and the 3rd mode, which should have been observed in our experimental bandwidth, was not seen due to saturation. We also extended the observed range to 8 THz, but only one new mode

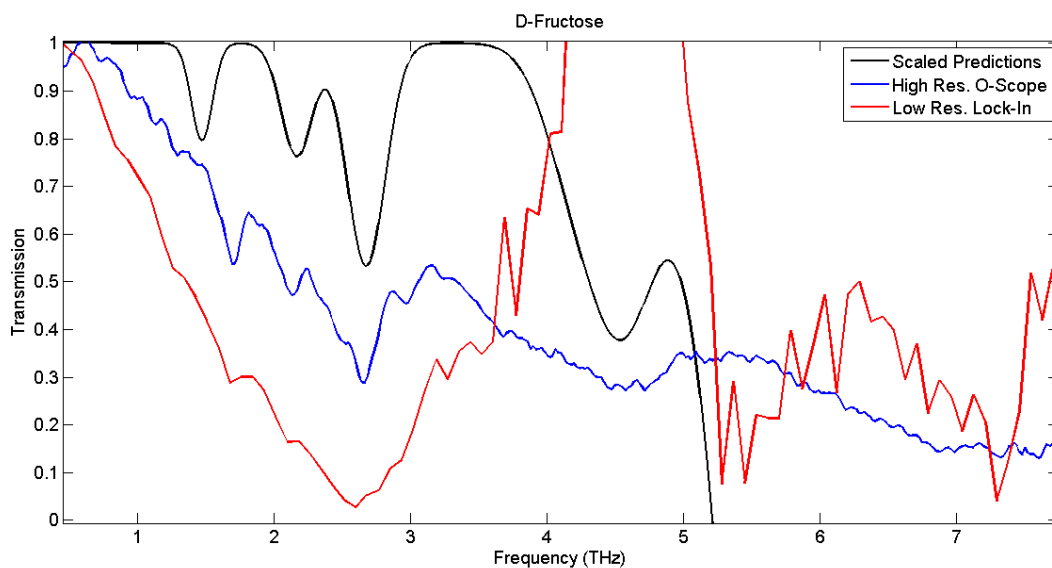


Figure 3.21: The measured transmission through a D-fructose pellet at room temperature compared with predicted results from DFT calculations, at the CAM-B3LYP/cc-pVTz level and scaled by a factor of 0.7 with a modified Gaussian line shape.

has been detected, as can be seen in Table 3.13. The predicted bands, as seen in Figure 3.21, show good agreement, but only after significant scaling, where the scaling factor was 0.70. This demonstrates that these modes have significant inter- and intra- molecular character since the *ab initio* fit is so poor.

3.5 Discussion

As a general rule, the transmission of all samples increases across the entire band as the temperature is reduced. Strangely, polyethylene was found to increase in absorption at low frequencies at reduced temperatures. This accentuated the effect of apparent increased transmission because the sample, whose FFT was ratioed against the spectrum of polyethylene, generally both became more transmissive at cooler temperatures due to the increased thermal order and a lower population of states, which was in turn divided by a lower number due to polyethylene. While the measured THz field is significantly lower at lower temperatures ($\sim 15\%$ at the peak frequency from 310 K to 10 K, for polyethylene) the transmission at frequencies above 3 THz

Table 3.13: D-Fructose Results

Mode	Temperature (K)	Experimental Freq (THz)	Int.	Literature Freq (THz)	Calculated Freq. (THz)	Scale Factor	Calculated Int (km/mol)	Fractional GS Population
1	295	1.27	vw	1.35, 1.29				0.187
2	310	1.6706	ms	1.69	1.4705	0.7	2.542	0.242
	295	1.699**	ms	1.68	"	"	"	0.253
	210	1.7028	ms		"	"	"	0.336
	110	1.7435	ms		"	"	"	0.542
	85	1.7704	ms		"	"	"	0.636
	60	1.7733	ms		"	"	"	0.761
	35	1.782	s		"	"	"	0.914
	10	1.7904	s	1.88	"	"	"	0.9998
3	310	2.1115	m	2.12	2.1665	0.7	2.958	0.2905
	295	2.1332**	m	2.11	"	"	"	0.303
	210	2.1506	ms		"	"	"	0.3975
	110	2.1725	ms		"	"	"	0.620
	85	2.1802	ms		"	"	"	0.714
	60	2.2000	s		"	"	"	0.830
	35	2.2075	s		"	"	"	0.952
	10	2.2173	s	2.25	"	"	"	0.9999
4	295	2.52	w	2.5				0.336
5	295	2.64	s	2.66, 2.61	2.673	0.7	5.837	0.349
6	295	2.96	m	2.97, 2.93				0.382
7	295	3.23	vw	3.22				0.409
8	295	4.48	s	4.6	4.564	0.7	6.81	0.5175
9	295	7.32	s		6.988	0.7	68.29	0.696

The predicted frequencies are calculated using CAM-B3LYP/cc-pVTz in Gaussian 09 [178] and multiplied by the Scale Factor. ** Results at 295 K are taken from separate measurements and thus may not agree exactly in frequency. The results at 295 K are anticipated to be more correct than the other measurements due to their higher spectral resolution and more appropriate calculation of the frequency axis.

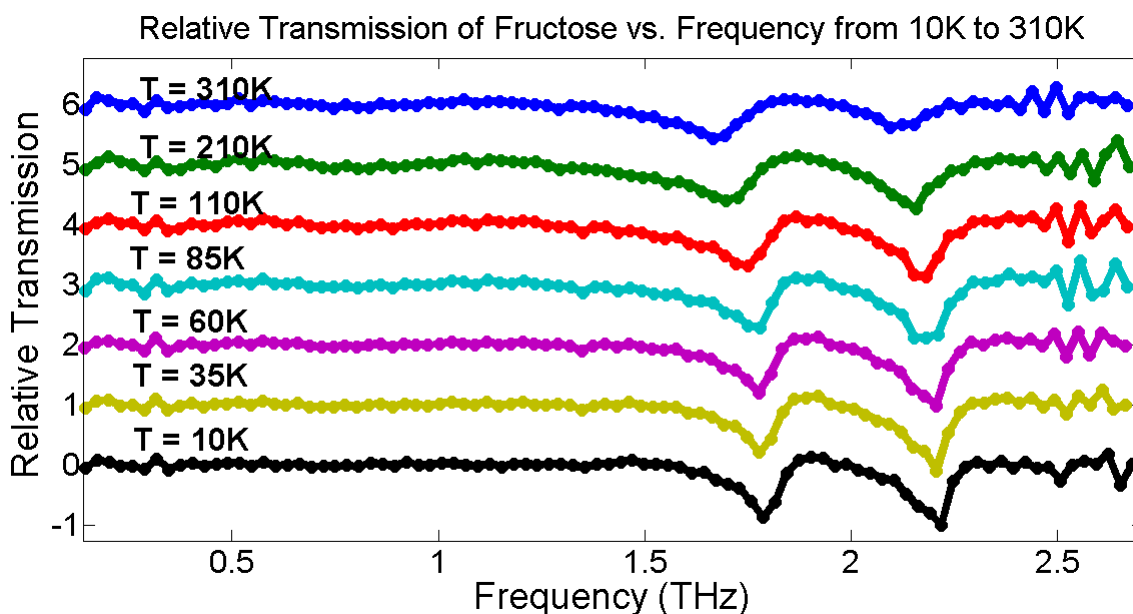


Figure 3.22: The measured transmission through a D-Fructose pellet as a function of temperature.

is increased. The increase in absorption at low temperatures has also been seen for other amorphous materials as well [142].

For amino acids and sugars, the detected THz spectral features typically blue shifted as samples were cooled to 10 K. This behavior is expected for a standard, Morse-like, anharmonic potential energy surface, where the lowest levels are most separated in energy. Only the ground state is expected to be populated at such low temperatures, since the thermal energy at 10 K is equivalent to an energy of $0.21 \text{ THz} \cdot h$. However, at room temperature, the thermal energy is approximately $6.21 \text{ THz} \cdot h$, and the population is expected to be spread among many states, causing an inhomogeneous broadening towards the low frequency side of the transition. The transition is also homogeneously broadened due to thermal motion of the atoms [142]. Some of the more interesting transitions either redshift as the temperature is reduced or blueshift to a point and then redshift. This bimodal behavior was found with sucrose and deuterated sucrose [142] and was confirmed in our study. The anomalous redshift with decreasing temperature was explained to be a consequence of van der Waals interactions weakening hydrogen bond-related

modes. Van der Waals forces are thought to increase because colder temperatures are known to decrease the crystal size and give rise to more dense packing, thus all atoms are closer to each other and induced dipole forces are more apt to occur, possibly altering the hydrogen bonds.

However, this interpretation is dubious since others have found the opposite behavior when only van der Waals interactions are present [230, 231] as in the case of CH stretching modes in sugars. Further, the hydrogen bonding is only expected to increase in significance with decreasing temperature [232]. Multiple studies of the temperature effects of in the OH stretching region of crystalline pyranoside carbohydrates have shown the same redshift with decreasing temperature, for example references [230, 231]. This was attributed to the strengthening of hydrogen bonds as a result of the tighter packing of the crystals, which lessens the force constants for the OH stretch. Others have found that the frequency shift with stronger hydrogen bonds is not constant but can be predicted based on the change in bond order and charge redistribution when the intermolecular hydrogen bonding strength is increased [232, 233]. This is the proposed mechanism in the THz case.

Assuming a Morse-like anharmonic potential, which is itself a large assumption, there will be some blueshift upon cooling, whose magnitude is given by the anharmonicity and the anticipated population change. When increased hydrogen bonding is factored in, the results are uncertain, though generally the intramolecular high frequency bonds will weaken somewhat, and a redshift is expected for the collective modes characteristic of the far-infrared. That is, an anomalous redshift upon cooling is likely caused by intermolecular hydrogen bonding and should be useful in identifying inter- versus intra- molecular related modes, in that the intermolecular modes are anticipated to undergo the largest shifts [234].

When studying spectra in a variety of phases or solvents, it has been well documented that some modes stay the same, and some shift dramatically or are absent [234] upon changes to the phase or solvent. The changing modes are often intermolecular in nature. This is due to the

fact that hydrogen bonding or other intermolecular interactions cause large changes to specific modes while leaving others unhindered. Intramolecular distances are thought to be relatively unchanged by a change in temperature, while intermolecular distances are anticipated to become significantly smaller with decreasing temperature, and thus the spectral shift of intermolecular modes should, in principle, be larger. This is not found in most cases here, as many of the lowest frequency intramolecular modes also have significant dependence on the changes to the intermolecular landscape, either directly or indirectly. Temperature dependence of the spectrum at higher frequencies, where intramolecular contributions are less likely, would help to confirm this.

Spectral features also typically narrowed at cryogenic temperatures. This is attributed to both homogenous and inhomogeneous broadening effects. First, the thermal disorder is reduced, and thus all transitions are homogeneously narrowed. Second, due to decreased population in the upper states of the presumably anharmonic potential energy surface, transitions were also narrowed because the range of eigenfrequencies that contribute to the absorption are also narrowed.

3.5.1 Theory

Assigning the observed spectral features to a specific motion, or set of motions, is quite difficult with present techniques/computation capacity. Predicting the spectrum of crystalline substances in the far-infrared or THz region can be quite challenging, and many methods have been tried, including *ab initio* and density functional methods B3LYP [146, 235, 236], HF, B3PW91 [146], and MP2 [236], mostly with the 6-311+G** basis set, as well as molecular mechanics based methods [237] and DFT plane-wave basis set-type calculations that employ periodic boundary conditions [149, 237, 238]. A recurring debate is whether or not modes can be adequately described as either intramolecular or intermolecular, having a character that is

fully vibrational, or with a character that is derived from rotation, translation, or center-of-mass motion (or some combination of the above). Jepsen and Clark performed some of calculations with the closest match(es) to experiment using the CASTEP code [217] and very strict convergence criteria [149]. The CASTEP calculations were based on plane-wave density functional theory while norm-conserving pseudo-potentials were used to describe the electron-ion interactions. Most notably, these authors concluded that modes could not be assigned as fully inter- or intra- molecular in the case of hydrogen bonded molecular crystals, even for the lowest frequency modes. The molecules studied were sucrose, benzoic acid, and thymine. They conclude that the modes are “best described as phonon modes with strong coupling to the intramolecular degrees of freedom” and argue for the need for a computational method that takes into account both the periodicity of the crystal as well as the intramolecular motion. Jepsen and Clark calculate and plot normalized motion amplitudes for internal and center-of-mass motions as a function of mode number. At low mode number, the center-of-mass motion is, as anticipated, a larger fraction of the total motion fraction. Unfortunately, dipole moment fluctuations in each mode are not calculated, so overall effect on the transition is not fully described. Burnett *et al.* [237] extended the idea of breaking down the contributions to the energy of each normal mode to include rotation. They studied pentaerythritol tetranitrate (PETN) in depth using three types of theory. CASTEP calculations along with molecular mechanics calculations and PWscf [239] all predicted the observed spectrum with similar accuracy. Unlike the hydrogen bonded crystals studied before, it was found that some modes, and nearly all high frequency modes, had exclusively intermolecular vibrational character, especially those with B_2 symmetry.

The general finding herein is that modes are either based on intramolecular modes, as would be seen in isolation, though possibly shifted in frequency due to interactions in crystal form, or are indicative of intermolecular bonding and are not directly related to an intramolecular mode. This statement breaks down where extremely strong and significant hydrogen bonding

exists, such as is true in glutamic acid and aspartic acid, and especially in the case of small molecules such as 2-aminoisobutyric acid, alanine, and glycolaldehyde. In support of the above claim, such small amino acids are known to exist as zwitterions in solution and in crystalline solids, but not in the gas phase, demonstrating a large change to the structure and hydrogen bonding landscape of the molecules. Convergence to the crystalline structure was not found when performing a geometry optimization for an isolated system, and the molecules reverted back to an uncharged species. Therefore, the results generated from the frequency calculations are anticipated to be incorrect, as is observed. Even for some hydrogen bonded crystals the modes can be well-predicted by DFT calculations on the isolated monomer, however, correction with linear scaling correction factors is required because the calculated frequencies are always higher than measured. Some modes are not predicted and are thought to be only seen in the crystal form. While these modes may have intramolecular contributions, they are not allowed without the presence of the crystal and phonon-like motion and should be regarded as intermolecular in character.

3.6 Conclusions

The transitions studied here are of some relevance to astrochemistry, due to the sometimes small spectral shifts upon changes to the structure, such as being embedded in a matrix or put into the gas phase, as will certainly exist in interstellar ices. The appeal of these THz modes for astronomical observations is that they will be present in both the gaseous and solid state, and the icy grains will continue to emit in the far-infrared even at low temperature – no background source is required as is true for measurements of ices at infrared wavelengths. Finally, measurements on small to medium size molecules may be of significant help in identifying strongly anharmonic potentials amenable to coherent control experiments, especially in

the unambiguous demonstration of such important concepts such as ladder-climbing [77].

Chapter 4

Time-Resolved THz Spectroscopy

4.1 Introduction

Due to the pulsed nature of THz-TDS, it can be performed with respect to an impulsive electromagnetic excitation of the system, allowing for the study of changing optical properties on a femtosecond timescale. Time-resolved THz Spectroscopy (TR-THz) probes the ultrafast change to the THz optical constants or derived parameters as a function of time after the initiation of the change, typically caused by an electronically resonant optical excitation pulse. Experimentally, two time frames are relevant, the delay between optical excitation and the acquisition of the THz spectrum, and the delay between the THz pump pulse and optical gating pulse for THz detection, giving rise to a 2D scan. The data are commonly acquired by sweeping the THz delay line as a function of a fixed optical pump to THz peak signal time. Most commonly probed are semi-conductors, since the change in the broadband conductivity is often relatively large and thus involves a large change to the THz reflectivity.

4.2 GaAs

Low temperature grown gallium arsenide (100) was used as a test of the TR-THz setup. Initially, a pump beam was directed at the reverse side of the sample from the THz beam at a small angle to the direction of propagation of the THz beam due to ease of experimental

implementation and lack of an appropriate beamsplitter. Significant temporal broadening of the TR-THz spectrometer response function was observed. In a revised experimental set up, the beam was therefore directed at the same side of the sample upon which the THz beam was incident, again at a small angle. The time resolution was found to be better, but the ultra-fast carrier response was orders of magnitude longer than predicted. Lastly, the beams were co-propagated using a transparent ITO beamsplitter, and the temporal resolution was vastly improved, as can be seen in Figure 4.1. The reason for this is geometrical and is a function of the difference in incidence angle. The pump beam photoexcites a small portion of the sample at the leading edge of the pulse (and thus over a short time). The entire beam cross section is not excited until the pulse front has completely passed through the sample. Even a tilt of ~ 30 degrees for an 8 mm beam gives an artificial 13 ps spread to the measured response. Clearly, it is essential to ensure coincidence for accurate time-resolved measurements.

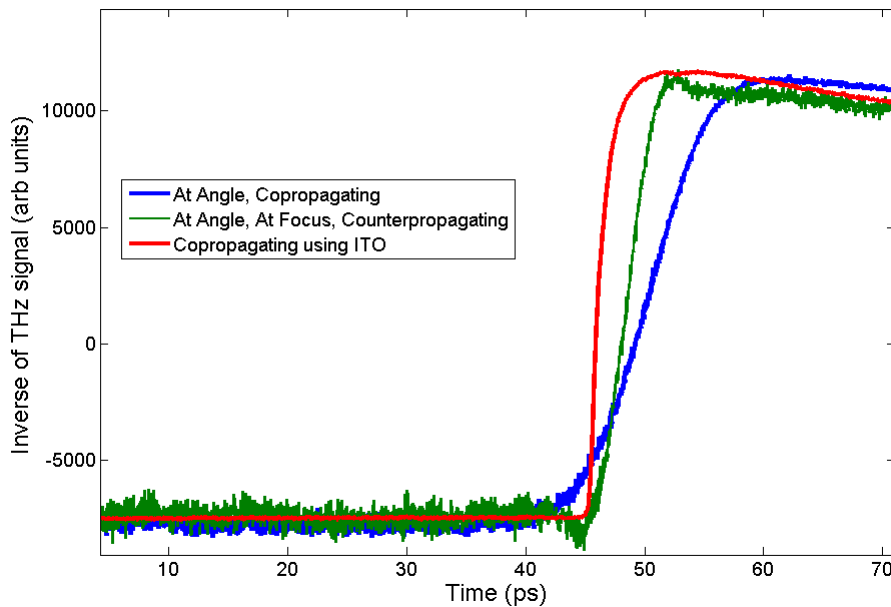


Figure 4.1: The measured change in THz signal, at peak intensity, as a function of pump-probe delay for low temperature grown GaAs illuminated under various experimental geometries. This demonstrates the importance of co-linear pumping for a true signal to be measured, even when the sample is at a THz beam waist.

4.3 Dye-Sensitized Solar Cells

Due to rapidly increasing energy demands, finite fossil fuel inventories, and environmental concerns, the development of cheap and efficient solar cells is topic of critical importance. Dye-sensitized solar cells (DSSCs) are a class of solar cell designed to be low in cost, because they use ubiquitous semiconductors derived from materials abundant in the earth's crust. However, in the standard design they typically only approach $\sim 10\%$ efficiency. This approach was first reported in 1991 [240] and DSSCs are often referred to as Grätzel cells, named after the author. Grätzel cells are typically made of thin films of a semiconductor, often mesoporous nanocrystalline titania, TiO_2 , followed by a layer of hole conducting electrolyte solution and an anode, with the cathode being a glass window coated with a thin layer of indium-tin oxide (ITO) [241]. The TiO_2 is sensitized by a dye that has an absorption band that is well matched to the solar emission spectrum and serves to inject charge into the TiO_2 conduction band. The dye is restored to its neutral state by a hole conductor in solution, which itself is regenerated at the counter electrode.

While much is known about the nanosecond to second scale dynamics of the system, the ultrafast charge excitation, the injection dynamics of the dye system, and the carrier mobility after injection are less well studied. These characteristics are thought to be important because charge transport can be problematic due to recombination at hopping sites or at surface defects near the dye molecules. While the most common dye, R-535 (Solaronix) or "N3" dye, had been studied [242], the full system has not been investigated, and the effect of changing dyes is not known. A long term goal of the TR-THz system was to work with the groups of Harry Gray and Nate Lewis to test out various dyes that had been synthesized to help enlighten future synthesis of better dyes. As a first step, the N3 dye was tested and some other dyes were ordered from Solaronix SA including Ruthenizer 620-1H3TBA, otherwise known as "black

dye,” which is one of the best dyes due to its very wide band-gap, which extends to 920 nm and thus allows photoexcitation at either 800 or 400 nm. Unfortunately, results using this dye were published in the meantime [243]. The results are largely the same, except that more carriers are injected into the TiO₂ per photon, but since the pump energy is not limiting, this change is not significant to the overall performance of the system. This is to be expected since the TR-THz response is only thought to be sensitive to the carriers in the TiO₂, and not to those in the dye, whose lifetime is expected to be much longer. Thus, changes to the structure of the titania give more noticeable changes to the observed response than do changes to the dye(s). Additionally, little work at Caltech is now performed on DSSCs, so the collaboration stopped with the graduation of Don Walker in 2010.

Dye-sensitized TiO₂ was successfully studied on two occasions in our lab. A thin layer of anatase nano-crystalline TiO₂ dissolved in paste with an organic solvent (Solaronix Ti-Nanoxide HT/SP) was deposited on a 1” z-cut crystalline quartz window using a screen printing-like technique, where the TiO₂ was forced through a polyester mesh. The TiO₂ was then baked for 30 minutes at 450° C, resulting in a sintered porous layer with an approximate thickness of 4 microns. It is estimated that the particle size is 8-10 nm, so the layer is quite transparent to visible light. The quartz and TiO₂ were allowed to cool to 120° C for two hours before being added directly to a solution of the N3 dye to avoid the absorption of water or other contaminants. It is important to keep the dye solution in the dark, or the dye rapidly degrades. The TiO₂ was allowed to sit in the dye solution for at least 1 day. In some cases the TiO₂ layer fell off of the quartz surface. To prevent this, the quartz was soaked in TiCl₄ solution before application of the nano-crystalline paste. It is also necessary to keep the dye free from oxygen when attached to the TiO₂ or the dye turns brown and becomes oxidized and does not function correctly. As such, the quartz window was placed in a demountable liquid cell (Harrick Scientific DLC-M25) with the dye/TiO₂ layer inside, separated from another quartz window by

a 1 mm teflon spacer. Dry nitrogen was flowed through the cell during scans.

At the end of scans, the area which was illuminated by the 400 nm pump light was observed to be clear and non-colored, as if the dye had been completely photo-bleached. This probably negatively impacted our signal levels. The THz probe-related delay line was fixed at the THz field maximum and the pump delay line was scanned. After 128 averages, the transient signal was only three to four times the noise level, amounting to a small fraction ($< 2\%$) of the total THz signal, and the signal could not be seen in a single scan due to large pulse-to-pulse source noise. It cannot be verified with certainty that the observed signal is fully impacted by the dye's presence, as TiO_2 has been shown to give a TR-THz response whose size is only $10\times$ less than that seen for the dye-sensitized case. However, our own studies on bare TiO_2 gave negligible signal, although the setup was not identical to that used for the DSSC measurements and less averaging was used.

The DSSC time-domain trace, presented in Figure 4.2, features a very rapid reduction in signal, due to THz reflection or absorption of the photo-generated carriers, followed by a relatively slow rise back toward baseline levels. The first drop takes place in approximately 400 fs and the slower rise is estimated to take place on the nanosecond to microsecond timescale. Interestingly, about 4 ps after the drop there is another bipolar feature. Initially this was assigned to reflections, but, in retrospect it more likely is due to a small THz signal generated by the 400 nm pump pulse in the sample or the quartz window. The trace was also measured in the cryostat at 20 K. No qualitative changes were observed at cryogenic temperatures, but these scans had even lower SNR due to a reduced signal (due to the cryostat windows) and added vibration of the sample, so no quantitative comparison could be made.

Black hydrogenated TiO_2 should be considered for testing in the future, as it shows great promise for solar cell and solar chemical applications [244] due to an increase in solar absorption and photocurrent density [245]. In order to increase the optical absorption under solar illumi-

nation, TiO_2 can be doped with metals, for example, to create donor and or acceptor states in the band gap and allow transitions that are typically not allowed. In light of this, hydrogen modification of the surface of nano-crystalline TiO_2 was performed to introduce disorder, but in such a way that the bulk properties of crystalline TiO_2 are retained. If this material forms suitable solar cells, it would be a vast improvement over DSSCs due to the simplicity of not having to use a solvent system to regenerate carriers and possibly improved stability with respect to oxidation. Some collaboration with the discoverers of this material has been started, but the amount of material provided is prohibitively small, does not appear black, but only light gray, and a non-destructive method of testing has not yet been established. It may be easier to hydrogenate TiO_2 layers after deposition as a means of testing if a hydrogenation chamber can be found on campus.

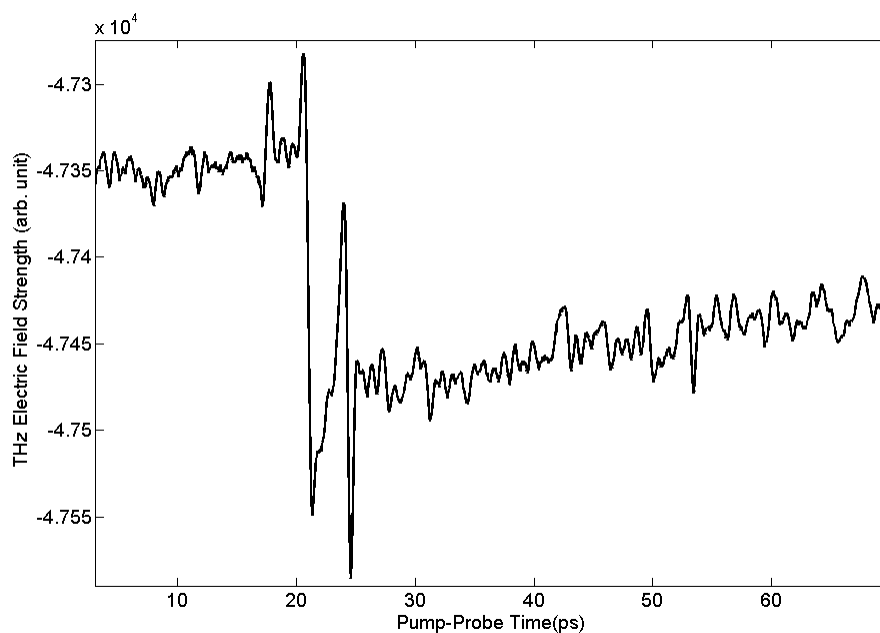


Figure 4.2: The measured change in THz signal, at peak intensity, as a function of pump-probe delay for dye-sensitized TiO_2 . The signal has been significantly smoothed using the Savitzky-Golay method, with care taken to maintain the same rise time and shape of the peak signal.

Chapter 5

Future Prospects

5.1 Introduction

This chapter is designed to serve as an outline and list of possible improvements and projects for future Blake group members. All of the ideas listed in this chapter are doable and most have been demonstrated previously.

5.2 Improvements to THz spectroscopy

For virtually all future experiments, there are a number of ways to improve upon the existing THz-TDS system. In particular, the THz dynamic range and SNR could use improvement for all future applications, and systematic tests of the THz detectivity should be the first priority. Better SNR would allow for faster acquisition times and more sensitive detection of small modulations to the THz signal for both TR-THz and THz-TDS or, minimally, for faster spectroscopic measurements and for the detection of weak emission, such as that from solvent reorganization around optically excited chromophores [246]. The most significant advances would come from single-shot, multi-channel, detection (Section 5.2.2) schemes in which the entire THz waveform is sampled on each regenerative amplifier pulse, so that the signal can be averaged at kHz repetition rates. Further advances would come from splitting off part of the THz beam and using it to normalize the detected THz waveform on a shot-by-shot basis. If

higher spectral bandwidth (or better temporal resolution) is desired, THz air based coherent detection can be employed.

In addition to improvements to the detection and THz pulse noise characteristics, the THz field should be increased to the maximum extent possible so that losses from optics or splitting and normalization can be more easily tolerated. Also, for coherent control and nonlinear spectroscopy purposes, the THz pump energy must be increased to the \sim MV/cm levels reported in the literature, likely via either two-color plasma techniques for frequencies above 3 THz (Section 5.2.3 or tilted pulse front (Section 1.1.3.3) or arrayed GaAs photoconductive antenna based generation with high bias fields [247], for spectroscopy below 3 THz. Possible implementations of these schemes are briefly discussed next.

5.2.1 Air-Based Coherent Detection

The interest in THz Air-Based Coherent Detection, or ABCD, stems from the desire to enable the phase sensitive detection of THz pulses at high frequencies. Indeed, extremely broad bandwidth detection (up to 200 THz) might be realized if the gating pulses are shortened to 10 fs and matched to a similar two-color plasma source [248]. While ABCD has been discussed previously in Sections 1.1.4.2 and 2.6, it has not yet been successfully implemented in the Blake labs. Since our first attempt, several important papers have been published [130, 249], including a successful demonstration of the technique by a group other than that of X. C. Zhang [250]. Additionally, Marco Allodi has visited with the Zhang group at Rochester to observe their implementation. The main problem observed previously, contamination of the signal from SHG, will remain and be difficult to deal with, but there are two possibilities to consider. First, an achromatic lens could be used to focus the probe beam through a hole in the parabolic mirror. This has the advantage that no additional optics are used that might produce SHG. This approach was used by Vieweg *et al.* and He *et al.* [130, 250]. An alternative is to use a

longer focal length parabolic mirror for focusing the THz beam so that there is more room for a pellicle beam splitter. This is the technique used by the Zhang group, and was successfully demonstrated for ESHG externally to the THz setup previously in our lab.

The biggest contribution to improved ABCD performance, however, will come from changes to the electrode geometry that maximize the SHG from the biased region. We will construct and employ “Christmas tree shaped” aluminum electrodes similar to that of reference [130] in order to better eliminate the Gouy phase shift-related degradation of the second harmonic signal (in addition to other phase matching conditions). This will give us a way to tune the optimal response of the system instead of being restricted by a specific focal length lens to fit with the wire electrodes that were available. For reference, He *et al.* used the following specific parameters: with all pulses polarized parallel to the applied electric field, the probe beam was focused by a 150 mm lens and passed through a hole in the focusing off-axis parabolic mirror. The stair-step electrodes were separated by 150 mm and had adjustable width between 1 and 6 mm with 1 mm increments. A bias voltage ± 1.5 kV was used with a duty cycle of 50%, and pulsed at 500 Hz. The ideal electrode width was found to be approximately 2 mm. Ideally, translation stages should be used for fine control of the electrode height, the width of the electrodes in the bias region, and their horizontal spacing.

5.2.2 Single-Shot Detection

For scans that do not require high spectral resolution, and thus long scans in the time domain, it may be most practical to detect the entire THz waveform at once [251–255] – especially with a plasma source, where fluctuations in the signal cause apparent noise when only one point is acquired for a given THz pump-optical probe delay. In one recent approach, the optical probe pulse is negatively chirped by a grating, causing a separation of the different frequency components of the pulse in time. The beam is then co-propagated through a detection crystal

and the THz signal appears as a modulation to the frequency spectrum of the pulse, which is detected by a monochromator and a CCD array [251, 252]. The main disadvantage to this method is that the spectral resolution is fundamentally limited by the time-frequency bandwidth uncertainty principle because the time-domain variations are effectively sensed in the frequency domain. The resolution is $\Delta T = \sqrt{T_c T_0}$, where T_c is the chirped pulse duration and T_0 is the unchirped duration. The pulse duration, and consequently bandwidth, of the probe pulse is thus quite important, along with the amount of chirp applied to the pulse.

Other techniques do exist, such as the use of dual echelons, right-angle prisms with a step-like structure that impart a variable delay to different spatial parts of the probe beam, thereby creating hundreds of “beamlets” which can be analyzed by a CCD camera [256]. Another technique uses an optical streak camera to spatially displace the probe beam onto a CCD as a function of time [257]. The latest implementation [254], which is conceptually similar to reference [251], uses a transmission grating tilted pulse in combination with well-optimized focusing optics in combination with detection in the crossed-Nichols arrangement or crossed polarizer method using a ZnTe (111) wafer [110] and a CCD camera. The drawbacks to this technique are that many corrections have to be made, and the signal is weak compared to normal optical rectification. For example, the frequency/intensity profile of the pulse is, of course, non-uniform due to the Gaussian-like nature of even an laser beam. Inhomogeneities in the beam and crystal exist in any real system, both of these effects cause the THz signal to drop away from the peak. Also, in the crossed-Nichols arrangement, the signal is nonlinear and must be adjusted, and compared to single temporal point detection schemes the field intensity is decreased since the beam is spread out in the detection crystal. Lastly, the resolution is decreased because of the above cited uncertainty relation, though since very short pulses are used this effect is thought to be minimized. Experimentally, when the spectrum of a lactose pellet was compared with standard THz-TDS results using photo-conductive dipole emitters

and detectors, many changes were noted, perhaps due to decreased signal-to-noise at high frequencies.

To summarize, the present approaches to single-shot THz detection are unfortunately riddled with distortions to the signal due to several fundamental challenges including inhomogeneities and synchronization of the THz and tilted probe pulses [258]. However, when the rapid acquisition of a low resolution spectrum is required or the pulse-to-pulse fluctuations dominate the SNR or dynamic range, single shot methods may be the best or only means of acquiring the necessary THz signatures.

5.2.3 OPA-Tuned Two-Color Plasma Emission

One of the most promising sources of high-field strength THz pulses is two-color plasma generated THz radiation (Sections 1.1.3.4 and 2.4.2). In a recent submission [101], Clerici *et al.* demonstrated exponential scaling of the THz energy when the wavelength of the generating pulses is increased. In fact, the THz yield scaled with a factor of $\lambda^{4.6}$! The maximum field strength was found at a fundamental wavelength of 1.8 μm (and so 900 nm second harmonic pulses), with the THz field estimated at 4.4 MV/cm for only 420 μJ of total pump energy [101]. This extremely steep increase with wavelength is predicted in the transverse photocurrent model [259].

Needless to say, we would like to take advantage of this discovery to better our spectrometer. The first piece of equipment needed is an optical parametric amplifier (OPA) to convert the 800 nm pump pulses to lower energy. Fortunately, we have started a collaboration with Professor David Hsieh's group at Caltech, and we will start initial experiments in this area with their ultrafast OPA. If successful, we can either buy one or build one (since little wavelength tuning is required). Ultrafast OPAs typically function in either type I or type II phase matching schemes. Both have advantages. Type II is more commonly used because the signal and idler

have opposite polarizations and can be easily separated from each other. The output is also narrower, but more consistent in bandwidth, which is often needed for spectroscopic studies [260]. Typically the designs feature a first type II OPA stage with a white light seed that is followed by another type II or type I stage to increase the output power dramatically [261, 262]. Type I OPAs deliver shorter pulses [263], albeit with a broader spectral profile that is not consistent as the output wavelength is tuned. Type I OPAs also feature more efficient interactions in the commonly used crystals, either β -BBO or BiBO, bismuth borate, BiB_3O_6 [260–262], but their output is not transform-limited. Operation at degeneracy has been shown to produce extremely broad emission that can be compressed to sub-2 cycle pulses, but the duration of the pulses at the output is unknown [264].

The preliminary experimental setup for testing will be deliberately simple, with THz average power measurements performed by a pyroelectric detector. The output of the OPA will be focused through a BBO crystal cut for Type I SHG at 800 nm ($\theta=29.02$ degrees) tilted at an angle to achieve phase matching at longer wavelengths. At 1.6 μm the desired cut angle is 20.66 degrees and at 1.8 μm the angle is 21.44 degrees. After considering Snell's law, the tilt angle should be approximately 14.5 degrees for phase matched propagation of both pulses. A silicon beam block will serve to eliminate the visible and near-infrared pump light so that the pyroelectric response is due only to the THz radiation.

5.2.4 THz Pulse-to-Pulse Noise Reduction

If the THz pulse energy is significantly increased via plasma generation techniques or by tilted pulse front optical rectification the pulse could be split using, for example, the reflection off the face of a high resistivity silicon wafer. In so doing, the THz dynamic range could be improved immensely. Even if the pulse energy remains the same, a THz quasi-optical detector [265] might be employed to sense pulse-to-pulse fluctuations in the THz light. Since the responsivity

is ≥ 100 V/W for this detector (VDI model WR0.65ZBD) and we have ~ 30 kW peak power, only a small fraction of the available pulse energy is necessary for high SNR measurements. While the responsivity is reduced above 1.7 THz, and the response time is slow compared to the duration of our pulses, the ability to normalize directly on the THz pulses themselves should significantly improve the quality of our data. We tested the above model with collaborators at the Jet Propulsion Laboratory, and saw very strong signal using a plasma source and an even stronger response using a tilted pulse front source. Further, these detectors can be run at room temperature and do not require tuning or bias, greatly simplifying their incorporation into the THz-TDS instrument.

5.2.5 Other Improvements

In this section, a list of ideas and areas of technology development are compiled. Most have been listed in the previous chapters of this thesis and are conceptually simple. Thus, we do not discuss them at length.

- Keep track of the progress of disk lasers using SESAM technology, since this architecture could soon replace the now fairly mature Ti:Sapphire-based designs because they have the potential to output higher average powers – to the point where optical-rectification and plasma based THz generation should become possible at MHz repetition rates. Additionally, most SESAM designs operate at longer wavelengths where phase-matching is significantly improved for OR and where two-color plasma THz generation scales at exponential rates.
- Test the large aperture ZnTe crystal for higher field strengths, especially for experiments below 3 THz.
- Pump GaP at higher optical powers for a more stable THz OR source up to 8 THz.

- Replace the separate EO detectors with a true balanced setup since the present devices are susceptible to electronic imbalance and non-ideal amplifier bandwidth. It is possible that we are throwing away the bulk of our signal because the detectors in use are too fast for the current amplifiers.
- Use trimethylamine or another low IP gas for TFISH detection.
- Interpolate acquired THz waveforms before averaging for an improvement in the determination of the optical constants. Think about means of absolute position markers with the delay lines (perhaps a white light fringe system).
- One relatively simple correction would be the correction of measured data to be representative of the true THz field strength. Equation 1.44 shows that this is very important when Γ is not small and the field strength is not linear with the detector signal. At the current maximum signal strength, the correction is on the order of 2% and may be significant (especially if the field strength is further increased).
- Employ THz waveguides or THz ATR for the study of solids.
- Reexamine glutamic acid and glycolaldehyde at higher frequencies and as a function of temperature.
- Future pellets should always be formed from recrystallized materials and ground for an extended period of time with mortar and pestle to limit line broadening and scattering of THz radiation.
- Create and test the ultrafast properties of black TiO₂ when pumped at 400 and 800 nm.

5.3 Future Experiments: THz Nonlinear Spectroscopy and Coherent Control

The future of far-infrared condensed phase spectroscopy will be performed using pulses with high-field strengths capable of exploiting nonlinear interactions. This spectral region, though notoriously hard to study and obtain meaningful results from, is thought to highlight modes essential to understanding many biochemically-relevant processes and solvent interactions. With well tailored pulses of controlled energy and phase, it may even be possible to almost completely control the population of states of said molecules coherently, which could enable the selective manipulation of large amplitude vibrations and control over reactions or biological processes. Even if neither of these is accomplished directly, it would provide a way of exploring the excited state potential landscape of the molecules. Nonlinear THz spectroscopy has been demonstrated a few times so far in simplistic quantum well systems [266–270] and slight coherent control has been seen in the form of ladder-climbing [77].

Nonlinear spectroscopy encompasses many possible techniques, and several have already been discussed in Section 1.1.2.4. Phase matching generally becomes more difficult at lower frequencies, however, due to the increased relative bandwidth of the pulses. Since $\Delta\nu/\nu$ is large and spans many octaves, the optical properties of materials often are not constant. Phase resolved detection, however is easier than in the optical and near-infrared regions of the spectrum due to the ease of directly sensing the electric field of radiation. 2D-THz spectroscopy, if realized, will be supremely useful for examining the true homogeneous line shape of biochemical and solvent interactions, where inhomogeneous broadening is quite limiting. The focus in the following section is on the spectrum of liquid water as a test case, but the analysis can equally be applied to solutions of proteins, DNA, or other systems of interest.

5.3.1 Two-Dimensional Far-Infrared Spectroscopy

Relaxation times for a variety of inter- and intramolecular motions can, in theory, be measured spectroscopically by virtue of the homogeneous linewidth of the relevant transition, Γ , where

$$\Gamma = (2\pi t_1)^{-1} + (\pi t_2)^{-1}. \quad (5.1)$$

Here, t_1 is the population decay time (relaxation) and t_2 is the 'vibrational' dephasing time [271]. Indeed, prior to the development of picosecond class lasers, and femtosecond class lasers for water, the vibrational dephasing time was measured from the linewidth of isotropic Raman linewidths [272]. Unfortunately, linear spectroscopies often demonstrate line shapes that are a convolution of both homogeneous and inhomogeneous contributions. With respect to vibration, the inhomogeneous contribution is thought to arise from a variety of differing local environments, whereas the homogeneous contributions arise from rapid interaction with the surrounding bath [273]. In this regard, liquids and solvated systems are poorly understood; they have both a broad distribution of local configurations and the ability to interconvert and interact on time scales spanning orders of magnitude, hence the distinction between homogeneous and inhomogeneous broadening may not be meaningful. However, multi-dimensional spectroscopy experiments have begun to breach this distinction. Indeed, much of what is experimentally known about the ultrafast dynamics of such systems stems from the ability of relevant spectroscopies to distinguish between the inhomogeneous and, notably and more relevantly, the homogeneous broadening of spectral features.

Perhaps the most relevant method for studying chemical systems and solvent interactions is 2D-IR, and for this reason it will be reviewed in detail. In the pioneering paper by Tanimura and Mukamel, these authors only briefly touched on the possibility of using infrared pulses to directly study dipole interactions, since, in 1993, ultrafast infrared spectroscopy was in its infancy.

Such experiments, while much simpler than the Raman processes due to the fundamentally much larger cross sections and the requirement of fewer pulses, were not feasible [273]. This treatment has since been extended to the THz range [274, 275]. The 2D-IR technique relies on the vibrational photon echo effect, which is semi-analogous to the spin echoes of 2D-NMR spectroscopy, but which probe dynamics on a much shorter time scale [276]. The photon echo effect necessarily entails a two-pulse sequence, but in practice a third pulse is used and will be considered here. Each pulse has a similar spectrum and power. The first pulse in the sequence excites a coherent superposition of the transition of interest in the sample, i.e. a superposition of the vibrational ground state and first excited state. At this point, the molecular vibrational modes in the excited area all oscillate in phase. The second pulse, at time τ_1 , serves to store the phase information imparted by the initial pulse as a patterned population of the ground and excited states. In practice, ultrashort pulses are used and by virtue of their inherently broad bandwidth, many transitions may be involved.

After a waiting time, τ_2 , the third pulse serves to initiate a rephasing of the oscillators. This time scale, τ_2 , serves as the relevant time frame for the experiment. The sample thus regains a macroscopic polarization and oscillating dipole due to the rephasing of the microscopic dipoles as patterned by the first pulses. Light is re-radiated at time τ_3 , as described by Maxwell's equations. This light is referred to as the photon echo. Detection of this pulse is enabled by spatial selection, made possible by the differing input angles of each previous pulse to the sample, but in the far-infrared, or even in modern mid-IR techniques, a collinear scheme can be realized [266, 267, 277]. This changes the experiment and relies on modulation of all pulses and combination of pulse pairs detected by lock-in detection. While this causes the subsequent data analysis to be more difficult, since the electric field of each pulse is measured directly, the phase, amplitude and frequency spectrum are directly accessible, and complex, or even incorrect, phasing procedures common to 2D-IR are not required [267]. Additionally, the

signal is stronger than the non-phase matched case due to a longer region of interaction in the sample as phases are matched over a greater physical and hence temporal region in the collinear geometry. Not only is the signal stronger, but the signal-to-noise ratio is vastly improved due to the 2D Fourier transform used in the collinear geometry which serves to decouple the noise along the two different frequency axes. The signal contains both the photon echo four-wave mixing signals as well as a pump-probe signals, each of which can be separated by isolation in the frequency domain.

Typically the data are presented as a three-dimensional plot with two frequency axes. One axis of the spectrum is commonly generated via optical heterodyne detection of the photon echo signal by mixing with a local oscillator, or LO, consisting of a small portion of the pump beam radiation propagating along the same path as the photon echo signal. The interference of these pulses is then dispersed in a monochromator and detected with an array of IR detectors, commonly mercury cadmium telluride (MCT). This gives both phase and frequency information. The other relevant frequency axis is generated as a result of a numerical Fourier transform of time domain data collected by recording the signal at each monochromator frequency as a function of τ_3 . The relative polarization of pulses one and two can be varied externally to probe orientation dependent phenomena, however, the focus is often rather on changes to the spectrum with time [278]. In the proposed THz analog EO detection with colinear phase matching will be used, as discussed previously. The same spectral information can be acquired and plotted.

In order to circumvent the extreme optical depth of many samples of interest, including those in aqueous solution, a very thin sample is required. A nanofluidic sample cell that provides a 500 nm thick layer of sample between two 800 nm thick Si_3N_4 windows has been previously employed [279]. This corresponds to an optical depth (OD) of 0.2 in water. At 600 cm^{-1} or $\sim 18\text{ THz}$, the molar extinction coefficient of water at $25\text{ }^\circ\text{C}$ is $\sim 25\frac{\text{L}}{\text{mol cm}}$, or ~ 4 times less

than at 3400 cm^{-1} [280], so a four times thicker sample should be used.

5.3.2 Coherent Control

Coherent control of chemical and physical processes has been dreamed of since the invention of the laser [281]. The possibility of selectively exciting a specific molecular motion, such as a vibration, to the point of breaking a bond – that is, of adding energy to the system in a non-thermodynamic way – affords tremendous possibilities for chemical synthesis. Such prospects include: achieving products that are not normally produced when considering the associated thermodynamics and kinetics, increasing selectivity, the production of extremely pure products with high yield, and isotope separation. Such control also serves as a means of “motion control” on very small length scales since vibrations are commonly modified. Control of biological molecules could have tremendous implications for drug design and production or for drug delivery and activation. Unfortunately, CW or even nanosecond duration pulsed lasers, for the most part, have no effect on chemistry, due to lack of selectivity, rapid intermolecular vibrational energy redistribution, and the relatively low power of the lasers commonly used.

Ultrafast lasers with femtosecond (fs) duration have shown some ability to control vibrational state populations, but complete control has been evasive due to lack of selectivity or incomplete population transfer. For example, one of the most studied fs methods of optimizing chemistry or optical processes, such as high-harmonic-generation and multi-photon absorption, is optical pulse shaping via genetic algorithms designed to adaptively identify regions of control [50]. Unfortunately, in most cases, the maximum transfer or control cannot be extended beyond that provided by a transform limited pulse. This was studied exhaustively by the group of Dantus in the case of molecular fragmentation using shaped pulses [282]. In other cases, where complete control has been demonstrated, the experiment or system becomes quite complicated, often requiring many lasers operating at different frequencies with pulses delivered to

the sample at varying times. While there are many ultrafast methods of molecular coherent control [50, 283], here it is the single pulse regime that will be described in further detail.

In the radio and microwave frequency regions of the spectrum, full population transfer from one state to another can easily be achieved due to the possibility of synthesizing a π pulse [50, 284], and is readily seen in NMR because spin-relaxation is slow and Rabi oscillations are relatively undamped. This control extends even to the weak field limit [285]. However, such pulses, which are often sinusoidal square waves, are not produced by lasers and cannot be extended deeply into the THz region or beyond. Recently theorists have begun to examine the possibility of population control in the sub-single optical cycle limit, where pulses have characteristics similar to square pulses due to their non-standard envelope [285–290]. When the resonance frequency sufficiently exceeds the carrier frequency, near complete control or inversion of the population can be obtained in a two-level system (2LS) with sufficient field strength [286]. In the optical and near- to mid-infrared regions of the spectrum, pulses of sub-single cycle duration cannot be produced due to limitations of current lasers and the intrinsically short duration of a single cycle of radiation at such wavelengths. In THz-TDS, “half-cycle” pulses are routinely generated. From a technical standpoint, 1-10 THz is the highest frequency window in which sub-cycle pulse durations are currently accessible. Additionally, both generation and detection methods are intrinsically phase sensitive since the electric field is directly probed, most commonly by EO sampling. Relative to the optical, this affords simplicity since neither carrier-envelope phase, CEP, stabilization nor heterodyne detection is required due to the intrinsic phase stability of the THz radiation and the phase sensitive detection commonly employed. Until recently, the limiting factor has been the field strength of the THz radiation, but by various measures discussed previously in this chapter, the situation is improving dramatically.

Beyond the lack of a source with high field intensity, one of the biggest challenges to using THz radiation to coherently control processes is the lack of optics or methods to control

radiation. Thus, the pulse shaping methods which have been invaluable to coherent control methods in the optical and infrared regions of the spectrum are not feasible. Optics design is quite difficult because there are no known materials with high dispersion and low absorption and broadband coverage in the THz regime (0.3-3 THz). Notably, this renders optical elements such as waveplates and prisms ineffective. The only means of THz pulse shaping is then by direct optical to electronic means, in which the optical pulse envelope is transformed into the THz pulse electric field in one of the conventional THz generating methods.

Since many vibrations involving large-amplitude motions fall near the THz spectral region, the systems of interest are vast, especially in large biological molecules. An appropriate choice of test systems is thus important. Ideally, a condensed phase biological system that has very intense bands in the THz region will eventually be controlled, however sample homogeneity and preparation is difficult and the presence of water as a solvent makes delivering strong THz pulses to the sample difficult. Crystals of various amino acids and sugars show intense THz bands and have shown promise in ladder-climbing [291]. However, due to line-broadening, a nearly harmonic potential, and the low resolution of THz-TDS, the individual transitions in the ladder are unresolvable. Hence, a system with greater anharmonicity and lower intrinsic linewidth is sought. Some such systems are the ring-puckering vibrational modes of certain pseudo four- or five-member ring molecules in the gas-phase, which show appreciable far-infrared intensity and are spectrally well separated and easily able to be resolved via THz spectroscopy. Another point of interest is that the potentials of this type of system are often quartic. Thus, the energy difference between successive levels increases, at least to a point, as opposed to reaching a quasi-continuum.

Experimental verification of the importance of pulse shape, intensity, and phase in the single pulse limit was examined in experiments using 100 MHz radiation to control the population of K atoms in a two-level system [284] via Rabi oscillations. The basis of this work was the

Table 5.1: Predictions for Ring Puckering Modes

Molecule	Highest Level of Theory	Scaled (cm^{-1})	Frequency	Experimental quency (cm^{-1})	Fre-	Intensity (km/mol)
cyclobutanone	CAM-B3LYP/cc-pVQZ	5.3		35.3		4.28
1,4 dioxin	CAM-B3LYP/AUG-cc-pV5Z	73.4		66.8		15.5
trimethylene oxide	CAM-B3LYP/AUG-ccpV5Z	53.2		53.4		4.45
trimethylene sulfide	CAM-B3LYP/cc-pVQZ	144.6		138.3		1.41
1,4 oxathiene	CAM-B3LYP/AUG-cc-pV5Z	106.4		Unknown		9.05

Predicted frequency and intensity of the lowest frequency bands for several gas phase molecules with restricted ring systems. All calculations were done by the author.

breakdown of Floquet theory. Floquet theory relates to ordinary differential equations. If a system of linear differential equations has the form

$$\dot{x} = A(t)x, \quad (5.2)$$

where $A(t)$ is a periodic function, Floquet's theorem allows transformation of the periodic system to a linear system. This theory works well when the pulses are *sinc*-like, with appreciable rise and fall time with respect to the inverse carrier frequency. In order to test the applicability to other situations, an experiment was designed in which K atoms are excited to the $21s$ state near the forbidden crossing with the $19f$ state. A phase, frequency, and rise-time controlled RF pulse was then delivered to the system to drive it to the upper state, followed by a field-ionization pulse with energy sufficient to ionize only the $19f$ state. Thus, after ion-sensitive detection, the population of the excited state could be monitored. When the rise-time of the microwave control pulse is lowered to be comparable to the single-cycle time, the frequency spectrum begins to develop a strong phase dependence. This spectrum change can thus have a strong effect on the system, the most clear demonstration of which can be seen when comparing the response of the system to 10 cycle pulses of phase $\phi = 0$, 6.3-ns rise time, to identical pulses with a 1.5-ns rise time. Similar phenomena are expected for sub-cycle ultrashort pulses, due to the non-sinc like pulse shape and high intensity, as will be discussed in the following section.

Uiberacker and Jakubetz have theoretically examined a phenomenon called strong-field dipole resonance [286] and its application to coherent control. When sub-cycle pulses are used to excite many-level systems, population transfer can occur within a fraction of the optical cycle. Typical considerations such as the carrier frequency, detuning, and the average population over field oscillations have significantly less importance, or can be entirely neglected when a sufficiently short pulse is considered. The concepts relevant to strong-field dipole resonance are the CEP and the interaction of the pulse with permanent or induced dipole moments. Particularly important is the the sign of the projection of the electric field onto the difference of permanent dipole moments of the involved states [287, 288]. Beyond the breakdown of Floquet theory, as described in the previous section, short, strong pulses cause the rotating wave approximation to break down, in that the rapidly oscillating terms in the Hamiltonian describing the system cannot be neglected and the CEP becomes important [285], especially at short times.

The rotating wave approximation relies on the fact that $\Delta = \omega_L - \omega_0 \ll \omega_L + \omega_0$, where ω_L is the carrier frequency of the exciting light pulse, and ω_0 is the transition frequency. Since the frequency spectrum of a sub-cycle pulse with carrier frequency ω_0 is broadened and blue-shifted with respect to a pulse with duration greater than 1 cycle, the detuning frequency, Δ , can become appreciable with respect to the sum. See Figure 5.1 for an example. Uiberacker and Jakubetz examined cases in which the Hamiltonian in the strong field limit can be approximated by non-time-ordered integrals. They discovered two detuned regimes of note, one in the limit of rapid variation of the field, $\max_{\{k,l\}} |\Delta\epsilon_{kl}| \ll |\Omega_{min}|$, where the highest frequency relative to the energy level difference of the system, $\max_{\{k,l\}} |\Delta\epsilon_{kl}|$, is small with respect to the minimum frequency component of the electric field, Ω_{min} ; and one in the limit of a slowly varying field, where $\min_{\{k,l\}} |\Delta\epsilon_{kl}| \gg |\Omega_{max}|$. In the rapidly varying field limit, not only was it found that the population dynamics cannot be controlled by the sign of the electric field, but also that

no population transfer can be achieved. However, in the slowly varying field limit, population dynamics were found to be related to a resonance that originates from the diagonal matrix elements of the coupling, resulting in a strong dependence on the sign of the electric field of the pulse with respect to the relative dipole moment difference. This allows for a method of state population control by changing the phase of the applied pulse.

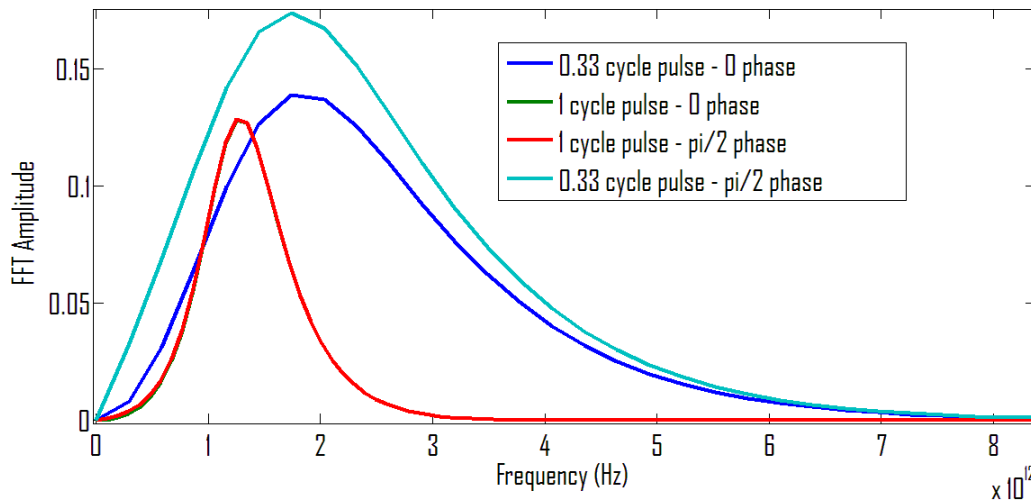


Figure 5.1: Simulation of the FFT amplitude spectrum of pulses with a carrier frequency of 1.2 THz for varying duration and phase.

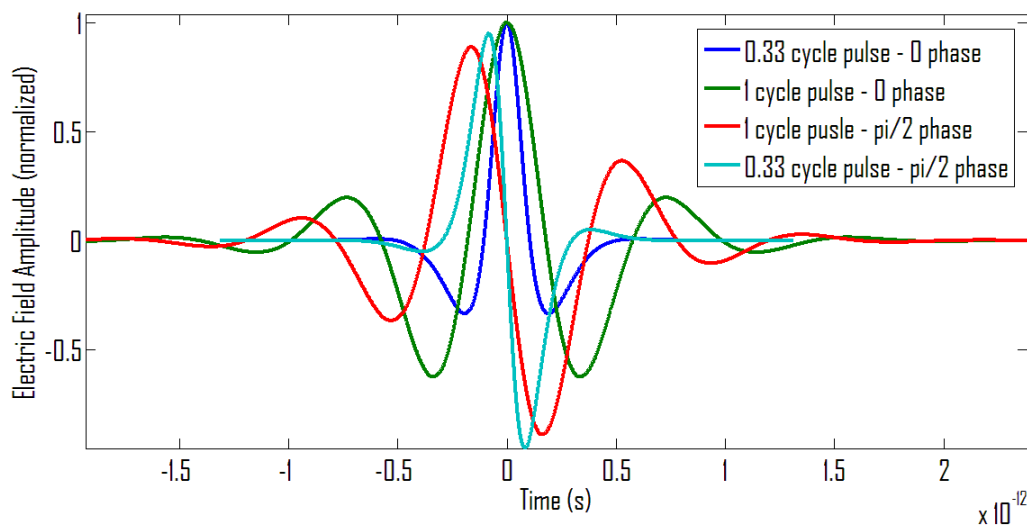


Figure 5.2: Simulation of the time domain waveforms of pulses with a carrier frequency of 1.2 THz and varying duration and phase.

Došlić is one of the first to theoretically pick up this thread and apply the theory of strong-

field dipole resonance to a real system [289, 290]. As opposed to either of the limits discussed in the previous section, Došlić considered the intermediate case, which featured only moderate detuning of the field from the resonance of interest. The system studied, acetyl acetone (ACAC), is a model for symmetric intramolecular hydrogen transfer. Based on a previously studied potential energy and dipole moment surface [292], the potential energy surface shows a double well symmetry which splits all the associated vibrational levels. The lowest frequency transition, $\omega = (0^+ \leftarrow 0^-)$, was calculated to be 3.5 THz. Based on the frequency shift of a sub-cycle pulse with respect to its carrier frequency,

$$\delta = \omega \left(1 - \frac{1 + m_c^2 \pi^2}{\sqrt{3 + 4m_c^2 \pi^2 + m_c^4 \pi^4}} \right), \quad (5.3)$$

where $m_c^2 = n_c / \ln(2 + \sqrt{3})$, and n_c is the number of cycles, a third of a cycle pulse with carrier frequency 2.34 THz is desired.

In the few- to sub-cycle pulse limit, either the number of cycles or the pulse duration can be fixed. Since control is not found in the weak field limit, the THz field strength must be sufficiently high. Considering a case where the number of pulses is fixed to $n_c = 0.33$, the maximum population transfer with a single pulse is 89 percent into the desired state. This corresponds to a frequency of 2.1 THz and a peak electric field of 0.00042 a.u., or 2.16 MV/cm. Also of note here is the decreased field requirement of a sine, $\phi = (\pi/2, 3\pi/2)$, as compared to a cosine, $\phi = (0, \pi)$ pulse. This is due to the increased fluence of a sine sech-shaped pulse over a cosine pulse given the same native field strength. Figures 5.1 and 5.2 depict the change to the frequency and intensity and time-domain waveform as a function of n_c . However, compared to the strong phase selectivity theorized by dipole resonance in the slowly varying field limit, there is very little dependence on phase.

Also of note are regions of control at lower frequency and higher field strength. Although

currently these are inaccessible due to experimental limitations, they begin to show phase sensitivity, which demonstrates a move from frequency driven control to dipole driven control, where the energy levels of the transition of interest are matched in the first case, and impulsive excitation dominates in the second – causing a rapid tuning of the energy levels of the system to those of the applied field. When the pulse is limited to 750 fs duration, the duration of a 0.33 cycle pulse at 2.3 THz, and the pulse frequency left to vary, there is a large area of relatively frequency independent control for cosine pulses, demonstrating the strong dependence on envelope function and not the carrier wave frequency. Lastly, Došlić showed that population could be further controlled by using a more optimum waveform consisting of two superposed pulses, one at frequency 2.3 THz and the other, at a later time, at frequency 4.5 THz. The second pulse serves to remove population from the higher state. The total population of the target state then became 98 percent. This shows the potential for more complicated pulse sequences in tightly controlling the target state populations.

One of the problems with ACAC as a system is that the $\omega(0^+ \leftarrow 0^-)$ transition has never been experimentally observed, and is theorized to be a very weak[292]. Not only might the transition be too weak to observe with a reasonable path length, detection would be difficult without resorting to ionization based schemes, which add unneeded complexity to the experiment. Another difficulty arises due to the frequency separation of the $\omega(0^+ \leftarrow 0^-)$ to the $\omega(1 \leftarrow 0^+)$ components. Instead, ring-puckering modes of a 4-, 5-, or 6- member ring system in the gas phase are more optimal. Many molecules have been studied, and several have strong spectra in the far-infrared [15, 293–296]. Not only are the spectral features intense, some systems show very well spaced Q-branches in the vibrational progression. Most show quartic potentials, however, and thus have higher energy spacings between successive levels.

To examine the feasibility of coherent control on such systems, the lowest vibrational mode of various possible molecules was simulated at various levels of theory. Of the molecules tested,

1,4-dioxin had the greatest intensity of its lowest frequency ring puckering mode at 15.5 km/mol. Given that this does not factor in the anharmonic nature of the potential [15], the intensity was divided by 10 to approximate the 10 anharmonic components seen in the spectrum. Given an estimated linewidth of 3 cm^{-1} and a maximum achievable pressure of 85 torr at room temperature, the total absorbance, $\log_{10} \left(\frac{I_0}{I} \right)$, is 0.2/cm of path length. This makes all of the transitions quite visible in common cell lengths for THz spectroscopy, $\sim 10 \text{ cm}$, at moderate pressures. See Table 5.1 for a list of all molecules examined. The Hamiltonian for ring puckering can be given by a one-dimensional Hamiltonian

$$H(x) = T(x) + V(x) = \frac{-\hbar^2}{2\mu} P_x^2 + bx^2 + ax^4, \quad (5.4)$$

where x is the ring-puckering coordinate in Angstroms. A fit of spectral data to the above Hamiltonian gives

$$V(x) = 2.949 \times 10^4 x^2 + 2.930 \times 10^6 x^4, \quad (5.5)$$

where $V(x)$ is in cm^{-1} .

5.3.2.1 Pulse Shaping

Optical pulse shaping (Section 1.1.2.3) has been extended all the way out into the mid-infrared using gratings and a Ge AOM [297]. However, extending to even longer wavelengths has many challenges. Although THz AOMs can be constructed [298, 299], the THz spectrum is difficult to disperse evenly. Gratings only function over less than an octave of bandwidth, whereas most THz pulses cover many octaves. Prisms can be made to operate over a much larger range, if a transparent material with appreciable dispersion can be obtained [52]. Unfortunately, in the THz region, materials generally either have very low dispersion, or strong absorption. A spectrometer based on a CsI prism cooled to 25 K has been demonstrated, but even at 10 K,

α is $>3 \text{ cm}^{-1}$ at 1 THz [300] and high electric fields cannot therefore be maintained.

Since optical methods are unavailable for THz pulse shaping, the alternative is optical to electronic conversion, wherein an optical pulse shaper is used to tailor the envelope shape of an optical pulse, which is then used to generate THz radiation. This was first demonstrated using antennas [301] and has been since demonstrated for optical rectification [302] and plasma sources [303–305] as well. Combinations of sinusoidal and triangular phase modulation can be used to create narrowband THz radiation free from spectral modulation [306]. Unfortunately, all of the above methods presently generate pulses of insufficient strength to enter a regime of significant coherent control. Very recently, however, control of the THz spectrum was demonstrated using tilted pulse front generation in lithium niobate [81]. The method used was the “chirp-and-delay” method, in which two chirped pulses are delayed with respect to each other and recombined to give a quasi-sinusoidal optical intensity modulation, which can be transferred to the THz pulse. In principle, an optical pulse shaper would allow for similar optical field modulation to that provided by the chirp-and-delay method; but with access to more complicated phase patterns, the THz pulse itself should be able to be semi-arbitrarily shaped or chirped, allowing for another mode of control.

5.3.2.2 Ladder Climbing

Ladder-climbing in a vibrational potential energy surface is usually not feasible with CW lasers. Ultrashort pulses with duration shorter than the IVR timescale can cause ladder-climbing even in anharmonic potentials, due to the large bandwidth associated with such pulses arising from the energy-time uncertainty relation. However, ladder-climbing can be significantly optimized or controlled by changing the frequency chirp of the pulse. This was demonstrated in simple gas phase systems relatively early on [307], but control even in condensed phase has been demonstrated [308, 309], where competition of ladder-climbing with energy dissipation processes

is extremely important. In optimizing the cleavage of CO from the ground state of chromium hexacarbonyl at 2000 cm^{-1} , for example, an increase of up to two orders of magnitude was found by adjusting the chirp of the excitation pulse [308]. Similar qualitative results have also been demonstrated in carboxyhemoglobin, a large biological system in the liquid phase, although quantitative measurement of the extent has been elusive [309].

Jewariya *et al.* [291] demonstrated the first and to date only evidence of ladder climbing initiated by a THz pulse. This was observed due to a red shift of the absorption spectrum with increasing peak THz electric field strength. Since the potential is Morse-like, the higher energy levels are more closely spaced than the bottom levels. Thus, as higher levels are populated, on average, the absorption spectrum redshifts. The higher states can be populated by increasing the temperature or by using a strong laser pulse. Additionally, the optical depth (OD) was observed to decrease as a function of the THz field strength, further demonstrating the onset of nonlinear behavior. GABA might be a better system for this type of demonstration due to the extremely large anharmonicity in a mode below 1 THz. It also might likely benefit from a chirp of the stimulating pulse to match the observed anharmonicity.

Bibliography

- [1] H. C. Urey, “On the Early Chemical History of the Earth and the Origin of Life”, *Proc. Natl. Acad. Sci. U. S.*, **38**, 351–363 (1952).
- [2] S. L. Miller, “A Production of Amino Acids under Possible Primitive Earth Conditions”, *Science*, **117**, 528–529 (1953).
- [3] J. F. Kasting, “Earth’s Early Atmosphere”, *Science*, **259**, 920–926 (1993).
- [4] C. Chyba and C. Sagan, “Endogenous Production, Exogenous Delivery and Impact-Shock Synthesis of Organic Molecules: An Inventory for the Origins of Life”, *Nature*, **355**, 125–132 (1992).
- [5] V. authors, *List of Interstellar and Circumstellar Molecules*, (2012) http://en.wikipedia.org/wiki/List_of_interstellar_and_circumstellar_molecules.
- [6] J. Cami, J. Bernard-Sala, E. Peeters, and S. E. Malek, “Detection of C₆₀ and C₇₀ in a Young Planetary Nebula”, *Science*, **329**, 1180–1182 (2010).
- [7] C. F. Chyba, P. J. Thomas, L. Brookshaw, and C. Sagan, “Cometary Delivery of Organic Molecules to the Early Earth”, *Science*, **249**, 366 (1990).
- [8] P. F. Bernath, *Spectra of Atoms and Molecules* (Oxford University Press, 2005).
- [9] M. L. Radhuber, J. A. Kroll, and S. L. Widicus, *Reaching the Line Confusion Limit: Analysis of the $\lambda=1.3$ mm Spectrum of Orion-KL*, International Symposium on Molecular Spectroscopy, 66th Meeting, (2011) adsabs.harvard.edu/abs/2011mss.confEFA05R.

- [10] T. Bergin, F. De Lucia, P. Goldsmith, H. Hasan, E. Herbst, G. Melnick, and J. Pearson, *Report from the Workshop on Laboratory Spectroscopy in Support of Herschel, Sofia, and ALMA*, (2006) <http://www.submm.caltech.edu/labspec/Workshop%20Report%20Final.pdf>.
- [11] H. Andernach, *Internet Resources for Radio Astronomy*, (1999) <http://ned.ipac.caltech.edu/level5/March01/Andernach/Ander2.html>.
- [12] N. R. Crockett, E. A. Bergin, S. Wang, D. C. Lis, T. A. Bell, G. A. Blake, A. Boogert, B. Bumble, S. Cabrit, E. Caux, C. Ceccarelli, J. Cernicharo, C. Comito, F. Daniel, M.-L. Dubernet, M. Emprechtinger, P. Encrenaz, E. Falgarone, M. Gerin, T. F. Giesen, J. R. Goicoechea, P. F. Goldsmith, H. Gupta, R. Güsten, P. Hartogh, F. Helmich, E. Herbst, N. Honingh, C. Joblin, D. Johnstone, A. Karpov, J. H. Kawamura, J. Kooi, J.-M. Krieg, W. D. Langer, W. D. Latter, S. D. Lord, S. Maret, P. G. Martin, G. J. Melnick, K. M. Menten, P. Morris, H. S. P. Müller, J. A. Murphy, D. A. Neufeld, V. Ossenkopf, J. C. Pearson, M. Pérault, T. G. Phillips, R. Plume, S.-L. Qin, P. Roelfsema, R. Schieder, P. Schilke, S. Schlemmer, J. Stutzki, F. F. S. van der Tak, A. Tielens, N. Trappe, C. Vastel, H. W. Yorke, S. Yu, and J. Zmuidzinas, “*HERSCHEL* OBSERVATIONS OF EXTRAORDINARY SOURCES (HEXOS): THE TERAHERTZ SPECTRUM OF ORION KL SEEN AT HIGH SPECTRAL RESOLUTION”, *Astronomy and Astrophysics*, **521**, L21 (2010).
- [13] S. L. Dexheimer, ed., *Terahertz Spectroscopy* (Academic Press Inc., 2008).
- [14] M. C. Beard, G. M. Turner, and C. A. Schmuttenmaer, “Terahertz Spectroscopy”, *J. Phys. Chem. B*, **106**, 7146–7159 (2002).
- [15] T. M. Hard and R. C. Lord, “A Double Beam, High Resolution Spectrometer for the Far Infrared”, *Appl. Optics*, **7**, 589–598 (1968).

- [16] P. B. Fellgett, “On the Ultimate Sensitivity and Practical Performance of Radiation Detectors”, *J. Opt. Soc. Am.*, **39**, 970–976 (1949).
- [17] P. R. Griffiths and C. Homes, “Instrumentation for Far-infrared Spectroscopy”, in *Handbook of Vibrational Spectroscopy* (2006), S0207.
- [18] J. H. Booske, R. J. Dobbs, C. D. Joye, C. L. Kory, G. R. Neil, G. Park, J. Park, and R. J. Temkin, “Vacuum Electronic High Power Terahertz Sources”, *IEEE Trans. THz. Sci. and Tech.*, **1**, 54–75 (2011).
- [19] E. R. Mueller, “Widely-Tunable Laser-sideband THz Source for Spectroscopy and LO Applications”, in Space Terahertz Technology Symposium (2001).
- [20] E. R. Mueller, *Optically-Pumped THz Laser Technology*, (2012) <http://www.coherent.com/downloads/OpticallyPumpedLaser.pdf>.
- [21] B. S. Williams, “Terahertz Quantum-Cascade Lasers”, *Nature Photonics*, **1**, 517–525 (2007).
- [22] R. Köhler, A. Tredicucci, F. Beltram, H. E. Beere, E. Linfield, A. G. Davies, D. A. Ritchie, R. C. Iotti, and F. Rossi, “Terahertz Semiconductor-Heterostructure Laser”, *Nature*, **417**, 156–159 (2002).
- [23] S. Kumar, “Recent Progress in Terahertz Quantum Cascade Lasers”, *IEEE J. Sel. Top. Quant. El.*, **17**, 38–47 (2011).
- [24] Q. Qin, B. Williams, S. Kumar, J. L. Reno, and Q. Hu, “Tuning a Terahertz Wire Laser”, *Nature Photonics*, **3**, 732–737 (2009).
- [25] M. S. Vitiello and A. Tredicucci, “Tunable Emission in THz Quantum Cascade Lasers”, *IEEE Trans. on Terahertz Sci. and Tech.*, **1**, 76–83 (2011).
- [26] C. Gmachl, “A Wrench of Wavelength”, *Nature Photonics*, **3**, 683 (2009).

- [27] Q. Wu and X. C. Zhang, “Ultrafast Electro-Optic Sensors”, *Appl. Phys. Lett.*, **68**, 1604–1606 (1996).
- [28] Q. Wu and X. C. Zhang, “7 Terahertz Broadband GaP Electro-Optic Sensor”, *Appl. Phys. Lett.*, **70**, 1784–1786 (1997).
- [29] J. Hebling, K. L. Yeh, M. C. Hoffmann, B. Bartal, and K. A. Nelson, “Generation of High-Power Terahertz Pulses by Tilted-Pulse-Front Excitation and Their Application Possibilities”, *J. Opt. Soc. Am. B*, **25**, B6–B18 (2008).
- [30] K. Y. Kim, A. J. Taylor, J. H. Glowina, and G. Rodriguez, “Coherent Control of Terahertz Supercontinuum Generation in Ultrafast Laser-Gas Interactions”, *Nat. Photon.*, **2**, 605–609 (2008).
- [31] P. B. Petersen and A. Tokmakoff, “Source for Ultrafast Continuum Infrared and Terahertz Radiation”, *Opt. Lett.*, **35**, 1962–1964 (2010).
- [32] D. J. Cook and R. M. Hochstrasser, “Intense Terahertz Pulses by Four-Wave Rectification in Air,” *Opt. Lett.*, **25**, 1210–1212 (2000).
- [33] J. Liu and X. C. Zhang, “Terahertz-Radiation-Enhanced Emission of Fluorescence from Gas Plasma”, *Phys. Rev. Lett.*, **103**, 235002 (2009).
- [34] P. F. Moulton, “Spectroscopic and Laser Characteristics of Ti:Al₂O₃”, *J. Opt. Soc. Am. B*, **3**, 125–132 (1986).
- [35] A. J. D. Maria, D. A. Stetser, and H. Heynau, “Self Mode-Locking of Lasers with Saturable Absorbers”, *Appl. Phys. Lett.*, **8**, 174–176 (1966).
- [36] D. Strickland and G. Mourou, “Compression of Amplified Chirped Optical Pulses”, *Opt. Comm.*, **56**, 219–221 (1985).

- [37] S. T. Cundiff and J. Ye, “*COLLOQUIUM: FEMTOSECOND OPTICAL FREQUENCY COMBS*”, *Rev. Mod. Phys.*, **75**, 325–342 (2003).
- [38] D. E. Spence, P. N. Kean, and W. Sibbett, “60-fsec Pulse Generation from a Self-Mode-Locked Ti:sapphire Laser”, in Conference on Lasers and Electro-Optics (CLEO) CPDP10 (1990).
- [39] D. E. Spence, P. N. Kean, and W. Sibbett, “60-fsec Pulse Generation from a Self-Mode-Locked Ti:sapphire Laser”, *Opt. Lett.*, **16**, 42–44 (1991).
- [40] T. Südmeyer, C. Kränkel, C. R. E. Baer, O. H. Heckl, C. J. Saraceno, M. Golling, R. Peters, K. Petermann, G. Huber, and U. Keller, “High-power Ultrafast Thin Disk Laser Oscillators and Their Potential for sub-100-Femtosecond Pulse Generation”, *Appl. Phys. B*, **97**, 281–295 (2009).
- [41] U. Keller, D. A. B. Miller, G. D. Boyd, T. H. Chiu, J. F. Ferguson, and M. T. Asom, “Solid-State Low-Loss Intracavity Saturable Absorber for Nd:YLF Lasers: An Antiresonant Semiconductor Fabry-Perot saturable absorber”, *Opt. Lett.*, **17**, 505–507 (1992).
- [42] T. Südmeyer, S. V. Marchese, S. Hashimoto, C. R. E. Baer, G. Gingras, B. Witzel, and U. Keller, “Femtosecond Laser Oscillators for High-Field Science”, *Nature Photonics*, **2**, 599–603 (2008).
- [43] R. Paschotta, *Chirped-Pulse Amplification*, (2012) http://www.rp-photonics.com/chirped_pulse_amplification.html.
- [44] D. Sutton, *Record Laser Shot Success on the Road to Fusion Energy*, (2012) http://www.canadianbusiness.com/blog/business_briefings/82067--record-laser-shot-success-on-the-road-to-fusion-energy.
- [45] R. Bhardwaj, “Making Ultrashort Light Pulses”, in Extreme Photonics Workshop (2011).

- [46] B. Xu, J. M. Gunn, J. M. Dela Cruz, V. V. Lozovoy, and M. Dantus, “Quantitative Investigation of the Multiphoton Intrapulse Interference Phase Scan Method for Simultaneous Phase Measurement and Compensation of Femtosecond Laser Pulses”, *J. Opt. Soc. Am. B*, **23**, 750–759 (2006).
- [47] W. Heisenberg, “The Actual Content of Quantum Theoretical Kinematics and Mechanics”, *Zeits. f. Phys.*, **43**, 172–198 (1927).
- [48] J. Briggs, “A Derivation of the Time-Energy Uncertainty Relation”, *Journal of Physics: Conference Series*, **99**, 012002 (2008).
- [49] S. T. Cundiff and A. M. Weiner, “Optical Arbitrary Waveform Generation”, *Nature Photonics*, **4**, 760–766 (2010).
- [50] M. Dantus and V. V. Lozovoy, “Experimental Coherent Laser Control of Physicochemical Processes”, *Chem. Rev.*, **104**, 1813–1859 (2004).
- [51] A. M. Weiner, “Ultrafast Optical Pulse Shaping: A Tutorial Review”, *Opt. Comm.*, **284**, 3669–3692 (2011).
- [52] E. Lioudakis, K. Adamou, and A. Othonos, “Prism Based Ultrafast Pulse Shaping Apparatus”, *Opt. Eng.*, **44**, 034203 (2005).
- [53] R. W. Boyd, *Nonlinear Optics* (Academic Press Inc., 1992).
- [54] S. Akturk, A. Couairon, M. Franco, and A. Mysyrowicz, “Spectrogram Representation of Pulse Self Compression by Filamentation”, *Opt. Express*, **16**, 17626–17636 (2008).
- [55] D. P. Shelton and A. D. Buckingham, “Optical Second-Harmonic Generation in Gases with a Low-Power Laser”, *Phys. Rev. A*, **26**, 2787–2798 (1982).

- [56] D. Grischkowsky, S. Keiding, M. van Exter, and C. Fattinger, “Far-Infrared Time-Domain Spectroscopy with Terahertz Beams of Dielectrics and Semiconductors”, *J. Opt. Soc. Am. B*, **7**, 2006–2015 (1990).
- [57] D. H. Auston, K. P. Cheung, and P. R. Smith, “Picosecond Photoconducting Hertzian Dipoles”, *Appl. Phys. Lett.*, **45**, 284–286 (1984).
- [58] H. Hertz, “see: Electric Waves”, *Weidemann’s Ann.*, **34**, 551 (1881).
- [59] H. Hertz, *Electric Waves*, trans. by D. E. Jones (Dover, 1962).
- [60] A. Hong, *Dielectric Strength of Air*, (2000) <http://hypertextbook.com/facts/2000/AliceHong.shtml>.
- [61] D. A. Turton, G. H. Welsh, J. J. Carey, G. D. Reid, G. S. Beddard, and K. Wynne, “Alternating High-Voltage Biasing for Terahertz Large-Area Photoconductive Emitters”, *Rev. Sci. Instr.*, **77**, 083111 (2006).
- [62] J. T. Darrow, X. C. Zhang, and D. H. Auston, “Power Scaling of Large-Aperture Photoconducting Antennas”, *Appl. Phys. Lett.*, **58**, 25–27 (1991).
- [63] D. You, R. R. Jones, P. H. Bucksbaum, and D. R. Dykaar, “Generation of High-Power Sub-Single-Cycle 500-fs Electromagnetic Pulses”, *Opt. Lett.*, **18**, 290–292 (1993).
- [64] J. T. Darrow, X. C. Zhang, and D. H. Auston, “Saturation Properties of Large-Aperture Photoconducting Antennas”, *IEEE J. Quant. Elec.*, **28**, 1607–1616 (1992).
- [65] A. Dreyhaupt, S. Winnerl, T. Dekorsy, and M. Helm, “High-Intensity Terahertz Radiation from a Microstructured Large-Area Photoconductor”, *Appl. Phys. Lett.*, **86**, 121114 (2005).

- [66] A. Dreyhaupt, S. Winnerl, M. Helm, and T. Dekorsy, “Optimum Excitation Conditions for the Generation of High-Electric-Field Terahertz Radiation from an Oscillator-Driven Photoconductive Device”, *Opt. Lett.*, **31**, 1546–1548 (2006).
- [67] G. P. Acuna, F. F. Buersegens, C. Lang, M. Handloser, A. Guggenmos, and R. Kersting, “Interdigitated Terahertz Emitters”, *Electronics Letters*, **44**, 04446196 (2008).
- [68] V. N. Trukhin, A. V. Andrianov, and N. N. Zinov’ev, “Generation of Terahertz Radiation by a Photoconductive Antenna”, *Acta Physica Polonica A*, **113**, 921–924 (2008).
- [69] P. K. Benicewicz, J. P. Roberts, and A. J. Taylor, “Scaling of Terahertz Radiation from Large-Aperture Biased Photoconductors”, *J. Opt. Soc. Am. B*, **11**, 2533–2545 (1994).
- [70] M. Bass, P. A. Franken, J. F. Ward, and G. Weinreich, “Optical Rectification”, *Phys. Rev. Lett.*, **9**, 446–448 (1962).
- [71] A. Nahata, A. S. Weling, and T. F. Heinz, “A Wideband Coherent Terahertz Spectroscopy System Using Optical Rectification and Electro-Optic Sampling”, *Appl. Phys. Lett.*, **69**, 2321–2323 (1996).
- [72] T. Löffler, Hahn, M. Thomson, F. Jacob, and H. G. Roskos, “Large-Area Electro-Optic ZnTe Terahertz Emitters”, *Opt. Express*, **13**, 5353–5362 (2005).
- [73] S. Casalbuoni, H. Schlarb, B. Schmidt, P. Schrüser, B. Steffen, and A. Winter, “Numerical studies on the electro-optic detection of femtosecond electron bunches”, *Phys. Rev. Spec. Top. - Acc. and Beams*, **11**, 072802 (2008).
- [74] F. Blanchard, L. Razzari, H. C. Bandulet, G. Sharma, R. Morandotti, J. C. Kieffer, T. Ozaki¹, M. Reid, H. F. Tiedje, H. K. Haugen, and F. A. Hegmann, “Generation of 1.5 μ J Single-Cycle Terahertz Pulses by Optical Rectification from a Large Aperture ZnTe Crystal”, *Opt. Express*, **15**, 13212 (2007).

- [75] J. Hebling, G. Almási, I. Z. Kozma, and J. Kuhl, “Velocity Matching by Pulse Front Tilting for Large-Area THz-Pulse Generation”, *Opt. Express*, **10**, 1161–1166 (2002).
- [76] J. Hebling, K. Yeh, M. C. Hoffmann, and K. A. Nelson, “High-Power THz Generation, THz Nonlinear Optics, and THz Nonlinear Spectroscopy”, *J. Sel. Top. Quant. Elec.*, **14**, 345–353 (2008).
- [77] M. Jewariya, M. Nagai, and K. Tanaka, “Enhancement of Terahertz Wave Generation by Cascaded $\chi(2)$ Processes in LiNbO₃”, *J. Opt. Soc. Am. B*, **26**, A101 (2009).
- [78] H. Hirori, A. Doi, F. Blanchard, and K. Tanaka, “Single-Cycle Terahertz Pulses with Amplitudes Exceeding 1 MV/cm Generated by Optical Rectification in LiNbO₃”, *Appl. Phys. Lett.*, **98**, 091106 (2011).
- [79] S. W. Huang, E. Granados, W. R. Huang, K. H. Hong, L. E. Zapata, and F. X. Kärtner, “High Conversion Efficiency, High Energy Terahertz Pulses by Optical Rectification in Cryogenically Cooled Lithium Niobate”, *Opt. Lett.*, **38**, 796–798 (2013).
- [80] J. A. Fülöp, L. Pálfalvi, G. Almási, and J. Hebling, “Design of High-Energy Terahertz Sources Based on Optical Rectification”, *Opt. Express*, **18**, 12311–12327 (2010).
- [81] Z. Chen, X. Zhou, C. A. Werley, and K. A. Nelson, “Generation of High Power Tunable Multicycle Terahertz Pulses”, *Appl. Phys. Lett.*, **99**, 071102 (2011).
- [82] M. Nagai, E. Matsubara, and M. Ashida, “High-Efficiency Terahertz Pulse Generation via Optical Rectification by Suppressing Stimulated Raman Scattering Process”, *Opt. Express*, **20**, 6509–6514 (2012).
- [83] M. I. Bakunov, S. B. Bodrov, and E. A. Mashkovich, “Terahertz Generation with Tilted-Front Laser Pulses: Dynamic Theory for Low-Absorbing Crystals”, *J. Opt. Soc. Am. B*, **28**, 1724–1734 (2011).

- [84] W. D. Johnston and I. P. Kaminow, “Contributions to Optical Nonlinearity in GaAs as Determined from Raman Scattering Efficiencies”, *Phys. Rev.*, **188**, 1209–1211 (1969).
- [85] J. Dai, J. Liu, and X. C. Zhang, “Terahertz Wave Air Photonics: Terahertz Wave Generation and Detection With Laser-Induced Gas Plasma”, *IEEE J. Sel. Top. Quant. El.*, **17**, 183–190 (2011).
- [86] J. Liu, J. Dai, X. Lu, I. Ho, and X. Zhang, *Int. J. High Speed El. and Sys.*, **In Press**, Accessed online <http://thz.phys.rpi.edu/Publications/Terahertz\%20Wave\%20Air\%20Photonics.pdf> (2010).
- [87] T. Bartel, P. Gaal, K. Reimann, M. Woerner, and T. Elsaesser, “Generation of Single-Cycle THz Transients with High Electric-Field Amplitudes”, *Opt. Lett.*, **30**, 2805–2807 (2005).
- [88] N. Karpowicz, J. Dai, X. Lu, Y. Chen, M. Yamaguchi, H. Zhao, X. C. Zhang, L. Zhang, C. Zhang, M. Price-Gallagher, C. Fletcher, O. Mamer, A. Lesimple, and K. Johnson, “Coherent Heterodyne Time-Domain Spectrometry Covering the Entire “Terahertz Gap””, *Appl. Phys. Lett.*, **92**, 011131 (2008).
- [89] T. Fuji and T. Suzuki, “Generation of Sub-Two-Cycle Mid-Infrared Pulses by Four-Wave Mixing through Filamentation in Air”, *Opt. Lett.*, **32**, 3330–3332 (2007).
- [90] M. D. Thomson, V. Blank, and H. G. Roskos, “Terahertz White-Light Pulses from an Air Plasma Photo-Induced by Incommensurate Two-Color Optical Fields”, *Opt. Express*, **18**, 23173–23182 (2010).
- [91] J. Dai and X. C. Zhang, “Terahertz Wave Generation from Gas Plasma using a Phase Compensator with Attosecond Phase-Control Accuracy”, *Appl. Phys. Lett.*, **94**, 021117 (2009).

- [92] K. Y. Kim, J. H. Glowonia, A. J. Taylor, and G. Rodriguez, “Terahertz Emission from Ultrafast Ionizing Air in Symmetry-Broken Laser Fields”, *Opt. Express*, **15**, 4577–4584 (2007).
- [93] D. Dietze, J. Darmo, S. Roither, A. Pugzlys, J. N. Heyman, and K. Unterrainer, “Polarization of Terahertz Radiation from Laser Generated Plasma Filaments”, *J. Opt. Soc. Am. B*, **26**, 2016–2027 (2009).
- [94] D. J. Cook, J. X. Chen, E. A. Morlino, and R. M. Hochstrasser, “Terahertz-Field-Induced Second-Harmonic Generation Measurements of Liquid Dynamics”, *Chem. Phys. Lett.*, **309**, 221–228 (1999).
- [95] R. S. Finn and J. F. Ward, “dc-Induced Optical Second-Harmonic Generation in the Inert Gases”, *Phys. Rev. Lett.*, **26**, 285–289 (1971).
- [96] T. Kress, M. Löffler, S. Eden, M. Thomson, and H. G. Roskos, “Terahertz-Pulse Generation by Photoionization of Air with Laser Pulses Composed of Both Fundamental and Second-Harmonic Waves”, *Opt. Lett.*, **29**, 1120–1122 (2004).
- [97] K. Y. Kim, J. H. Glowonia, A. J. Taylor, and G. Rodriguez, “High-Power Broadband Terahertz Generation via Two-Color Photoionization in Gases”, *IEEE J. Quant. Elec.*, **48**, 797–805 (2012).
- [98] N. Karpowicz, X. Lu, and X. C. Zhang, “Topical Review: Terahertz gas photonics”, *J. Modern Opt.*, **56**, 1137–1150 (2009).
- [99] Unknown, *Ionization Potentials for Common Industrial Gases*, (2011) http://www.indsci.com/docs/manuals/VX500_IP.pdf.
- [100] Y. Chen, M. Yamaguchi, M. Wang, and X. C. Zhang, “Terahertz Pulse Generation from Noble Gases”, *Appl. Phys. Lett.*, **91**, 251116 (2007).

- [101] M. Clerici, M. Peccianti, B. E. Schmidt, L. Caspani, M. Shalaby, M. Giguère, A. Lotti, A. Couairon, F. Légaré, T. Ozaki, D. Faccio, and R. Morandotti, “Scaling Mechanism for Efficient Wavelength Conversion in Laser Plasmas”, *ArXiv*, 1207.4754 (2012).
- [102] A. Sell, A. Leitenstorfer, and R. Huber, “Phase-Locked Generation and Field-Resolved Detection of Widely Tunable Terahertz Pulses with Amplitudes Exceeding 100 MV/cm”, *Opt. Lett.*, **33**, 2767–2769 (2008).
- [103] F. Junginger, A. Sell, O. Schubert, B. Mayer, D. Brida, M. Maragoni, G. Cerullo, A. Leitenstorfer, and R. Huber, “Single-Cycle Multiterahertz Transients with Peak Fields Above 10 MV/cm”, *Opt. Lett.*, **35**, 2645–2647 (2010).
- [104] K. Reimann, R. P. Smith, W. A. M., T. Elsaesser, and M. Woerner, “Direct Field-Resolved Detection of Terahertz Transients with Amplitudes of Megavolts per Centimeter”, *Opt. Lett.*, **28**, 471–473 (2003).
- [105] C. Kübler, R. Huber, S. Tübel, and A. Leitenstorfer, “Ultrabroadband Detection of Multi-Terahertz Field Transients with GaSe Electro-Optic Sensors: Approaching the Near Infrared”, *Appl. Phys. Lett.*, **85**, 3360–3362 (2004).
- [106] J. Dai, X. Xie, and X. C. Zhang, “Detection of Broadband Terahertz Waves with a Laser-Induced Plasma in Gases”, *Phys. Rev. Lett.*, **97**, 103903 (2006).
- [107] V. authors, *Refractive Index Database*, (2012) <http://refractiveindex.info/>.
- [108] J. A. Valdmanis and G. Mourou, “Subpicosecond Electrooptic Sampling: Principles and Applications”, *IEEE J. Quant. Elec.*, **QE-22**, 69–78 (1986).
- [109] M. Izdebski, W. Kucharczyk, and R. E. Raab, “On Relationships Between Electro-Optic Coefficients for Impermeability and Nonlinear Electric Susceptibilities”, *J. Opt. A: Pure Appl. Opt.*, **6**, 421–424 (2004).

- [110] Z. Jiang, F. G. Sun, Q. Chen, and X. C. Zhang, “Electro-Optic Sampling Near Zero Optical Transmission Point”, *Appl. Phys. Lett.*, **74**, 1191–1193 (1999).
- [111] X. Lu and X. C. Zhang, “Terahertz Wave Gas Photonics: Sensing with Gases”, *J. Infrared and Milli. Terahz. Waves*, **32**, 562–569 (2011).
- [112] X. Lu, N. Karpowicz, and X. C. Zhang, “Broadband Terahertz Detection with Selected Gases”, *J. Opt. Soc. Am. B*, **26**, A66–A73 (2009).
- [113] L. DuVillaret, F. Garet, and J. Coutaz, “A Reliable Method for Extraction of Material Parameters in Terahertz Time-Domain Spectroscopy”, *IEEE J. Sel. Top. Quant. Elec.*, **2**, 739–746 (1996).
- [114] J. T. Kindt and C. A. Schmuttenmaer, “Far-Infrared Dielectric Properties of Polar Liquids Probed by Femtosecond Terahertz Pulse Spectroscopy”, *J. Phys. Chem.*, **100**, 10373–10379 (1996).
- [115] N. Katzenellenbogen and D. Grischkowsky, “Electrical Characterization to 4 THz of *N*- and *P*- Type GaAs using THz Time-Domain Spectroscopy ”, *Appl. Phys. Lett.*, **61**, 840–842 (1992).
- [116] M. C. Beard, G. M. Turner, and C. A. Schmuttenmaer, “Subpicosecond Carrier Dynamics in Low-Temperature Grown GaAs as Measured by Time-Resolved Terahertz Spectroscopy”, *J. Appl. Phys.*, **90**, 5915–5923 (2001).
- [117] *THz Emitter and Detector for 800 nm Wavelength Lasers*, (2006) <http://www.ekspla.com/product/thz-emitter-and-detector-for-800-nm-wavelength-lasers>.
- [118] J. Dai, N. Karpowicz, and X. C. Zhang, “Coherent Polarization Control of Terahertz Waves Generated from Two-Color Laser-Induced Gas Plasm”, *Phys. Rev. Lett.*, **103**, 023001 (2009).

- [119] Y. S. You, T. I. Oh, and K. Y. Kim, “Off-Axis Phase-Matched Terahertz Emission from Two-Color Laser-Induced Plasma Filaments”, *Phys. Rev. Lett.*, **109**, 183902 (2012).
- [120] G. Rodriguez and G. L. Dakovski, “Scaling Behavior of Ultrafast Two-Color Terahertz Generation in Plasma Gas Targets: Energy and Pressure Dependence”, *Opt. Express*, **18**, 15130–15143 (2010).
- [121] J. Dai, T. Tongue, and X.-C. Zhang, “In-Line Phase Compensator for Intense THz Generation in Selected Gases”, in *Infrared, Millimeter, and Terahertz Waves, 2009. IRMMW-THz 2009. 34th International Conference on* (2009).
- [122] Y. Minami, T. Kurihara, K. Yamaguchi, M. Nakajima, and T. Suemoto, “High-Power THz Wave Generation in Plasma Induced by Polarization Adjusted Two Color Laser Pulses”, *Appl. Phys. Lett.*, **102**, 041105 (2013).
- [123] Y. Oishi, M. Kaku, A. Suda, F. Kannari, and K. Midorikawa, “Generation of Extreme Ultraviolet Continuum Radiation Driven by a sub-10-fs Two-Color Field”, *Opt. Express*, **14**, 7230–7237 (2006).
- [124] Y. Shen, T. Watanabe, D. A. Arena, C.-C. Kao, J. B. Murphy, T. Y. Tsang, X. J. Wang, and G. L. Carr, “Nonlinear Cross-Phase Modulation with Intense Single-Cycle Terahertz Pulses”, *Phys. Rev. Lett.*, **99**, 043901 (2007).
- [125] A. Hernandez-Cabrera, C. Tejedor, and M. F., “Linear Electro-Optic Effects in Zinc Blende Semiconductors”, *J. Appl. Phys.*, **58**, 4666–4669 (1985).
- [126] F. B. Foote, D. T. Hodges, and H. B. Dyson, “Calibration of Power and Energy Meters for the Far Infrared/Near Millimeter Wave Spectral Region”, *Int. J. Infrared Millimeter Waves*, **2**, 773–782 (1981).

- [127] S. Brewer and S. Franzen, “Optical Properties of Indium Tin Oxide and Fluorine-Doped Tin Oxide Surfaces: Correlation of Reflectivity, Skin Depth, and Plasmon Frequency with Conductivity”, *J. Alloys and Comp.*, **338**, 73–79 (2002).
- [128] T. Bauer, J. S. Kolb, T. Löffler, E. Mohler, and H. G. Roskos, “Indium-tin-oxide-Coated Glass as Dichroic Mirror for Far-Infrared Electromagnetic Radiation”, *J. Appl. Phys.*, **92**, 2210–2212 (2002).
- [129] J. Borysow, H. Golnabi, R. H. Taylor, and J. W. Keto, “Techniques for Measuring Small Changes in the Intensity of a Pulse Laser”, *Appl. Optics*, **31**, 2814–2819 (1992).
- [130] H. He and X. C. Zhang, “Analysis of Gouy Phase Shift for Optimizing Terahertz Air-Biased-Coherent-Detection”, *Appl. Phys. Lett.*, **100**, 061105 (2012).
- [131] X. C. Zhang and J. Xu, *Introduction to THz Wave Photonics* (Springer, 2010) Chap. 3 - Terahertz Spectroscopy and Imaging.
- [132] P. U. Jepsen and B. M. Fischer, “Dynamic Range in Terahertz Time-Domain Transmission and Reflection Spectroscopy”, *Opt. Lett.*, **30**, 29–31 (2005).
- [133] W. Withayachumnankul, B. M. Fishcer, H. Lin, and D. Abbott, “Uncertainty in Terahertz Time-Domain Spectroscopy Measurement”, *J. Opt. Soc. Am. B*, **25**, 1059–1072 (2008).
- [134] *PDA36A Si Switchable Gain Detector User Guide*, Thorlabs, (2012) <http://www.thorlabs.com/Thorcat/13000/PDA36A-Manual.pdf>.
- [135] M. Naftaly and R. E. Miles, “A Method for Removing Etalon Oscillations from THz Time-Domain Spectra”, *Opt. Comm.*, **280**, 291–295 (2007).
- [136] J. R. Fletcher, G. P. Swift, D. Dai, and J. M. Chamberlain, “Pulsed Terahertz Signal Reconstruction”, *Journal of Applied Physics*, **102**, 113105 (2007).

- [137] P. Kužel, H. Nímec, F. Kadlec, and C. Kadlec, “Gouy Shift Correction for Highly Accurate Refractive Index Retrieval in Time-Domain Terahertz Spectroscopy”, *Opt. Express*, **18**, 15338–15348 (2010).
- [138] S. Feng, H. G. Winful, and R. W. Hellwarth, “Gouy Shift and Temporal Reshaping of Focused Single-Cycle Electromagnetic Pulses”, *Opt. Lett.*, **23**, 385–387 (1998).
- [139] A. B. Ruffin, J. V. Rudd, J. F. Whitaker, S. Feng, and H. G. Winful, “Direct Observation of the Gouy Phase Shift with Single-Cycle Terahertz Pulses”, *Phys. Rev. Lett.*, **83**, 3410–3413 (1999).
- [140] E. Hecht, *Optics* (Addison Wesley, 2001).
- [141] O. Mitrofanov, L. N. Pfeiffer, and K. W. West, “Generation of Low-Frequency Components due to Phase-Amplitude Modulation of Subcycle Far-Infrared Pulses in Near-Field Diffraction”, *Appl. Phys. Lett.*, **81**, 1579–1581 (2002).
- [142] M. Walther, B. M. Fischer, and P. U. Jepsen, “Noncovalent Intermolecular Forces in Polycrystalline and Amorphous Saccharides in the Far Infrared”, *Chem. Phys.*, **288**, 261 (2003).
- [143] Z. Zheng, W. Fan, Y. Liang, and H. Yan, “Application of Terahertz Spectroscopy and Molecular Modeling in Isomers Investigation: Glucose and Fructose”, *Opt. Comm.*, **285**, 1868–1871 (2012).
- [144] J. Nishizawa, K. Suto, T. Sasaki, T. Tanabe, and T. Kimura, “Spectral Measurement of Terahertz Vibrations of Biomolecules using a GaP Terahertz-Wave Generator with Automatic Scanning Control”, *J. Phys. D: Appl. Phys.*, **36**, 2958–2961 (2003).
- [145] P. C. Upadhyaya, Y. C. Shen, A. G. Davies, and L. E. H., “Far-Infrared Vibrational Modes of Polycrystalline Saccharides”, *Vib. Spec.*, **35**, 139–143 (2004).

- [146] Z. Zheng, W. Fan, and H. Yan, “Terahertz Absorption Spectra of Benzene-1,2-diol, Benzene-1,3-diol, and Benzene-1,4-diol”, *Chemical Physics Letters*, **526**, 140–143 (2012).
- [147] K. Siegrist, C. R. Bucher, I. Mandelbaum, A. R. H. Walker, R. Balu, S. K. Gregurick, and D. F. Plusquellic, “High-Resolution Terahertz Spectroscopy of Crystalline Trianiline: Extreme Sensitivity to β -Sheet Structure and Cocrystallized Water”, *J. Am. Chem. Soc.*, **128**, 5764–5775 (2006).
- [148] P. F. Taday, L. V. Bradley, D. D. Arnone, and M. Pepper, “Using Terahertz Pulse Spectroscopy to Study the Crystalline Structure of a Drug: A Case Study of the Polymorphs of Ranitidine Hydrochloride”, *J. Pharma. Sci.*, **92**, 831–838 (2003).
- [149] P. U. Jepsen and S. J. Clark, “Precise *ab initio* Prediction of Terahertz Vibrational Modes in Crystalline Systems”, *Chem. Phys. Lett.*, **442**, 275–280 (2007).
- [150] D. F. Plusquellic, K. Siegrist, E. J. Heilweil, and O. Esenturk, “Applications of Terahertz Spectroscopy in Biosystems”, *ChemPhysChem*, **8**, 2412–2431 (2007).
- [151] O. Esenturk, A. Evans, and E. J. Heilwil, “Terahertz Spectroscopy of Dicyanobenzenes: Anomalous Absorption Intensities and Spectral Calculations”, *Chem. Phys. Lett.*, **442**, 71–77 (2007).
- [152] D. G. Allis and T. M. Korter, “Theoretical Analysis of the Terahertz Spectrum of the High Explosive PETN”, *ChemPhysChem*, **7**, 2398–2408 (2006).
- [153] D. G. Allis, D. A. Prokhorova, and T. M. Korter, “Solid-State Modeling of the Terahertz Spectrum of the High Explosive HMX”, *J. Phys. Chem. A*, **110**, 1951–1959 (2006).
- [154] K. A. Kvenvolden, J. G. Lawless, and C. Ponnampereuma, “Nonprotein Amino Acids in the Murchison Meteorite”, *Proc. Natl. Acad. Sci.*, **68**, 486–490 (1971).
- [155] C. F. Chyba, “Extraterrestrial Amino Acids and Terrestrial Life”, *Nature*, **348**, 113–114 (1990).

- [156] G. Cooper, N. Kimmich, W. Bellsie, J. Sarinana, K. Brabham, and L. Garrel, “Carbonaceous Meteorites as a Source of Sugar-Related Organic Compounds for the Early Earth”, *Science*, **414**, 879–883 (2001).
- [157] M. A. Sephton, “Organic Compounds in Carbonaceous Meteorites”, *Nat. Prod. Rep.*, **19**, 292–311 (2002).
- [158] M. H. Engel and B. Nagy, “Distribution and Enantiomeric Composition of Amino Acids in the Murchison Meteorite”, *Nature*, **296**, 837–840 (1982).
- [159] M. Yamaguchi, F. Miyamaru, K. Yamamoto, M. Tani, and M. Hangyo, “Terahertz Absorption Spectra of L-, D-, and DL-alanine and their Application to Determination of Enantiomeric Composition”, *Appl. Phys. Lett.*, **86**, 053903 (2005).
- [160] D. A. McCormick, “GABA as an Inhibitory Neurotransmitter in Human Cerebral Cortex”, *J. Neurophysiology*, **62**, 1018–1027 (1989).
- [161] M. Wantanabe, K. Maemura, K. Kanbara, T. Tamayama, and H. Hayasaki, “GABA and GABA Receptors in the Central Nervous System and Other Organs”, *Int. Rev. Cytol.*, **213**, 1–47 (2002).
- [162] K. Tomita, “Crystal Data and Some Features of γ -aminobutyric acid, 3-aminopropane Sulfonic Acid and their Derivatives”, *Tetrahedron Lett.*, **12**, 2587–2588 (1971).
- [163] A. J. Dobson and R. E. Gerkin, “ γ -Aminobutyric Acid: a Novel Tetragonal Phase”, *Acta Cryst.*, **C52**, 3075–3078 (1996).
- [164] E. G. Steward, R. B. Player, and D. Warner, “The Crystal and Molecular Structure of γ -Aminobutyric Acid Determined at Low Temperature”, *Acta Cryst.*, **B29**, 2038–2040 (1973).

- [165] H. P. Weber, B. M. Craven, and R. K. McMullan, "The Neutron Structure of and Thermal Motion in γ -Aminobutyric Acid (GABA) at 122K", *Acta Cryst.*, **B39**, 360–366 (1983).
- [166] E. G. Steward, R. B. Player, and D. Warner, "The Crystal Structure of γ -Aminobutyric Acid Hydrochloride: A Refinement", *Acta Cryst. B*, **29**, 2825 (1973).
- [167] K. Tomita, H. Higashi, and T. Fujiwara, "Crystal and Molecular Structure of ω -Amino Acids, ω -Amino Sulfonic Acids and Their Derivatives. IV. The Crystal and Molecular Structure of γ -Aminobutyric Acid (GABA), a Nervous Inhibitory Transmitter", *Bull. Chem. Soc. Japan*, **46**, 2199–2204 (1973).
- [168] K. Tomita, "Unknown", *Jap. J. Brain Physiol.*, **61**, 1–4 (1965).
- [169] B. M. Craven and H. P. Weber, "Charge Density in the Crystal Structure of γ -Aminobutyric Acid at 122 K - An Intramolecular Methylene H Bridge", *Acta Cryst.*, **B39**, 743–748 (1983).
- [170] S. Blanco, J. C. Lopez, S. Mata, and J. L. Alonso, "Conformations of γ Aminobutyric Acid (GABA): The Role of the $n \rightarrow \pi^*$ Interaction", *Angew. Chem. Int. Ed.*, **49**, 9187–9192 (2010).
- [171] K. Tanaka, H. Akutsu, Y. Ozaki, Y. Kyogoku, and K. Tomita, "Molecular Conformations of γ -Aminobutyric Acid and γ -Amino- β -hydroxybutyric Acid in Aqueous Solution", *Bull. Chem. Soc. Japan*, **51**, 2654–2658 (51).
- [172] I. K. Song and Y. K. Kang, "Conformational Preferences of γ -aminobutyric Acid in the Gas Phase and in Water", *J. Mol. Struct.*, **1024**, 163–169 (2012).
- [173] N. Larman, S. S. Harsha, D. Grischkowsky, and J. S. Melinger, "High-Resolution Waveguide THz Spectroscopy of Biological Molecules.", *Biophysical Journal*, **94**, 1010–1020 (2008).

- [174] A. D. Becke, "Density-Functional Thermochemistry The Role of Exact Exchange", *J. Chem. Phys.*, **98**, 5648–5652 (1993).
- [175] P. J. Stephens, F. J. Devlin, C. F. Chabalowski, and M. J. Frisch, "AB INITIO CALCULATION OF VIBRATIONAL ABSORPTION AND CIRCULAR DICHROISM SPECTRA USING DENSITY FUNCTIONAL FORCE FIELDS", *J. Phys. Chem.*, **98**, 11623–11627 (1994).
- [176] T. Yanai, D. P. Tew, and N. C. Handy, "A New Hybrid Exchange-Correlation Functional Using the Coulomb-Attenuating Method (CAM-B3LYP)", *Chem. Phys. Lett.*, **393**, 51–57 (2004).
- [177] J. W. Ochterski, *Vibrational Analysis in Gaussian*, Gaussian, (1999) www.gaussian.com/g_whitepap/vib.htm.
- [178] M. J. Frisch, G. W. Trucks, H. B. Schlegel, G. E. Scuseria, M. A. Robb, J. R. Cheeseman, G. Scalmani, V. Barone, B. Mennucci, G. A. Petersson, H. Nakatsuji, M. Caricato, X. Li, H. P. Hratchian, A. F. Izmaylov, J. Bloino, G. Zheng, J. L. Sonnenberg, M. Hada, M. Ehara, K. Toyota, R. Fukuda, J. Hasegawa, M. Ishida, T. Nakajima, Y. Honda, O. Kitao, H. Nakai, T. Vreven, J. A. Montgomery, Jr., J. E. Peralta, F. Ogliaro, M. Bearpark, J. J. Heyd, E. Brothers, K. N. Kudin, V. N. Staroverov, R. Kobayashi, J. Normand, K. Raghavachari, A. Rendell, J. C. Burant, S. S. Iyengar, J. Tomasi, M. Cossi, N. Rega, J. M. Millam, M. Klene, J. E. Knox, J. B. Cross, V. Bakken, C. Adamo, J. Jaramillo, R. Gomperts, R. E. Stratmann, O. Yazyev, A. J. Austin, R. Cammi, C. Pomelli, J. W. Ochterski, R. L. Martin, K. Morokuma, V. G. Zakrzewski, G. A. Voth, P. Salvador, J. J. Dannenberg, S. Dapprich, A. D. Daniels, J. J. Farkas, J. B. Foresman, J. V. Ortiz, J. Cioslowski, and D. J. Fox, *Gaussian 09, Revision A.1*, Gaussian, Inc., Wallingford CT, 2009.

- [179] R. P. Bell, "The Occurrence and Properties of Molecular Vibrations with $V(x) = ax^4$ ", *Proc. Royal Soc. London A*, **183**, 328–337 (1945).
- [180] R. C. Lord and T. C. Rounds, "Far-Infrared Spectra of Ring Compounds. XIII. The Spectrum and Structure of 1,4-dioxacyclohexadiene-2,5", *J. Chem. Phys.*, **58**, 4344–4349 (1973).
- [181] D. O. Harris, H. W. Harrington, A. C. Luntz, and W. D. Gwinn, "Microwave Spectrum, Vibration-Rotation Interaction, and Potential Function for the Ring-Puckering Vibration of Trimethylene Sulfide", *J. Chem. Phys.*, **44**, 3467–3480 (1966).
- [182] S. Chan, D. Stelman, and L. E. Thompson, "Quartic Oscillator as a Basis for Energy Level Calculations of Some Anharmonic Oscillators", *J. Chem. Phys.*, **41**, 2828–2835 (1964).
- [183] D. Secrest, K. Cashion, and J. O. Hirschfelder, "Power-Series Solutions for Energy Eigenvalues", *J. Chem. Phys.*, **37**, 830–835 (1962).
- [184] A. M. Shorb and R. Schroeder, "Wave Functions for Anharmonic Oscillators by Perturbation Methods", *J. Chem. Phys.*, **37**, 1043–1055 (1962).
- [185] B. S. Meldrum, "Glutamate as a Neurotransmitter in the Brain: Review of Physiology and Pathology", *J. Nutrition*, **130**, 1007S–1015S (2000).
- [186] Z. Yan, D. Hou, P. Huang, B. Cao, G. Zhang, and Z. Zhou, "Terahertz Spectroscopic Investigation of L-glutamic Acid and L-tyrosine", *Meas. Sci. Technol.*, **19**, 015602 (2008).
- [187] A. Matei, N. Drichko, B. Gompf, and M. Dressel, "Far-Infrared Spectra of Amino Acids", *Chem. Phys.*, **316**, 61–71 (2005).
- [188] Y. Ueno, R. Rakchanok, I. Tomita, and K. Ajito, "Quantitative Measurements of Amino Acids by Terahertz Time-Domain Transmission Spectroscopy", *Anal. Chem.*, **78**, 5424–5428 (2006).

- [189] P. F. Taday, I. V. Bradley, and D. D. Arnone, "Terahertz Pulse Spectroscopy of Biological Materials: L-Glutamic Acid", *J. Biol. Phys.*, **29**, 109–115 (2003).
- [190] W. N. Wang, H. Q. Li, Y. Zhang, and C. L. Zhang, "Correlations between Terahertz Spectra and Molecular Structures of 20 Standard α -Amino Acids", *Acta Phys. -Chim. Sin.*, **25**, 2074–2079 (2009).
- [191] S. Hirokawa, S. Kuribayashi, and I. Nitta, "The Crystal Structure of Alpha-amino Isobutyric Acid", *Bull. Chem. Soc. Japan*, **25**, 192–195 (1952).
- [192] N. Laman, S. S. Harsha, D. Grischkowsky, and J. S. Mellinger, "High-Resolution Waveguide THz Spectroscopy of Biological Molecules", *Biophysical Journal*, **94**, 1010–1020 (2008).
- [193] J. M. Hollis, F. J. Lovas, and P. R. Jewell, "Interstellar Glycolaldehyde: The First Sugar", *Ap. J.*, **540**, L107–L110 (2000).
- [194] S. Pizzarello and E. Shock, "The Organic Composition of Carbonaceous Meteorites: The Evolutionary Story Ahead of Biochemistry", *Cold Spring Harb. Perspect. Biol.*, **2**, a002105 (2010).
- [195] R. K. Summerbell and L. K. Rochen, "The Structure of Glycolaldehyde Dimer", *J. Am. Chem. Soc.*, **63**, 3241–3244 (1941).
- [196] J. Ceponkus, W. Chin, M. Chevalier, M. Broquier, A. Limongi, and C. Crépin, "Infrared Study of Glycolaldehyde Isolated in Parahydrogen Matrix", *J. Chem. Phys.*, **133**, 094502 (2010).
- [197] A. Aspiala, J. Murto, and P. Stén, "IR-Induced Conformer Interconversion Processes of Glycolaldehyde in Low-Temperature Matrices, and Ab Initio Calculations on the Energetics and Vibrational Frequencies of the Conformers", *Chemical Physics*, **106**, 399–412 (1986).

- [198] M. L. Senet, “Ab initio Study of the Torsional Spectrum of Glycolaldehyde”, *J. Phys. Chem. A*, **108**, 6286–6293 (2004).
- [199] J. Nishizawa, T. Tanno, T. Yoshida, and K. Suto, “Consequence of a Defect on the Terahertz Spectra of L-Asparagine Monohydrate”, *Chemistry Letters*, **36**, 134–135 (2007).
- [200] J. L. Derissen, H. J. Endeman, and A. F. Peerdeman, “The Crystal and Molecular Structure of L-Aspartic Acid”, *Acta Cryst. B*, **24**, 1349–1354 (1968).
- [201] K. Kvenvolden, J. Lawless, K. Pering, E. Peterson, J. Flores, C. Ponnampereuma, I. R. Kaplan, and C. Moore, “Evidence for Extraterrestrial Amino-acids and Hydrocarbons in the Murchison Meteorite”, *Nature*, **228**, 923–926 (1970).
- [202] P. Ehrenfreund, D. P. Glavin, O. Botta, G. Cooper, and J. L. Bada, “Extraterrestrial Amino Acids in Orgueil and Ivuna: Tracing the Parent Body of CI Type Carbonaceous Chondrites”, *Proc. Natl. Acad. Sci.*, **98**, 2138–2141 (2001).
- [203] M. Zhao and J. L. Bada, “Extraterrestrial Amino Acids in Cretaceous/Tertiary Boundary Sediments at Stevns Klint, Denmark”, *Nature*, **339**, 463–465 (1989).
- [204] J. Bandekar, L. Genzel, F. Kremer, and L. Santo, “The Temperature-Dependence of the Far-Infrared Spectra of L-alanine”, *Spectrochim. Acta*, **39 A**, 357–366 (1983).
- [205] C. H. Wang and R. D. Storms, “Raman Study of Hydrogen Bonding and Long-Wavelength Lattice Modes in an L-Alanine Single Crystal”, *J. Chem. Phys.*, **55**, 5110–5119 (1971).
- [206] T. Sakamoto, T. Tanabe, T. Sasaki, Y. Oyama, J. Nishizawa, T. Kawanishi, and Y. Hiyama, “Chiral Analysis of Re-Crystallized Mixtures of D-, L- Amino Acid using Terahertz Spectroscopy”, *Malays. J. Chem.*, **11**, 088–093 (2009).
- [207] A. R. Taulbee, J. A. Heuser, W. U. Spindel, and G. E. Pacey, “Qualitative Analysis of Collective Mode Frequency Shifts in L-alanine Using Terahertz Spectroscopy”, *Anal. Chem.*, **81**, 2664–2667 (2009).

- [208] R. Fu, Z. Li, B. Jin, C. Zhang, H. Dai, Y. Xue, and J. Chen, “A Study of Vibrational Spectra of L-, D-, DL- alanine in Terahertz Domain, Spectroscopy and Spectral Analysis”, *Spectroscopy and Spectral Analysis*, **30**, 2023–2026 (2010).
- [209] P. R. Tulip and S. J. Clark, “Dielectric and Vibrational Properties of Amino Acids”, *J. Chem. Phys.*, **121**, 5201–5210 (2004).
- [210] Z. Zheng and W. Fan, “First Principles Investigation of L-alanine in the Terahertz Region”, *J. Biol. Phys.*, **38**, 405–413 (2012).
- [211] Y. Y. Zheng, Y. B. Li, and W. N. Wang, “THz Time Domain Spectrum of Beta-alanine”, *Acta Chimica Sinica*, **65**, 72–76 (2007).
- [212] C. S. Ponseca, O. Kambara, S. Kawaguchi, K. Yamamoto, and K. Tominaga, “Low-Frequency Spectra of Amino Acids and Short-Chain Peptides Studied by Terahertz Time-Domain Spectroscopy”, *J Infrared Milli Terahz Waves*, **31**, 799–809 (2010).
- [213] K. Yamamoto, K. Tominaga, H. Sasakawa, A. Tamura, H. Murakami, H. Ohtake, and N. Sarukura, “Terahertz Time-Domain Spectroscopy of Amino Acids and Polypeptides”, *Biophysical Journal*, **89**, L22–L24 (2005).
- [214] G. Wang and W. N. Wang, “Experimental and Theoretical Investigations on the Terahertz Vibrational Spectroscopy of Alanine Crystal”, *Acta Physico-Chimica Sinica*, **28**, 1579–1585 (2012).
- [215] R. F. Doolittle, “Redundancies in Protein Sequences”, in *Prediction of Protein Structures and the Principles of Protein Conformation*, edited by G. D. Fasman (New York: Plenum, 1989), pp. 599–623.
- [216] E. L. Shock and M. D. Schulte, “Summary and Implications of Reported Amino Acid Concentrations in the Murchison Meteorite”, *Geochimica et Cosmochimica Acta*, **54**, 3159–3173 (1990).

- [217] M. D. Segall, P. J. D. Lindan, M. J. Probert, C. J. Pickard, P. J. Hasnip, S. J. Clark, and M. C. Payne, “First-Principles Simulation: Ideas, Illustrations and the CASTEP Code”, *Condes. Mat.*, **14**, 2717–2744 (2002).
- [218] M. Ge, H. W. Zhao, T. Ji, X. H. Yu, W. F. Wang, and W. X. Li, “Terahertz Time-Domain Spectroscopy of Some Pentoses”, *Science in China Series B- Chemistry*, **49**, 204–208 (2006).
- [219] C. S. Liang and G. Zhao, “Terahertz Spectroscopic Inspection and Analysis of Xylitol and D-Xylose”, *Spectroscopy and Spectral Analysis*, **31**, 323–327 (2011).
- [220] R. Singh, D. K. George, J. B. Benedict, T. M. Korter, and A. G. Markelz, “Improved Mode Assignment for Molecular Crystals Through Anisotropic Terahertz Spectroscopy”, *J. Phys. Chem. A*, **116**, 10359–10364 (2012).
- [221] J. Krool, J. Darmo, and K. Unterrainer, “Terahertz Optical Activity of Sucrose Single-Crystals”, *Vibrational Spectroscopy*, **43**, 324–329 (2007).
- [222] D. Šišak, L. B. McCusker, G. Zandomenighi, B. H. Meier, D. Bläser, R. Boese, B. Schweizer, R. Gilmour, and J. D. Dunitz, “The Crystal Structure of d-Ribose - At Last!”, *Angew. Chem. Int. Ed.*, **49**, 4503–4505 (2010).
- [223] M. M. Nazarov, A. P. Shkurinov, E. A. Kuleshov, and V. V. Tuchin, “Terahertz Time-Domain Spectroscopy of Biological Tissues”, *Quantum Electron.*, **38**, 647–654 (2008).
- [224] J. I. Nishizawa, T. Sasaki, K. Suto, M. Ito, T. Yoshida, and T. Tanabe, “High-resolution GaP Terahertz Spectrometer and Its Application to Detect Defects in Gamma-irradiated Glucose Crystal”, *Int. J. Infrared Milli Waves*, **29**, 291–297 (2008).
- [225] P. C. Upadhyya, Y. C. Shen, A. G. Davies, and E. H. Linfield, “Terahertz Time-Domain Spectroscopy of Glucose and Uric Acid”, *J. Biol. Phys.*, **29**, 117–121 (2003).

- [226] H. B. Liu and X. C. Zhang, “Dehydration Kinetics of D-glucose Monohydrate Studied using THz Time-Domain Spectroscopy”, *Chem. Phys. Lett.*, **429**, 229–233 (2006).
- [227] M. Hineno and H. Yoshnag, “Far Infrared Spectra of Glucose and Saccharose”, *Bull. Chem. Soc. Japan*, **43**, 3308 (1970).
- [228] M. Hineno and H. Yoshinag, “Far-Infrared Spectra of Glucose, Sorbose, Saccharose and Cellobiose at Liquid He Temperature”, *Spectrochimica Acta A- Mol. Spect.*, **28**, 2263 (1972).
- [229] M. Hineno and H. Yoshinag, “Far-Infrared Spectra of β -D-Glucose, Cellbiose, Galactose, Lactose, α -D-Glucose and Saccharose in 50-30 cm^{-1} at Liquid He Temperature”, *Spectrochimica Acta A*, **29**, 1575–1578 (1973).
- [230] E. T. G. Lutz and J. H. van der Maas, “Hydrogen Bonding in Crystalline Carbohydrates A Variable-Temperature FT-IR Study”, *J. Mol. Struc.*, **324**, 123–132 (1994).
- [231] E. T. G. Lutz, Y. S. J. Veldhuizen, J. A. Kanters, J. H. van der Maas, J. Baran, and H. Ratajczak, “A Variable Low-Temperature FT-IR Study of Crystalline β -D-fructopyranose and Deuterated Analogues”, *J. Mol. Struc.*, **270**, 381–392 (1992).
- [232] H. O. Desseyn, K. Clou, R. Keuleers, R. Miao, V. E. Van Doren, and N. Blaton, “The Effect of Pressure and Temperature on the Vibrational Spectra of Different Hydrogen Bonded Systems”, *Spectrochimca Acta Part A*, **57**, 231–246 (2001).
- [233] P. Hobza and Z. Havlas, “Blue-Shifting Hydrogen Bonds”, *Chem. Rev.*, **100**, 4253–4264 (2000).
- [234] B. Sloodmaekers and H. O. Desseyn, “Characterization of Inter- and Intramolecular Hydrogen Bonding in the Solid State Using Variable-Temperature IR Spectroscopy”, *Applied Spectroscopy*, **45**, 118–120 (1991).

- [235] Y. Chen, H. Liu, Y. Deng, D. Schauki, M. J. Fitch, R. Osiander, C. Dodson, J. B. Spicer, M. Shur, and X. C. Zhang, “THz Spectroscopic Investigation of 2,4-dinitrofluorene.”, *Chem. Phys. Lett.*, **400**, 357–361 (2004).
- [236] T. Motley and T. M. Kortner, “Terahertz Spectroscopy and Molecular Modeling of 2-pyridone Clusters.”, *Chem. Phys. Lett.*, **464**, 171–178 (2008).
- [237] A. D. Burnett, J. Kendrick, J. E. Cunningham, M. D. Hargreaves, T. Munshi, H. G. M. Edwards, E. H. Linfield, and A. G. Davies, “Calculation and Measurement of Terahertz Active Normal Modes in Crystalline PETN”, *ChemPhysChem*, **11**, 368–378 (2010).
- [238] R. Dovesi, R. Orlando, B. Civalleri, C. Roetti, V. R. Saunders, and C. M. Zicovich-Wilson, “CRYSTAL: A Computational Tool for the *ab initio* Study of the Electronic Properties of Crystals”, *Z. Kristallogr.*, **220**, 571–573 (2005).
- [239] A. D. C. S. Baroni, S. de Gironcoli, P. Giannozzi, G. B. C. Cavazzoni, S. Scandolo, G. Chiarotti, P. Focher, K. L. A. Pasquarello, A. Trave, R. Car, N. Marzari, and A. Kokalj, *Quantum Espresso*, (2012) <http://www.pwscf.org>.
- [240] B. Oregan and M. Grätzel, “A Low-Cost, High-Efficiency Solar Cell Based on Dye-Sensitized Colloidal TiO₂ Films”, *Nature*, **353**, 737–740 (1991).
- [241] B. Li, L. Wang, B. Kang, P. Wang, and Y. Qiu, “Review of Recent Progress in Solid-State Dye-Sensitized Solar Cells”, *Solar En. Mat. Solar Cells*, **90**, 549–573 (2006).
- [242] G. M. Turner, M. C. Beard, and C. A. Schmuttenmaer, “Carrier Localization and Cooling in Dye-Sensitized Nanocrystalline Titanium Dioxide”, *J. Phys. Chem. B*, **106**, 11716–11719 (2002).
- [243] C. Richter and C. A. Schmuttenmaer, “Exciton-Like Trap States Limit Electron Mobility in TiO₂ nanotubes”, *Nature Nanotech.*, **5**, 769–772 (2010).

- [244] X. Chen, L. Liu, P. Y. Yu, and S. S. Mao, “Increasing Solar Absorption for Photocatalysis with Black Hydrogenated Titanium Dioxide Nanocrystals”, *Science*, **331**, 746–749 (2011).
- [245] G. Wang, H. Wang, Y. Ling, Y. Tang, X. Yang, R. C. Fitzmorris, C. Wang, J. Z. Zhang, and Y. Li, “Hydrogen-Treated TiO₂ Nanowire Arrays for Photoelectrochemical Water Splitting”, *Nano Lett.*, **11**, 3026–3033 (2011).
- [246] M. C. Beard, G. M. Turner, and C. A. Schmuttenmaer, “Measurement of Electromagnetic Radiation Emitted during Rapid Intramolecular Electron Transfer”, *J. Am. Chem. Soc.*, **122**, 11541–11542 (2000).
- [247] A. Pourzaki and H. Mirzaee, “New High Voltage Pulse Generators”, *Recent Patents on Electrical Engineering*, **2**, 65–76 (2009).
- [248] E. Matsubara, M. Nagai, and M. Ashida, “Ultrabroadband Coherent Electric Field from Far Infrared to 200 THz using Air Plasma Induced by 10 fs Pulses”, *Appl. Phys. Lett.*, **101**, 011105 (2012).
- [249] I. C. Ho, X. Guo, and X. C. Zhang, “Design and Performance of Reflective Terahertz Air-Biased-Coherent-Detection for Time-Domain Spectroscopy”, *Opt. Express*, **18**, 2872–2883 (2010).
- [250] N. Vieweg, B. M. Fischer, M. Reuter, P. Kula, R. Dabrowski, M. A. Celik, G. Frenking, M. Koch, and P. U. Jepsen, “Ultrabroadband Terahertz Spectroscopy of a Liquid Crystal”, *Opt. Express*, **20**, 28249–28256 (2012).
- [251] Z. Jiang and X. C. Zhang, “Electro-Optic Measurement of THz Field Pulses with a Chirped Optical Beam”, *Appl. Phys. Lett.*, **72**, 1945–1947 (1998).
- [252] F. G. Sun, Z. Jiang, and X. C. Zhang, “Analysis of Terahertz Pulse Measurement with a Chirped Probe Beam”, *Appl. Phys. Lett.*, **73**, 2233–2235 (1998).

- [253] J. Shan, A. S. Weling, E. Knoesel, L. Bartels, M. Bonn, A. Nahata, G. A. Reider, and T. F. Heinz, “Single-Shot Measurement of Terahertz Electromagnetic Pulses by use of Electro-Optic Sampling”, *Opt. Lett.*, **25**, 426–428 (2000).
- [254] Y. Kawada, T. Yasuda, A. Nakauishi, K. Akiyama, and H. Takahashi, “Single-Shot Terahertz Spectroscopy using Pulse-Front Tilting of an Ultra-Short Probe Pulse”, *Opt. Express*, **19**, 11228–11235 (2011).
- [255] G. Hu, A. Lei, B. Shen, R. Li, and Z. Xu, “Single-Shot Coherent Detection of Terahertz Pulse with Broadband Spectral Coverage”, *Physics of Plasmas*, **16**, 043116 (2009).
- [256] K. Y. Kim, B. Tellampalle, A. J. Taylor, G. Rodriguez, and J. H. Glowina, “Single-Shot Terahertz Pulse Characterization via Two-Dimensional Electro-Optic Imaging with Dual Echelons”, *Optics Lett.*, **32**, 1968–1970 (2007).
- [257] Z. Jiang, F. G. Sun, and X. C. Zhang, “Terahertz Pulse Measurement with an Optical Streak Camera”, *Opt. Lett.*, **24**, 1245–1247 (1999).
- [258] X. Y. Peng, Z. M. Sheng, X. H. Zhang, J. H. Teng, H. C. Guo, Y. L. Foo, and Z. J., “Distortion of Terahertz Signals due to Imperfect Synchronization with Chirped Probe Pulses”, *J. Opt. Soc. Am. A*, **28**, 2049–2056 (2011).
- [259] L. Bergél, S. Skupin, C. Köhler, I. Babushkin, and J. Herrmann, “3D Numerical Simulations of THz Generation by Two-Color Laser Filaments”, *Phys. Rev. Lett.*, **110**, 073901 (2013).
- [260] G. Cerullo and S. De Silvestri, “Ultrafast Optical Parametric Amplifiers”, *Rev. Sci. Inst.*, **74**, 1–18 (2003).
- [261] M. Ghotbi, M. E. Ebrahim-Zadeh, V. Petrov, P. Tzankov, and F. Noack, “Efficient 1 kHz Femtosecond Optical Parametric Amplification in BiB₃O₆ Pumped at 800 nm”, *Opt. Express*, **14**, 10621–10626 (2006).

- [262] M. Ghotbi, M. Beutler, V. Petrov, A. Gaydardzhiev, and F. Noack, “High-Energy, sub-30 fs Near-IR Pulses from a Broadband Optical Parametric Amplifier Based on Collinear Interaction in BiB_3O_6 ”, *Opt. Lett.*, **34**, 689–691 (2009).
- [263] R. López-Martens, S. Fournier, C. Le Blanc, E. Baubeau, and F. Salin, “Parametric Amplification and Self-Compression of Ultrashort Tunable Pulses”, *IEEE J. Sel. Top. Quant. El.*, **4**, 230–237 (1998).
- [264] D. Brida, G. Cirimi, C. Manzoni, S. Bonora, P. Villoresi, S. De Silvestri, and G. Cerullo, “Sub-Two-Cycle Light Pulses at $1.6 \mu\text{m}$ from an Optical Parametric Amplifier”, *Optics Letters*, **33**, 741–743 (2008).
- [265] J. L. Hesler, L. Liu, H. Xu, Y. Duan, and R. M. Weikle, *The Development of Quasi-Optical THz Detectors*, Virginia Diodes Inc., (2008) <http://vadiodes.com/VDI/pdf/HeslerQuasiOpticalDetectors.pdf>.
- [266] W. Kuehn, K. Reimann, M. Woerner, T. Elsaesser, R. Hey, and U. Schade, “Strong Correlation of Electronic and Lattice Excitations in GaAs/AlGaAs Semiconductor Quantum Wells Revealed by Two-Dimensional Terahertz Spectroscopy”, *Phys. Rev. Lett.*, **107**, 067401 (2011).
- [267] W. Kuehn, K. Reimann, M. Woerner, T. Elsaesser, and R. Hey, “Two-Dimensional Terahertz Correlation Spectra of Electronic Excitations in Semiconductor Quantum Wells”, *J. Phys. Chem. B*, **115**, 5448–5455 (2011).
- [268] M. C. Hoffmann, N. C. Brandt, H. Y. Hwang, K. L. Yeh, and K. A. Nelson, “Terahertz Kerr Effect”, *Applied Physics Letters*, **95**, 231105 (2009).
- [269] M. C. Hoffmann, J. Hebling, H. Y. Hwang, K. L. Yeh, and K. A. Nelson, “THz-Pump/THz-Probe Spectroscopy of Semiconductors at High Field Strengths”, *J. Opt. Soc. Am. B*, **26**, A29–A34 (2009).

- [270] M. Clerici, L. Caspani, E. Rubino, M. Peccianti, M. Cassataro, A. Busacca, O. T., D. Faccio, and R. Marandotti, “Counterpropagating Frequency Mixing with Terahertz Waves in Diamond”, *Opt. Lett.*, **38**, 178–180 (2013).
- [271] D. Haarer and R. Silbey, “Hole-Burning Spectroscopy of Glasses”, *Phys. Today*, **43**, 58–65 (1990).
- [272] R. F. Loring and S. Mukamel, “Selectivity in Coherent Transient Raman Measurements of Vibrational Dephasing in Liquids”, *J. Chem. Phys.*, **83**, 2116–2128 (1985).
- [273] Y. Tanimura and S. Mukamel, “Two-Dimensional Femtosecond Vibrational Spectroscopy of Liquids.”, *J. Chem. Phys.*, **99**, 9496–9511 (1993).
- [274] T. Hattori, “Classical Theory of Two-Dimensional Time-Domain Terahertz Spectroscopy”, *J. Chem. Phys.*, **133**, 204503 (2010).
- [275] K. Okumura and Y. Tanimura, “Two-Dimensional THz Spectroscopy of Liquids: Non-Linear Vibrational Response to a Series of THz Laser Pulses”, *Chem. Phys. Lett.*, **295**, 298–304 (1998).
- [276] J. Zheng, K. Kwak, and M. D. Fayer, “Ultrafast 2D IR Vibrational Echo Spectroscopy”, *Acc. Chem. Res.*, **40**, 75–83 (2007).
- [277] W. Kuehn, K. Reimann, M. Woerner, and T. Elsaesser, “Phase-Resolved Two-Dimensional Spectroscopy Based on Collinear n -Wave Mixing in the Ultrafast Time Domain”, *J. Chem. Phys.*, **130**, 164503 (2009).
- [278] M. Khalil, N. Demirdöven, and A. Tokmakoff, “Coherent 2D IR Spectroscopy: Molecular Structure and Dynamics in Solution”, *J. Phys. Chem. A*, **107**, 5258–5279 (2003).
- [279] M. L. Cowan, B. D. Bruner, N. Huse, J. R. Dwyer, B. Chugh, E. T. J. Nibbering, T. Elsaesser, and R. J. D. Miller, “Ultrafast Memory Loss and Energy Redistribution in the Hydrogen Bond Network of Liquid H₂O”, *Nature*, **434**, 199–202 (2005).

- [280] J. E. Bertie and Z. Lan, “Infrared intensities of liquids XX: The intensity of the OH stretching band of liquid water revisited, and the best current values of the optical constants of H₂O at 25°C between 15,000 and 1 cm⁻¹”, *Appl. Spec.*, **50**, 1047–1057 (1996).
- [281] D. L. Rousseau, “Laser Chemistry”, *J. Chem. Educ.*, **43**, 566–570 (1966).
- [282] V. V. Lozovoy, X. Zhu, T. C. Gunaratne, D. A. Harris, J. C. Shane, and M. Dantus, “Experimental Coherent Laser Control of Physicochemical Processes”, *Chem. Rev.*, **104**, 1813–1860 (2004).
- [283] R. E. Carley, E. Heesel, and H. H. Fielding, “Femtosecond Lasers in Gas Phase Chemistry”, *Chem. Soc. Rev.*, **34**, 949–969 (2005).
- [284] W. M. Griffith, M. W. Noel, and T. F. Gallagher, “Phase and Rise-Time Dependence using RF Pulses in Multiphoton Processes”, *Phys. Rev. A*, **57**, 3698–3704 (1998).
- [285] C. Jiraushek, L. Duan, O. D. Mücke, F. X. Kärtner, M. Wegener, and U. Morgner, “Carrier-Envelope Phase-Sensitive Inversion in Two-Level Systems”, *J. Opt. Soc. Am. B*, **22**, 2065–2075 (2005).
- [286] C. Uiberacker and W. Jakubetz, “Strong-Field Dipole Resonance: Limiting Analytical Cases”, *Phys. Rev. A*, **80**, 063406 (2009).
- [287] C. Uiberacker and J. W., “Molecular Isomerization Induced by Ultrashort Infrared Pulses. I. Few-Cycle to Sub-One-Cycle Gaussian Pulses and the Role of the Carrier-Envelope Phase”, *J. Chem. Phys.*, **120**, 11532–11539 (2004).
- [288] C. Uiberacker and J. W., “Molecular Isomerization Induced by Ultrashort Infrared Pulses. II. Pump-Dump Isomerization using Pairs of Time-Delayed Half-Cycle pulses”, *J. Chem. Phys.*, **120**, 11540 (2004).

- [289] N. Došlić, “Terahertz-Laser Control of Large Amplitude Vibrational Motion in the Sub-One-Cycle Pulse Limit”, *J. Phys. Chem. A*, **110**, 12400–12405 (2006).
- [290] N. Došlić, “Generalization of the Rabi Population Inversion Dynamics in the Sub-One-Cycle Pulse Limit”, *Phys. Rev. A*, **74**, 013402 (2006).
- [291] M. Jewariya, M. Nagai, and K. Tanaka, “Ladder Climbing on the Anharmonic Intermolecular Potential in an Amino Acid Microcrystal via an Intense Monocycle Terahertz Pulse”, *Phys. Rev. Lett.*, **105**, 203003 (2010).
- [292] L. Matanivić and N. Došlić, “Infrared Spectroscopy of the Intramolecular Hydrogen Bond in Acetylacetone: A Computational Approach”, *J. Phys. Chem. A*, **109**, 4185 (2005).
- [293] J. R. Durig and R. C. Lord, “Far-Infrared Spectra of Four-Membered-Ring Compounds. I. Spectra and Structure of Cyclobutanone, Cyclobutanone-d₄, Trimethylene Sulfide, and Perfluorocyclobutanone”, *J. Chem. Phys.*, **45**, 61–66 (1966).
- [294] J. Laane and R. C. Lord, “Far-Infrared Spectra of Ring Compounds. II. The Spectrum and Ring-Puckering Potential Function of Cyclopentene”, *J. Chem. Phys.*, **47**, 4941–4945 (1967).
- [295] J. Laane and R. C. Lord, “Far Infrared Spectra of Ring Compounds: VI. Spectrum and Conformation of 1,4-cyclohexadiene”, *J. Mol. Spec.*, **39**, 340–344 (1971).
- [296] J. Choo, J. Laane, R. Majors, and J. R. Villarreal, “Far-infrared Spectra and Ring-Puckering Potential Energy Function of 4H-pyran. Conformations and Bonding of 1,4-cyclohexadiene and its Oxygen Analogs”, *J. Am. Chem. Soc.*, **115**, 8396–8400 (1993).
- [297] S. Shim, D. B. Strasfeld, E. C. Fulmer, and M. T. Zanni, “Generation and Characterization of Phase and Amplitude Shaped Femtosecond mid-IR Pulses”, *Opt. Lett.*, **31**, 060838 (2006).

- [298] Y. Ma, S. C. Saha, A. L. Bernassau, and D. R. S. Cumming, “Terahertz Free Space Communication Based on Acoustic Optical Modulation and Heterodyne Detection”, *Elec. Lett.*, **47**, 868–U1956 (2011).
- [299] R. H. Poolman, A. L. Ivanov, and E. A. Muljarov, “Ultrasonic Control of Terahertz Radiation via Lattice Anharmonicity in LiNbO₃”, *Appl. Phys. Lett.*, **98**, 263505 (2011).
- [300] J. J. H. Meijer, A. S. Pijpers, H. K. Nienhuys, M. Bonn, and W. J. van der Zande, “A THz Spectrometer Based on a CsI Prism”, *J. Opt. A.*, **10**, 096303 (2008).
- [301] Y. Liu, S. G. Park, and A. M. Weiner, “Terahertz Waveform Synthesis via Optical Pulse Shaping”, *IEEE J. Quantum Electron.*, **2**, 709–719 (1996).
- [302] J. Ahn, A. V. Efimov, R. D. Averitt, and A. J. Taylor, “Terahertz Waveform Synthesis via Optical Rectification of Shaped Ultrafast Laser Pulses”, *Opt. Express*, **11**, 2486–2496 (2003).
- [303] J. Das and M. Yamaguchi, “Effects of Optical Pulse Shape on THz Wave Generation in Laser Induced Gas Plasma”, in 2011 36th International Conference on Infrared, Millimeter and Terahertz Waves (2011).
- [304] J. Das and M. Yamaguchi, “Tunable Narrow Band THz Wave Generation from Laser Induced Gas Plasma”, *Opt. Express*, **18**, 7038 (2010).
- [305] Y. Bai, R. Song, C. Xu, P. Li, Z. Liu, Z. Zeng, Z. Zhang, H. Lu, R. Li, and Z. Xu, “Waveform-Controlled Terahertz Radiation from the Air Filament Produced by Few-Cycle Laser Pulses”, *Phys. Rev. Lett.*, **108**, 255004 (2012).
- [306] S. Vidal, J. Degert, J. Oberlé, and E. Freysz, “Femtosecond Optical Pulse Shaping for Terahertz Pulse Generation”, *J. Opt. Soc. Am. B*, **27**, 1044–1050 (2010).

- [307] D. J. Maas, J. J. Vrakking, and L. D. Noordam, “Rotational Interference in Vibrational Ladder Climbing in NO by Chirped Infrared Laser Pulses”, *Phys. Rev. A*, **60**, 1351–1362 (1999).
- [308] T. Witte, T. Hornung, L. Windhorn, D. Proch, R. de Vivie-Riedle, M. Motzkus, and K. L. Kompa, “Controlling Molecular Ground-State Dissociation by Optimizing Vibrational Ladder Climbing”, *J. Chem. Phys.*, **118**, 2021–2024 (2003).
- [309] C. Ventalon, J. M. Fraser, M. H. Vos, A. Alexandrou, J. Martin, and M. Joffre, “Coherent Vibrational Climbing in Carboxyhemoglobin”, *PNAS*, **101**, 13216–13220 (2004).
- [310] J. W. Cooley and J. W. Tukey, “An Algorithm for the Machine Computation of the Complex Fourier Series”, *Mathematics of Computation*, **19**, 297–301 (1965).
- [311] V. Liepeņš, *Extended DFT*, (2012) <http://www.mathworks.com/matlabcentral/fileexchange/11020>.
- [312] V. Liepeņš, “High Resolution Spectral Analysis by Using Basis Function Adaptation Approach”, PhD thesis (Univ. of Latvia, Riga (Latvia). Inst. of Electronics and Computer Science, 1996).
- [313] N. Corporation, *ESP300 Motion Controller/Driver*, (2012) <http://assets.newport.com/webDocuments-EN/images/14293.PDF/>.
- [314] L. Corporation, *XStream Remote Control: Configuring DCOM Connectivity*, (2009) http://www.lecroy.com/tm/library/AppNotes/DCom/XStream_DS0s-Configuring_DCOM_Connectivity.pdf.
- [315] L. Corporation, *X-Stream Oscilloscopes: Remote Control Manual*, (2005) http://cdn.lecroy.com/files/manuals/wm-rcm-e_rev_d.pdf.

- [316] L. Corporation, *WaveMaster WavePro 7000 Series DDA5005 Serial Data Analyzerr Automation Manual*, (2003) http://cdn.lecroy.com/files/manuals/entire_x-stream_automation_manual.pdf.
- [317] T. O'Haver, *Filter: interactive Fourier Filter, version 3*, (2011) <http://terpconnect.umd.edu/~toh/spectrum/InteractiveFourierFilter.htm>.
- [318] E. E. Russell and E. E. Bell, "Measurement of the Optical Constants of Crystal Quartz in the Far Infrared with the Asymmetric Fourier-Transform Method", *J. Opt. Soc. Am.*, **57**, 341–348 (1967).
- [319] C. A. Schmuttenmaer, "Exploring Dynamics in the Far-Infrared with Terahertz Spectroscopy", *Chem. Rev.*, **104**, 1759–1779 (2004).
- [320] I. Pupeza, R. Wilk, and M. Koch, "Highly Accurate Optical Material Parameter Determination with THz Time-Domain Spectroscopy", *Opt. Express*, **15**, 4335–4350 (2007).
- [321] L. Duvillaret, F. Garet, and J. Coutaz, "Highly Precise Determination of Optical Constants and Sample Thickness in Terahertz Time-Domain Spectroscopy", *Appl. Opt.*, **38**, 409–415 (1999).
- [322] J. R. Birch, "The Far Infrared Optical Constants of Polyethylene", *Infrared Phys.*, **30**, 195–197 (1990).
- [323] R. S. Irving, *Integers, Polynomials, and Rings* (Springer, 2004).

Chapter 6

Appendices

6.1 Matlab Code for THz Scanning Software

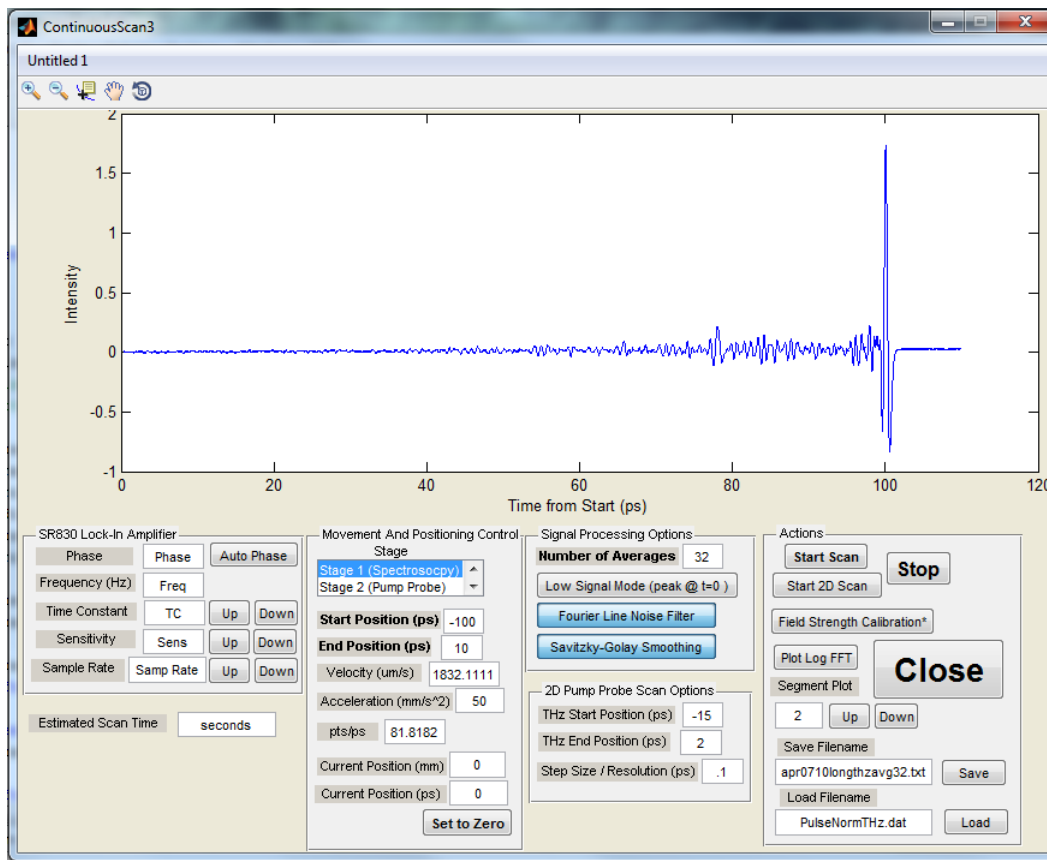


Figure 6.1: The graphical user interface for the continuous scan option for use with the lockin amplifier.

Two Matlab programs were written for use with, respectively, the lock-in amplifier (Figure 6.1, ContinuousScan3.m) and the oscilloscope (Figure 6.2, PulseNormalizationScan2.m). Some

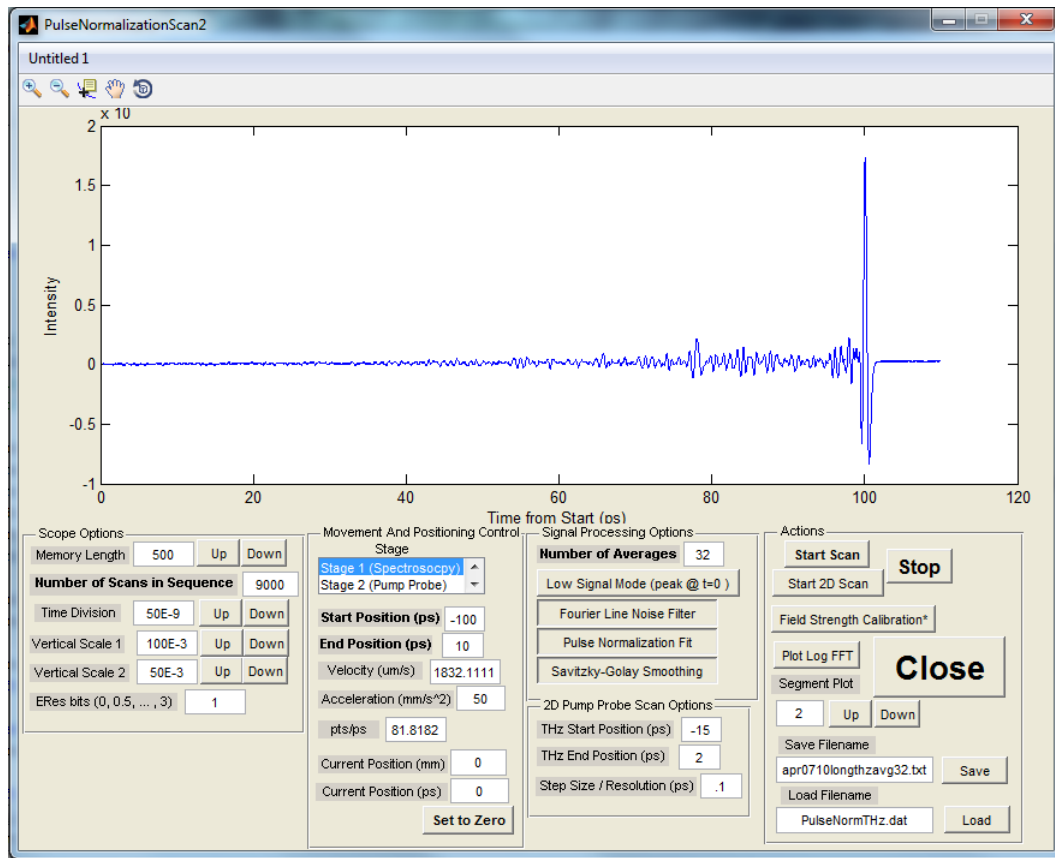


Figure 6.2: The graphical user interface for the pulse normalization scan option for use with the oscilloscope.

parts of the code are very similar in that the control of the delay line is accomplished by serial commands to the ESP300 motion controller. Data processing is also similar. The graphical user interface (GUI) was made using the GUIDE GUI builder, and these elements are common as well. The first function in a GUIDE made GUI is "GUIDE_OpeningFcn." This function activates all instruments, contains initialization parameters and settings, and displays them in the interface.

The most complicated thing about the Matlab code is the use of the handles structure. It is explained in the Help documentation, but what the user needs to know is that all variables or information that are to be used in other functions (i.e. global variables) need to use handles. For example, if I want to use a matrix $data = []$; in a different function which is not called from the previous function, I must instead call it *handles.data*. After updating any handle in a function

it is mandatory that you refresh the handles data using the following code: `guidata(hObject, handles)`).

Each interface object also has its own handle by default which is named with the interface object's title. When an object, such as a text box, for example, is constructed, the code is updated with two functions, one that executes upon the creation of the object, entitled "TextBoxName_CreateFcn()," and the other for when the object is activated, by, in this example, typing in the box and is entitled "TextBoxName_Callback()."

The most important function in the program is the `Start_Scan_Callback()` function, which moves the delay line, acquires data, processes data and stores it in memory. It also has the possibility of returning data if a 2D scan is being performed. This data is stored until it is saved to the hard disk or a new scan starts. First the equations of motion are solved for an actual starting and ending position, given a known velocity and acceleration in combination with the desired starting and ending positions of the region of the scan where the acceleration is 0 and velocity constant. Data is taken in this region. Inputs are generally in ps, since this is a more relevant scale for the position of the delay line in terms of a THz spectrum, as opposed to millimeters, the natural unit of the device. The delay line is double passed, so the conversion has a factor of two in combination with the speed of light. After the start location has been determined, the stage is rapidly moved there and given time to settle. The scan then begins and after the waiting time while the stage accelerates, and the lock-in amplifier or oscilloscope starts to take data. The Matlab program then waits the time anticipated for the scan and acquires the data from the device of choice. If the lock-in is used, the signal is directly proportional to the THz electric field strength. If the oscilloscope is used, methods must be employed to obtain information from each waveform. This is described more in Section 6.1.2. At this point, the THz waveform has been obtained and the process is repeated multiple times depending on the number of averages desired. It is observed that the position in the scan corresponding to the

maximum THz signal, “time zero” so to speak, often shifts from scan to scan. This is attributed to slight variation in the delay line start time changes from scan to scan. If data is averaged directly, the signal is diminished or broadened. To correct for this, if the signal for each scan is significantly above the noise, each maximum can be aligned in time. The edges of the data ranges of the scan, which are not common to all scans, are removed. If this mode is enabled and a maximum is incorrectly sensed, it will cause the data to be shortened significantly and improperly averaged. There is currently no way around this, so be sure to check your signal level before starting a long scan with this enabled. If a TR-THz scan is being performed and stage 2 is being scanned, the program seeks to align each scan to the inflection point. Again, noise in the signal can significantly reduce the effectiveness of this procedure. Two-dimensional scans can be performed as well, where THz scans can be taken as a function of pump-probe delay (stage 2). A range must be specified as well as a step size in units of picoseconds. Direct averaging and alignment of the time-zeros is currently unavailable in 2D mode. If averages are taken, one can plot each individually, without data processing applied to them, by using the segment plot functionality on the GUI. The “Close” button should be used when done using the GUI, so as to shut down the instruments correctly so that the program can successfully reconnect to the instruments when restarted.

Smoothing was typically done with the Savitzky-Golay algorithm with span rounded to the odd integer closest to the resolution divided by ten, with a minimum of three. This is not usually beneficial for lock-in data, but works well for the scope, where the THz waveform must be oversampled to avoid laser noise.

The FFT routine takes the modified data and gets the number of points in the data set. The number of points in the FFT is set to two raised to the next power of two greater than that number. The data is adjusted around its mean and then it is FFTed using the standard Matlab FFT method based on that of Cooley and Tukey [310]. The x-axis is generated linearly from

the resolution, which is effectively a sampling frequency. The extended DFT method of Liepiņš [311, 312] was tested and can provide, in some cases, higher resolution data in the THz band of interest when the data is oversampled. It can also, in principle handle nonuniform data sets, where the sampling is not exactly uniform. This functionality has not yet been successfully performed on a data set obtained by the Blake group, though the exact trigger time of each point in an oscilloscope scan can be obtained. If very precise data is required, this option should be considered.

ESP300handle1.m and ESP300handle2.m initialize the first and second stages. The standard passing of a command to the instrument in Matlab is:

```
fprintf(handles.obj, 'command');
```

where handles.obj is the Matlab handle for the serial instrument and 'command' has format: <stage number><command><value>, where the stage number is from 1-3, the command is a two letter abbreviation, and the value is either an integer or float depending on the command. Thus, a command to move stage number 2 to 1.3245 mm would be:

```
fprintf(handles.ESP300, '2PA1.3245');
```

The value can be replaced by a '?' to query the instrument if relevant. Some commands have no value associated with them. The manual, including details on all commands for this box, is readily available online [313]. A list of frequently used commands follows.

- AC - set acceleration

- AG - set deceleration

- DH - define home

- PA - move to absolute position

- PR - move to relative position

- ST - stop motion
- TP - tell (read) actual position - followed by fscanf(handles.obj);
- VA - set velocity

The data is saved in a y-x format. This originated from the way that data is acquired, with the y data being taken from the oscilloscope or lock-in and a time assigned after the fact.

6.1.1 Continuous Scan

The “Continuous Scan” program is the used with the lock-in amplifier. It is referred to as “Continuous” to differentiate it from the old, step-scanned, software, which is very inefficient in terms of the time required for one scan. The file lockin.m initializes the SR830 lock-in amplifier. A list of serial (RS232) commands can be found in the manual, of which there are numerous hard copies in the office. The command format is nearly identical to the delay line command format. A list of the most commonly used parameters follows. A list is established in the code to relate the SENS, OFLT, and SRAT integers to the actual values.

- PHAS - sets or queries the reference phase shift
- FREQ - sets or queries the reference frequency
- SENS - sets or queries the sensitivity integer parameter
- OFLT - sets or queries the time constant integer parameter
- SRAT - sets or queries the sample rate integer parameter
- STRT - starts data storage
- PAUS - pauses data storage
- REST - reset data storage buffer

- SPTS? - queries the number of points in the buffer
- TRCA? - data transfer command to obtain the buffer contents in ASCII format

The SR830 can store 16383 points of data in internal memory. This capability is used to perform a continuous scan. The downfall of this technique is that data transfer of that many points over the serial cable is extremely slow. A better method would be to pass the output of the locking into a simple data acquisition card in the computer running the Matlab program. This would allow for an increased number of points as well as faster transfers. The time data in this case is calculated based on the assumption that the lock-in's internal sampling is accurate. After many tests, this does seem to be the case, though sometimes averages with the same settings will have unequal number of points if a high sampling rate is used. Since oversampling is not helpful, attempt to avoid it if possible. Since the time required for a set of averages can be considerable, the time is estimated whenever the scan length, sampling rate, or resolution (the number of points per picosecond) is changed. The resolution is proportional to the sampling rate divided by the stage velocity. The maximum velocity should be kept quite low if high frequency coverage is desired, and the resolution is thus high. If the signal to noise is high, a faster chopping rate might be appropriate.

2D scans may not yet work with the lock-in based scanning program.

6.1.2 Pulse Normalization Scan

Initially the code for the oscilloscope was designed to accommodate pulse-to-pulse normalization to minimize the effect of laser noise every time the Legend fired. Thus, the code is entitled Pulse Normalization Scan, while, practically, this nomenclature is usually inaccurate since the pulse normalization setup is not used. It is to be used whenever the oscilloscope is used to acquire data. The scope is interacted with via two means, an active X control driver,

'Lecroy.ActiveDSOctrl1.1' and by using the XStream remote control via DCOM connectivity, in order to change more advance parameters like the enhanced resolution. The XStream software must be installed. I followed Lecroy's online instructions [314] to set up the XStream remote control, in combination with the fact that Windows requires you to have a password on the account in order to engage in networking, and it eventually worked. XStreamBrowser is also needed. It can be found at <http://ftp.lecroy.com> with login username: TechSupport and password: TechFiles4You.

A list of commands and variables for the ActiveDSO driver can be found in the online X-stream remote control manual [315]. Meanwhile, full control can be achieved by issuing scripts over DCOM and functionality is described by the automation manual [316]. For the ActiveDSO control in matlab, the format of a command is as follows:

```
invoke(handles.DSO, 'Command', 'String' (or 'Option'), true);
```

A list of those commands from the ActiveDSO driver used in the Matlab GUI are listed below:

- MakeConnection - Makes a connection to the oscilloscope on a given IP address
- GetNativeWaveform - Gets the waveform from the instrument
- WriteString - Sends a string based command to the instrument. A series of commands can be issued and separated by semicolons.
- ReadString - This command takes format `invoke(handles.DSO, 'WriteString', 1000);` where 1000 is the character length of the response.

A list of possible strings for the WriteString command follows. The string can be followed by a question mark to query the instrument.

- BUZZ BEEP - Makes the scope beep

- TDIV - Changes the time division
- C_n :VDIV - Changes the vertical division on channel n
- SEQ ON - Turns sequence mode on
- SEQ OFF - Turns sequence mode off
- TRMD AUTO - Sets the trigger mode to automatic
- TRMD SINGLE - Sets the trigger mode to single
- TRMD STOP - Sets the trigger mode to stop
- MSIZ - Data transfer command to obtain the buffer contents in ASCII format
- ARM - Arms the scope to begin acquisition after the next single trigger
- WAIT - Waits for acquisition to complete

The data is acquired in sequence mode, which stacks triggers back to back in one long waveform that is then transferred to the computer in one large chunk. This is limited in two ways. First, there are a maximum of 10,000 waveforms / triggers in one sequence mode acquisition. Secondly, it is limited by the memory of the scope (12.5 Mbyte). Each waveform is set to the minimum value of 500 points/bytes to allow for possible storage of the full number of triggers in a sequence, and to improve transfer speed. Depending on the time division value, the waveform length is reduced if the enhanced resolution, ERes, settings are used. The sequence mode acquisition then has 354 bytes of initial data that corresponds to the settings plus the number of waveforms in the sequence times the waveform length. Of this initial data, only the trigger time is of importance. This value is in a binary format and must be converted to double format, which is has value of seconds (fractional). A Matlab script, bin2double.m, was written to decode the data, however, the conversion is very slow. For speed's sake, linearity is

assumed on the time axis, and only the first, zero, and last points are used for generation of a time axis. The consequence of this is that the scans rely on the oscilloscope clock to generate a time and frequency axis. Any absolute difference is not noticed when comparing measured to reference transitions, since the resolution is quite low with respect to any anticipated offset. The values of the y-axis data of the waveform are unscaled and are unsigned integers. These values must be converted to signed integers because the convention, for whatever reason, is to have 0-127 correspond to positive values and 128-255 correspond to negative values and the scale is not linear. After this conversion, the area under the waveform is integrated numerically using the trapz method in Matlab. The trapz method fits trapezoids between each point on the curve. The error introduced by the trapezoidal approximation is less than 1 %. This area corresponds to the difference amplifier signal and is related to the THz electric field strength. An integration is used instead of simply the height because the shape of the amplified photodiode signal changes as the power increases. The validity of this assumption should be checked if precise field strength or relative intensity is required of a scan.

After acquisition, the THz waveform is processed in up to four ways to improve the observed waveform. The different signal processing options can be toggled on or off in the THz scanning software before the scan begins. First, filters of line-noise in the laser or electronics are removed, as 60 Hz and 120 Hz and multiples thereof are the dominant noise source. A numerical Fourier band pass filter was used to remove these spurs from the spectrum. The code is in the file FouFilter.m and was written by T. C. O'Haver [317]. The time-domain data is converted to the frequency domain via FFT, has the spurs removed and then is returned to the time-domain using an inverse FFT. The noise spurs are fit to the following Gaussian-like function of specified half-width to a transition at a specified frequency.

$$g = \exp \frac{-(x - x_{\text{position}})^{2n}}{0.6006 * x_{\text{width}}}, \quad (6.1)$$

where x_{position} is the center frequency and x_{width} is the width, and n is an integer that controls the 'squareness' of the filter and is set to four, in the pulse normalization code. Next, if pulse-to-pulse normalization has been performed, i.e. data has been taken on two channels, one being a reference, a least squares fit is performed in a region expected to be free from THz signal. This region is typically found in the region where the probe pulse arrives to the electro-optic crystal before the THz pulse, or before the optical pulse arrives, in the case of a TR-THz scan. This region is selected to be from the maximum THz signal plus 1 ps to the end of the scan (if scanning from negative values of time to positive values of time on the delay line) if high signal is expected; or 3 ps if low signal is expected (and consequently the center position is poorly known). Once this data is selected, a nonlinear least squares fit is performed using the Matlab function `lsqnonlin`. A series of functions of type $F = f(x) - c_1g(x) + c_2$ were generated at each point, where c_i are constants that are obtained from the fit and f and g are observed data from both channels that should be equivalent. These functions are then minimized since they should be as close to zero as possible. The output results are the constants and uncertainties. The THz data is corrected throughout the entire scan based on the parameters found for the initial region. After this, if each average in the scan is of sufficient signal-to-noise, the data is aligned in time to the point of highest intensity in the case of THz-TDS scan or to the inflection point in the case of a TR-THz scan. The data is then summed in order to average each scan. Lastly, since the data is oversampled when using the scope, this data can then safely be smoothed if a more visually appealing time-domain plot is desired. Note that this should not affect the THz frequency spectrum at all, and thus is unnecessary if only a frequency spectrum is desired.

6.2 Matlab Code for Optical Constant Determination

Two Matlab scripts were written. One describes a sample where $FP(\omega)$ of Equation 1.60 is set to 1, and the sample is surrounded by quartz windows. This is good for samples where the index is low, so that sample related reflections or etalons are minimal in amplitude or are well separated in time from the majority of the THz signal so that they can be safely disregarded. The other script is for samples which are not surrounded by quartz, commonly where the index is large or much different from the reference. Additionally, if the sample should be thin, and reflections cannot be separated from the main THz signal while maintaining a desirable THz resolution, the $FP(\omega)$ correction can be employed.

Since determination of both the real and imaginary optical constants is one of the defining features of THz-TDS, it is important to be able to readily extract both constants. The theoretical background is described in Section 1.1.5. Two Matlab scripts were written in order to determine both constants from the data. The first is applicable when the sample is surrounded on both sides by air. The other works when quartz windows surround the medium being analyzed. In principle it is simple to substitute the THz-inclusive Sellmeier-type equation of any material in place of that of quartz and the program becomes much more general. For quartz, the extraordinary ray data taken by asymmetric FT-IR [318] for the real and imaginary indices of refraction were fit to a 6th degree polynomial as functions of frequency and compared to the results from Grishkowsky *et al.* taken by THz-TDS [56]. The script takes the sample and reference time-domain data as inputs. A complex FFT is performed and the sample is divided by the reference. For each frequency in the FFT, this result is compared to an array of points with different values of $n(\omega)$ and $\kappa(\omega)$ since the solution to Equation 1.60 cannot be found analytically. The experimental data must be phase corrected, trending towards 0 near $\omega = 0$. The phase of the sample data must also be corrected so that it trends towards 0 when

$n = 1$. This can be rationalized by the fact that n of less than 1 is impossible for the group velocity. It also gives the correct answer when this condition is met, whereas the wrong answer is found otherwise. The first point is taken from the highest frequency desired in the output, a parameter that can be set in the program. The default is 3 THz. The noise here is actually lower than at the lower frequencies due to scaling with the value of ω . The initial values of the optical constants are found using a grid of 100 by 100 points. Following the procedure of Duvillaret *et al.* [113] and the supplementary information from Reference [116], the minimum of the function

$$\delta(n, \kappa) = \delta\rho(n, \kappa)^2 + \delta\phi(n, \kappa)^2 \quad (6.2)$$

was found, where

$$\delta\rho(n, \kappa) = \ln(|H_{\text{test}}(\omega)|) - \ln(|H_{\text{exp}}|), \quad (6.3)$$

and

$$\delta\phi(n, \kappa) = \arg(H_{\text{test}}(\omega)) - \arg(H_{\text{exp}}), \quad (6.4)$$

where $H_{\text{test}}(\omega)$ is tabulated in the above mentioned grid and then minimized. This procedure avoids the ineffectiveness of the Newton-Raphson method as solved for an oscillating function [113], while not being as computationally efficient. With regards to the efficiency, it is simply not required using modern computers and calculations take a matter of seconds for the entire range. Several iterations are performed in order to lower the variance in the previously determined coefficients to less than 1e-6. Example figures of the real and imaginary index of chloroform are shown in Figures 6.4 and 6.3. The noise seen is a result of reflections in the detector crystal that are not removed by the routine. The data can be safely smoothed and the result is shown as well. This compares very well to previously reported constants measured via THz spectroscopy [319]. Such calculations might be improved by considering the improvements of Pupeza *et al.*

[320] and DuVillaret *et al.* [321], wherein the sample length is also accurately determined from the data, and by reducing the effect of etalon reflections in the sample and detector. An attempt was made to include Fabry-Perot related reflections. This is described in the following section.

The Fabry-Perot correction is calculated as

$$\text{FP}(\omega) = \frac{1}{1 - \left(\frac{\tilde{n}_2 - \tilde{n}_1}{\tilde{n}_2 + \tilde{n}_1}\right) \left(\frac{\tilde{n}_2 - \tilde{n}_3}{\tilde{n}_2 + \tilde{n}_3}\right) \cdot \exp\left[-2i\tilde{n}_2 \frac{\omega L}{c}\right]}. \quad (6.5)$$

In the approximation of $\text{FP}(\omega)$, the optical constants are first approximated. The real index is easily approximated as

$$n_2 \simeq n_{\text{subst}} + \frac{\arg(T_{\text{meas}}(\omega))}{\omega L/c}. \quad (6.6)$$

The imaginary index is much more complicated and requires the solving of a cubic equation of form

$$AX^3 + X \simeq D \quad (6.7)$$

where

$$X = \exp\left[-\kappa_2 \frac{\omega L}{c}\right], \quad (6.8)$$

and

$$A = \frac{(n_2 - n_1)(n_2 - n_3)}{(n_2 + n_1)(n_2 + n_3)} \cdot \cos\left(2n_2 \frac{\omega L}{c}\right), \quad (6.9)$$

and

$$D = \frac{(n_2 + n_1)(n_2 + n_3)}{2n_2(n_1 + n_3)} \exp\left[-\kappa_{\text{subst}} \frac{\omega L}{c}\right] \cdot |T_{\text{meas}}(\omega)|. \quad (6.10)$$

The optical constants n_{subst} and κ_{subst} represent the medium that has been substituted by the sample from the reference case. In this case, the substituted material is high-density polyethylene, and so the optical constants of that are used [322]. The roots of the cubic equation can be found via Cardano's method, or a generic 3rd order polynomial solution [323]. There are

always three roots; however, depending on the coefficients, there are either three real or one real and two imaginary roots. Since the listed solutions for the roots, either from Cardano's method or otherwise, do not work for all cases, the correct root formulas were identified through empirical testing. Also, Matlab has two methods of finding the n th root of a number. The *nthroot* command gives the real solution and requires that the operand be real. Secondly, if a number is raised to the to the $1/n$ th power, the operand can be complex, but the result favors the complex solution if both real and imaginary solutions exist, for example if the operand is negative or possibly complex. If

$$\frac{D}{2A} - \sqrt{\frac{D^2}{4A^2} + \frac{1}{27A^3}} \quad (6.11)$$

is complex or imaginary then the desired root is

$$X = \frac{(1 + i * \sqrt{3})}{6A} \left(\frac{1}{2}(27A^2 - D + \sqrt{-27 * A^2 * \delta}) \right)^{\frac{1}{3}} + \frac{(1 - i * \sqrt{3})}{6A} \left(\frac{1}{2}(27A^2 - D + \sqrt{-27 * A^2 * \delta}) \right)^{\frac{1}{3}}, \quad (6.12)$$

where

$$\delta = -4A - 27A^2D^2. \quad (6.13)$$

Otherwise the desired root is

$$X = \sqrt[3]{\frac{D}{2A} - \sqrt{\frac{D^2}{4A^2} + \frac{1}{27A^3}}} - \frac{1}{3A \sqrt[3]{\frac{D}{2A} - \sqrt{\frac{D^2}{4A^2} + \frac{1}{27A^3}}}}, \quad (6.14)$$

where the *nthroot* function is used because the operand is real, and there is only one real solution. In the case that κ_2 is complex, which occurs when X is negative due to noise, the value from the previously determined real solution is used to keep $\kappa(\omega)$ continuous. $\text{FP}(\omega)$ is then estimated and T_{meas} is divided by it to remove oscillations, and then the procedure of the previous section is used and the estimation procedure is repeated.

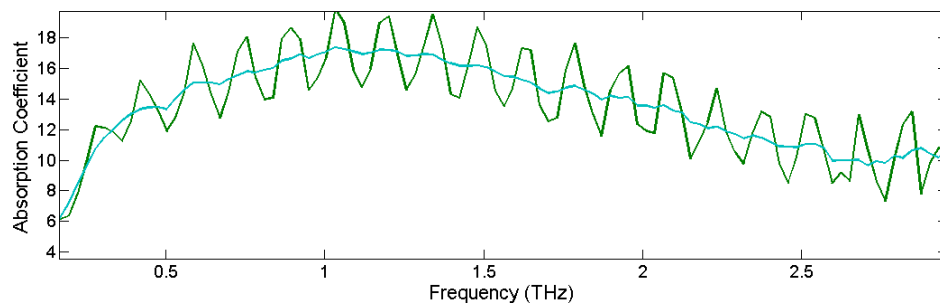


Figure 6.3: The absorption coefficient of chloroform, $\alpha(\omega)$, cm^{-1} , measured in 1 cm pathlength between two quartz windows.

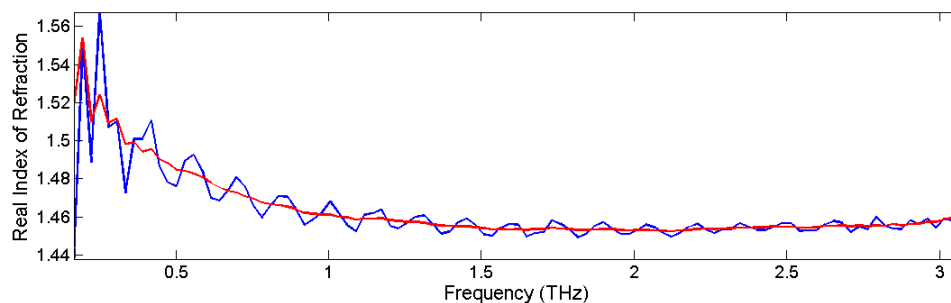


Figure 6.4: The real index of refraction, $n(\omega)$, of chloroform measured in 1 cm pathlength between two quartz windows.

6.3 Laser Alignment and Maintenance

Ideally, we would not have to do much to maintain the lasers. Unfortunately, this is not the case and something is almost always not working properly or up to spec. It is important to take data during times when everything is working. For basic maintenance, the water in the chillers should be changed every six months and corrosion inhibitor added in the appropriate amount (Optishield II, 10% by volume). The oscillators should have the back crystal face cleaned at least every month, but typically more frequently when the CW or mode-locked power has dropped by $\sim 20\%$. Monitor this daily and record it in a notebook or on the computer. Whenever the oscillator is cleaned or realigned at all, the Legend must be reseeded. This procedure is fairly simple once you have done it a few times and have practiced using mirror pairs to control the position and angle of the beam on the entrance to the Legend and as it propagates towards the

grating. A check of the stretcher grating with the IR viewer should show the pattern shown on page 5-9 of the Legend manual.

6.3.1 Mantis

The Mantis manual is particularly insufficient. I attempt to remedy this here.

The first step towards resolving any optical problem is cleaning. Gloves should be worn at all times when the case is open. Coherent oscillators are particularly sensitive to dirt on the crystal, particularly on the back side, nearest to M5 (D2). Many oscillator problems begin with this. It is important to realize that every time you open the Mantis case, you are exposing the inside to more dirt, dust, hair, and oil. Clean the bottom of the laser case as well. If you are unsure if you are doing a good job cleaning (it is very easy to do more harm than good), check the CW power before and after each optic is cleaned.

The Mantis output power should be turned to minimum. The green pump light will appear to speckle or reflect off of a very dirty crystal. This is much easier to see on the Micra, because the pump beam rasters. Cleaning all optics is best achieved by folding approximately 7 pieces of lens cleaning tissue lengthwise 3 times, ideally without touching the tissue with your gloved hand, but only with clean hemostats, and clamped with a clean hemostat. Using another clean hemostat, grab a section of paper a few millimeters away from the edge. Using clean scissors, cut the paper with length equivalent to the diameter or length of the surface to be cleaned. Using a dropper, apply a few drops of fresh and pure solvent to the paper. It is critical not to use too much solvent, since cleaning is mostly achieved by the wicking away of dirt, dust, and debris caused by rapidly evaporating solvent. If the solvent does not evaporate quickly, the dirt can dissolve or float in the solvent adhered to the optical surface and leave behind spots. If cleaning a mirror, typically one is able to do one swipe per side of the lens tissue to speed up the process and conserve tissue. This is different to cleaning the crystal. The crystal

is primarily sapphire, $\alpha\text{-Al}_2\text{O}_3$, which has a Mohs hardness of 9, and as such, is not easily scratched, unlike other optical coatings. To remove buildup, several steps should be performed. First, using acetone or methanol, scrub the back face of the crystal being careful to avoid the gold crystal holder, as you can easily contaminate the crystal face and make things worse. Also avoid touching the crystal with the metal hemostat. After scrubbing, take a new piece of lens tissue and wipe as if cleaning a standard optic. Repeat until you have reestablished good lasing conditions. In some cases, if you cannot achieve a clean crystal face, you may need to use deionized water as a solvent in the rubbing step. Sapphire is mildly hygroscopic, so be prepared to immediately wipe with acetone afterwards. If you are confident that cleaning is not the cause of your troubles, proceed to optical alignment.

Beyond cleaning, the alignment may need to be adjusted slightly from time to time. The procedure for fixing the laser depends on the problem. Among the common problems are: low power, trouble modelocking, low mode-locked power, and a complete lack of lasing. It cannot be emphasized enough: **the first step is ALWAYS cleaning**, as this may fix your problem. Nearly all of the characteristics of the laser are determined by the extent and angle of overlap of the pump beam and the 800 nm NIR beam in the crystal. The sole exception to this is the bandwidth as determined by the wedge positions, and very slightly on the angles of the four negative dispersion mirrors. The appropriate pattern on M5 as viewed by an IR viewer is much closer to centered than the Micra or Mantis manual suggests. The vast majority of mirrors in the cavity are irrelevant and are solely turning mirrors. The ability to lase through apertures placed between various mirrors is largely irrelevant as more than a check of alignment. As such, the general order for adjustment is as follows: 1.) A single mirror (M3 or M1 most commonly since M3 fails the “tap - test” and is possibly unstable to mechanical vibrations) 2.) The combination of M14 and then M1 to compensate 3.) the D2 micrometer, which moves M5 to and from the crystal and lastly, 4.) the angle of M5 or M6. It is highly recommended to

avoid large changes to D2 and to never adjust the angle of M5 or M6 if at all possible. Read the next paragraph before making adjustments. Never solely attempt to maximize CW power, as this may lead you to the wrong alignment. Once the laser is mode-locked, the power can be maximized safely.

Before adjusting anything, check the pump power before the pump mirror. It should read within 5 % of the set point. If it is low, increase the pump power until it is at or near 5 W, or clean the laser window. If there is reason to believe that the pump beam has moved, reduce the power and ensure that it is as close to centered on irises placed along the beam path, before the beam dump, and between M4 and M5. Very small changes in the pump alignment can require large changes to the IR cavity. Some Coherent representatives will recommend adjusting the pump mirrors. While possibly valid, I very much disagree with this approach since they are so sensitive. If there is no lasing, place a photodiode-based power meter outside the case and adjust M14 and M1 iteratively along both horizontal and vertical axes, maximising the power on the photodiode. This corresponds to maximizing the pump fluorescence transmitted through the cavity by each “leg”. Alternatively, a notecard and IR viewer can be used near the output face of the laser box. The fluorescence spots should be moved to converge on the center of the output coupler. At some point the laser will begin to lase. Make a brief effort to increase the CW output power. As indicated in the previous paragraph, the attempt to maximize the CW power will most likely only lead you to the wrong alignment if the CW wavelength is incorrect. At this point, the goal is to achieve mode-locked operation. Once the laser is mode-locked, it can be optimized for output power by optimizing both axes of M14 and M1. If pressing the starter in a couple times does not achieve it, switch to a thermal detector and use a spectrometer to simultaneously check the output spectrum. The CW wavelength is stable at one of two or three values ranging between 800 and 830 nm. Stable modelocking will occur when the CW power is > 300 mW and the spectrum is in the most blue of the two most stable wavelength

modes. Observe the pattern on M5 with an IR viewer. Typically the NIR spot will be on the left side of the pump spot (thermal emission). If power is low, typically the NIR beam must be walked to the left by adjusting M14 and compensating with M1. If more stable mode locking is required, walk the NIR beam to the right, corresponding in a decrease in the CW wavelength, provided that the power remains sufficient. Small changes can be made to the D2 micrometer to favor modelocking as well. Be sure to record any such changes. Lastly, if all else fails, the angle of the M5 or M6 can be adjusted. If you reach this point, you will have already achieved laser-zen, and this guide will no longer help you. Generally Coherent recommends that the ratio of CW to mode-locked power be greater than 0.8 for output stability and jitter. I have not tested these claims. If possible, try to keep the ratio as high as possible.

6.4 THz Optical Alignment

The THz optical alignment is mostly concerned with ensuring equal light transit times in both arms of the spectrometer, the optical pump plus THz pulse arm and the optical probe arm. This time can be approximated by the distance that the pulses travel if the distance traveled in optics and other non-air materials with high index is low. If the index and thickness of these materials is known, the exact match can be calculated. Usually this is not necessary and it is faster to get close enough so that the strongest signal can be found somewhere on the delay line, look for signal, and adjust distances after the fact.

Alignment of the balance electro-optic detection setup is very sensitive to the polarization and timing of the pulses on the detectors. In order to achieve well-balanced detection, the same length of BNC cable should be used since impedance matching is necessary for the pulses to align in time in the difference frequency amplifier. If electronics do not cause any issues but the signals are not equal, check the optical beams and ensure that the beam does not clip on

any aperture or at the entrance to the prism. The beam must be centered on the detectors and should not overfill the detector. The EO probe beam should be focused onto the detector so as to minimize the effects of the delay line travel. Move each detector in both horizontal and vertical directions to maximize the signal. Be sure that the detector is normal to the direction of travel of the beam, as a tilted detector will illuminate more of the photodiode surface and will artificially give additional signal in that detector. Note that if BBO is used to produce SHG at the output of the Legend, any adjustment to it will change the polarization of the probe beam and will unbalance the detection.

6.5 Autocorrelator

We have a Delta single shot autocorrelator (SSA) that was purchased from Minioptic. The autocorrelator is cheaper than others due to the design of a triangular shaped interferometer and a small, compact component set. The geometry of the pulses going through the crystal are such that the geometrical width of the 2nd harmonic pulse relates to the pulse duration. A CCD array senses this. For pulses less than ~ 50 fs, a cylindrical lens must be used to disperse the pulse to avoid pixelation. This was included with the Delta SSA. Operation of the Delta SSA is well described by the manual, however it is sometimes difficult to find signal when first using the SSA. There are many things to adjust to increase the signal obtained from the SSA. First, ensure that the beam enters at the level of the SSA and is level with the table. The beam should pass through the center of the input iris (which should be open), the $\lambda/2$ waveplate, and hit the first mirror in the center. After this is achieved, securely fasten the SSA base to the optical table. There should be approximately equal intensity in both beams after the beamsplitter, and the beams should be centered on the β -BBO crystal. Use an IR viewer or IR card, or a combination of both, and rotate the entire SSA about its optical post to ensure that the beams

cross in the crystal. Now, turn out the lights if necessary and rotate the crystal and check for three blue spots. Two arise from the input pulses and should be rather large. These should always be visible if short pulses with sufficient intensity are used. They are seen when the BBO crystal is angled with respect to the axes of the autocorrelator. Check the vertical position with respect to the CCD entrance slit. If they are not centered on this, adjust axes of the stage of the autocorrelator platform to reposition them. The autocorrelation signal should appear as a vertically directed, very narrow blue line. The BBO crystal should be oriented approximately parallel to the CCD slit and to the short side of the SSA box. Sometimes the autocorrelation signal will be quite weak. First check the SSA output on an oscilloscope. If you cannot find the signal, do *not* adjust the micrometer controlling the delay between the pulses until you are certain it needs to be adjusted. Typically the center position does not vary much between uses and signal can be found without tweaking this micrometer. For reference, the position is typically $\sim 1.47 \pm 5$. The first thing to try is adjusting the polarization of the input beam. Remember the initial position and slightly adjust the waveplate. If it is off, typically because someone last used an input beam of the opposite polarization, you should be able to see signal even with a small rotation. If this does not appear to be a problem, recheck overlap of the beams in the crystal in all three directions and then tweak the micrometer slightly. You should see signal. Tweak all of the above mentioned parameters to optimize the signal. Attenuate the input to the autocorrelator or place neutral density filters in front of the CCD slit so as to avoid saturation of the CCD. This saturation is very common when using pulses from the Legend. The Legend pulses at the output of the laser were measured to have a duration of 36.2 fs FWHM.